UNIVERSITY OF COPENHAGEN
FACULTY OF SCIENCE

PhD Thesis

Carlos Francisco Castro Soto Reyes

The crustal and sedimentary structure of the Amundsen Basin, Arctic Ocean, derived from seismic reflection and refraction data

Supervisor: Klaus Mosegaard

Submitted on: 1 August 2018

Name of department:	Niels Bohr Institute
Author(s):	Carlos Francisco Castro Soto Reyes
Title and subtitle:	The crustal and sedimentary structure of the Amundsen Basin, Arctic Ocean, derived from seismic reflection and refraction data
Supervisor:	Klaus Mosegaard
Submitted on:	1 August 2018

Cover photo: *Icebreaker Odin* by Åsa Lindgren

Table of contents

Preface and Acknowledgements

This dissertation presents a study of the velocity structure of the crust in the Amundsen Basin, Arctic Ocean, as well as the basin's ensuing depositional history. This region is only poorly studied due to the challenges of acquiring geophysical data in areas with permanent sea ice cover. However, scientific activity increased over the last decade when coastal states started to map their extended continental shelves under the United Nations Convention on the Law of the Sea (UNCLOS). From 2007 to 2012, the Kingdom of Denmark carried out three expeditions to the Arctic Ocean utilizing the Swedish icebreaker *Oden*. The expeditions acquired a total of 1020 km of seismic reflection data. In addition, 118 expendable sonobuoys were deployed along the seismic lines to obtain information on the velocity structure in the underground. The seismic data collected during these cruises forms the basis of this dissertation.

The dissertation consists of a monograph divided into four sections:

- **Chapter I** is an introduction to the research project in the context of state-of-the art. This section addresses our motivation to study the crustal character of the Amundsen Basin as well as its sedimentary depositional history.
- **Chapter II** is a chapter entitled: *The crustal structure of the western Amundsen Basin derived from refraction/wide-angle reflection seismic data*. The section investigates the crustal structure of the Amundsen Basin by developing P-wave velocity models for the sediments and the underlying crust. In addition, empirical relationships were used to convert seismic velocities to density in order to check the consistency of the velocity models with gravity data. This chapter is written as a paper in preparation.
- **Chapter III** is a chapter entitled: *Depositional evolution of the western Amundsen Basin, Arctic Ocean: paleoceanographic and tectonic implications*. This section presents a new stratigraphic model and estimated sedimentation rates of the western Amundsen Basin based

on seismic data, magnetic data, and limited samples from cores and drilling. Four distinct phases of basin development are proposed that places new constraints on the Cenozoic depositional history of the basin. This section is currently a manuscript under review at *AGU Paleoceanography and Paleoclimatology*.

- **Chapter IV** is a conclusion and perspectives for further research.
- An **Appendix** containing all of the modeled record sections of the sonobuoy data. Information regarding access to data and databases archived at GEUS is available at https://www.geus.dk.

Acknowledgements

This work was supported by a scholarship from the Consejo Nacional de Ciencia y Tecnología (CONACYT). Data acquisition was funded by the Continental Shelf Project of the Kingdom of Denmark. Many thanks go to Arne Døssing (National Space Institute, DTU Space) and John Hopper (Geological Survey of Denmark and Greenland) for their assistance in the processing of gravity data and multichannel reflection seismic data. Special thanks to Lars Kjærgaard for his assistance with the loading of multichannel seismic reflection data and GEUS-IT for all their technical support.

I deeply thank my advisor, Thomas Funck, for his instrumental support throughout the entire process and for pushing me to become the scientist that I am today. I would like to express my gratitude to Klaus Mosegaard, my supervisor from Niels Bohr Institute, for providing support in administrative matters. I am also grateful to my coauthors, Paul Knutz and John Hopper from GEUS, for their valuable support and sound advice.

I want to thank my colleagues at the Geophysics Department at GEUS for always being friendly and welcoming. To my colleagues and friends Julia, Elina, and Katrien, I am will always be deeply grateful for your support, your kindness, and for the warm memories.

Agradezco profundamente a mi familia que siempre me ha apoyado incondicionamente en todas mis metas y esfuerzos. Los quiero mucho.

Till min fru, tack för din oöverträffade stöd alla dessa år. Jag är alltid tacksam och jag älskar dig.

English Summary

The Amundsen Basin is the deepest abyssal plain in the Arctic Ocean that separates the continental Lomonosov Ridge from the Gakkel Ridge, the current seafloor spreading axis in the Eurasian Basin. The basin was created by ultraslow seafloor spreading at the Gakkel Ridge and consists of alternating magmatic and amagmatic ridge segments; however, it is unclear if this is true for the entire opening history of the basin. The sedimentary history of the basin is still poorly constrained due to perennial sea ice cover and the associated logistical challenges of acquiring geophysical, geological and in particular also well data. This dissertation analyses one of the few geophysical data sets available for the western Amundsen Basin to improve the understanding of both the stratigraphic and the crustal accretional history of the basin.

From 2007 to 2012, three expeditions (LOMROG I through III) were carried out to acquire seismic data in the western Amundsen Basin in the Arctic Ocean. The data of the LOMROG expeditions consist of 1028 km of seismic reflection data and 118 sonobuoys deployed along the seismic lines to obtain information on the velocity structure of the sediments and crust. For the analysis and interpretation, additional information was used including published multichannel seismic data in the Amundsen Basin, refraction seismic data, magnetic data, gravity data, and the wells of the Arctic Coring Expedition (ACEX).

The seismic refraction data were used to develop P-wave velocity models for the sediments, crust, and uppermost mantle utilizing forward modeling techniques of travel times. The initial geometry of the sediment layers in the models were made in combination with the coincident multichannel seismic data, allowing to add more detail down to the basement than what would have been possible with refraction data alone. The multichannel seismic data were used to develop a stratigraphic model based on the reflection character, seismic facies, and geometries of each stratigraphic unit. Once both the velocity and the stratigraphic models were complete, sedimentation rates were calculated for each unit based on the velocities obtained from the refraction data, two-way travel times in the seismic reflection data, and age constraints from magnetic data and known tectonic and oceanographic events in the Arctic Ocean. The sedimentation rates were then used to infer possible depositional environments within the basin's history.

The seismic stratigraphy analysis places new constraints on the Cenozoic depositional history. Four distinct phases of basin development are recognized. From the onset of spreading up to the mid-Oligocene, a small, isolated basin dominated by processes that are tectonically controlled is indicated. During the late Oligocene to early Miocene, widespread passive infill associated with hemipelagic deposition reflects a phase of tectonic quiescence, most likely in a freshwater estuarine setting. During the middle Miocene, mounded sedimentary build-ups along the Lomonosov Ridge suggest the onset of geostrophic bottom-currents that likely formed in response to a deepening and widening of the Fram Strait. In contrast, the Plio–Pleistocene stage is characterized by erosional features such as scarps and channels adjacent to levee accumulations, indicative of a change to a higher-energy environment. These deposits are suggested to be partly associated with dense shelf water-mass plumes driven by supercooling and brine formation originating below thick multi-year sea-ice over the northern Greenland continental shelf.

P-wave modeling of the crust and upper mantle was supplemented with gravity modeling in order to determine the Moho depth in areas with low seismic resolution. The velocity models reveal a detailed picture of the crustal velocity structure of the basin. Three distinct basement types are identified: oceanic crust with layers 2 and 3, oceanic crust with a layer 3 that is absent, and an exhumed and serpentinized mantle. The total maximum observed thickness in the basin is 6 km but typically ranges between 2–5 km. Moreover, the seismic modeling indicates the presence of velocities compatible with an oceanic layer 2 and 3 within the extensions of the amagmatic sector of the Gakkel Ridge. These results are different than previous observations along the Gakkel Ridge, where no oceanic layer 3 has been documented. The different basement types therefore indicate that there exists both a spatial and temporal variation in crustal accretion processes at the ridge.

Dansk Resumé

Amundsen Bassinet er den dybeste abyssale slette i det Arktiske Ocean, og adskiller den kontinentale Lomonosov Ryggen fra Gakkel Ryggen – den nuværende oceanbundsspredningsakse i det Eurasiske Basin. Bassinet blev dannet ved meget langsom havbundsspredning langs Gakkel Ryggen og består skiftevis af magmatiske og amagmatiske sedimenter langs oceanryggen; det er dog uklart, om dette er tilfældet gennem hele åbningsforløbet for bassindannelsen. På grund af flerårigt havisdække er forståelsen af bassinets aflejringshistorie stadig begrænset, hvilket også hænger sammen med de logistiske udfordringer ved at indsamle geofysiske og geologiske data, og i særdeleshed fra boringer. I denne afhandling analyseres et af de få tilgængelige geofysiske datasæt for det vestlige Amundsen Bassin for at øge forståelsen af både den stratigrafiske udvikling samt skorpedannelseshistorien i bassinet.

I perioden 2007-2012 blev der foretaget tre ekspeditioner i det Arktiske Ocean (LOMROG I-III) for at indsamle seismisk data i det vestlige Amundsen Bassin. Dataene fra LOMROG ekspeditionerne består af 1028 km refleksionsseismik samt 118 sonarbøjer, som var placeret langs med de seismiske linjer for at indsamle information om hastighedsfordeling i sedimenterne og skorpen. Til analysen og fortolkningen blev der yderligere anvendt publiceret multikanal seismisk data fra Amundsen Bassinet samt, blandt andet, refraktionsseismisk data, magnetisk data, gravimetrisk data og boringerne fra Arctic Coring Expedition (ACEX).

Gennem modellering af løbetider blev de refraktionsseismiske data brugt til at udvikle P-bølgehastigheder for sedimenterne, skorpen og den øverste del af kappen. Den indledende geometri for sedimentlagene i modellen blev genereret i kombination med de sammenfaldende multikanal seismiske data, hvilket muliggjorde en højere opløselighed af detaljer ned til grundfjeldet, end det ville have været muligt med refraktionsdata alene. Baseret på refleksionens karakter, de seismiske facies og geometrierne for hver enhed, blev multikanal-dataene brugt til at udvikle en stratigrafisk model. Efter færdiggørelsen af hastighedsmodellen og den stratigrafiske model blev sedimentationsrater udregnet for hver enhed, baseret på hastigheder fra de refraktionsseismiske data, to-vejs-tider i de refleksionsseismiske data, aldersbegrænsninger fra de magnetiske data samt kendte tektoniske og oceanografiske begivenheder i det Arktiske Ocean. Sedimenteringsraterne blev derefter brugt til at udlede mulige aflejringsmiljøer inden for bassinet historie.

Analysen af den seismiske stratigrafi sætter nye rammer for den Kænozoiske aflejringshistorie. Der er identificeret fire markante faser i bassinudviklingen. Fra begyndelsen af spredningen og op til Midt Oligocæn ses indikation på et isoleret mindre bassin domineret af tektonisk kontrollerede processer. Gennem Sen Oligocæn til Tidlig Miocæn ses en udbredt passiv sedimentation associeret med hemipelagisk aflejring, som afspejler en tektonisk rolig periode, formentlig i et estuarint ferskvandsmiljø. Opbygning af sedimenter langs med Lomonosov Ryggen i løbet af Midt Miocæn foreslår begyndelsen af geostrofiske bund-strømme, som formentlig blev dannet som resultat af, at Fram Strædet blev dybere og bredere. I kontrast til dette, er det Pliocæne-Pleistocæne stadie karakteriseret af erosive elementer, såsom skrænter og kanaler med tilstødende levée-aflejringer, hvilket indikerer et skift i aflejringsmiljøet til et højere energiniveau. Det er foreslået, at disse aflejringer er delvist associeret med kompakte ”shelf water-mass plumes” drevet af underafkøling og saltvandsdannelse, hvilket er opstået under tykke lag af flereårig havis over den grønlandske kontinentalsokkel.

P-bølge modellering af skorpen og den øvre kappe blev suppleret med gravimetrisk modellering for at bestemme dybden til Moho i områder med lav seismisk opløsning. Hastighedsmodellerne afslører et detaljeret billede af skorpens hastighedsfordeling i bassinet. Tre markante grundfjeldstyper er identificeret: Oceanbundsskorpe med lag 2 og 3, oceanbundsskorpe med et manglende lag 3 samt blottet og serpentiniseret kappe. Den maksimale tykkelse observeret i bassinet er 6 km, men ligger typisk mellem 2 og 5 km. Derudover indikerer den seismiske model tilstedeværelsen af hastigheder, der er kompatible med ”oceanic layer” 2 og 3 inden for udbredelsen af den amagmatiske sektor langs med Gakkel Ryggen (SMZ). Disse resultater afviger fra tidligere observationer langs med Gakkel Ryggen, hvor ”oceanic layer 3” ikke er dokumenteret tidligere. De forskellige grundfjeldstyper indikerer derfor, at der er både rummelig og midlertidig variation i processerne for skorpetilvækst langs ryggen.

List of Abbreviations

ACEX – Arctic Coring Expedition

AMORE – Arctic Mid-Ocean Ridge Expedition

AWI – Alfred Wegener Institute for Polar Research

BS – Barents Shelf

CB – Canada Basin

CK – *Chernykh and Krylov* [2011].

CK92 – *Cande and Kent* [1992]

CK95 – *Cande and Kent* [1995]

EAB – Eastern Amundsen Basin

ESS – East Siberian Shelf

EVZ – Eastern Volcanic Zone

EI – Ellesmere Island

FS – Fram Strait

GEUS – Geological Survey of Denmark and Greenland

GR – Gakkel Ridge

IBCAO – International Bathymetric Chart of the Arctic Ocean

IODP – Integrated Ocean Drilling Program

ka – thousand years

KS – Kara Shelf

LOMROG – Lomonosov Ridge off Greenland

LR – Lomonosov Ridge

LRP – Lomonosov Ridge Plateau

LS – Lincoln Shelf

LVS – Laptev Shelf

Ma – million years

MJR - Morris Jessup Rise

NB – Nansen Basin

NS – Nares Strait

OBS – ocean bottom seismometer

O12 – *Ogg* [2012]

RU – Russia

SAT – St. Anna Trough

SI – Supplementary Information

SMZ – Sparsely Magmatic Zone

TWT – two-way travel time

UNCLOS – United Nations Convention on the Law of the Sea

WAB – Western Amundsen Basin

WVZ – Western Volcanic Zone

YP – Yermak Plateau.

Chapter I

Introduction

The Amundsen Basin, named after the Norwegian polar explorer Roald Amundsen, is the deepest abyssal plain in the Arctic Ocean (Chapter II, Fig. 1). The 4.3 km-deep basin forms part of the greater Eurasian Basin and is located between the Lomonosov Ridge, a continental sliver, and the Gakkel Ridge, the current seafloor spreading axis in the Eurasian Basin. The basin is situated in the high Arctic and, due to the basin's remoteness and inaccessibility, remains an exciting frontier region for scientific exploration. Only during the last decades were scientists able to collect significant geophysical information about the basin's character and geological history.

Today, the Amundsen Basin is part of the world's slowest spreading system, with full spreading rates decreasing from 14.6 mm/yr at the western end to 6.3 mm/yr in the Laptev Sea [*DeMets et al*., 1994]. Ultraslow accretionary ridges, such as the Gakkel Ridge, differ fundamentally from other faster spreading centers. Typically, seafloor spreading is a process where mantle material rises, decompresses, and melts [*McKenzie and Bickle*, 1988]. The newly formed magma then ascends towards the surface and gathers into magma chambers in the shallow crust. Some of the magma is ejected to the surface, while the rest cools in place, creating the distinctive ~6–7 km thick [*White et al*., 2001] layered structure of pillow basalts, sheeted dikes, and gabbro [*Snow and Edmonds*, 2007]. When new melt material rises and is emplaced, the older material is pushed gradually away from the ridge, thus enabling the formation of new crust.

Ultraslow ridges are different from faster spreading ridges because they do not always involve decompressional melting. Previous geophysical studies along the Gakkel Ridge [e.g., *Jokat et al*., 2003; *Michael et al*., 2003] and the South West Indian Ridge [*Dick et al*., 2003] have shown that ultraslow spreading ridges consist of linked magmatic and amagmatic accretionary segments. Thus, some segments of the ridges are marked by unmelted mantle material that has been exhumed at the seafloor. The mantle material then comes into contact with seawater and starts a metamorphic process that changes the mantle rock peridotite into serpentinite, thereby reducing its density and rheological strength [*Hirth and Guillot*, 2013]. This process is known as serpentinization and is commonly found in highly fractured and thin crust where water penetration is possible. Intense faulting, in addition to the variable melt supply generally found at ultraslow spreading rates, produces substantial topography and relief that is conserved in the older oceanic crust. This process results in a rough basement topography [*Ehlers and Jokat*, 2009] and various crustal structures marked by magmatic oceanic crust and different degrees of mantle serpentinization.

Ultraslow spreading ridges remain a poorly understood type of plate boundary. Limited seismic refraction studies have imaged the crustal structure in the Arctic ridge system (e.g., *Klingelhöfer et al*. [2000] at the Mohns Ridge; *Kandilarov et al*. [2010, 2008] at the Knipovich Ridge]. In the western Amundsen Basin, seismic refraction data are generally concentrated on the Gakkel Ridge [*Jokat et al*., 2003; *Jokat and Schmidt-Aursch*, 2007]. The sparse seismic refraction data provide some velocity information below the acoustic basement [*Jokat et al*., 1995a; *Jokat and Micksch*, 2004; *Døssing et al.*, 2014]. The seismic profiles are also widely spaced, leaving substantial data gaps.

As the newly formed oceanic crust cools and subsides, it is eventually covered by sediments. Using seismic stratigraphy, geoscientists are able to provide a timeline of the sedimentary record and relate it to known tectonic, climatic, and paleoceanographic events. The sedimentary depositional evolution of the Amundsen Basin, however, remains largely unknown due to the challenges of obtaining seismic and sedimentological data in the high Arctic. This is related in part to the permanent sea ice cover in this part of the Arctic Ocean. Seismic imaging is significantly hampered by restrictive acquisition capabilities, especially by short streamers. There are only few rock samples from the Arctic Ocean, mostly from dredging [e.g., *Michael et al.*, 2003; *Brumley et al*., 2015; *Knudsen et al.*, 2017] and gravity and piston cores [*Backman et al*., 2004], but these shallow sedimentary samples constrain only the most recent Quaternary depositional history. The only source of deep stratigraphic information comes from the Arctic Coring Expedition (ACEX) of the Integrated Ocean Drilling Program (IODP) Leg 302 in 2004, where samples were recovered on the central Lomonosov Ridge down to a depth of 428 m [*Backman et al*., 2005]. Thus, major questions remain in relation to the tectono-oceanographic history in the western Amundsen Basin and how it influenced the sedimentary record.

Scientific activity in the high Arctic increased over the last decade when coastal states started to map their extended continental shelves under the United Nations Convention on the Law of the Sea (UNCLOS). From 2007 to 2012, three expeditions along the Lomonosov Ridge off Greenland (LOMROG I through III) were carried out to acquire marine seismic data in the Amundsen Basin and on the Lomonosov Ridge. The seismic data collected during these cruises consists of 1020 km of reflection seismic data and 118 sonobuoys deployed along the seismic lines to obtain information on the velocity structure of the sediments and the crust. For the analysis and interpretation, additional information was used consisting among other of published multichannel seismic data in the Amundsen Basin [e.g., *Jokat et al*., 1995a; *Jokat et al*., 1995b; *Jokat and Micksch*, 2004], refraction seismic data [e.g., *Jokat et al*., 2003; *Jokat and Schmidt-Aursch*, 2007; *Engen et al*, 2009), magnetic data [*Gaina et al*., 2011], gravity data [*Andersen, 2010*], ACEX drill sites [*Backman et al.* 2005; *Moran et al*., 2006; *Jakobsson et al.*, 2007], among others. Combining these data sets thus offers the opportunity to investigate the nature and origin of the crust and the sedimentary evolution of the Amundsen Basin in much greater detail.

Objectives

The seismic refraction and reflection data were analyzed to investigate the crustal velocity structure and depositional history of the basin. Our objectives are therefore:

1) To map the crustal character and thickness in the western Amundsen Basin and in particular check for the possible presence of exhumed mantle in the basin based on refraction/wide-angle seismic data, coincident multichannel seismic reflection lines, magnetic data, and gravity data (Chapter II).
2) To investigate the Cenozoic depositional history of the western Amundsen Basin by developing a new stratigraphic model and estimated sedimentation rates based on multichannel seismic reflection data, magnetic data, and information from drill sites (Chapter III).

Chapter II

The crustal structure of the western Amundsen Basin derived from refraction/wide-angle reflection seismic data

The crustal structure of the western Amundsen Basin derived from refraction/wide-angle reflection seismic data

Carlos F. Castro [1,2,*], Thomas Funck [1], and John R. Hopper [1]

[1] Geological Survey of Denmark and Greenland, Øster Voldgade 10, 1350 Copenhagen K, Denmark

[2] Niels Bohr Institute, University of Copenhagen, Copenhagen, Denmark

Abstract

Two geophysical expeditions (LOMROG II and III) were carried out in 2009 and 2012 to acquire seismic data in the western Amundsen Basin in the Arctic Ocean, a basin that was created by ultraslow seafloor spreading at the Gakkel Ridge. Previous studies show alternating magmatic and amagmatic segments at the ridge but it is unclear if this is true for the entire opening history of the basin. The seismic refraction data were used to develop P-wave velocity models down to the upper mantle employing forward modeling techniques of travel times. For the modeling and interpretation, information from the coincident seismic reflection data were used. Two-dimensional gravity modeling was used to determine the Moho depth in areas with low seismic resolution. The models distinguish three different basement types: oceanic crust with layers 2 and 3, oceanic crust that is lacking a layer 3, and exhumed and serpentinized mantle. The maximum observed crustal thickness is 6 km. Areas with thin crust (< 3 km) may be underlain by partially serpentinized mantle. Where exhumed mantle is observed, a serpentinization front is separating highly serpentinized mantle at the top from partially serpentinized mantle below. The presence of oceanic crust within the extension of the presently amagmatic sector of the Gakkel Ridge indicates that there is both a spatial and temporal variation of crustal accretion processes at the ridge.

1. Introduction

Crust created by ultraslow spreading, such as the one present in the western Amundsen Basin in the Arctic Ocean (Fig. 1), differs fundamentally from crust created by faster spreading. Typically, seafloor spreading is a process where mantle material rises, decompresses, and melts [*McKenzie and Bickle*, 1988]. The newly formed magma then ascends towards the surface and gathers into magma chambers in the shallow crust. Some of the magma is ejected to the surface, while the rest cools in place, creating the distinctive 6–7 km thick [*White et al*., 2001] layered structure of pillow basalts, sheeted dikes, and gabbro [*Snow and Edmonds*, 2007]. When new melt material rises and is emplaced, the older material is pushed gradually away from the ridge, thus enabling the formation of new crust.

Ultraslow ridges are different from faster spreading ridges because they do not always involve decompressional melting. Previous geophysical studies along the Gakkel Ridge [e.g., *Jokat and Schmidt-Aursch*, 2007; *Jokat et al*., 2003; *Michael et al*., 2003], the current seafloor spreading axis in the Eurasia Basin, show that the ridge consists of alternating magmatic and amagmatic segments at the ridge. Thus, some segments of the ridge may display oceanic crust while other segments may result in direct emplacement of mantle at the seafloor [*Michael et al*., 2003]. Uncertainty remains, however, on whether the magmatic processes described above are valid for the entire history of the basin.

Only few seismic studies have been carried out in the western Amundsen Basin. This is related to the permanent sea ice cover in this part of the Arctic Ocean. Seismic refraction data in the region were acquired by sonobuoys, and a few cases, recoverable ice stations [e.g., *Ostenso and Wold*, 1997; *Fütterer*, 1992; *Jokat et al.* 1995a; *Jokat and Micksch*, 2004]. Moreover, many of the seismic refraction surveys concentrated on the Gakkel Ridge [*Jokat et al*., 2003; *Jokat and Schmidt-Aursch*, 2007]. In the western Amundsen Basin, a few seismic refraction experiments provide some velocity information directly below the acoustic basement [*Jokat et al*., 1995a;

Jokat and Micksch, 2004; *Døssing et al.*, 2014]. The seismic profiles are widely spaced, which is why large parts of the Amundsen Basin are not studied at all.

The main objectives of this investigation are to map the crustal character and thickness in the western Amundsen Basin, and in particular check for the possible presence of exhumed mantle in the basin. To achieve this aim, we rely on new refraction/wide-angle reflection seismic lines collected in the western side of the Amundsen Basin (Fig. 1). The data are supplemented by coincident multichannel seismic reflection lines, magnetic data, and gravity data. The distribution of our data off-axis from the spreading center offers the opportunity to investigate the nature, distribution, and origin of the crust in greater detail and thus advance our understanding of the prevalent crustal accretionary processes in the basin. In this contribution, we present the results of a seismic refraction dataset that fills in many of the data gaps in the western Amundsen Basin.

2. Geological setting

The Arctic Ocean is composed of two main ocean basins: the Amerasian Basin and the Eurasian Basin (Fig. 1) that are separated by the Lomonosov Ridge. The ridge is a continental sliver that extends from the North American to the Siberian margin. The geological history in the Amerasian Basin remains heavily contested due to sparse geophysical and geological data [*Chian et al.*, 2016; *Grantz et al.*, 2011; *Vogt et al.*, 1979]. This scientific dispute has resulted in a number of plate-reconstruction models associated to the origin of the basin that are summarized in *Lawver* [1990]. In contrast, there is general consensus that seafloor spreading in the Eurasian Basin began in the early Cenozoic as the Lomonosov Ridge split off the Barents and Kara shelves when Greenland and North America separated from Eurasia [*Poselov et al.*, 2014; *Jokat et al.*, 1992; *Talwani and Eldholm*, 1977; *Vogt et al.*, 1979]. Magnetic anomalies indicate that spreading along the Gakkel Ridge may have started at Chron C24 (≈ 53 Ma;

timescale after *Ogg* [2012]) [*Engen et al*., 2008; *Glebovsky et al*., 2006; *Vogt et al*., 1979] or at Chron C25 (≈ 57 Ma) [*Døssing et al.*, 2013a, 2013b; *Cochran et al*., 2006; *Brozena et al.*, 2003]. West of 3° 30' E, spreading began at a later stage at around 33 to 31 Ma when the Morris Jesup Rise and the Yermak Plateua became separated [*Brozena et al*., 2003]. Today, the Gakkel Ridge connects the global mid-ocean ridge system via the Lena Trough and the Molloy/Knipovich ridges and is the world's slowest spreading center, with full spreading rates decreasing from 14.6 mm/yr at the western end to 6.3 mm/yr in the Laptev Sea [*DeMets et al*., 1994].

The earliest crustal investigations of the Amundsen Basin and the Gakkel Ridge were carried out by ice stations during the late 1970s/ early 1980s by *Ducksworth et al*. [1982] and *Jackson et al*. [1982]. Here, *Jackson et al*. [1982] report a 2-3 km thick oceanic crust at the Gakkel Ridge. Early models of melt generation beneath mid-ocean ridges [*Reid & Jackson*, 1981; *Bown & White*, 1994;] predicted low melt production and thinner crust than the global average of 7 km for normal oceanic crust [*White et al*., 1992]. These predictions were partially supported by subsequent seismic refraction investigations among other slow spreading ridges (e.g., *Klingelhöfer et al.* [2000] at the Mohns Ridge; *Crane et al*. [2001] and *Okino et al*., [2002] at the Knipovich Ridge, and *Muller et al.*, [1999, 2000] at the South West Indian Ridge) indicating that once the spreading rate dropped to about < 20 mm yr^{-1}, conductive cooling limited melt supply [*Reid & Jackson*, 1981; *Bown & White*, 1994; *White et al*. 2001]. Additionally, these seismic studies offered a more detailed view of the velocity structure at slow spreading centers: unlike normal oceanic crust, seismic velocities above 6.5 km s^{-1} are seldomly observed and an oceanic layer 3 is either very thin or absent [J*okat and Schmidt-Aursch*, 2007].

In 2001, the Arctic Mid-Ocean Ridge Expedition (AMORE) performed detailed geophysical and petrological mapping of a 1000 km long section of the axis and walls of the Gakkel Ridge [Jokat et al. 2003; *Michael et al*., 2003]. Results of the study indicate that some sections of the ridge do not generate an igneous crust as evidenced by peridotite dredge samples along the ridge [*Michael et al.*, 2003]. Unexpectedly, the Gakkel Ridge also displayed an abundance of hydrothermal activity, magmatism, and discrete volcanic centers [*Michael et al.*, 2003; *Jokat et al.*, 2003] than what was predicted from the earlier models of melt generation [*Reid & Jackson*, 1981; *Bown & White*, 1994]. The results of this expedition, combined with investigations of the Southwest Indian Ridge, led *Dick et al*. [2003] to introduce a new class of mid-ocean ridges – the ultraslow spreading ridges. The key results of *Dick et al*. [2003] show that there exists a correlation between spreading rate and crustal thickness for ultraslow spreading ridges at rates up to approximately 20 mm yr^{-1}. Variations in crustal thickness in crust created by ultraslow spreading seem to be caused by focused magmatism [*Sauter et al*. 2004] and episodic and along-axis variations in melt supply to sites of passive upwelling [*Dunn*, 2015; *Niu et al*., 2015; *Schlindwein et al*., 2013; *Standish et al*., 2008].

The discoveries of the AMORE expedition also led to the division of the Gakkel Ridge into three tectono-magmatic provinces: the Western Volcanic Zone (WVZ), the Sparsely Magmatic Zone (SMZ), and the Eastern Volcanic Zone (EVZ). The crustal thickness in these provinces ranges between 1.4-2.9 km s^{-1} at amagmatic segments and up to 3.5 km in centers of focused magmatism [*Jokat and Schmidt-Aursch*, 2007]. The crust also displays no velocities above 6.4 km s^{-1}, indicating that oceanic layer 3 is either very thin or missing [*Jokat and Schmidt-Aursch*, 2007]. The WVZ (6° 30 W'-3° 30 E') displays extensive magmatism and a strong, positive magnetic anomaly along the central valley. The SMZ (3° 30E' - 29°E) consists of long amagmatic segments dominated by peridotite, variable magnetic anomalies, and an absence of long transform faults [*Jokat and Schmidt-Aursch*, 2007]. In the EVZ (29°E'-85°E), basalts dominate the seafloor and are associated with focused magma supply at volcanic centers [*Michael*, 2003]. At the termination of the EVZ (85°E'), ongoing volcanic activity in this region has been documented by sonar data associated to an earthquake swarm in 1999 [*Edwards*, 2001].

Off-axis from the spreading ridge, gravity studies in the western section of the Amundsen Basin show variable crustal thicknesses. *Urlaub et al*. [2010] predict a crustal thickness of less than 1 km in the oldest parts of the basin, increasing to a maximum value of 6 km near the Gakkel Ridge; in contrast, 3D gravity inversion by *Døssing* et al. [2014] predicts a crustal thickness of about 7 km in the oldest parts of the basin, decreasing to about 4 km near the Gakkel Ridge. 3D gravity models by *Cochran* et al. [2003] and *Glebovsky et al*. [2013] predict crustal thicknesses in the Amundsen Basin between 3 and 8 km. Oceanic crust accreted prior to magnetic Chrons C5/C6 is also predicted to be generally very thin (1-3 km) [*Schmidt-Aursch and Jokat*, 2016]. More seismic information is needed, however, to calibrate and substantiate crustal thickness calculations that are based on gravity data.

3. Methods and Data

3.1 Data acquisition

The seismic data used in this study were acquired during two Lomonosov Ridge off Greenland surveys (LOMROG II and III) in 2009 and 2012 using the Swedish icebreaker Oden as part of the Continental Shelf Project of the Kingdom of Denmark. The LOMROG expeditions collected bathymetric, seismic, gravimetric, and CTD (conductivity, temperature, and pressure) along the Eurasian flanks of the Lomonosov Ridge and in the Amundsen Basin. Key acquisition parameters for the multichannel reflection seismic data are summarized in Table 1 and details from each survey are provided in *Lykke-Andersen et al*. [2010] and *Varming et al.* [2012]. The source array consisted of G and G-I guns with various configurations and a streamer length of up to 300 m with a group interval of 6.25 m. The nominal towing depth of both the source and receiver arrays were set to 20 m to minimize interference with the sea ice. The data quality was enhanced by a basic processing sequence that included band pass filtering, spectral shaping filtering, spike and noise burst editing, f-k filtering, static corrections, trace equalization, shot-mixing, stacking, and velocity migrations.

The seismic refraction data were obtained by sonobuoys (type AN/SSQ-53D(3) from ULTRA Electronics), which recorded the shots from the seismic reflection experiments (Fig. 3). The disposable sonobuoys were equipped with a hydrophone (depth 30 m), which radioed the seismic signals back to the receiving system installed onboard the acquisition vessel Oden. The seismic energy produced by the airgun cluster (volume between 605 and 1040 cu. in.) could be recorded up to offsets of ~33 km and was sufficient to detect mantle refractions and P_mP reflections on some of the sonobuoy records. During the two surveys, a total of 878 km of seismic reflection data were acquired and 107 sonobuoys were deployed, whereof 89 successfully radioed data back to the ship. In this study, we incorporate 58 sonobuoys distributed along 19 profiles (~ 700 km) in the central part of the basin (Fig. 2).

Gravity data were continuously carried out during the seismic acquisition using a Lacoste & Romberg gravimeter installed onboard Oden. The data were acquired every 10 s. The data processing includes corrections for instrumental drift, tide effects, latitude corrections, and Eötvös effect. Further details on the gravimetric acquisition are given by *Marcussen et al*. [2009, 2012].

3.2 Velocity modeling

This study models travel times by using 2D kinematic raytracing modeling based on the RAYINVR modeling software of Zelt and Smith (1992). This method consists of matching the observed variation of travel time against offset with the travel times predicted by a model. For more information on RAYINVR please refer to *Zelt and Smith* [1992] and *Zelt and Ellis* [1988].

Travel times of reflected and refracted phases were picked on each record section and uncertainty estimates were assigned to all travel time picks. The uncertainty estimates were determined based on the signal to noise ratio and on the dominant frequency of the signal.

The velocity models were developed by forward modeling. The modeling took place layer by layer moving from top to bottom. In each layer the velocities were constrained by the refraction phase going through the layer. The lower boundary of each layer was constrained by reflections from there and by the refraction phase underneath the boundary.

The detailed geometry of the sedimentary layers was introduced by comparison with the coincident multichannel reflection seismic data.

3.3 Sonobuoy Processing and Drift corrections

The sonobuoy data were converted from SEG-D into SEGY format. Static corrections for the sonobuoys were applied for both the variable gun depth and the fixed depth of the hydrophone on the sonobuoy. For this correction, an airgun depth of 0 m and a hydrophone depth of 0 m were assumed, using a water velocity determined by the CTD measurements.

The sonobuoys were not equipped with a navigation system and, once deployed, drifted freely in the water. Since the sonobuoy position through time was unknown, the correct distance of the sonobuoy from the shot position had to be calculated. The shot-receiver distance was computed by picking the travel times for the direct water arrivals. Then, the distances to the sonobuoys were calculated by using the water velocities from the collected CTD measurements. The drift component along the line can thus be quantified by the difference between the theoretical offset using the deployment position of the sonobuoy and the recalculated shot-receiver distance determined from the direct wave.

The raytracing modeling used here assumes that the sonobuoys are stationary and are arranged in common receiver geometry. For a drifting sonobuoy, this geometry is not valid because the receiver (sonobuoy) is not stationary [*Bruguier and Minshull*, 1997]. Even though the source-receiver offsets can be accurately calculated from the arrival times of the direct wave along the line, there exists an additional drift component out of the plane of the experiment where information on the basement depths is unknown. This became evident in sonobuoy 9 where initial ray tracing revealed a mismatch between the observed crustal refractions and the calculated travel times while using the basement constraints from the multichannel seismic data. In order to match our calculated travel times with the observed data, a different basement geometry than the multichannel seismic data was used and the sonobuoy was checked for velocity consistencies with the other adjacent sonobuoys.

In regions with pronounced basement topography, such as the western Amundsen Basin, a large sonobuoy rate drift may also lead to incorrect basement depths and displaced shot locations [*Bruguier and Minshull*, 1997]. These effects may be minimized, however, by using a variable sonobuoy position during the modeling and treating each position as a separate common receiver gather. This approach was used in four sonobuoys (2, 3, 32, and 38) in areas with steep topography where the calculated travel times had a significant mismatch with the observed data. Here, the sonobuoy position was varied once, which proved sufficient for matching our calculated travel times to the observed data. For the remaining sonobuoys, only the offset correction between the sonobuoys and the shots was applied and the deployment position of the sonobuoy was used in the modeling.

4. Results

Figures 4 through 6 display the final velocity models obtained in this study. The models are divided into a sedimentary cover, crust, and upper mantle. A description of each model is given below while an in-depth discussion is given in sections 5.1 to 5.3.

4. 1 Transect 1

Figure 3 shows the final velocity model for transect 1. The sedimentary column along the 80-km-long transect has a maximum thickness of 1.7 km and comprises four sedimentary layers (S1-S4). The velocity for the youngest sedimentary layer (S1) is 1.6 km s^{-1}. Velocities within layer S2 change at the basement around km 70 from 1.9–2.0 km s^{-1} in the NW to 2.7–2.8 km s^{-1} in the SE. Velocities for layers S3 and S4 are 2.3–2.5 km s^{-1} and 2.6–2.9 km s^{-1}, respectively.

The underlying crust displays lateral variations in its thickness and velocity structure. Four distinct zones (1-4) are recognized:

Zone 1: At the northern end of the line (between km 0 and 30), the crust is divided into two layers. The upper layer is 1.3 km thick with velocities of 4.1–4.9 km s^{-1}, while the lower layer (5.3–6.0 km s^{-1}) is up to 1.8 km thick. The base of the crust is constrained by a strong wide-angle reflection between km 15 and 20, with mantle velocities of 7.8 km s^{-1} underneath.

Zone 2: Near the center of the profile (km 30–45), the crust was modelled as a 1.2 to 2.4-km-thick upper layer with velocities between 4.0–4.9 km s^{-1} and an underlying layer with a top velocity of 6.6 km s^{-1}. There are no seismic constraints on the Moho depth and upper mantle velocities.

Zone 3: Between km 45–60, a three-layered crust is observed. The uppermost crustal layer is 400 m thick and thins towards the basement high in the center of the zone. Velocities in this layer range from 3.0 to 3.4 km s^{-1}. The mid-crustal layer is between 1 and 2 km thick and has velocities between 5.1 and 5.9 km s^{-1}. The velocities for the lowermost crustal layer are similar to the ones observed in zone 2 (6.6–6.9 km s^{-1}). The base of this layer is characterized by a strong wide-angle reflection and velocities of 7.8 km s^{-1} in the underlying mantle.

Zone 4: In the southeast (km 60–80), the crust is divided into two layers. The uppermost layer is 2–3 km thick with velocities of 3.8–5.9 km s^{-1}. The base of this layer is marked by a wide-angle reflection and velocities of 6.9 km s^{-1} are observed immediately beneath. No further seismic information was available to model the deeper crust and mantle.

4. 2 Transect 2

The P-wave velocity model for the 262-km-long transect 2 (Fig. 4) divides the sedimentary column into six sedimentary layers (S1-S6) with a combined maximum thickness of 2 km. Layers S1 and S2 have velocities of 1.6 km s^{-1} and 1.7–2.2 km s^{-1}, respectively. Layer S3 is observed locally between km 0–24 and km 122–165 with velocities between 2.1 and 2.2 km s^{-1}. Layers S4, S5, and S6 display velocities of 2.4–2.8 km s^{-1}, 2.7–3.0 km s^{-1}, and 3.2–3.4 km s^{-1} respectively. The crust displays significant lateral variations in velocity and thickness. Here, the crustal layers are described for each of the five individual seismic lines the transect is composed of.

From km 0–24, the crust is composed of two layers. The upper crust has a thickness of 2.0–2.5 km with velocities ranging from 4.9 km s^{-1} at the top to 6.0 km s^{-1} at the bottom. The lower crust has a thickness of 3.0–3.5 km with a velocity of 6.0 km s^{-1} at the top and 7.0 km s^{-1} at the bottom. Mantle velocities are not constrained.

From km 56–98, significant lateral variations within the crustal structure are recognized. Between km 56 and 75, the velocity structure is similar to the one between km 0 and 24 but the Moho shallows from 11 km at km 56 to 8 km 74 where the lower crust disappears. The maximum thickness for the upper crust is about 2.5 km and for the lower crust 1.5 km. Between km 76 and 85, a single crustal layer with velocities of 5.2–5.9 km s^{-1} is observed and its thickness varies between 2.0 and 2.5 km. Headwaves define the velocity in the underlying mantle as 7.0 km s^{-1}. Between km 85 and 98, the velocity structure essentially continues but a 700-m-thick cover layer with a top velocity of 3.9 km s^{-1} is observed.

Between km 122 and 165, a two-layered crust is recognized. The upper crust is generally between 1 and 2 km thick, but thins to about 500 m at the basement high around km 135. Velocities within the upper crust are variable. They are 4.6–5.0 at km 122 but decrease to 4.1–4.4 km s^{-1} at the basement high at km 135, from where they increase again to 4.6–5.5. The lowest velocities (3.5-5.4 km s^{-1}) are found around the basement high at km 158. Lower crustal velocities are 6.5 km s^{-1} at the top and 6.7 km s^{-1} at the bottom. The Moho deepens beneath the basement highs to maintain isostatic balance. Some P_mP reflections define the depth of the Moho that is otherwise defined by gravity modeling (see section 4.4). With that, the lower crustal thickness varies between 2 and 7.5 km. No P_n phases were observed to constrain the mantle velocity.

From km 173–199, the crust is composed of a single layer that has velocities of 4.2 km/s at the top and 6.0 km s^{-1} at its base. The crustal thickness varies between 2.0 and 2.5 km. A strong P_mP reflection is observed and the mantle velocities are approximately 7.3 km s^{-1}.

The crust between km 244 and 262 is composed of three layers. The upper crust consists of two distinct layers with a combined thickness of 1.5 km and velocities ranging from 3.9 to 4.2 km s^{-1} in the upper layer and 5.0 to 5.8 km s^{-1} in the lower layer. The lower crust varies in thickness from 2 to 3 km with velocities ranging from 6.6 km s^{-1} at the top to 6.6 km s^{-1} at the bottom. Mantle velocities are not constrained.

4. 3 Transect 3

The P-wave velocity model for transect 3 is shown in Figure 5. The transect is 203 km long and displays six sedimentary layers (S1-S6) with a total maximum thickness of 2 km. Similar to transect 2, sedimentary layers S1 and S2 display a lateral continuity with velocities of 1.6 and 1.8–2.3 km s^{-1}, respectively. Layer S3 is only present between km 0–32 and has a velocity of 2.2 km s^{-1}. Layer S4 is observed between km 0 and 32 and km 108 to 203 with velocities of 2.5–2.8 km s^{-1}. Layers S5 and S6 were only identified in the deeper basins and display velocities of 2.7–3.0 km s^{-1} and 3.2–3.3 km s^{-1}, respectively.

The crust is divided into three crustal layers where the upper crust is composed of two layers. One upper crustal layer with velocities of ~4–6 km s^{-1} and thickness of about 2 km is observed between km 0 and 32, while there are two layers between km 65 to 206. The upper crustal layer observed at km 0 thins to about ~1 km at km 145 and remains at that thickness until the end of the line. The upper crustal layer observed at km 65 is about 200 m thick and then thickens to about 1 km at km 115 and remains so with only little variation. At about km 65, velocities are 4.7 km s^{-1} for this layer but decrease to 4.1–4.5 km s^{-1} at around km 90. The velocities then remain mostly constant up to km 175 where they decrease to about 3.8–4.1 km s^{-1} towards the end of the transect.

At km 0, the lower crust displays a top velocity of 6.7 km s^{-1} and a bottom velocity of 7.0 km s^{-1}. The velocities decrease to 6.3 km s^{-1} at the top and 6.6 km s^{-1} at the bottom at around km 65, where they remain constant up to km 149. The velocities then change between km 170–190 to 6.0 km s^{-1} and 6.5 km s^{-1} and increase to 6.2–6.5 km s^{-1} towards the end of the line at around km 190. The thickness of the layer varies since the Moho deepens below the basement high. Between 0–32 km, the lower crust is 3 to 4 km thick, between km 66–149 the crust is between 3 and <1 km, and between km 153–203 the crustal thickness is about 2 km. No P_n phases were identified on the record sections to resolve the velocities in the mantle.

4.4 Gravity modeling

The limited P_mP and P_n phases observed in the seismic refraction dataset results in a rather discontinuous mapping of the Moho depth (Figs. 4–6). On transect 1, the Moho is seismically constrained by P_mP reflections and P_n refractions observed on sonobuoy records 3 and 9 (Fig. 3). Along transect 2, sonobuoys 40, 43, 49–51, 53, 55–56, 60, and 63 recorded P_mP

reflections, while P_n phases were registered by sonobuoy 48–51, 56, and 59. Along transect 3, P_mP reflections are present on sonobuoy records 20, 21, 30, 33, 34, 37, and 39; no clear Pn phase could be identified.

Two-dimensional gravity modeling was performed by converting P-wave velocities to density in order to constrain the Moho depth in areas with no seismic constraints. The gravity data were extracted from the shipborne gravimeter while the density models were derived from the P-wave velocity models (Figs. 4–6) by coverting the velocities to density using the empirical relationship of *Ludwig et al.* [1970]:

$$\rho = -0.00283v^4 + 0.0704v^3 - 0.598v^2 + 2.23v - 0.7$$

where v is the P-wave velocity in km/s and ρ is density in g/cm^3. In order to avoid edge effects in the modeling, the models were extended 300 km in each direction. Since transects 2 and 3 were composed of lines with a variable orientation (see Fig. 2), each line was modeled separately. Two-dimensional gravity modeling was then performed by using the algorithm of *Talwani* [1959] and compared with the shipborne gravity measurements (Figs. 8–10). The Moho geometry was adjusted in the unconstrained areas to obtain a good match between the observed and calculated gravity. The greatest mismatch between the calculated gravity response and the observed gravity for transects 1 and 3 is 5 mGal, while it is 10 mGal for transect 2.

4. 5 Basement velocities

Basement velocities recorded by the sonobuoys were mapped alongside gravity and magnetic field data to identify potential velocity patterns within the data (Figure 7). The basement velocities in this study are supplemented with additional basement velocities from previous studies in the Amundsen Basin [*Jokat et al.*, 1995a; *Jokat and Micksch*, 2004], the Gakkel Ridge [*Jokat and Schmidt-Aursch*, 2007] and the Nansen Basin [*Engen et al.*, 2009]. Based on the LOMROG data, three distinct velocity variations are observed:

1) Velocities between ~4.0–4.7 (green colors) are widespread throughout the basin;
2) Lower velocities between ~3.0–3.8 km s^{-1} (blue colors) are observed both locally (e.g., zone 3 in transect 1, see Fig. 4) and closer towards the Gakkel Ridge (e.g., between km 170–200 in transect 3, see Fig. 6);
3) Higher velocities (~4.8–5.4 km s^{-1}) are observed in the region corresponding to km 0–98 in transect 2 (Fig. 5).

5. Discussion

The crust created by ultraslow spreading in the western Amundsen Basin displays significant variations in its structure and composition (Figs. 4–6). The velocity models obtained from the sonobuoy data can be divided into three main groups: crust resembling normal oceanic crust, crust with no observed oceanic layer 3, and exhumed mantle. We will begin by discussing each group individually and providing relevant examples from each of our three transects. Then we will compare our data with other seismic data in the Eurasian Basin.

5. 1 Normal oceanic crust

Typical oceanic crust consists of two main layers: oceanic layer 2, and oceanic layer 3. Oceanic layer 2 displays a wide range of seismic velocities (2.7-6.3 km s^{-1} in *Juteau and Maury* [1997]; 2.5-6.6 km s^{-1} in *White et al.* [1992]) and is usually associated with extrusive basalt lavas and dikes formed at the spreading center. Oceanic layer 2 has an average thickness of 2 km and a high velocity gradient (gradients are ~1-2 s^{-1}) [*White et al*., 1992]. Oceanic layer 3 is characterized by comparable low velocity gradient (0.1-0.2 s^{-1}) and is usually associated with intrusive gabbroic rocks. Oceanic layer 3 is on average 5 km thick and velocities range between 6.6-7.7 km s^{-1} [*Juteau and Maury*, 1997; *White et al.*, 1992]. Away from the influence of fracture zones, hotspots and marginal basins, normal oceanic crust exhibits a relatively uniform crustal thickness (6-7 km) at full spreading rates of 20 mm yr^{-1} and above [*Bown and White*, 1994; *White et al.*, 1992; *White et al.*, 2001].

The velocity structure observed in a typical oceanic layer 2 may also display variations in velocity and thickness. Normally, oceanic layer 2 may be subdivided into three layers: 2A, 2B, and 2C [*Houtz and Ewing*, 1976]. The uppermost sublayer 2A consists of a porous and low-density basaltic layer (i.e., lava flows) marked by numerous fractures and voids. Seismic velocities range from 2.7–4.5 km s^{-1} and the layer's thickness may reach up to 1 km. The presence of layer 2A is considered to be a temporal phenomenon [*Houtz and Ewing*, 1976; *Grevemeyer and Weigel*, 1996; *Carlson*, 1998] since the thickness of the layer decreases away from the spreading axis until it eventually merges with sublayer 2B [*Juteau and Maury*, 1997]. The transformation from layer 2A to 2B is thus thought to represent an alteration boundary caused by crack closures, hydrothermal alteration, and sealing [*Christeson et al*., 2007; *Klingelhöfer*, 2000; *Vera et al*., 1990]. Sublayer 2B characterizes either the deepest part of the young basaltic layer or a sheeted diabasic dike complex after the transformation of sublayer 2A into 2B [*Christeson et al*., 2007; Wilson *et al*., 2006]. Sublayer 2B is characterized by velocities of 4.8 to 5.5 km s^{-1} and a thickness of 0.5 to 1 km [*Juteau and Maury*, 1997]. When identified, sublayer 2C is thought to represent a significant quantity of intrusive basic rocks (e.g., dikes and sills) that differ from sublayer 2B in the intensity of alteration, metamorphism, and/or progressive closure of cracks and pore spaces at greater depths [*Wright and Rothery*, 1998; *Juteau and Maury*, 1997]. Sublayer 2C normally shows velocities between 5.8 to 6.5 km s^{-1} (5.8 to 6.2 km s^{-1} in *Juteau and Maury* [1997]; 5.8 to 6.5 km s^{-1} in *Houtz and Ewing* [1976]) and a thickness of about 1 km [*Juteau and Maury*, 1997].

Transects 2 and 3 (km 0–32 and km 0–24 respectively) closely resemble the description mentioned above (Figs. 3, 5, and 6). Here, the velocity models display top upper and lower crustal velocities of 4.1–4.9 and 6.6–6.7 km/s, respectively, compatible with typical oceanic layer 2 and 3 velocities. Moreover, high-amplitude P_mP reflections are observed, and indicate a strong velocity contrast between the lower crust and the mantle as opposed to a gradual transition to upper mantle velocities. Crustal thicknesses in this region (~5–6 km) are less than typical (6–7 km) oceanic crust; however, this is expected since ultraslow spreading is typically related with a reduced crustal thickness compared to crust created by faster spreading [*Dick et al*., 2003].

The presence of a local crustal layer underneath the acoustic basement in some regions is also observed in this group. One such example is the presence of an uppermost crustal layer in zone 3 recorded by sonobuoy 3 (Figs. 3 and 4). The layer is relatively thin (400 m), displays low P-wave velocities (3.0–3.4 km s^{-1}), shows strong basement reflectivity (Fig. 11), and is located in the vicinity of basement highs (Fig. 4).

Two interpretations are proposed to explain the presence of these local layers. The first interpretation is that the layers relate to oceanic sublayer 2A. Compatible velocities for our observations have been documented in crust created by magma poor spreading ridges such as the Mohns Ridge (Fig. 14). Here, thin crust dated at 22.4 Ma is characterized by an uppermost crustal layer with velocities of 3.1–3.2 km s^{-1} and an approximate thickness of 100 m [Klingelhöfer et al. 2000]. *Klingelhöfer et al.* [2000] suggest that the observed thickening of oceanic layer 2A at topographic highs might be locally linked to volcanic activity. Previous magnetic modeling of sublayer 2A [*Tivey and Johnson*, 1993] have revealed that the thickness of this sublayer along ridges could represent thickening due to excess volcanic material. If so, the locally observed layer in our dataset would imply an excess of extrusive basalt lavas.

A second possibility is that the layers are related to large-scale sill injections. Sills are often marked by high-amplitude reflectivity, abrupt terminations [*Planke et al*., 2005; *Thomson and Hutton*, 2004; *Tucholke et al*., 1989], and have been demonstrated to correlate with high-amplitude reflectivity in multichannel seismic data [*Shillington et al.*, 2007]. Sills have been recognized within transitional crust [e.g., *Peron-Pinvidic et al.*, 2010] but also recently with crust created along the ultraslow Southwest Indian Ridge [*Meier and Schlindwein,* 2017], most likely due to off-axis volcanism [*Peron-Pinvidic et al*., 2010]. At the Newfoundland margin, sill emplacement could have occurred at a time when there was a thin sedimentary cover on top of the basement that was later destroyed by intrusives or extrusives, resulting in a seismic basement that is indiscernible from true basement [*Peron-Pinvidic et al*., 2010]. Given the limited data constraints for these layers, however, more geophysical information is required to confirm either interpretation.

5. 2. Crust with no oceanic layer 3

In ultraslow spreading crust, seismic velocity studies show that the velocity structure is significantly different than that observed at faster spreading ridges [*Dunn*, 2015]. P-wave velocities above 6.5 km s^{-1} are rarely observed [*Jokat and Schmidt-Aursch*, 2007] and while an oceanic layer 2 is often present, oceanic layer 3 tends to be thin or absent as crustal thickness decreases [*White et al*., 2001]. In some cases, the crust is underlain by partially serpentinized mantle. For some sections of these ridges, the limited melt supply also results in the direct emplacement of mantle at the seafloor [*Cannat et al.*, 2006; *Michael et al.*, 2003]. A thickness of < 4 km thick is common in crust created by ultraslow spreading [e.g. *Klingelhöfer et al*., 2000; *Czuba et al*. 2011; *Hermann and Jokat,* 2013; *Delescluse et al*. 2015], well below the global average of 7 km for faster spreading rates [*White et al.*, 1992].

Crust underlain by partially serpentinized mantle was observed conclusively along portions of transect 2 (Fig. 4). Where partial serpentinization is observed, the crust is thin (about 2 km) and the data show a strong reflection at the base of this crust. The observed velocities of 7.0–7.3 km s^{-1} underneath thin crust in this region indicate that the volume percent of serpentinite in the mantle is around 30–35%.

The interpretation between an oceanic layer 2 or an oceanic layer 2 with a thin oceanic layer 3 remains ambiguous in some regions. One clear example is the presence of a crustal layer with velocities of 6.0–6.5 km s^{-1} along transect 3 at km 170–190 (Fig. 6). Here, the velocity range falls within velocities that are compatible with either an oceanic sublayer 2C (5.8 to 6.5 km s^{-1}) [*Houtz and Ewing*, 1976; *Juteau and Maury*, 1997] or a modified layer 3.

Support for velocities compatible to ours corresponding to an oceanic sublayer 2C may be found in the Boreas Basin where the crust was created by ultraslow spreading. P-wave velocity models show a 3 km thick oceanic crust with seismic velocities less than 6.3 km s^{-1}, indicating the lack of any significant oceanic layer 3 [*Hermann and Jokat*, 2013]. Here however, it is questioned whether the modeled layer corresponding to sublayer 2C in *Hermann and Jokat* [2013] is unique. The velocity models show mismatches between the observed travel times and the calculated travel times; in addition, the calculated travel times are usually late arrivals when compared to the observed phase arrivals, thus leading to question whether some parts of sublayer 2C could be remodeled with faster velocities corresponding to a thin oceanic layer 3.

Alternatively, the crustal layer with velocities of 6.0–6.5 km s^{-1} could represent an atypical oceanic layer 3. One possible interpretation to explain the velocity structure is that the modified layer 3 represents a mesh between basalt and gabbro. Higher basalt content in gabbro during melt formation may contribute to lower velocities observed in the gabbro. Whole-rock major and trace element compositions analyzed on the ultraslow South West Indian Ridge for a suite of gabbroic samples show evidence of such mesh [*Coogan et al.*, 2001]. In the interpretation by *Coogan et al*. [2001], melts are removed from the melting column, crystallize, and add themselves to the crust, forming eruptible reservoirs. As these small magma packets are added into the crust, some interstitial liquid is mixed into subsequently erupted magma reservoirs, leading to a mixture of cumulate crystals and significant proportions of basalt.

A second interpretation for an atypical oceanic layer 3 could be that the low velocities are related to a highly tectonized oceanic crust. Given that the crust in the Amundsen Basin is marked by limited magma supply, it is possible that the lower velocities in the crust can be explained by the fractures leading to an increased fluid circulation in the crust. In particular, oceanic layer 3 velocities in this region would be compatible with ultraslow crust at the extinct Labrador Sea spreading center [*Delescluse et al*., 2015] (Figure 14), where tectonic extension was thought to occur during the waning stage of the Labrador Sea and where faulting became dominant as the spreading rate decreased to extinction. The low crustal velocities (~6.0–7.1 km/s) and thin (3.5 km) crust would therefore imply a decreasing supply of partial melt associated with an increasing degree of tectonism.

Figure 7 shows the gravity anomalies from Andersen [2010] in the Amundsen Basin. A distinct gravity low can be recognized between km 153 and 203 that continues perpendicularly to a strong bend along the spreading center of the Gakkel Ridge. This gravity low correlates well with the 6.0–6.5 km s^{-1} velocities lowermost layer 3 velocities observed for the lower crust in transect 3 (Fig. 6). Here, the lower crustal velocities in this zone increase to 6.2–6.5 km s^{-1} at ~km 195 in transect 3 and to ~6.3–6.6 km s^{-1} at ~km 130.

The low oceanic layer 3 velocities and the pattern of the gravity anomaly perpendicular to the spreading ridge may suggest that this area represents a fracture zone. Fracture zones, located at the ends of convection cells, are marked by lower magma supply and likely lower temperatures in the magma [Detrick et al., 1993]. Fracture zones are therefore frequently associated with thin crust and the absence of a normal oceanic layer 3 [*Detrick et al*., 1993; *White et al.* 1984]. If an oceanic layer 3 is present, fracture zones may display lower than typical oceanic layer 3 velocities (e.g. Oceanographer Fracture Zone in *White et al.* [1984] and *Ambos and Hussong* [1986]; Kane Fracture Zone in *Detrick and Purdy* [1980] and *Abrams et al.* [1988]).

5. 3 Exhumed mantle

Between km 80 and 90 on transect 2 (Figs. 2, 5, and 7), basement velocities range from 5.2 to 5.4 km s^{-1} and display strong wide-angle reflections from the base of the upper crust (Fig. 3). These velocities are compatible with highly serpentinized mantle rocks or with oceanic layer 2. Velocities of 5.2 km/s would correspond to a serpentinization rate of approximately 80% [*Christensen*, 2004]. The sharp velocity contrast between 5.9 km s^{-1} (poorly resolved) at the base of the layer and 7.0 km s^{-1} underneath could represent a serpentinization front, separating highly serpentinized mantle from partially serpentinized mantle. The serpentinization front would be the result of the volume expansion during the serpentinization process, which closes cracks and fractures in the rock and thereby the pathway for water into deeper portions of the mantle. The serpentinization front would thus represent the depth to which water was able to travel down fault planes cutting deep into the upper mantle [*Dean et al.*, 2000].

The interpretation and seismic character discussed above should be similar to other regions marked by undoubted exhumed mantle and ultraslow spreading. For this reason, we compare our results to the Newfoundland/Iberia conjugate margin pair, a well-documented area of magma poor rifting marked by wide areas of exhumed mantle and peridotite ridges [*Cannat et al.*, 2009; *Peron-Pinvidic et al.*, 2010; *Reston et al.*, 1996] (Fig. 12). A comparison between the basement character in our data and the basement in the continent-ocean transition zone at the Newfoundland and Iberia margins displays several similarities (Fig. 12). In the Iberia abyssal plain, *Pickup et al.* [1996] identify a transition zone characterized by a thin (1.0–2.5 km) seismically unreflective upper basement layer lying over reflective basement. Likewise, basement ridges thought to be exhumed mantle in this region were characterized by no coherent internal seismic structure [*Dean et al.*, 2015]. These observations support the notion that vigorous seawater circulation along the faults in the uppermost basement resulted in highly serpentinized mantle and a weak reflective top basement [*Dean et al.*, 2000].

At the Newfoundland margin, *Peron-Pinvidic et al.* [2010] identify three basement domains based on seismic character: continental, transitional, and embryonic oceanic. The transitional domain, suggested to be predominantly serpentinized mantle [*Sibuet et al.*, 2007], displays a limited basement roughness with a smooth, short-wavelength basement topography. In contrast, the embryonic oceanic domain consists of significantly stronger relief than the transitional domain, reaching up to 1–1.5 km. The basement character observed between km 80 and 90 (Figs. 5 and 12) displays a similar smooth basement structure to that of what would be expected in the transitional domain defined by Peron- *Peron-Pinvidic et al.* [2010]. This observation, in combination with the compatible basement reflectivity and P-wave velocities, would suggest the possible presence of exhumed mantle in this segment.

5. 4 Comparison to seismic data in the Eurasian Basin

Based on the magmatic activity, *Michael et al.* [2003] divide the western part of the Gakkel Ridge into three segments: the WVZ, SMZ, and EVZ. This segmentation is also visible in seismic refraction data showing distinct variations in the crustal velocity structure [*Jokat and Schmidt-Aursch,* 2007]. In the WMZ, extensive magmatism consisting entirely of glassy pillow basalts indicates velocities within the range of 2.4–5.2 km s^{-1} [*Schmidt-Aursch and* Jokat, 2016; Jokat *and Schmidt-Aursch,* 2007]. In the SMZ, the velocity models of *Jokat and Schmidt-Aursch* [2007] show focused magmatism and velocities within the range of 3.4–6.0 km s^{-1} along the Gakkel Ridge. High velocities close to or above 4 km s^{-1} are usually observed in areas where mostly peridotites were dredged [*Jokat and Schmidt-Aursch*, 2007; *Michael et al*., 2003]. However, *Jokat and Schmidt-Aursch* [2007] are not able to decide whether the basement there consists of oceanic crust or altered mantle material. In the EVZ, predominantly basalts were dredged and, consistent with this, crustal velocities above 6 km s^{-1} are observed around volcanic centers. Oceanic layer 3 is absent in both the SMZ and EVZ.

The SMZ is marked by very low amplitude magnetic anomalies compared to the EVZ (Fig. 7). These low amplitudes persist up to Chron C8, where the pattern of magnetic anomalies in the SMZ changes to high amplitudes. Due to this change, however, uncertainty exists on whether the distinction between the EVZ and SMZ remains valid for crust older than Chron C8. In order to test this, velocity profiles from our data set are compared with velocity profiles of the EVZ and SMZ (Fig. 13). The velocity-depth curves are plotted alongside stacked velocity curves from *White et al.* [1992] for 0 to 7 Ma (orange shading) and 59 to 127 Ma (blue shading) old oceanic crust in the North Atlantic and from stacked velocity data from *Jokat and Schmidt-Aursch* [2007] in the EVZ (green shading) and SMZ (purple shading) at the Gakkel Ridge. Transect 1 (black lines) lies on 43 to 31 Ma old crust within continuation of the SMZ. Velocities within zone fall within the range that is typically observed in oceanic layer 2 [*White et al.* 1992]. Within zones 2, 3 and 4, an oceanic layer 3 is observed, which is inconsistent with the observations by *Jokat and Schmidt-Aursch* [2007]. Along transects 2 and 3 (red lines), corresponding to older crust away from what is nowadays the EVZ, all velocity profiles fall within the range of what is typically observed in oceanic layers 2 and 3. The observations above indicate that the velocity profiles on transect 1 do not seem to share any significant similarity with crustal observations along the SMZ. In addition, recent geophysical analyses have suggested that the magmatic processes observed within the SMZ may extend onto older crust. In the Nansen Basin, *Lutz et al.* [2018] use multichannel seismic data complemented by gravity and magnetic modeling to study the basement configuration in the oldest part of the basin and within the continent-ocean transition zone. Seismic imaging revealed large faulted basement blocks, similar to the ones observed along zone 1 in transect 1 (Figs. 4 and 11). Based on structural similarities between the young basement located along the SMZ and the older basement near the Barents Sea margin, *Lutz et al.* [2018] suggest that mantle exhumation has likely been active since the opening of the basin and that a regular, layered, fully igneous oceanic crust is unlikely. The seismic modeling along transect 1, marked by velocities compatible with an oceanic layer 2 and 3 throughout the entire transect, clearly disputes this. Our results reveal that highly variable crust is present on the western Amundsen Basin and, as shown in previous studies [e.g., *Døssing et al.*, 2014; *Glebovsky et al*., 2013], reduced crustal thicknesses are observed.

6. Conclusions

Interpretation of new seismic refraction data in combination with coincident seismic reflection lines is used to obtain information on the crustal accretion processes in the western Amundsen Basin. The study reveals a detailed picture of the crustal velocity structure in the basin in an area that is only sparsely covered by seismic profiles due to the harsh climate there and the associated logistical challenges of acquiring data.

The crust created by ultraslow spreading in the western Amundsen Basin displays significant variations in its velocity structure and composition. The sonobuoy data indicate three main basement types:

1) Crust resembling normal oceanic crust composed of oceanic layers 2 and 3. However, the total crustal thickness is less than the global average of 7 km [*White et al.*, 1992]. The maximum observed thickness is 6 km but, in most areas, the crust is only between 2 and 5 km thick. Such a reduced thickness is typical for crust produced at ultraslow spreading rates [e.g., *Dick et al*., 2003].
2) Oceanic crust that displays a layer 2 but where layer 3 is absent. Here the crust may be underlain by partially serpentinized mantle.
3) Exhumed mantle consisting of two layers separated by a serpentinization front. The upper layer consists of exhumed and highly serpentinized mantle, while the lower layer represents partially serpentinized mantle. There is a distinct velocity change across the serpentinization front.

Our seismic modeling indicates the presence of velocities compatible with an oceanic layer 2 and 3 within the extensions of the SMZ. These results are different than previous observations along the Gakkel Ridge, where no oceanic layer 3 has been documented. The different basement types therefore indicate that there is both a spatial and temporal variation in crustal accretion processes at the ridge.

Acknowledgements

This work was supported by a scholarship from the Consejo Nacional de Ciencia y Tecnología (CONACYT). Data acquisition was funded by the Continental Shelf Project of the Kingdom of Denmark. Many thanks go to Arne Døssing (National Space Institute, DTU Space) and John Hopper (Geological Survey of Denmark and Greenland) for their assistance in the processing of gravity data and multichannel reflection seismic data. Special thanks to Lars Kjærgaard for his assistance with the loading of multichannel seismic reflection data and GEUS-IT for all their technical support.

References

Abrams, L. J., R. S. Detrick, and P. J. Fox (1988), Morphology and crustal structure of the Kane Fracture Zone Transverse Ridge, *Journal of Geophysical Research: Solid Earth*, *93*(B4), 3195-3210, doi: 10.1029/JB093iB04p03195s.

Ambos, E. L., and D. M. Hussong (1986), Oceanographer transform fault structure compared to that of surrounding oceanic crust: Results from seismic refraction data analysis, *Journal of Geodynamics*, *5*(1), 79-102, doi: http://dx.doi.org/10.1016/0264-3707(86)90024-4s.

Andersen, O. B. (2010), The DTU10 Gravity field and Mean sea surface, Second internationalsymposium of the gravity field of the Earth (IGFS2), Fairbanks, Alaska.

Bown, J. W., and R. S. White (1994), Variation with spreading rate of oceanic crustal thickness and geochemistry, *Earth and Planetary Science Letters*, *121*(3–4), 435-449, doi: http://dx.doi.org/10.1016/0012-821X(94)90082-5s.

Brozena, J. M., V. A. Childers, L. A. Lawver, L. M. Gahagan, R. Forsberg, J. I. Faleide, and O. Eldholm (2003), New aerogeophysical study of the Eurasia Basin and Lomonosov Ridge: Implications for basin development, *Geology*, *31*(9), 825-828, doi: 10.1130/g19528.1s.

Bruguier, N. J., and T. A. Minshull (1997), Accurate Modelling of Sonobuoy Refraction Data to Determine Velocity Variations in Oceanic Crust, *Marine Geophysical Researches*, *19*(1), 25-36, doi: 10.1023/a:1004249108479s.

Cannat, M., G. Manatschal, D. Sauter, G. Peron-Pinvidic (2009), Assessing the conditions of continental breakup at magma-poor rifted margins: What can we learn from slow spreading mid-ocean ridges?, *Comptes Rendus Geoscience*, 341 (5), 406-427, doi: 10.1016/j.crte.2009.01.005.

Cannat, M., D. Sauter, V. Mendel, E. Ruellan, K. Okino, J. Escartin, V. Combier, and M. Baala (2006), Modes of seafloor generation at a melt-poor ultraslow-spreading ridge, *Geology*, *34*(7), 605-608, doi: 10.1130/g22486.1s.

Carlson, R. L. (1998), Seismic velocities in the uppermost oceanic crust: Age dependence and the fate of layer 2A, *Journal of Geophysical Research: Solid Earth*, *103*(B4), 7069-7077, doi: 10.1029/97jb03577s.

Chian, D., H. R. Jackson, D. R. Hutchinson, J. W. Shimeld, G. N. Oakey, N. Lebedeva-Ivanova, Q. Li, R. W. Saltus, and D. C. Mosher (2016), Distribution of crustal types in Canada Basin, Arctic Ocean, *Tectonophysics*, doi: 10.1016/j.tecto.2016.01.038s.

Christensen, N. I. (2004), Serpentinites, Peridotites, and Seismology, *International Geology Review*, *46*(9), 795-816, doi: 10.2747/0020-6814.46.9.795s.

Cochran, J. R., M. H. Edwards, and B. J. Coakley (2006), Morphology and structure of the Lomonosov Ridge, Arctic Ocean, *Geochemistry, Geophysics, Geosystems*, *7*(5), doi: 10.1029/2005gc001114s.

Cochran, J. R., G. J. Kurras, M. H. Edwards, and B. J. Coakley (2003), The Gakkel Ridge: Bathymetry, gravity anomalies, and crustal accretion at extremely slow spreading rates, *Journal of Geophysical Research: Solid Earth*, *108*(B2), doi: doi:10.1029/2002JB001830s.

Coogan, L. A., C. J. MacLeod, H. J. B. Dick, S. J. Edwards, A. Kvassnes, J. H. Natland, P. T. Robinson, G. Thompson, and M. J. O'Hara (2001), Whole-rock geochemistry of gabbros from the Southwest Indian Ridge: constraints on geochemical fractionations between the upper and lower oceanic crust and magma chamber processes at (very) slow-spreading ridges, *Chemical Geology*, *178*(1–4), 1-22, doi: http://dx.doi.org/10.1016/S0009-2541(00)00424-1s.

Crane, K., H. Doss, P. Vogt, E. Sundvor, G. Cherkashov, I. Poroshina, and D. Joseph (2001), The role of the Spitsbergen shear zone in determining morphology, segmentation and evolution of the Knipovich Ridge, *Marine Geophysical Researches*, *22*(3), 153-205, doi: 10.1023/a:1012288309435s.

Czuba, W., M. Grad, R. Mjelde, A. Guterch, A. Libak, F. Krüger, Y. Murai, J. Schweitzer, and I. P. Group (2011), Continent—ocean-transition across a trans-tensional margin segment: off Bear Island, Barents Sea, *Geophysical Journal International*, *184*(2), 541-554, doi: 10.1111/j.1365-246X.2010.04873.xs.

Dean, S. L., D. S. Sawyer, and J. K. Morgan (2015), Galicia Bank ocean–continent transition zone: New seismic reflection constraints, *Earth and Planetary Science Letters*, *413*(0), 197-207, doi: http://dx.doi.org/10.1016/j.epsl.2014.12.045s.

Dean, S. M., T. A. Minshull, R. B. Whitmarsh, and K. E. Louden (2000), Deep structure of the ocean-continent transition in the southern Iberia Abyssal Plain from seismic refraction profiles: The IAM-9 transect at 40°20′N, *Journal of Geophysical Research: Solid Earth*, *105*(B3), 5859-5885, doi: 10.1029/1999jb900301s.

Delescluse, M., T. Funck, S. A. Dehler, K. E. Louden, and L. Watremez (2015), The oceanic crustal structure at the extinct, slow to ultraslow Labrador Sea spreading center, *Journal of Geophysical Research: Solid Earth*, *120*(7), 5249-5272, doi: 10.1002/2014jb011739s.

DeMets, C., R. G. Gordon, D. F. Argus, and S. Stein (1994), Effect of recent revisions to the geomagnetic reversal time scale on estimates of current plate motions, *Geophysical Research Letters*, *21*(20), 2191-2194, doi: 10.1029/94GL02118s.

Detrick, R. S., and G. M. Purdy (1980), The crustal structure of the Kane fracture zone from

seismic refraction studies, *J. Geophys. Res.*, 85, 3759-3778.
Detrick, R. S., R. S. White, and G. M. Purdy (1993), Crustal structure of North Atlantic Fracture Zones, *Reviews of Geophysics*, *31*(4), 439-458, doi: 10.1029/93rg01952s.
Dick, H. J. B., J. Lin, and H. Schouten (2003), An ultraslow-spreading class of ocean ridge, *Nature*, *426*(6965), 405-412.
Duckworth, G. L., A. B. Baggeroer, and H. R. Jackson (1982), Crustal structure measurements near FRAM II in the pole abyssal plain, *Tectonophysics*, *89*(1), 173-215, doi: http://dx.doi.org/10.1016/0040-1951(82)90038-5s.
Dunn, R. A. (2015), 1.13 - Crust and Lithospheric Structure - Seismic Structure of Mid-Ocean Ridges, in *Treatise on Geophysics (Second Edition)*, edited by G. Schubert, pp. 419-451, Elsevier, Oxford.
Døssing, A., J. R. Hopper, A. V. Olesen, T. M. Rasmussen, and J. Halpenny (2013a), New aero-gravity results from the Arctic: Linking the latest Cretaceous-early Cenozoic plate kinematics of the North Atlantic and Arctic Ocean, *Geochemistry, Geophysics, Geosystems*, *14*(10), 4044-4065, doi: 10.1002/ggge.20253s.
Døssing, A., T. M. Hansen, A. V. Olesen, J. R. Hopper, and T. Funck (2014), Gravity inversion predicts the nature of the Amundsen Basin and its continental borderlands near Greenland, *Earth and Planetary Science Letters*, *408*(0), 132-145, doi: 10.1016/j.epsl.2014.10.011s.
Døssing, A., H. R. Jackson, J. Matzka, I. Einarsson, T. M. Rasmussen, A. V. Olesen, and J. M. Brozena (2013b), On the origin of the Amerasia Basin and the High Arctic Large Igneous Province—Results of new aeromagnetic data, *Earth and Planetary Science Letters*, *363*(0), 219-230, doi: 10.1016/j.epsl.2012.12.013s.
Edwards, M. H., G. J. Kurras, M. Tolstoy, D. R. Bohnenstiehl, B. J. Coakley, and J. R. Cochran (2001), Evidence of recent volcanic activity on the ultraslow-spreading Gakkel ridge, *Nature*, *409*(6822), 808-812.
Engen, Ø., J. I. Faleide, and T. K. Dyreng (2008), Opening of the Fram Strait gateway: A review of plate tectonic constraints, *Tectonophysics*, *450*(1–4), 51-69, doi: 10.1016/j.tecto.2008.01.002s.
Engen, Ø., J. A. Gjengedal, J. I. Faleide, Y. Kristoffersen, and O. Eldholm (2009), Seismic stratigraphy and sediment thickness of the Nansen Basin, Arctic Ocean, *Geophysical Journal International*, *176*(3), 805-821, doi: 10.1111/j.1365-246X.2008.04028.xs.
Fütterer, D. (1992), ARCTIC '91: die Expedition ARK-VIII/3 mit FS "Polarstern" 1991 = ARCTIC '91: the expedition ARK-VIII/3 of RV "Polarstern" in 1991, Alfred Wegener Institute for Polar and Marine Research, Bremerhaven.
Gaina, C., S. C. Werner, R. Saltus, S. Maus, and t. C.-G. GROUP (2011), Chapter 3 Circum-Arctic mapping project: new magnetic and gravity anomaly maps of the Arctic, *Geological Society, London, Memoirs*, *35*(1), 39-48, doi: 10.1144/m35.3s.
Glebovsky, V. Y., V. D. Kaminsky, A. N. Minakov, S. A. Merkur'ev, V. A. Childers, and J. M. Brozena (2006), Formation of the Eurasia Basin in the Arctic Ocean as inferred from geohistorical analysis of the anomalous magnetic field, *Geotectonics*, *40*(4), 263-281, doi: 10.1134/s0016852106040029s.
Glebovsky, V. Y., E. G. Astafurova, A. A. Chernykh, M. A. Korneva, V. D. Kaminsky, and V. A. Poselov (2013), Thickness of the Earth's crust in the deep Arctic Ocean: Results of a 3D gravity modeling, *Russian Geology and Geophysics*, *54*(3), 247-262, doi: http://dx.doi.org/10.1016/j.rgg.2013.02.001s.
Grantz, A., P. E. Hart, and V. A. Childers (2011), Chapter 50 Geology and tectonic development of the Amerasia and Canada Basins, Arctic Ocean, *Geological Society, London, Memoirs*, *35*(1), 771-799, doi: 10.1144/m35.50s.
Grevemeyer, I., and W. Weigel (1996), Seismic velocities of the uppermost igneous crust versus age, *Geophysical Journal International*, *124*(2), 631-635, doi: 10.1111/j.1365-246X.1996.tb07041.xs.

Hermann, T., and W. Jokat (2013), Crustal structures of the Boreas Basin and the Knipovich Ridge, North Atlantic, *Geophysical Journal International*, *193*(3), 1399-1414, doi: 10.1093/gji/ggt048s.

Houtz, R., and J. Ewing (1976), Upper crustal structure as a function of plate age, *Journal of Geophysical Research*, *81*(14), 2490-2498, doi: 10.1029/JB081i014p02490s.

Jackson, H. R., I. Reid, and R. K. H. Falconer (1982), Crustal structure near the Arctic Mid-Ocean Ridge, *Journal of Geophysical Research: Solid Earth*, *87*(B3), 1773-1783, doi: 10.1029/JB087iB03p01773s.

Jakobsson, M., et al. (2012), The International Bathymetric Chart of the Arctic Ocean (IBCAO) Version 3.0, *Geophysical Research Letters*, *39*(12), doi: 10.1029/2012GL052219s.

Jokat, W., and U. Micksch (2004), Sedimentary structure of the Nansen and Amundsen basins, Arctic Ocean, *Geophysical Research Letters*, *31*(2), L02603, doi: 10.1029/2003gl018352s.

Jokat, W., and M. C. Schmidt-Aursch (2007), Geophysical characteristics of the ultraslow spreading Gakkel Ridge, Arctic Ocean, *Geophysical Journal International*, *168*(3), 983-998, doi: 10.1111/j.1365-246X.2006.03278.xs.

Jokat, W., G. Uenzelmann-Neben, Y. Kristoffersen, and T. M. Rasmussen (1992), Lomonosov Ridge—A double-sided continental margin, *Geology*, *20*(10), 887-890, doi: 10.1130/0091-7613(1992)020<0887:lradsc>2.3.co;2s.

Jokat, W., E. Weigelt, Y. Kristoffersen, T. Rasmussen, and T. Schöone (1995), New insights into the evolution of the Lomonosov Ridge and the Eurasian Basin, *Geophysical Journal International*, *122*(2), 378-392, doi: 10.1111/j.1365-246X.1995.tb00532.xs.

Jokat, W., O. Ritzmann, M. C. Schmidt-Aursch, S. Drachev, S. Gauger, and J. Snow (2003), Geophysical evidence for reduced melt production on the Arctic ultraslow Gakkel mid-ocean ridge, *Nature*, *423*(6943), 962-965, doi: http://www.nature.com/nature/journal/v423/n6943/suppinfo/nature01706_S1.htmls.

Juteau, T. M., René (1997), Structure and lithology of the oceanic crust of the present-day oceans, in *The Oceanic Crust, from Accretion to Mantle Recycling*, edited, p. 390, Springer.

Klingelhöfer, F., L. Géli, L. Matias, N. Steinsland, and J. Mohr (2000), Crustal structure of a super-slow spreading centre: a seismic refraction study of Mohns Ridge, 72° N, *Geophysical Journal International*, *141*(2), 509-526, doi: 10.1046/j.1365-246x.2000.00098.xs.

Lawver, L. A., and Scotese, C.R. (1990), A review of tectonic models for the evolution of the Canada Basin, in *The Arctic Ocean Region*, edited by A. Grantz, Johnson, L., and Sweeney, J.F., pp. 593-617, Geological Society of America, The Geology of North America, Boulder, Colorado.

Ludwig, W.J., J. E. Nafe, and C. L. Drake (1970), Seismic refraction in *The Sea*, Editor: Maxwell, A.E., *4*, Wiley-Interscience, New York, 53-84.

Lutz, R., D. Franke, K. Berglar, I. Heyde, B. Schreckenberger, P. Klitzke, and W. H. Geissler (2018), Evidence for mantle exhumation since the early evolution of the slow-spreading Gakkel Ridge, Arctic Ocean, *Journal of Geodynamics*, *118*, 154-165, doi: https://doi.org/10.1016/j.jog.2018.01.014s.

Lykke-Andersen, H., Funck, T., Hopper, J.R., Trinhammer, P., Marcussen, C., Gunvald, A. K., & Jørgensen, E. V. (2010). Seismic Acquisition Report - LOMROG 2009. Danmarks and Grønlands Geologiske Undersøgelse Rapport, 2010/53, 73pp. (excl. appendices).

Marcussen, C., and the LOMROG III Scientific Party (2012), Lomonosov Ridge off Greenland 2012 (LOMROG III) – Cruise Report *Rep. 2012/119*, 220 pp, Danmarks og Grønlands Geologiske Undersøgelse Rapport.

Marcussen, C., and the LOMROG II Scientific Party (2009), Lomonosov Ridge off Greenland 2009 (LOMROG II) Cruise Report *Rep. 2011/106*, 154 pp, Danmarks og Grønlands Geologiske Undersøgelse Rapport.

Meier, M. and V. Schlindwein (2017), Potential sill intrusion recorded at ultraslow spreading Southwest Indian Ridge, AGU Fall Meeting, New Orleans, 11 December 2017 - 15 December 2017.

Michael, P. J., et al. (2003), Magmatic and amagmatic seafloor generation at the ultraslow-spreading Gakkel ridge, Arctic Ocean, *Nature*, *423*(6943), 956-961.
Muller, M. R., T. A. Minshull, and R. S. White (1999), Segmentation and melt supply at the Southwest Indian Ridge, *Geology*, *27*(10), 867-870, doi: 10.1130/0091-7613(1999)027<0867:samsat>2.3.co;2s.
Muller, M. R., T. A. Minshull, and R. S. White (2000), Crustal structure of the Southwest Indian Ridge at the Atlantis II Fracture Zone, *Journal of Geophysical Research: Solid Earth*, *105*(B11), 25809-25828, doi: 10.1029/2000jb900262s.
Mutter, C. Z., and J. C. Mutter (1993), Variations in thickness of layer 3 dominate oceanic crustal structure, *Earth and Planetary Science Letters*, *117*(1–2), 295-317, doi: http://dx.doi.org/10.1016/0012-821X(93)90134-Us.
Niu, X., A. Ruan, J. Li, T. A. Minshull, D. Sauter, Z. Wu, X. Qiu, M. Zhao, Y. J. Chen, and S. Singh (2015), Along-axis variation in crustal thickness at the ultraslow spreading Southwest Indian Ridge (50°E) from a wide-angle seismic experiment, *Geochemistry, Geophysics, Geosystems*, *16*(2), 468-485, doi: 10.1002/2014gc005645s.
Ogg, J. G. (2012), Chapter 5 - Geomagnetic Polarity Time Scale, in *The Geologic Time Scale*, edited by F. M. Gradstein, J. G. Ogg, M. D. Schmitz and G. M. Ogg, pp. 85-113, Elsevier, Boston.
Okino, K., D. Curewitz, M. Asada, K. Tamaki, P. Vogt, and K. Crane (2002), Preliminary analysis of the Knipovich Ridge segmentation: influence of focused magmatism and ridge obliquity on an ultraslow spreading system, *Earth and Planetary Science Letters*, *202*(2), 275-288, doi: http://dx.doi.org/10.1016/S0012-821X(02)00790-2s.
Ostenso, N. A., and R. J. Wold (1977), A seismic and gravity profile across the Arctic Ocean Basin, *Tectonophysics*, *37*(1), 1-24, doi: 10.1016/0040-1951(77)90036-1s.
Peron-Pinvidic, G., D. J. Shillington, and B. E. Tucholke (2010), Characterization of sills associated with the U reflection on the Newfoundland margin: evidence for widespread early post-rift magmatism on a magma-poor rifted margin, *Geophysical Journal International*, *182*(1), 113-136, doi: 10.1111/j.1365-246X.2010.04635.xs.
Pickup, S. L. B., R. B. Whitmarsh, C. M. R. Fowler, and T. J. Reston (1996), Insight into the nature of the ocean-continent transition off West Iberia from a deep multichannel seismic reflection profile, *Geology*, *24*(12), 1079-1082, doi: 10.1130/0091-7613(1996)024<1079:IITNOT>2.3.CO;2s.
Poselov, V., V. Butsenki, A. Chernykh, V. Glebovsky, H. R. Jackson, D. P. Potter, G. Oakey, J. Shimeld, and C. Marcussen (2014), The structural integrity of the Lomonosov Ridge withhe North American and Siberian continental margins, paper presented at International Conference on Arctic Margins VI, Fairbanks, Alaska, May 2011.
Reid, I., and H. R. Jackson (1981), Oceanic spreading rate and crustal thickness, *Marine Geophysical Researches*, *5*(2), 165-172, doi: 10.1007/bf00163477s.
Reston, T., C. Krawczyk, and D. Klaeschen (1996), The S reflector west of Galicia (Spain): Evidence from prestack depth migration for detachment faulting during continental breakup, J. Geophys. Res., 101(B4), 8075–8091, doi:10.1029/95JB03466.
Sauter, D., V. Mendel, C. Rommevaux-Jestin, L. M. Parson, H. Fujimoto, C. Mével, M. Cannat, and K. Tamaki (2004), Focused magmatism versus amagmatic spreading along the ultra-slow spreading Southwest Indian Ridge: Evidence from TOBI side scan sonar imagery, *Geochemistry, Geophysics, Geosystems*, *5*(10), n/a-n/a, doi: 10.1029/2004gc000738s.
Schlindwein, V., A. Demuth, W. H. Geissler, and W. Jokat (2013), Seismic gap beneath Logachev Seamount: Indicator for melt focusing at an ultraslow mid-ocean ridge?, *Geophysical Research Letters*, *40*(9), 1703-1707, doi: 10.1002/grl.50329s.

Schmidt-Aursch, M. C., and W. Jokat (2016), 3D gravity modelling reveals off-axis crustal thickness variations along the western Gakkel Ridge (Arctic Ocean), *Tectonophysics*, doi: http://dx.doi.org/10.1016/j.tecto.2016.03.021s.

Shillington D.J., B.E. Tucholke, G.D. Karner, D.S. Sawyer, W.S. Holbrook, and H. Delius (2007), Linking core and seismic data without logs: core-seismic correlation at site 1276, in Proceedings of the ODP Science Results, 210, eds Tucholke B.E. Sibuet J.-C. Klaus A., Ocean Drilling Program, College Station, TX.

Sibuet, J. C., S. Srivastava, and G. Manatschal (2007) Exhumed mantle-forming transitional crust in the Newfoundland-Iberia rift and associated magnetic anomalies, *J. geophys. Res*., 112(B6), doi:10.1029/2005JB003856.

Standish, J. J., H. J. B. Dick, P. J. Michael, W. G. Melson, and T. O'Hearn (2008), MORB generation beneath the ultraslow spreading Southwest Indian Ridge (9–25°E): Major element chemistry and the importance of process versus source, *Geochemistry, Geophysics, Geosystems*, *9*(5), Q05004, doi: 10.1029/2008gc001959s.

Talwani, M., and O. Eldholm (1977), Evolution of the Norwegian-Greenland Sea, *Geological Society of America Bulletin*, *88*(7), 969-999, doi: 10.1130/0016-7606(1977)88<969:eotns>2.0.co;2s.

Talwani, M., J. L. Worzel, and M. Landisman (1959), Rapid gravity computations for two-dimensional bodies with application to the Mendocino submarine fracture zone, J. Geophys. Res., 64, 49–59.

Tivey, M. A., and H. P. Johnson (1993), Variations in oceanic crustal structure and implications for the fine-scale magnetic anomaly signal, *Geophysical Research Letters*, *20*(17), 1879-1882, doi: 10.1029/93gl01485s.

Tucholke B.E., J.A. Austin, and E. Uchupi (1989), Crustal structure and rift-drift evolution of the Newfoundland Basin, in Extensional Tectonics and Stratigraphy of the North Atlantic Margins , *AAPG Memoir*, 46, pp. 247–263, eds Tankard A.J. and H.R. Balkwill, American Association of Petroleum Geologists, Tulsa, OK.

Urlaub, M., M. C. Schmidt-Aursch, W. Jokat, and N. Kaul (2010), Gravity crustal models and heat flow measurments for the Eurasia Basin, Arctic Ocean, *Marine Geophysical Researches*, doi: doi:10.1007/s11001-010-9093-xs.

Varming, T., Funck, T., Hopper, J.R., Trinhammer, P., Ejlertsen, S., Rödel, L., Schiling, J., Kvist-Lassen, T., Rasmussen, M.L., Ugelvig, S., & Marcussen, C. (2012). Seismic Acquisition Report - LOMROG 2012. Danmarks and Grønlands Geologiske Undersøgelse Rapport 2012/120, 77pp (excl. appendices).

Vogt, P. R., P. T. Taylor, L. C. Kovacs, and G. L. Johnson (1979), Detailed aeromagnetic investigation of the Arctic Basin, *Journal of Geophysical Research: Solid Earth*, *84*(B3), 1071-1089, doi: 10.1029/JB084iB03p01071s.

White, R. S., D. McKenzie, and R. K. O'Nions (1992), Oceanic crustal thickness from seismic measurements and rare earth element inversions, *Journal of Geophysical Research: Solid Earth*, *97*(B13), 19683-19715, doi: 10.1029/92jb01749s.

White, R. S., R. S. Detrick, M. C. Sinha, and M. H. Cormier (1984), Anomalous seismic crustal structure of oceanic fracture zones, *Geophysical Journal of the Royal Astronomical Society*, *79*(3), 779-798, doi: 10.1111/j.1365-246X.1984.tb02868.xs.

White, R. S., T. A. Minshull, M. J. Bickle, and C. J. Robinson (2001), Melt Generation at Very Slow-Spreading Oceanic Ridges: Constraints from Geochemical and Geophysical Data, *Journal of Petrology*, *42*(6), 1171-1196, doi: 10.1093/petrology/42.6.1171s.

Wilson, D. S., et al. (2006), Drilling to Gabbro in Intact Ocean Crust, *Science*, *312*(5776), 1016-1020, doi: 10.1126/science.1126090s.

Wright, J., and D. A. Rothery (1998), Chapter 4 – The structure and formation of oceanic lithosphere, in *The Ocean Basins: Their Structure and Evolution*, edited by J. Wright and D. A. Rothery, pp. 68-95.

Zelt, C. A. and R. M. Ellis (1988), Practical and efficient ray tracing in two-dimensional media for rapid traveltime and amplitude forward modelling, *Canadian Journal of Exploration Geophysics*, *24*, 16-31.
Zelt, C. A., and R. B. Smith (1992), Seismic traveltime inversion for 2-D crustal velocity structure, *Geophysical Journal International*, *108*(1), 16-34, doi: 10.1111/j.1365-246X.1992.tb00836.xs.

	LOMROG II	LOMROG III
Source	1 Sercel G and 1 Sercel GI gun	2 Sercel G-guns
Chamber volume	605 cu. inch	1040 cu. inch
Gun pressure	180 bar (2600 psi)	180 bar (2600 psi)
Nominal tow depth	20 m	20 m
Streamer	Geometrics GeoEel	Geometrics GeoEel
Length of tow cable	43 m	30 m
Total no. of groups	32 / 40	32
Group interval	6.25 m	6.25 m
Nominal tow depth	20 m	20 m

Table 1. Summary of Key Acquisition Parameters during LOMROG II and III

Table 1. Summary of the key acquisition parameters during the LOMROG cruises.

Figure Captions

Figure 1. Bathymetric map of the Amundsen Basin and surrounding areas in the Arctic Ocean. Yellow lines indicate the location of LOMROG multichannel seismic reflection profiles collected in 2007, 2009, and 2012. White lines mark seismic reflection data from AMORE 2011 [*Jokat and Micksch*, 2004]. Green lines show the seismic reflection lines from NP-28 [*Fütterer*, 1992] and Arlis-II [*Ostenso and Wold*, 1977]. Red lines mark the seismic profiles from the LOMROG expeditions that are featured in this paper (Figs. 4–6). The location of Integrated Ocean Drilling Program 302 (ACEX) is marked by a red circle. Bathymetric data are from the IBCAO 3.0 grid (Jakobsson et al., 2012). Abbreviations: BS – Barents Shelf; CB – Canada Basin; ESS – East Siberian Shelf; EAB – Eastern Amundsen Basin; EI – Ellesmere Island; FS – Fram Strait; KS – Kara Shelf; LVS – Laptev Shelf; LS – Lincoln Shelf; NS – Nares Strait; RU – Russia; SAT – St. Anna Trough; WAB – Western Amundsen Basin; YP – Yermak Plateau.

Figure 2. Bathymetric map shown together with the interpreted magnetic anomalies of *Brozena et al.* [2003]. White lines: normal polarity chrons. The "y" and "o" refer to the young and old side of the anomalies respectively. Yellow lines indicate the location of LOMROG multichannel seismic reflection profiles collected in 2007, 2009, and 2012. Orange circles indicate the deployment positions of the LOMROG sonobuoys used in this study.

Figure 3 Raw record section with phase interpretations for sonobuoys 3, 9 and 50. The vertical scale for the record sections is the travel time using a reduction velocity of 6.8 km/s, and the horizontal scale is the shot-receiver distance (offset).

Figure 4. (top) P-wave velocity model along transect 1. Numbers indicate velocities in km s^{-1}. Pale colors indicate sections unconstrained by multichannel seismic or refraction data. The red triangles mark the location of the sonobuoys. (bottom) P-wave velocity model converted to two-way travel time (TWT) and overlaid on the multichannel seismic record for comparison.

Figure 5. (top) P-wave velocity model along transect 2. Numbers indicate velocities in km s^{-1}. Pale colors indicate sections unconstrained by multichannel seismic or refraction data. The red triangles mark the location of the sonobuoys. (bottom) P-wave velocity model converted to two-way travel time (TWT) and overlaid on the multichannel seismic record for comparison.

Figure 6. (top) P-wave velocity model along transect 3. Numbers indicate velocity in km s^{-1}. The red triangles on the ocean surface mark the location of the sonobuoys. (bottom) P-wave velocity model converted to two-way travel time (TWT) and overlaid on the multichannel seismic record for comparison.

Figure 7. Free-air gravity anomaly (top) and magnetic anomaly map (bottom). The gravity data (DTU10 grid) was collected from *Andersen* [2010] while the magnetic data (CAMP-M grid) was collected from *Gaina et al.* [2011]. Filled circles indicate the top basement velocity from the sonobuoy data collected the Amundsen Basin [*Jokat et al.*, 1995a; *Jokat and Micksch*, 2004; *Jokat and Schmidt-Aursch*, 2007] and in the Nansen Basin [*Engen et al.*, 2009]. The black dashed line marks the boundary

between the Sparsely Magmatic Zone and the Eastern Volcanic Zone. The black arrow in the gravity map shows the gravity low discussed in the text. The black line in the magnetic map displays the location of Chron C8. EVZ – Eastern Volcanic Zone; SMZ – Sparsely Magmatic Zone.

Figure 8. Two-dimensional gravity model for transect 1. The P-wave velocity (Figure 4) was converted to density using the velocity-density relationship of *Ludwig et al*. [1970]. The numbers indicate the density in g/cm^3. (Top) Observed magnetic anomaly data (blue line) are extracted from the DTU10 grid from *Andersen* [2010] while the gravity data (black dots)) were collected from the shipborne gravimeter. The calculated gravity from the density model (red line) was obtained from two-dimensional gravity modelling.

Figure 9. Two-dimensional gravity model for transect 2. The P-wave velocity (Figure 4) was converted to density using the velocity-density relationship of *Ludwig et al*. [1970]. The numbers indicate the density in g/cm^3. (Top) Observed magnetic anomaly data (blue line) are extracted from the DTU10 grid from *Andersen* [2010] while the gravity data (black dots)) were collected from the shipborne gravimeter. The calculated gravity from the density model (red line) was obtained from two-dimensional gravity modelling.

Figure 10. Two-dimensional gravity model for transect 3. The P-wave velocity (Figure 4) was converted to density using the velocity-density relationship of *Ludwig et al*. [1970]. The numbers indicate the density in g/cm^3. (Top) Observed magnetic anomaly data (blue line) are extracted from the DTU10 grid from *Andersen* [2010] while the gravity data (black dots)) were collected from the shipborne gravimeter. The calculated gravity from the density model (red line) was obtained from two-dimensional gravity modelling.

Figure 11. Detail from Fig. 4 showing key seismic features from the multichannel seismic data along transect 1. Top: large faulted basement blocks. Bottom: high-amplitude basement identified along zone 3.

Figure 12. Comparison of basement character in seismic data. Top: portion of transect 2 approximately between km 75 and 90. Middle: Nansen Basin [*Lutz et al*., 2018]. Bottom: details from CAM 155 profile at the Iberian margin showing peridotite ridge 4 [R4; *Minshull et al*., 2014].

Figure 13. Stacked velocity-depth curves for 0 to 7 Ma (orange shading) and 59 to 127 Ma (blue shading) oceanic crust in the Atlantic Ocean [*White et al.* 1992]. The green and purple envelope indicate the range of the velocity data from the Gakkel Ridge [*Jokat and Schmidt-Aursch,* 2007] for the Eastern Volcanic Zone and the Sparsely Magmatic Zone, respectively. The black lines represent the velocity-depth curves for transect 1 of our study, while the red lines show the velocity-depth curves for transects 2 and 3. Mantle velocities are not included.

Figure 14 Comparison of P-wave velocity profiles of crust created by ultraslow seafloor spreading. The velocities for the extinct Labrador Sea spreading center are taken from *Delescluse et al*. [2015] and those from the South West Indian Ridge are from *Niu et al.* [2015]. Mohns Ridge velocities for 22.4-Ma-old crust are taken from *Klingelhöfer et al*. (2000) and for 20.2-Ma-old crust from *Czuba et al*. (2011). The light orange shows upper crustal velocities, the dark orange indicates lower crustal velocities, and the purple marks upper mantle.

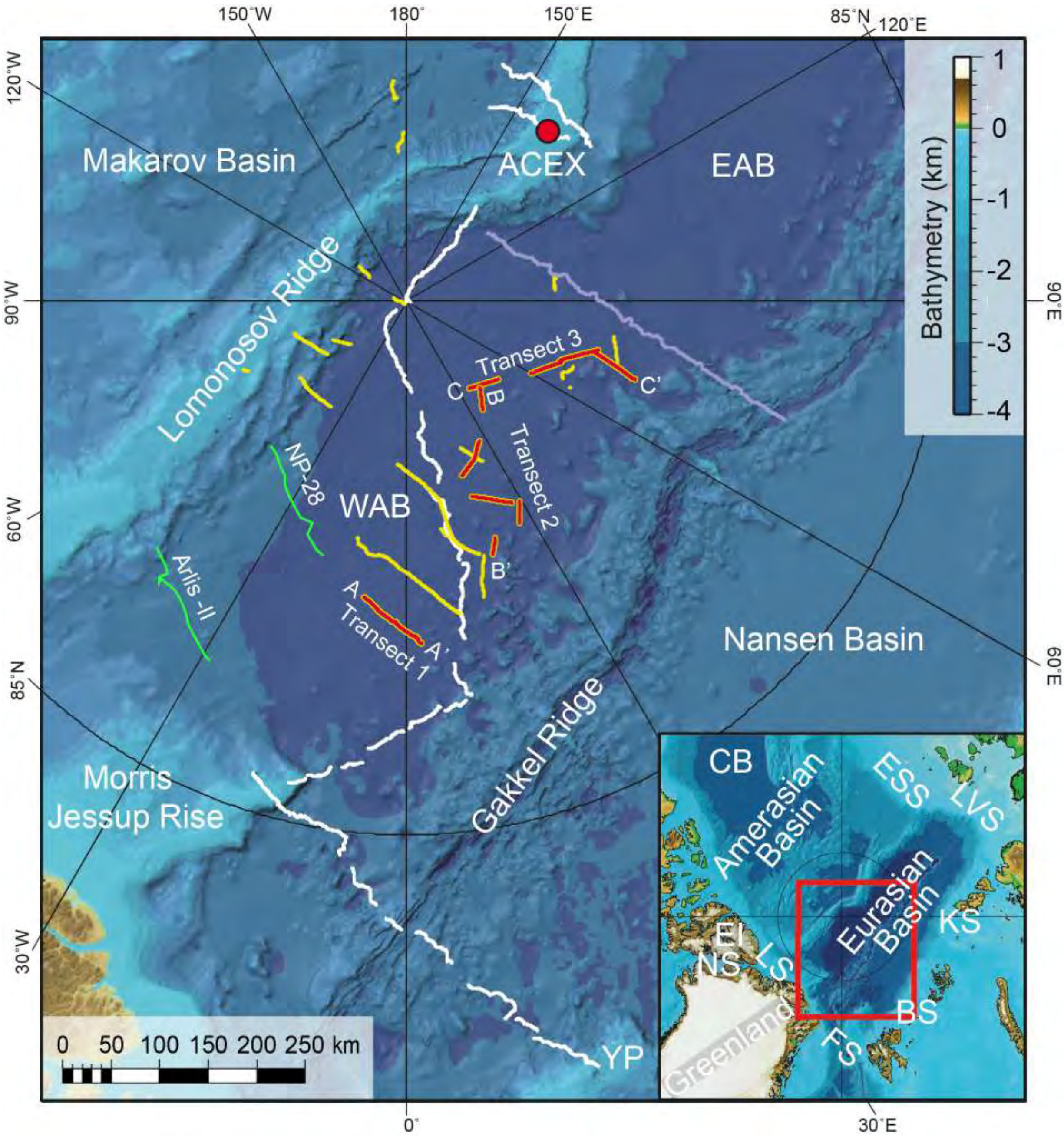

150°W
180°
150°E
85°N
120°E
120°W
90°W
60°W
85°N
30°W
0°
30°E
90°E
60°E
Makarov Basin
ACEX
EAB
Lomonosov Ridge
Transect 3
C
B
C'
Transect 2
NP-28
WAB
B'
Arlis -II
A
A'
Transect 1
Nansen Basin
Gakkel Ridge
Morris
Jessup Rise
YP
0 50 100 150 200 250 km
Bathymetry (km)
1
0
-1
-2
-3
-4
CB
Amerasian
Basin
ESS
LVS
Eurasian
Basin
EI
NS
LS
KS
BS
FS
Greenland

Fig. 1

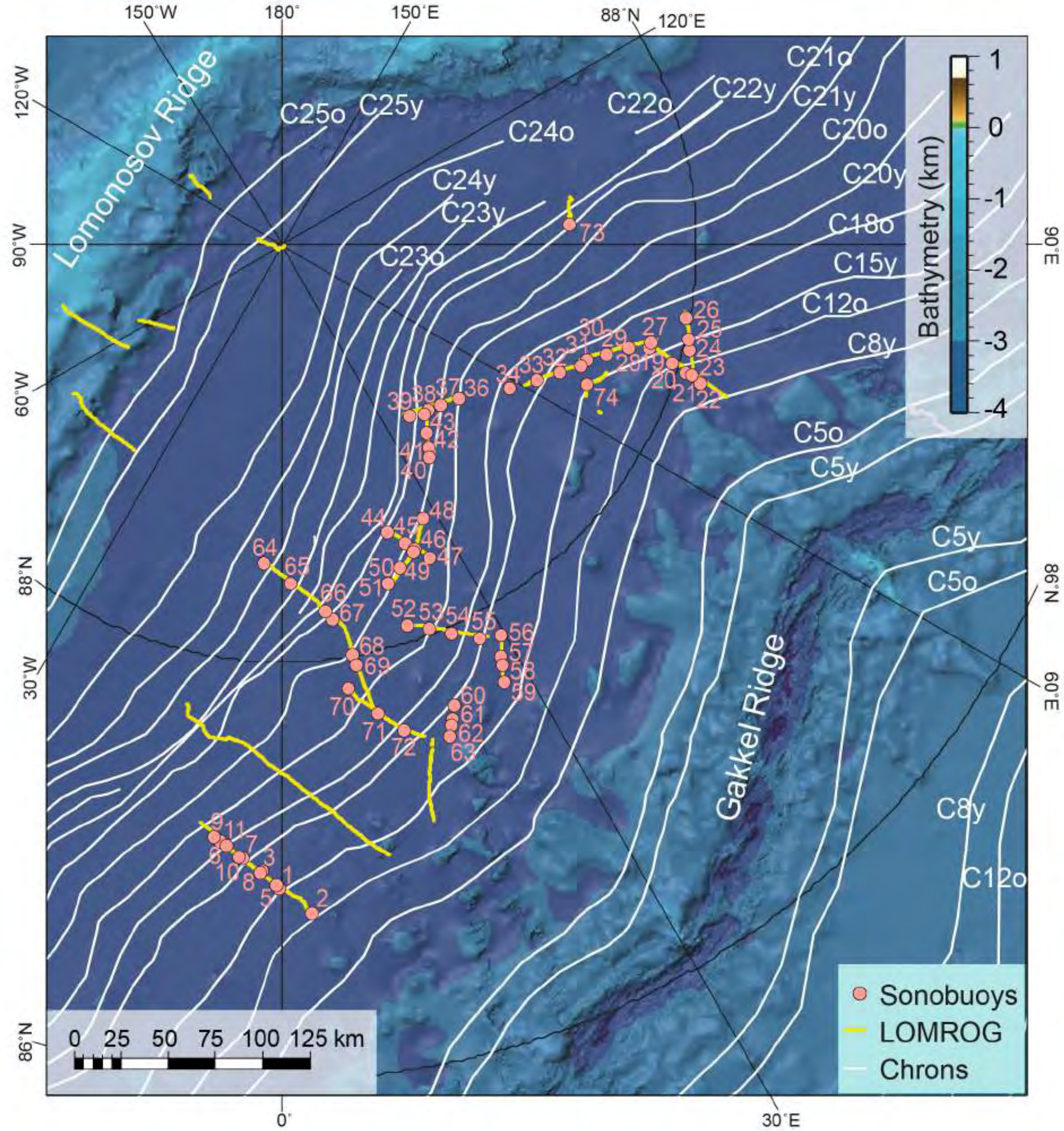
150°W
180°
150°E
88°N
120°E
120°W
90°W
60°W
88°N
30°W
86°N
0°
30°E
90°E
86°N
60°E
Lomonosov Ridge
Gakkel Ridge
C25o
C25y
C24o
C24y
C23y
C23o
C22o
C22y
C21o
C21y
C20o
C20y
C18o
C15y
C12o
C8y
C5o
C5y
Bathymetry (km)
1
0
-1
-2
-3
-4
0 25 50 75 100 125 km
Sonobuoys
LOMROG
Chrons

Fig. 2

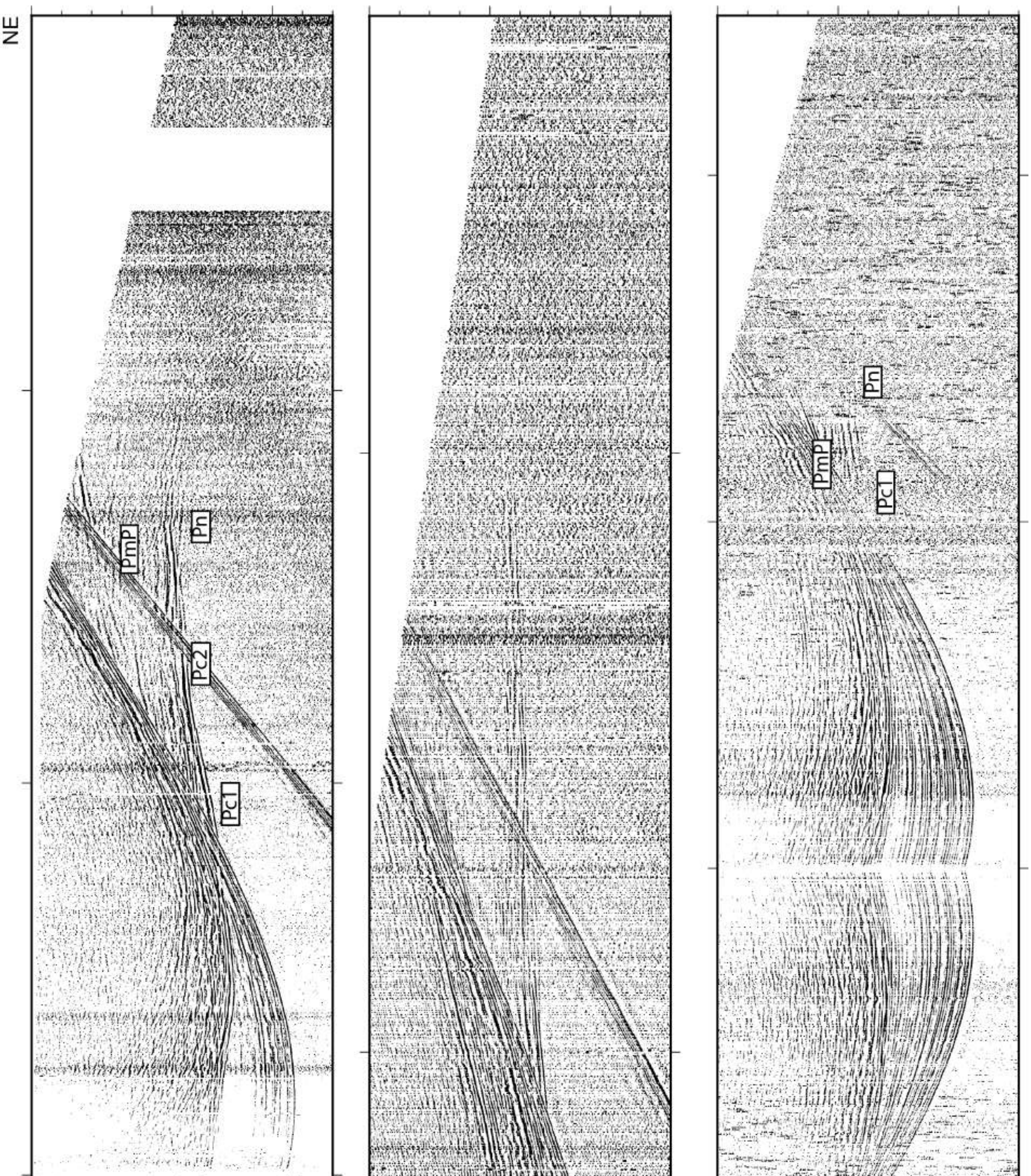

Fig.3

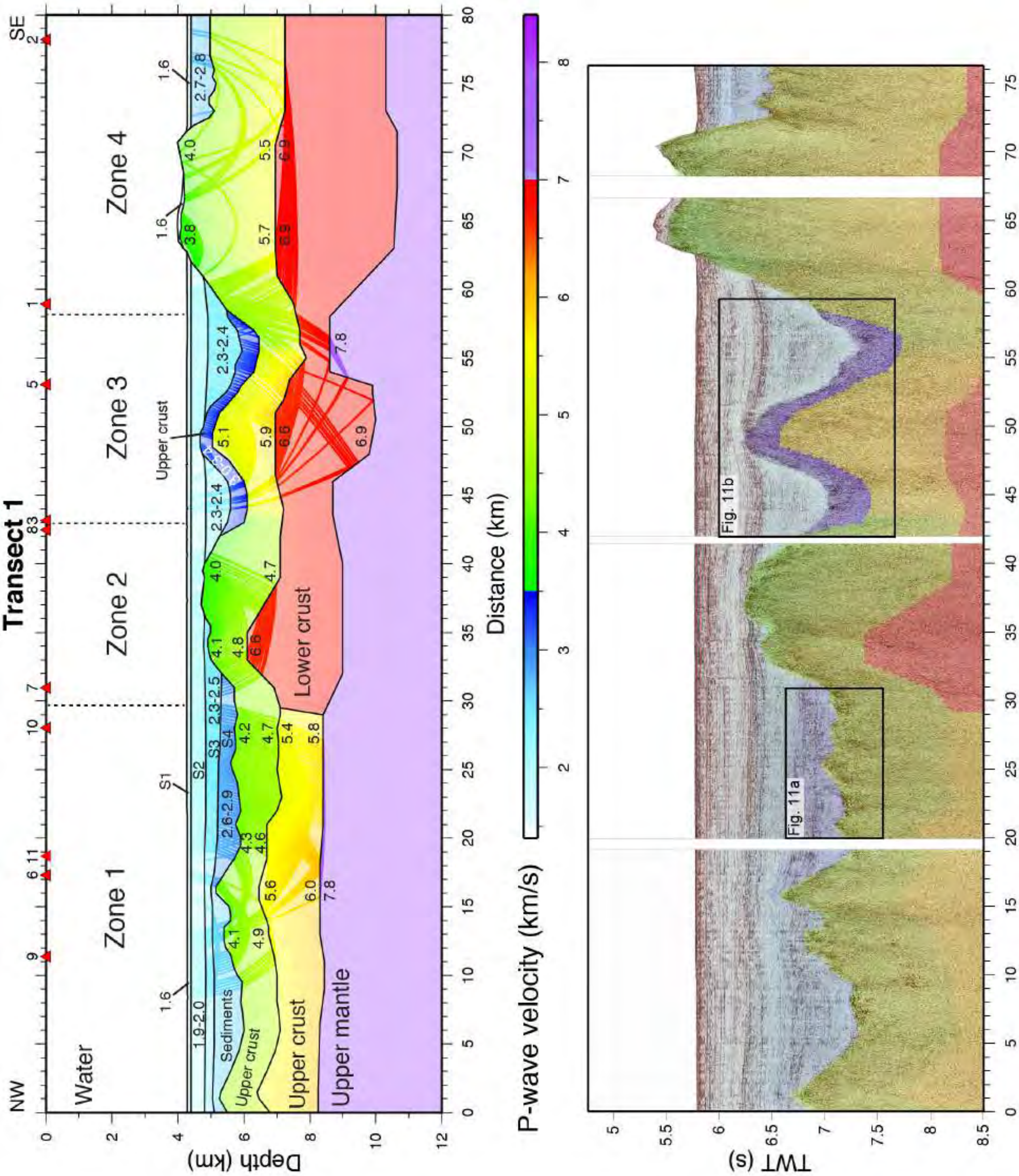

Transect 1
NW
SE
Zone 1
Zone 2
Zone 3
Zone 4
Water
Sediments
Upper crust
Lower crust
Upper mantle
Depth (km)
Distance (km)
P-wave velocity (km/s)
TWT (s)
Fig. 11a
Fig. 11b

Fig. 4

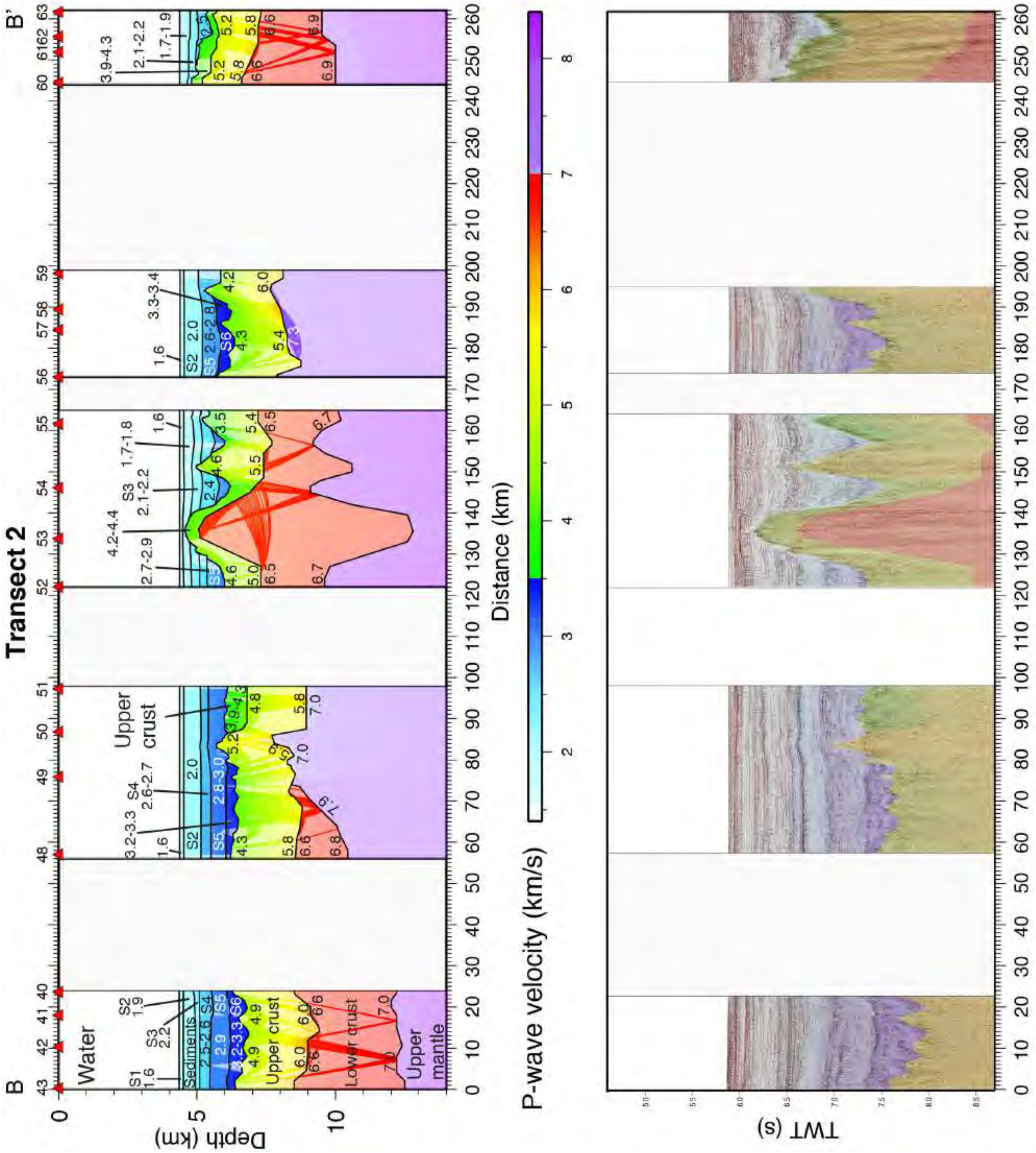
Transect 2
B
B'
Water
Sediments
Upper crust
Lower crust
Upper mantle
Depth (km)
Distance (km)
P-wave velocity (km/s)
TWT (s)

Fig. 5

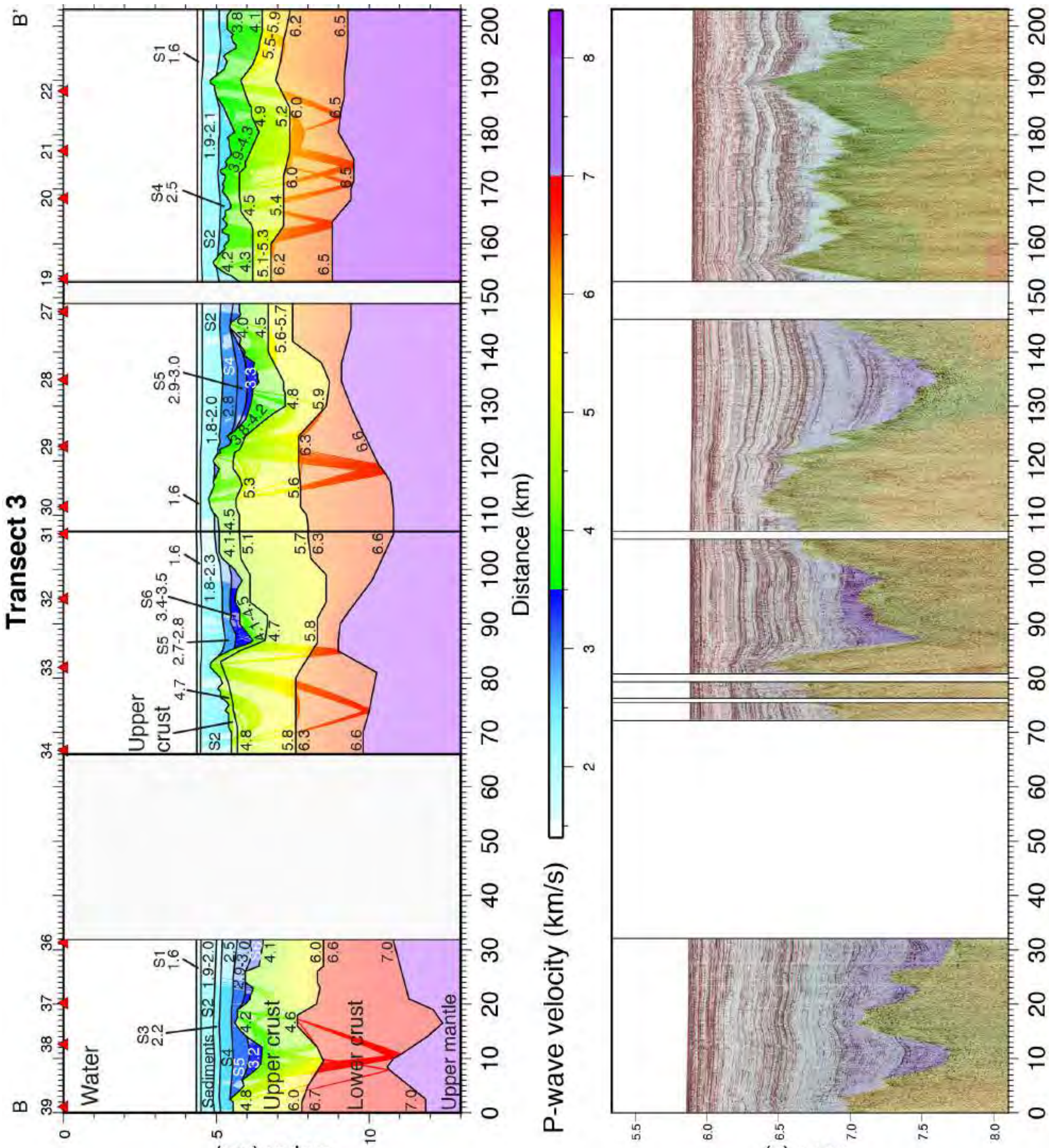
Transect 3
B
B’
Water
Sediments
Upper crust
Lower crust
Upper mantle
Depth (km)
Distance (km)
P-wave velocity (km/s)
TWT (s)

Fig. 6

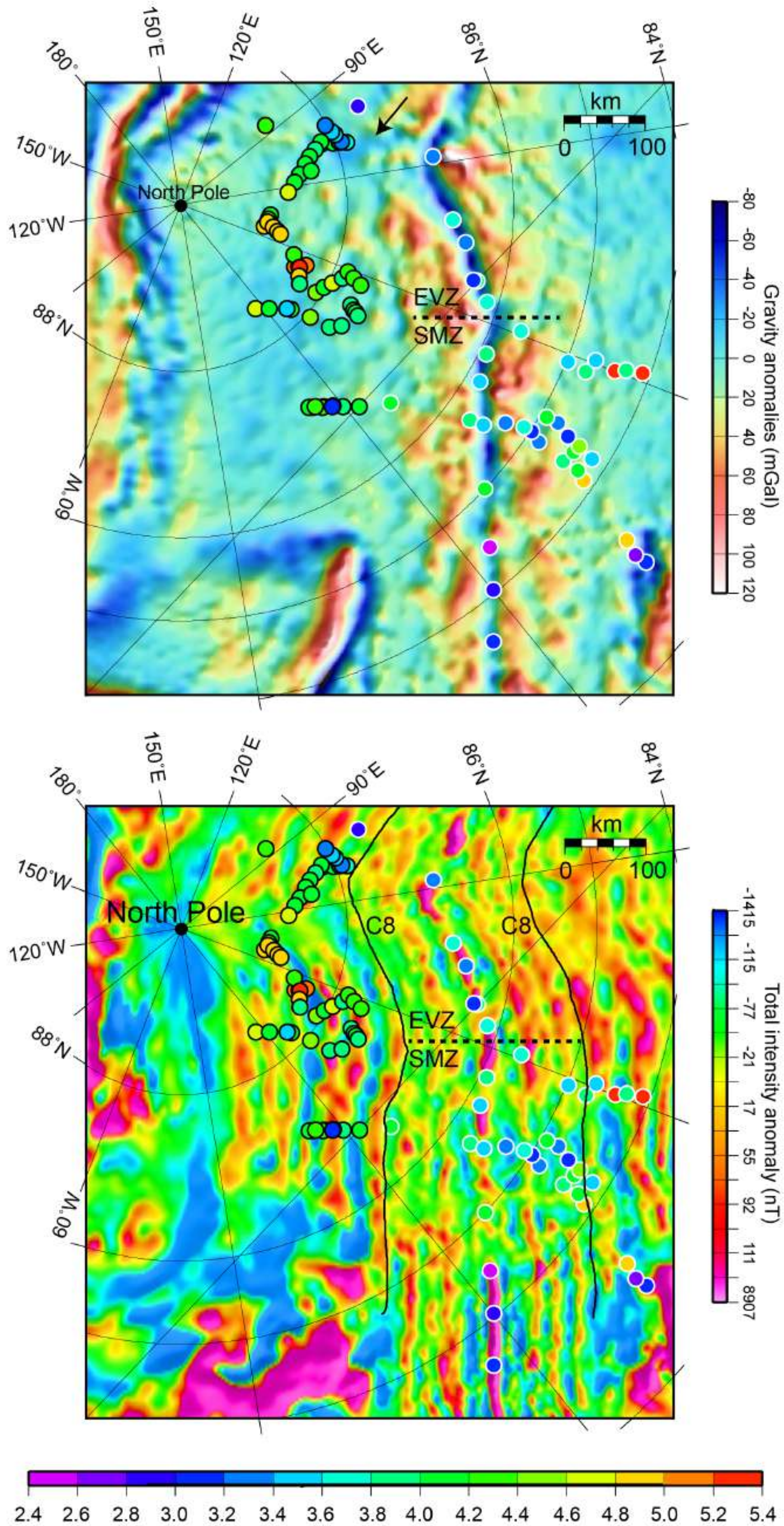
180°
150°E
120°E
90°E
86°N
84°N
150°W
120°W
88°N
60°W
North Pole
km
0
100
EVZ
SMZ
Gravity anomalies (mGal)
-80
-60
-40
-20
0
20
40
60
80
100
120
C8
C8
Total intensity anomaly (nT)
-1415
-115
-77
-21
17
55
92
111
8907
2.4
2.6
2.8
3.0
3.2
3.4
3.6
3.8
4.0
4.2
4.4
4.6
4.8
5.0
5.2
5.4
P-wave velocity (km/s)

Fig. 7

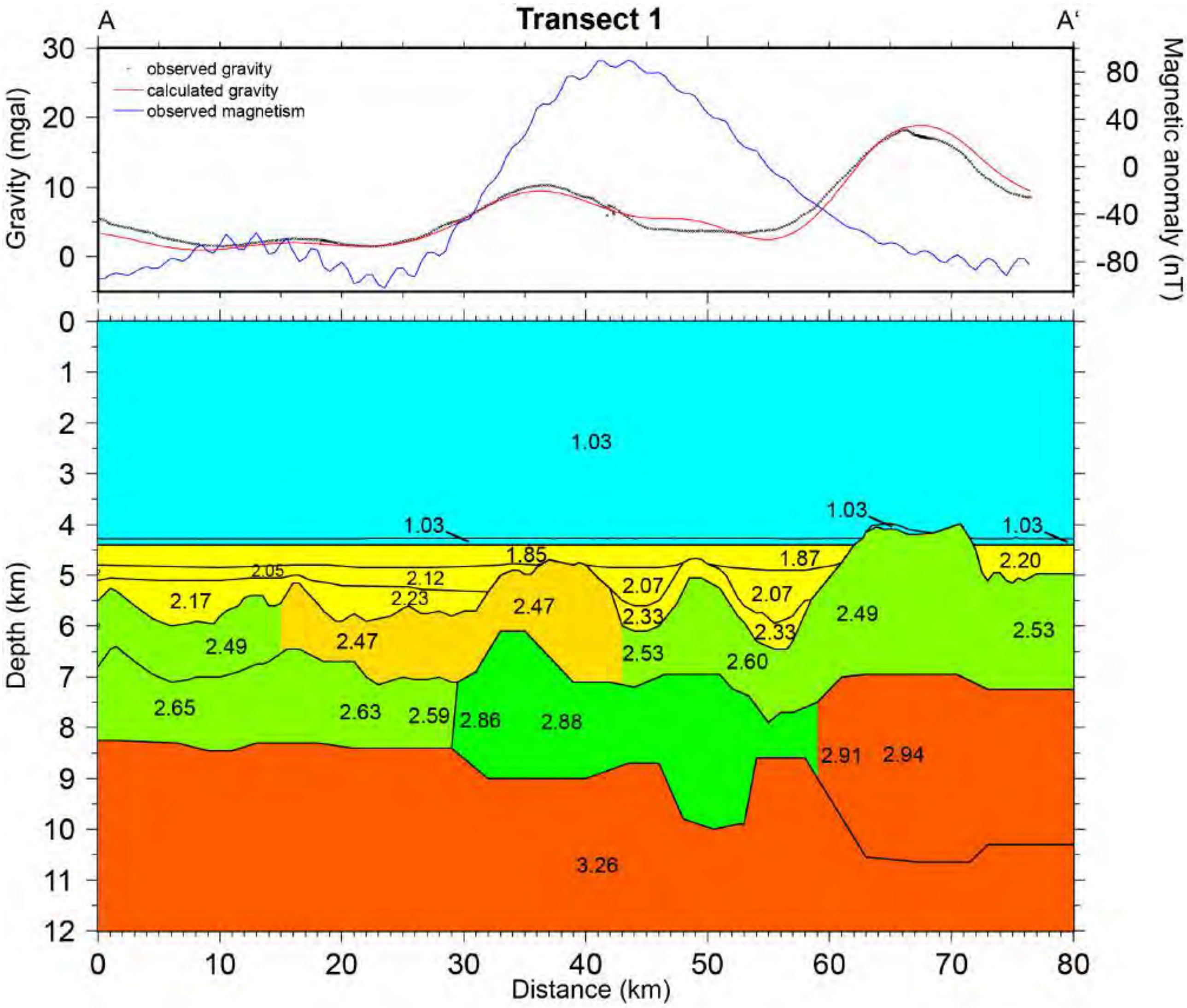

A
Transect 1
A'
observed gravity
calculated gravity
observed magnetism
Gravity (mgal)
Magnetic anomaly (nT)
Depth (km)
Distance (km)
1.03
1.03
1.03
1.03
1.85
1.87
2.20
2.05
2.12
2.23
2.17
2.47
2.07
2.07
2.33
2.33
2.49
2.53
2.49
2.47
2.53
2.60
2.65
2.63
2.59
2.86
2.88
2.91
2.94
3.26

Fig. 8

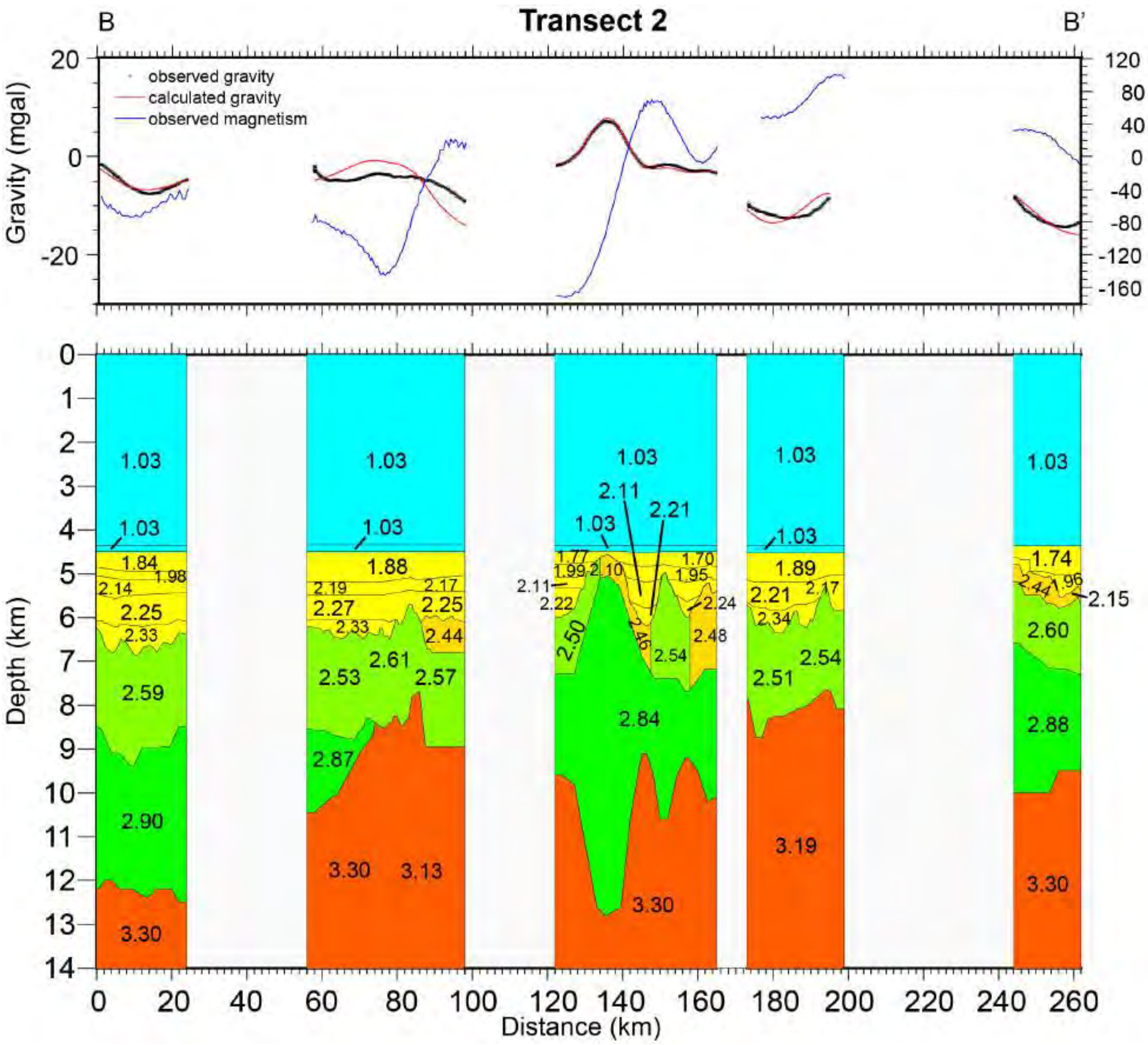

Transect 2
B
B'
observed gravity
calculated gravity
observed magnetism
Gravity (mgal)
Magnetic anomaly (nT)
Depth (km)
Distance (km)
1.03
1.84
1.88
1.89
1.74
2.25
2.27
2.59
2.53
2.61
2.57
2.87
2.90
3.30
3.13
2.84
2.51
2.54
3.19
2.60
2.88
2.11
2.21
2.15

Fig. 9

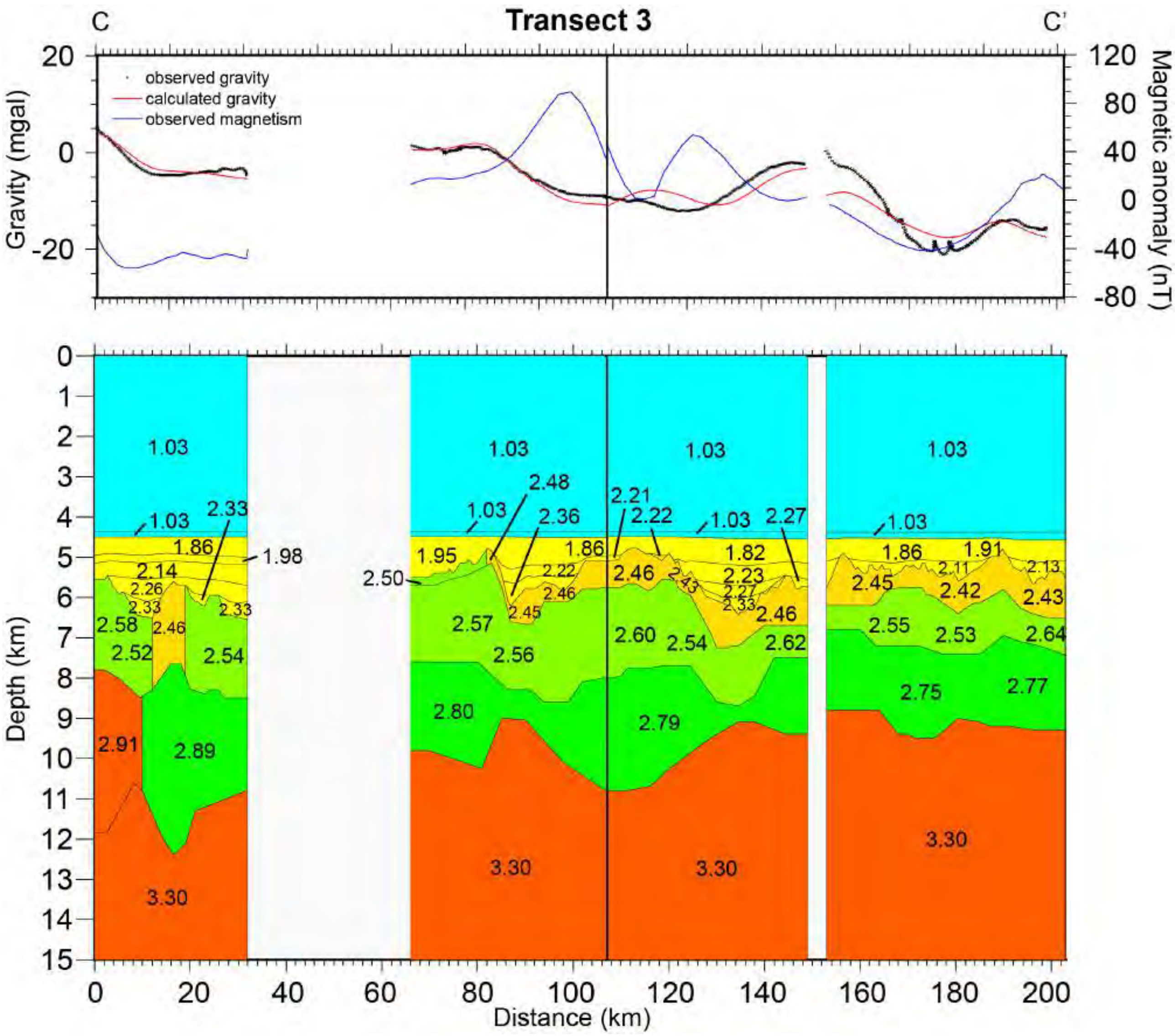
C
Transect 3
C'
observed gravity
calculated gravity
observed magnetism
Gravity (mgal)
Magnetic anomaly (nT)
Depth (km)
Distance (km)

Fig. 10

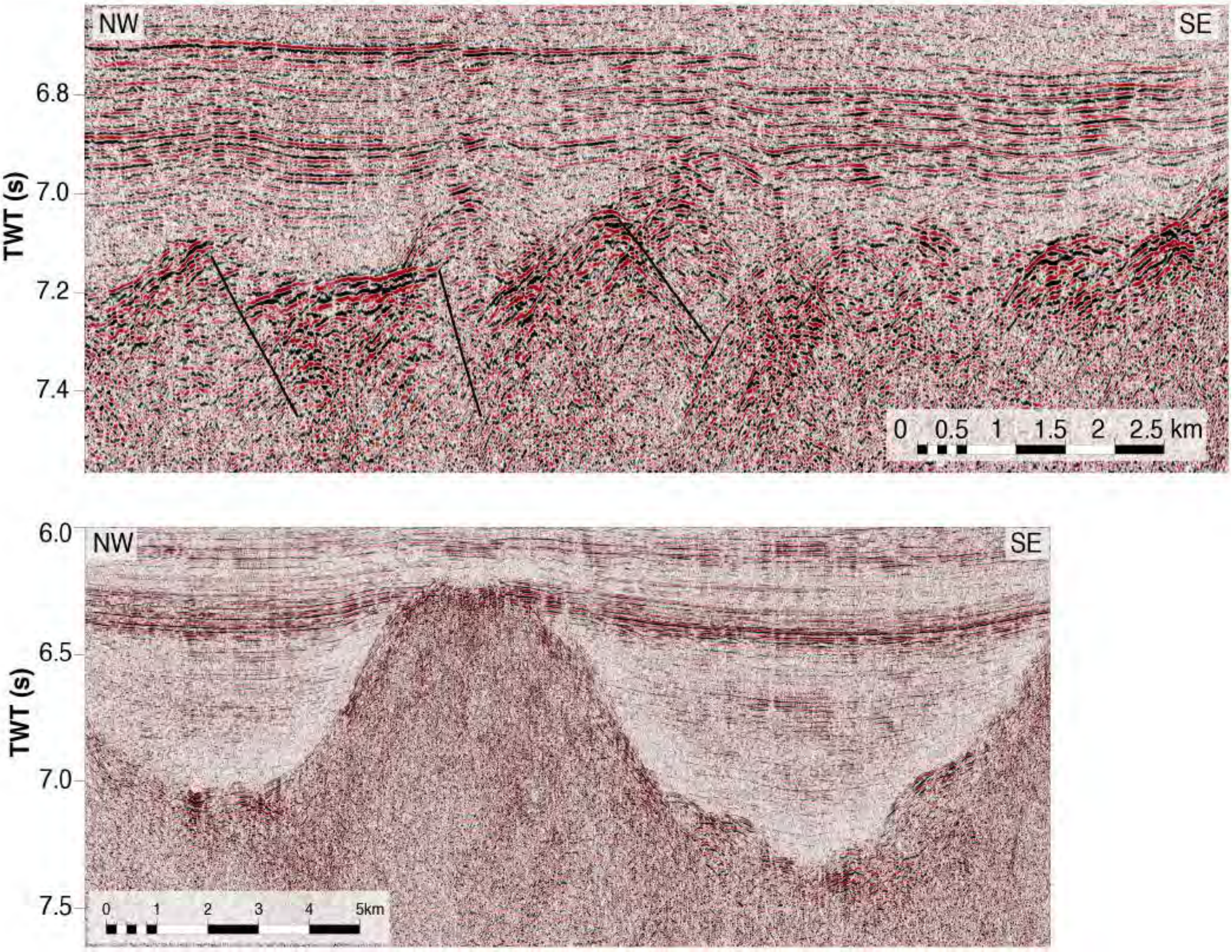
NW
SE
6.8
7.0
7.2
7.4
TWT (s)
0 0.5 1 1.5 2 2.5 km
6.0
6.5
7.0
7.5
TWT (s)
NW
SE
0 1 2 3 4 5km

Fig. 11

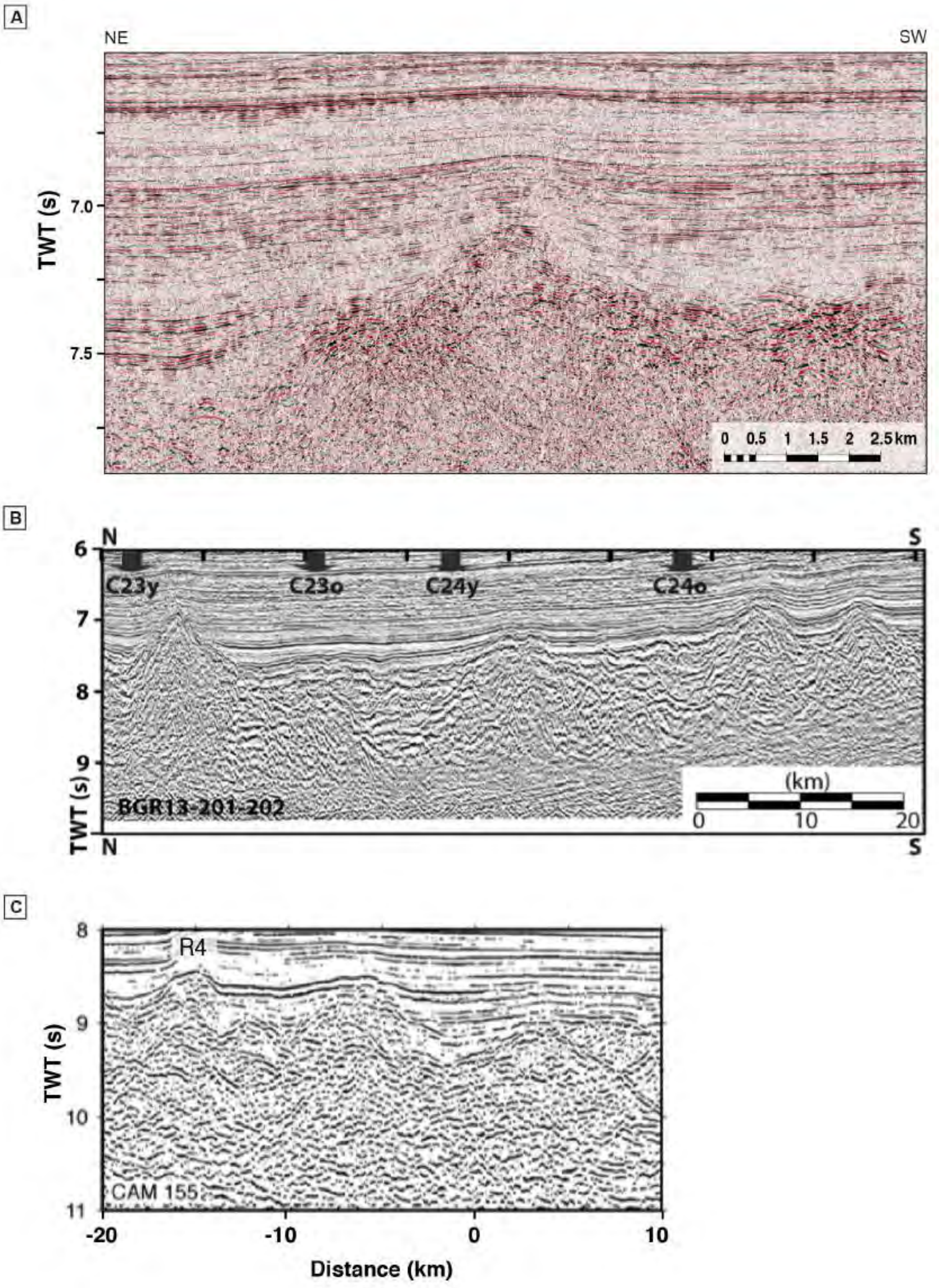
A
NE
SW
TWT (s)
7.0
7.5
0 0.5 1 1.5 2 2.5 km
B
N
S
6
7
8
9
TWT (s)
C23y
C23o
C24y
C24o
BGR13-201-202
(km)
0
10
20
N
S
C
8
9
10
11
TWT (s)
R4
CAM 155
-20
-10
0
10
Distance (km)

Fig. 12

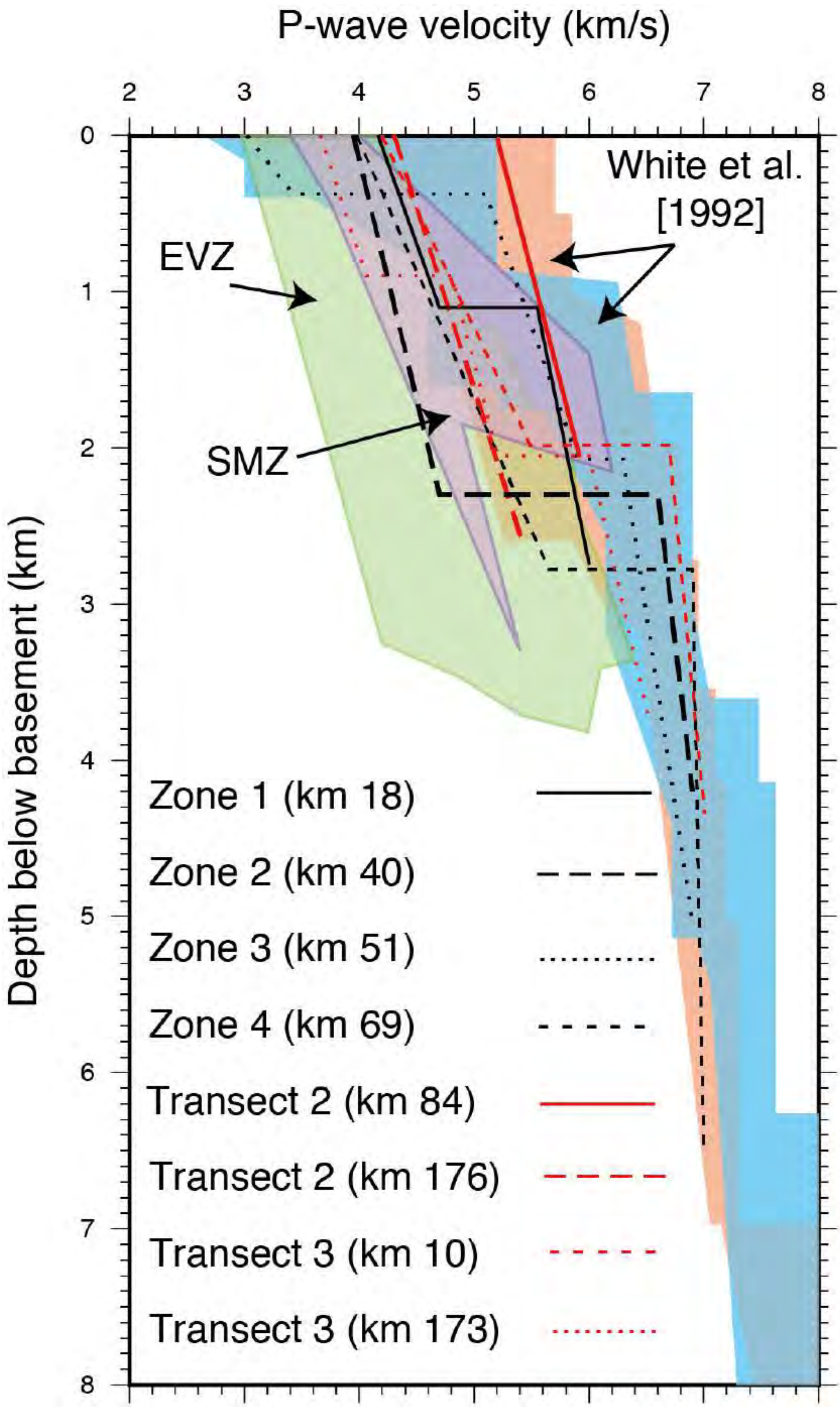
P-wave velocity (km/s)
2
3
4
5
6
7
8
0
1
2
3
4
5
6
7
8
Depth below basement (km)
White et al.
[1992]
EVZ
SMZ
Zone 1 (km 18)
Zone 2 (km 40)
Zone 3 (km 51)
Zone 4 (km 69)
Transect 2 (km 84)
Transect 2 (km 176)
Transect 3 (km 10)
Transect 3 (km 173)

Fig. 13

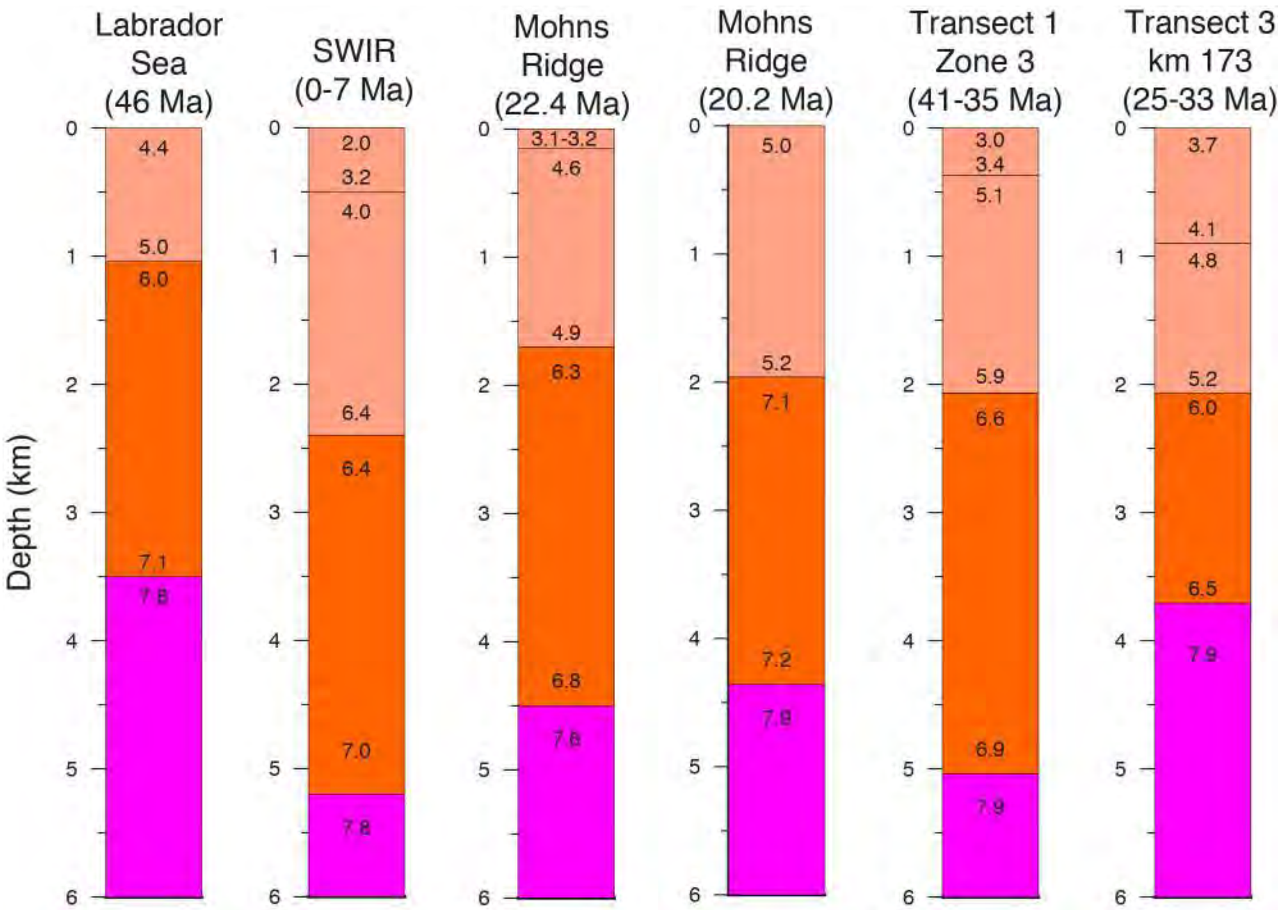
Labrador Sea (46 Ma)
SWIR (0-7 Ma)
Mohns Ridge (22.4 Ma)
Mohns Ridge (20.2 Ma)
Transect 1 Zone 3 (41-35 Ma)
Transect 3 km 173 (25-33 Ma)
Depth (km)
0
1
2
3
4
5
6
4.4
5.0
6.0
7.1
7.8
2.0
3.2
4.0
6.4
6.4
7.0
7.8
3.1-3.2
4.6
4.9
6.3
6.8
7.6
5.0
5.2
7.1
7.2
7.9
3.0
3.4
5.1
5.9
6.6
6.9
7.9
3.7
4.1
4.8
5.2
6.0
6.5
7.9

Fig. 14

Chapter III

Depositional evolution of the western Amundsen Basin, Arctic Ocean: paleoceanographic and tectonic implications

Depositional evolution of the western Amundsen Basin, Arctic Ocean: paleoceanographic and tectonic implications

Carlos F. Castro [1,2,*], Paul C. Knutz [1], John R. Hopper [1], and Thomas Funck[1]

[1] Geological Survey of Denmark and Greenland, Øster Voldgade 10, 1350 Copenhagen K, Denmark

[2] Niels Bohr Institute, University of Copenhagen, Copenhagen, Denmark

Corresponding author: Carlos F. Castro (cfc@geus.dk)

Key Points

- New multichannel seismic reflection data constrain the Cenozoic depositional history of the Amundsen Basin in the Arctic Ocean.
- Four key development stages explain the basin evolution based on facies interpretation and estimated sedimentation rates.
- Plio-Pleistocene cascading plumes, possibly from brine formation, affected the North Greenland shelf and influenced deep circulation.

Abstract

A new stratigraphic model and estimated sedimentation rates of the western Amundsen Basin, Arctic Ocean, are presented based on multichannel seismic reflection data, seismic refraction data, magnetic data, and limited samples from cores and drilling. This places new constraints on the Cenozoic depositional history of the basin and improves the understanding of the tectonic, climatic, and oceanographic conditions in the central Arctic region. Four distinct phases of basin development are proposed. During the Paleocene–mid-Oligocene, high sedimentation rates are linked to terrestrial input and increased pelagic deposition in a restricted basin. Sediment wedging and mass transport into marginal depocenters reflect a period of tectonic instability linked to compression associated with the Eurekan Orogeny in the Arctic. During the late Oligocene–early Miocene, widespread passive infill associated with hemipelagic deposition reflects a phase of tectonic quiescence, most likely in a freshwater estuarine setting. During the middle Miocene, mounded sedimentary build-ups along the LR suggest the onset of geostrophic bottom-currents that likely formed in response to a deepening and widening of the Fram Strait beginning around 18 Ma. In contrast, the Plio–Pleistocene stage is characterized by erosional features such as scarps and channels adjacent to levee accumulations, indicative of a change to a higher-energy environment. These deposits are suggested to be partly associated with dense shelf water-mass plumes driven by supercooling and brine formation originating below thick multi-year sea-ice over the northern Greenland continental shelf.

Keywords

Seismic stratigraphy, brine formation, contourite drifts, channel-levee deposits, Eurekan compression, Arctic Ocean

1 Introduction

The Cenozoic development of the Amundsen Basin (Fig. 1) and its role in the paleoceanographic evolution of the Arctic Ocean remains poorly understood. This lack of knowledge is due in part to the challenges of acquiring data in areas with perennial sea ice cover. Only a limited number of seismic profiles have been acquired in the region and there is a lack of stratigraphic control. Seismic reflection data are mostly restricted to short streamers with small source arrays and seismic refraction data are restricted to sonobuoys, and in some instances, recoverable ice stations [e.g., *Ostenso and Wold*, 1977; *Fütterer, 1992*; *Jokat et al.*, 1995a; *Jokat and Micksch*, 2004; *Chernykh and Krylov*, 2011]. Samples from the Arctic Ocean remain sparse, mostly from limited dredging [*Michael et al*., 2003; *Brumley et al.,* 2015; *Knudsen et al.*, 2017] and gravity and piston cores, but these shallow samples constrain only the most recent Quaternary depositional history. The only source of deep stratigraphic information comes from the Arctic Coring Expedition (ACEX) of the Integrated Ocean Drilling Program (IODP) Leg 302, where samples were recovered on the central Lomonosov Ridge (LR) in 2004 [*Backman et al.*, 2005]. Thus, much of the tectono-oceanographic history of the Amundsen Basin and the adjacent LR remains elusive.

The objective of this paper is to investigate the Cenozoic depositional history of the Amundsen Basin using new multichannel seismic reflection data gathered as part of the United Nations Convention on the Law of the Sea (UNCLOS) program for the continental shelf project of the Kingdom of Denmark. The lines were collected in the western part of the Amundsen Basin and along the flank of the Eurasian side of the LR (Fig. 1). The data are supplemented by published multichannel seismic data in the Amundsen Basin [*Jokat et al.*, 1995a; *Jokat et al.*, 1995b; *Jokat and Micksch*, 2004], magnetic data [*Brozena et al.,* 2003], and information from ACEX drill sites [*Moran et al.,* 2006; *Jakobsson et al.*, 2007]. Linking these data sets offers the opportunity to advance previous stratigraphic interpretations in the Amundsen Basin [e.g., *Jokat et al*., 1995a;

Chernykh and Krylov, 2011] and improve our understanding of the sedimentary processes and tectonic evolution of the Arctic Ocean. In this contribution, a new stratigraphic model of the Amundsen Basin is presented and four main evolutionary stages are proposed.

2 Geological and oceanographic setting

The LR is a sliver of continental crust that connects the Lincoln Shelf north of Greenland and Ellesmere Island to the East Siberian Shelf, separating the Arctic Ocean into two main basins — the Amerasian Basin and Eurasian Basin (Fig. 1). The Eurasian Basin is bisected by the world's slowest mid-ocean ridge spreading center, with present day full spreading rates of 14.6 mm yr^{-1} at the western end, decreasing to 6.3 mm yr^{-1} in the Laptev Sea [*DeMets et al.*, 1994]. It is generally agreed that seafloor spreading began in the early Cenozoic as the LR rifted away from the Barents and Kara shelves when Greenland and North America separated from Eurasia [*Talwani and Eldholm*, 1977; *Vogt et al.*, 1979; *Jokat et al.*, 1992; *Poselov et al.*, 2014]. Magnetic anomalies indicate that spreading began no later than Chron C24N (~53 Ma, the timescale of *Ogg* [2012] is used throughout this paper) and possibly during Chron C25 (~57 Ma) [*Vogt et al.*, 1979; *Brozena et al.*, 2003; *Cochran et al.*, 2006; *Glebovsky et al.*, 2006; *Engen et al.*, 2008; *Døssing et al.*, 2013a; *Døssing et al.*, 2013b].

The LR was first proposed as a continental fragment by *Heezen and Ewing* [1961] and was confirmed subsequently by seismic data [*Ostenso and Wold*, 1977; *Sweeney et al.*, 1982]. Seismic profiles across the LR show structures dominated by crustal scale extension as evidenced by tilted continental fault blocks [*Jokat et al.*, 1992; *Jokat*, 2005]. The oldest sedimentary rocks recovered by the ACEX drilling leg are Late Cretaceous age (i.e., pre-breakup) [*Backman et al.*, 2005]. Metamorphic sandstones recovered by dredging the Eurasian flank of the ridge have a Mid-Ordovician deformation age, showing that the LR was involved in a collisional event at that time

[Knudsen et al., 2017]. The combined evidence shows unequivocally the continental nature of the ridge.

Another key discovery of the ACEX expedition was the presence of a depositional hiatus spanning from the mid-Eocene–early Miocene [*Moran et al.*, 2006] based on biostratigraphic data [*Backman et al.*, 2008]. This hiatus is unexpected because it is inconsistent with established post-rift thermal subsidence models [*McKenzie*, 1978]. *O'Regan et al.* [2008] suggested that the ridge remained at or near sea level during the duration of the time gap while sediment erosion or non-deposition transpired. Based on an analysis of the consolidation, strength, and permeability of the sediments recovered, *O'Regan et al.* [2010] suggest that the hiatus arose from a period of prolonged low to non-deposition. The cause of non-deposition and/or erosion has been related to tectonic uplift, either as a result of mantle phase changes [*Minakov and Podladchikov*, 2012] or as a result of the Eurekan orogeny, which reached its peak during the Eocene [*Døssing et al.*, 2014]. Others have related the hiatus to erosion by oceanic bottom currents [*Jokat et al.*, 1992; *Moore and the Expedition 302 Scientists*, 2006a] implying that a vigorous circulation system became established in the late Eocene, although this may have happened in combination with tectonic uplift [*O'Regan et al.*, 2008].

An alternative chronology to the 26 Ma hiatus model by *Backman et al.* [2008] was derived from Re-Os isotope data produced by *Poirier and Hillaire-Marcel* [2009; 2011], who proposed that middle Cenozoic sedimentation rates on the LR were continuous (albeit ultra-slow) with a time gap of <0.4 Ma at about 36 Ma. The two different age models have drastically different implications for the timing of a fully ventilated Arctic Ocean and for the tectonic evolution of the LR [*O'Regan et al.*, 2011; Stein et al., 2014]. In the original *Backman et al.* [2008] model (hereafter referred to as age model 1), the LR is linked to a period of delayed subsidence and the transition from a lake to a marine setting is placed at approximately 17.5 Ma [*Jakobsson et al.*, 2007]. In the second model by *Poirier and Hillaire-Marcel* [2009; 2011] (hereafter referred to as age model 2), the onset of marine conditions in the Arctic is inferred at approximately 36 Ma, suggesting instead that the LR experienced a gradual change in relative sea level during the Oligocene – Miocene. Throughout the paper, when discussing timing and ages with respect to specific features and interpretations, we refer to age model 1, since it is well established in the literature. The implications for age model 2 are discussed separately in a subsection of the discussion.

Weigelt et al. [2014] summarized previous stratigraphic models of the Arctic Ocean and proposed a new model based primarily on data from the Siberian Shelf and Laptev Sea. Currently, there are two principal stratigraphic models for the western Amundsen Basin (WAB), with very different implications for sedimentation rates and oceanographic settings. *Jokat et al.* [1995a] suggest that prior to polarity Chron C13N (~34 Ma), sedimentation rates were uniformly high, varying from 10 to 15 cm ka $^{-1}$. Since that time, sedimentation rates have decreased to 1.5 cm ka^{-1}. Alternatively, *Chernykh and Krylov* [2011] suggest that the sedimentation rates have gradually decreased from about 30 cm ka $^{-1}$ to < 4 cm ka $^{-1}$ from the onset of spreading until the late Oligocene (Chattian, approximately 28–23 Ma), after which sedimentation rates sharply increased to about 10 cm ka $^{-1}$ due to a global marine regression, and then later decreased to < 2 cm ka $^{-1}$ during the Miocene. These different models have important implications for understanding the paleoceanographic environment of the Arctic Ocean.

The Arctic Ocean serves two key roles in the ocean circulation system: (1) it provides a passage between the Atlantic and Pacific oceans; and (2) it provides a receptacle for Atlantic water masses, alters them, and then returns them back to the Atlantic [*Rudels and Friedrich*, 2000]. The Atlantic water inflow, primarily via the Fram Strait and the St. Anna Trough in the Barents Sea, is mainly driven by thermohaline circulation [*Beszczynska-Möller et al.*, 2011]. The Atlantic water current system, termed the Atlantic Ocean boundary current, is a subsurface water mass (depths between about 150–900 m) that flows in a cyclonic (anti-clockwise) direction following the topographic basin slopes and along the ocean ridges [*Tomczak and Godfrey*, 1994; *Rudels*, 1995;

Rudels, 2012; *Woodgate*, 2013]. In contrast, the uppermost waters are wind-driven and flow anti-cyclonically in the Beaufort Gyre in the southern Canada Basin, where it contributes to the transpolar sea-ice drift from Siberia towards the Fram Strait [*Rudels*, 2012]. Despite the present understanding of Arctic oceanography, little is known about deep ocean currents formed in the region, their role in sediment transportation and deposition, and possible influence on the global meridional overturn circulation.

3 Seismic database

The seismic data used in this study consists of several recent and vintage surveys acquired along the central Amundsen Basin and the flanks of the LR within a region where seismic coverage is very sparse. The database consists primarily of 2D-reflection data from several marine seismic expeditions collected for the UNCLOS program of the Kingdom of Denmark, described briefly below and in more detail in the supplementary material. In addition, seismic lines from two older surveys were used (Fig. 1): ARCTIC’91 (~1500 km) and AMORE 2001 (550 km) [*Jokat et al.*, 1995a; *Jokat et al.*, 1995b; *Jokat and Micksch*, 2004].

The LOMROG surveys were acquired in 2007, 2009, and 2012 using a high-resolution seismic system designed for use in Arctic sea ice and was deployed from the Swedish icebreaker *Oden* [*Hopper & Trinhammer et al.*, 2012]. Key acquisition parameters are summarized in Table 1 and details from each survey are provided in *Marcussen et al*. [2008], *Lykke-Andersen et al*. [2010], and *Varming et al*. [2012]. The source array consisted of G and G-I guns with various configurations and a streamer of up to 300 m long with a group interval of 6.25 m. The nominal towing depth of both the source and receiver arrays were set to 20 m to minimize interference with ice. Further acquisition and processing details are provided in the supplementary material.

The seismic refraction data were obtained by sonobuoys, which recorded the shots from the seismic reflection experiments. In this study, four sonobuoys were used for constraining sediment velocities in the Amundsen Basin (Fig. 2). The velocity modeling and sonobuoy data are presented in the supplementary material (SI Figs. S1-S4). The seismic energy produced by the airgun cluster could be recorded up to offsets of 20 km. P-wave velocity models of the sediments and the underlying crust were then obtained by forward modeling of the travel times using RAYINVR software based on the algorithm of *Zelt and Smith* [1992]. The coincident seismic reflection data were used to guide the velocity modeling down to the basement.

4 Description and timing of main seismic units

The key seismic units were identified based on reflection character, seismic facies, and geometries [*Mitchum et al.,* 1977]. Ages for the top of the older units were derived by establishing the point where seismic horizons onlap the basement, and then infer basement ages from the magnetic anomaly interpretation of *Brozena et al.* [2003]. The thicknesses of the units were derived from the two-way travel time (TWT) in the seismic reflection data and from the velocities obtained from the refraction data. For each unit, a range of sedimentation rates (min/max) was calculated based on sediment thickness variations between individual basin segments (e.g. between structural highs) and the correlation of key horizons to the magnetic time scale.

4.1 Seismic stratigraphy

The sediments within the western Amundsen Basin (WAB) are dominated by parallel strata forming a uniform and continuous drape over the oceanic basement, which has a highly variable relief and in some places protrudes above the otherwise flat and uniform basin floor. The WAB succession is divided into six seismic units, each bounded by reflections that clearly demarcate changes in seismic facies and generally appear to be disconformable. The thickest unit, unit 1, was further subdivided based on facies changes or locally developed internal reflections.

Fig. 3 shows a summary overview of long transects through the basin running perpendicular to the strike of the Lomonosov and Gakkel ridges. A similar transect running parallel to the ridges through the central part of the basin is shown in the supplementary material (SI Fig. S5). Detailed seismic sections crossing the flank of the LR into the WAB are shown in Figs. 3-8, and detailed sections of the stratigraphy in the central parts of the basin are shown in Fig. 9.

4.1.1 Unit 1

The lowermost unit is the thickest unit in the basin, with a maximum thickness of about 1450 ms (~2150 m). The base of the unit is marked by the top of the igneous oceanic crust, which shows significant relief and often appears to be faulted. Throughout the rest of this paper, basement refers to the top oceanic crust. Unit 1 is thickest in the oldest part of the basin and thins towards the Gakkel Ridge. In the central WAB, the unit is often confined by the uneven topography and fills isolated sub-basins (Fig. 3a). At the LR flank, the thickness of unit 1 ranges from about 700 to 1000 ms (~1000 to 1450 m) (Figs. 3 and 4).

The unit can be subdivided into three subunits (Figs. 3a and 3b). The lower subunit, 1a, consists of variable internal reflections, ranging from weak or poorly defined to strong and continuous (Figs. 3a and 3b). It is not observed in areas where the basement shallows. The middle subunit, 1b, consists of predominantly weak reflections and is often transparent (Fig. 5). The thickness of subunit 1b is typically about 400 ms (~500 m); however, in profile LOMROG2007-01 across the central Amundsen Basin, it reaches up to 700 ms (~900 m; Fig. 3b). The upper subunit, 1c, is marked by semi-continuous relatively coherent reflections. The seismic geometries are strongly influenced by basement relief and within the thickest sections internal discontinuities are common (Fig. 3c). The thickness of subunit 1c ranges from about 150 to 300 ms (~200–425) and is thickest near the LR. Towards the Gakkel Ridge, subunit 1c shows a more variable distribution throughout the central basin (Fig. 3a-c).

Near the LR, subunit 1c is about 300 ms (~425 m) thick adjacent to the ridge flank and thins to about 150 ms (~190 m) toward the WAB, apparently influenced by a broad intra-basin topographic relief defined by the top of subunit 1b (dark blue horizon in Fig. 3a). Likewise, seismic lines AWI1991 98 and 100 (Fig. 2) show distinct thinning of subunit 1c (to < 40 ms) over an intra-basin high. However, the regional coherency of these basinal structures and resulting strata patterns cannot be established with the current data.

In the central WAB, subunit 1c shows onlap and thinning toward the basement highs (Fig. 3). In some areas, evidence for slope instability and mass transport deposits are observed (Fig. 9b). These areas are commonly related to deep-seated faults that bound the basement highs, suggesting active tectonism during deposition.

In the lower part of subunit 1c, a sedimentary wedge characterized by a steep, lenticular reflection pattern extends out from the LR (Fig. 7). The wedge is about 3.5 km wide and has an approximate dip of 10 degrees. The maximum thickness of the wedge is about 325 ms (~450 m) and pinches out toward the LR with strata downlapping toward the base horizon of unit 2 (Fig. 7). Internal reflections of the wedge are weak and discontinuous to semi-chaotic. Similar wedge-like features are observed in other areas along the ridge flank (Fig. 4) including AWI line 91-097 [*Jokat et al.* 1995a].

4.1.2 Unit 2

Unit 2 ranges from about 120 to 270 ms (~140–310 m) thickness (Figs. 3, 4, and 9) and is typically more transparent than unit 1, although it is occasionally marked by weak reflections showing a continuous to semi-continuous distribution (Figs. 3, 9b, and SI Fig. S5). Towards the Gakkel Ridge, unit 2 shows a gradual thickening. In addition, local thickness decreases and episodic truncation is observed over the topographic highs in the central basin (Fig. 3a-c). The draping monotonic sedimentary cover of this unit observed throughout the basin implies formation in a predominantly hemipelagic setting far from point sources of sedimentary input.

Near the LR, unit 2 has a relatively uniform thickness of about 225 ms (~275 m) along seismic profile LOMROG2009-11 (Figs. 3a, 4, and 7); however, a distinct thinning of the unit (to < 40 ms) similar to subunit 1c is observed over an intra-basin high along seismic lines AWI1991 98 and 100 (Fig. 2). Unit 2 therefore also seems to be affected by a broad-intra-basin topographic relief in some areas along the LR.

4.1.3 Unit 3

This unit is characterized by parallel, coherent reflections that show extensive lateral continuity (Fig. 3a and SI Fig. S5). As a consequence, top unit 3 forms a distinct horizon that can be traced with a high degree of confidence throughout the WAB. Unit 3 has a relatively uniform thickness of 225 ms (~240 m) with a maximum of 260 ms (~270 m) in the central parts of the basin. Along seismic profile LOMROG2009-11, unit 3 thins towards the ridge flank to about 80 ms (~100 m) and shows depositional pinch-out toward the underlying unit 2 (Fig. 5). The strong, continuous reflection pattern seen in unit 3 combined with depocenter development in the central basin points to a predominantly hemipelagic depositional environment with limited input from marginal sources.

Thinning and occasionally truncation of unit 3 is seen over the protruding basement structures in the central WAB (Figs. 3c and SI Fig. S5). In some locations, the thinning is associated with an upward decrease in dip of onlapping strata (Fig. 9a). This suggests that deposition was influenced by local structural development of the central basement highs that could provide a sediment source from submarine weathering of oceanic crust.

4.1.4 Unit 4

Unit 4 varies in thickness from 125–190 ms (~120–180 m). In contrast to the underlying unit 3, this unit shows a general thickening from the central basin toward the LR (Fig. 3a). In addition, local thickness increases are seen to be associated with sub-basin structures toward the Gakkel Ridge (Fig. 3c). The unit consists of weak to poorly defined reflections, although some strong and laterally continuous reflections are also observed in some basinward locations (Figs. 3a-c and SI Fig. S5). In the central WAB, reflections are semi-parallel but interspersed with hummocky geometries and occasionally gentle convex geometries that tend to form around basement highs (Fig. 3a-c and SI Fig. S5).

LOMROG lines 2009-11 and 2009-10 show gentle mounded build-up features juxtaposed to marked topographic lows developed against the LR flank (Figs. 4, 5 and 8). The widths and depths of the troughs respectively range from 1–1.5 km and 50–80 ms (~50–80 m). The asymmetric mounded geometries are observed with internal discontinuous reflections formed above an erosive base representing top unit 3. LOMROG line 2012-10 also displays a similar mounded expression of unit 4 perched against a topographic high (Fig. 9c). Although the internal reflection patterns often appear dimmed or vaguely defined, aggradational geometries can be recognized (Fig. 9c).

4.1.5 Unit 5

Unit 5 shows a consistent thickening from north to south, i.e., toward the Gakkel Ridge, with basinal depocenters increasing from about 160 to 320 ms (~150 m to 300 m thick) (Fig. 3a-c). A moderate thinning of unit 5 is observed in the seismic transect going from west to east (SI Fig. S5). The LR profiles indicate the development of a more localized depocenter (>250 m thick) expressing an overall positive relief along the northern basin margin (Figs. 3a and 8).

The seismic facies of unit 5 is generally characterized by coherent, parallel to semi-parallel reflections across the basin (Fig. 3a-c and SI Fig. S5), although more uneven and discontinuous seismic facies are seen within the depocenter in vicinity of the LR (Figs. 5, 6 and 8). Some of the seismic sections reveal an internal organization of unit 5 into several subunits that onlap the top unit 4 horizon in a direction toward the LR (Figs. 3a and 3c). Internal reflections appear phase reversed (i.e., negative impedance contrast), which may suggest that the continuous reflectivity is caused by clayey intervals interspersed by more silty-sandy deposits. Below the LR flank, the seismic facies becomes more discontinuous with mounded geometries interspersed laterally with concave reflection patterns commonly showing erosive signatures (Figs. 5-6). This reflection pattern is interpreted as incised channel segments that are up to 50 ms deep (~50 m) and 1 km wide, bounded by levee deposits. In the key profile, Figs. 3a and 4, the channelized deposits are seen to accumulate over the inclined, unconformable top unit 4 horizon, which dips ~2° into the basin. The channel deposits infill the buried trough along the ridge flank (see also Fig. 8).

4.1.6 Unit 6

The uppermost unit drapes the WAB and has a thickness that ranges from 125 to 250 ms (~100–200 m). The regional thickness variations and unit geometry indicates two depositional trends: (1) a small gradual increase in accumulation toward the basin sector bordering the Gakkel Ridge; and (2) discrete, mounded sedimentary build-ups associated with a recent channel system (Figs. 3a-c and SI Fig. S5). This channel accumulation is also imaged on the AWI lines east of the LOMROG transect in Fig. 3a, suggesting that it extends at least up to 70 km from the flank of the LR.

The basinward accumulation of unit 6 is characterized by sets of strong, continuous reflections displaying a positive impedance (Figs. 3a-c and SI Fig. S5). They demarcate individual depositional units that internally show arcuate and contorted to chaotic reflection patterns. These depositional units tend to thicken into the low-relief sub-basins and are defined by the top of unit 5. In some places, they are seen to evolve from erosional scarps and faults above deep structures. Based on the seismic expression, they are interpreted as mass-flow deposits, i.e., debrites (Gong et al., 2014). Accordingly, the small-scale arcuate- clinoformal patterns may represent thrusted layers generated by slow-moving mass-transport processes, although it should be noted that these features approach the limit of seismic resolution (Fig. 3c).

The accumulation zone of unit 6 along the LR is associated with a modern channel system, referred to as NP-28, that extends from the Lincoln Shelf margin into the Amundsen Basin [*Svindland and Vorren*, 2002; *Kristoffersen et al.*, 2004]. The channel itself, about 5 km wide and 80 ms ~(60 m) deep, is marked by erosional surfaces separated by gentle scarps that back-step at three distinct levels toward the LR flank. The deepest channel segment is flanked by a scarp approximately 70 ms (~50 m) tall and dipping about 10° (Fig. 5). The scarp truncates strata that form part of a prominent levee build-up on the basinward side. Offset reflections and discontinuities suggest the development of small growth faults within the levee deposits (Fig. 5). The levee construction eventually merges with the abyssal plain >20 km away from the channel. Discontinuous, truncated reflection patterns displaying internal onlap and lenticular to concave features are seen below the modern channel (Figs. 5 and 8). The channelized seismic facies suggests that high-energy current flows shape the modern seafloor and have been active throughout the deposition of the unit. The basal horizon (top unit 5) forms an erosional surface that demarcates a buried channel about 1.5 km wide and 50 ms (~40 m) deep, filled by small clinoforms (Fig. 5). The position of the buried channel relative to the modern counterpart suggests that the main channel pathway has shifted 3.5 km in a basinward direction during deposition of the unit. A channel feature is also observed in the southern part of the WAB bounded by the outer Gakkel Ridge structure and a thick incised strata package, probably representing units 5-6 (AWI-91-104, Fig. 3c). Aside from its location and deeper bathymetry on the opposite side of the basin, this feature differs from the NP-28 system by its dimension (~150 m vs. 60 m deep) and symmetric left-side levee formation. Hence, its mode of origin is most likely different from the NP-28 channel.

4.2 Chronology and sedimentation rates

The WAB contains a more than 2 km thick, relatively conformable and continuous seismic stratigraphic succession (Figs. 3 and 5) forming a complete sedimentary record since the onset of deposition in the early Cenozoic. Because no deep borehole data is available, the chronology can only be inferred based on the stratigraphic pinch-outs on oceanic basement, for which ages can be estimated based on magnetic spreading anomalies (Fig. 2). This primarily applies to the older units where the basement onlap relationships are clearly imaged on the limited seismic data. Here, the magnetic anomaly interpretation of *Brozena et al*. [2003] is used and ages are assigned based on the geomagnetic time scale of *Ogg [2012]*. *Jokat et al.* [1995a] derived ages based on the magnetic anomaly interpretation by *Vogt et al.* [1979] using ages from Cande and Kent [1992], while *Chernykh and Krylov* [2011] provided their own anomaly interpretation calibrated to *Cande and Kent [1995]*. We report horizon ages and sedimentations rates based on new data alongside the previously published results and their respective geomagnetic polarity timescales for better comparison (Fig. 10).

Dating of the units using magnetic anomalies has a number of limitations. First, there is a large uncertainty due to the ultraslow spreading. Closely spaced anomalies are difficult to distinguish from shipboard and aeromagnetic surveys because the sensor is too far away from the anomalies [*Russell*, 1999]. Second, the sparse seismic data coverage in the region spanning Chrons C25N–C23N (~57–53 Ma) introduces significant correlational gaps, leading to uncertainty of the age of deepest units (in particular unit 1). Finally, rough basement topography can complicate the onlap relationships so that a horizon pinches out locally on older crust. For horizons dated this way, several seismic lines were checked when possible and the pinch-outs were remarkably consistent relative to the magnetic anomaly pattern, giving some confidence that the approach provides reasonable age estimates. Thus, despite the drawbacks of dating seismic horizons this way, it remains the only option for the deeper units and provides some information for estimating sedimentation rates.

The range of sedimentation rates presented in Fig. 10 includes the thickness variation between individual sub-basins and variation in seismic velocities for each unit. Parameters for calculating sedimentation rates are shown in Table 2 and the locations of key sonobuoys used for the velocity estimates are shown in Fig. 2. To be as representative as possible, the sedimentation rates were calculated by combining the velocities and two-way travel time thickness observed along the different profiles (Figs. 3a-c and SI Fig. S5). If the measured two-way travel time thickness of a unit was located along a profile containing sonobuoy data, the 1D velocity model was used to calculate the sedimentation rates. Otherwise, the sonobuoy closest to the measurement was used. If the measured two-way travel time thickness was located at a similar distance between two sonobuoys (e.g., LOMROG2007-01, see Fig. 2), the sediment rates were calculated by averaging the velocities of the two sonobuoys closest to the profile. The velocity modeling and sonobuoy data are presented in the supplemental material (SI Fig. S1-S4).

For comparison to previous work, the correlative seismic units dated by *Jokat et al.* [1995a] are shown in Fig. 10. Subunit 1a corresponds to seismic units AB-1 through AB-3 identified by *Jokat et al.* [1995a] while subunit 1b roughly corresponds to AB-4. For the remaining units, the ages between this study and the corresponding units differ due to the assumption made by *Jokat et al.* [1995a] of a constant sediment rate of about 1.5 cm ka^{-1} from the late Eocene onward for dating their remaining horizons (Fig. 10). Based on the revised chronology, subunit 1c and unit 2 are largely equivalent with AB-5 and AB-6. Finally, the uppermost succession, represented by units 3-6, corresponds to AB-6 through AB-8 defined by *Jokat et al*. [1995a]. Due to the sparse LOMROG data within the older part of the basin (Chron C21y onward), a subdivison of the oldest unit, 1a, into the three smaller units as defined by *Jokat et al.* [1995a] was not possible. However, two additional sedimentary units are identified, unit 2 and unit 4, within AB-6 and AB-7 respectively. In addition, a more detailed description of unit geometries and seismic facies of the basin succession are presented, notably along the LR flank (Figs. 3 and 4).

The ages of the horizons top unit 1a, top unit 1b, and top unit 1c were assigned based on where the horizons onlap the oceanic basement (Fig. 2). The approximate ages are 46 Ma, 38 Ma, and 29 Ma respectively. These ages indicate that the early basin evolution correspond to relatively high sedimentation rates, >10 cm ka^{-1}, peaking during the early Eocene (Fig. 10). The ages for the horizons top unit 1a and top unit 1b are the most robust in the data based on the multiple locations where onlap is observed (Fig. 2 and SI Fig. S6). These units correspond to the seismic units AB-1 through AB-4 identified by *Jokat et al.* [1995a], which were also dated by the same sections of onlap but using an alternate magnetic anomaly interpretation as discussed above.

This study differs in the dating method used by *Jokat et al.* [1995a] for subunits 1c and unit 2 (AB-5 and AB-6). In the model by *Jokat et al.* [1995a], AB-5 was calculated by assuming an average sediment rate of about 1.5 cm ka^{-1} and a 40 m thickness for the entire unit, yielding a span of ~3 Ma and an age of ~36 Ma for the top boundary of AB-5 (Fig. 10). In contrast, this study incorporates the subsequent AWI data presented by *Jokat and Micksch* [2004]. Whereas the original profiles by *Jokat et al.* [1995a] show gaps and/or high basement topography when crossing Chron C8y (e.g., A91-102 and A91-104 located in Fig. 2), *Jokat and Micksch* [2004] show a continuous profile that appears typical for the basin (SI Fig. 5). Thus, the age for unit 1c, corresponding to the lowermost interval of AB-5, was assigned based on the youngest two onlaps observed in the AWI and LOMROG data between Chrons C12o and C8y (SI Figs. 6 and 7).

The age of horizon top unit 2 was inferred from seismic profiles 12-07 and AWI2001-0300. In the AWI profile, a clear onlap for unit 2 is observed (Fig. 2 and SI Fig. S6) at about Chron C8y (~25 Ma). This onlap coincides with regional basement shallowing towards the Gakkel Ridge. In the nearby LOMROG profile, unit 2 is observed at the same time interval with no clear onlap and no significant basement shallowing (SI Fig. S7). Since unit 2 shows no significant thinning here and seems to continue beyond Chron C8y along 12-07, it is possible that that this horizon is likely younger than 25 Ma, probably ~25–20 Ma. However, more data is required to validate and/or constrain the age for the top of unit 2.

The magnetic anomalies do not provide age constraints beyond Chron C8y (~25 Ma). Ages for units 3–6 are estimated based on comparison to previous work and correlations with changes in facies patterns that can be related to known tectonic and oceanographic events in the Arctic Ocean. The top of unit 3 is assigned an age of 20-15 Ma based on the inferred onset of a ventilated regime in the Arctic Ocean according to age model 1 (Fig. 10). Thus, we correlate the oxygenated late Miocene interval at site 302 (starting at 193 m core depth) to a phase of sediment drift accumulation along the LR indicated within unit 4. The top of unit 4 is assigned an age of 11.5-8 Ma based on the presence of a hiatus at site 302 (ACEX, *Frank et al.* [2008]) and the onset of ferromanganese crust growth on the LR flank [*Knudsen et al*., 2018]. This latter observation is consistent with the onset of a higher energy environment inferred above unit 4 and that is necessary for the crust to grow and be preserved [*Föllmi*, 2016]. Unit 4 thus represents a relatively long interval with sedimentation rates estimated between 1.3–1.9 cm ka^{-1}. The lower end of this range is comparable with that found in previous studies for the same interval corresponding to seismic units AB-6 through AB-8 [*Jokat et al*., 1995a].

An age of 8 Ma for the top of unit 4 yields gross sedimentation rates between 3.1–6.3 cm ka^{-1} for the youngest units, 5 and 6. This is within the lower range of the shallow core results obtained by *Svinland and Vorren [2002]* (5.9–24.7 ka^{-1} over the last 17 ka) and *Backman et al. [2004]* (1–25 ka^{-1}). The rates imply that the base of unit 6 is approximately 2–4 Ma, i.e., late Pliocene – early Pleistocene.

5. Sedimentary and paleoceanographic evolution of the Amundsen Basin

Analyses of the LOMROG seismic data and the tie of key horizons to the magnetic stratigraphy of the Arctic Ocean (4.2) provides significant new input to the evolution of the WAB (Fig. 11). The Cenozoic development is discussed based on seismic geometries and facies pertaining to the updated stratigraphic scheme of the present study. The paleoceanographic history inferred from our results is discussed in relationship to previous studies that notably builds on the sedimentary records derived from the ACEX samples. As noted earlier, recently published age models have called into question the nature of the late Eocene–mid-Miocene hiatus based on earlier ACEX results. In this discussion, the original ACEX age model [*Backman et al.*, 2008] is used. The implications of the alternative age model [*Poirier and Hillaire-Marcel*, 2009; 2011] are considered in a separate subsection.

5.1 Eocene–early Miocene evolution (units 1-3)

Deposition of subunit 1a began from the onset of spreading in WAB in the late Paleocene at ~57 Ma until the mid-Eocene at ~45 Ma. Lines LR-2007-01, LR-2009-12, and LR-2012-11, indicate thicknesses greater than 1 km and thus high sedimentation rates. This likely reflects enhanced supply of terrestrial material, possibly derived from weathering and erosion from the LR, although sediments may have also originated from regional highs that are now at conjugate positions, e.g., the Barents Shelf and Yermak Plateau margins. The high sedimentation rates may also be linked to increased pelagic deposition associated with high biological productivity [*Stein*, 2006] that characterizes the early–mid-Eocene greenhouse climate conditions [*Zachos et al.*, 2008]. Moreover, an intensified hydrological cycle [*Pagani et al.*, 2006; *Carmichael et al.*, 2016] resulting in episodic fresh water accumulation [*Brinkhuis et al.*, 2006] apparently enabled a high biological productivity as evidenced by the large quantities of the freshwater fern Azolla in the central Arctic [*Brinkhuis et al*., 2006; *Speelman et al.*, 2009; *van der Burgh et al.*, 2013] and in adjacent regions [e.g., *Collinson et al.*, 2010].

The upper range of the sedimentation rates for subunit 1a is poorly constrained due to sparsity of data within the older part of the basin (Chron C21y onward). Although precise paleo-water depth estimates for the LR are challenging due to the absence of micropaleontological markers in the ACEX record, benthic agglutinated foram assemblages dated around the Paleocene-Eocene thermal maximum (~55 Ma) suggests that the LR was close to sea level at that time [*O'Regan et al.*, 2008].

Deposition of subunit 1b, approximately mid-Eocene to late Eocene, is marked by a decrease in sedimentation rates compared to subunit 1a (Fig. 10). The lower range of the rates estimated, 6 cm ka^{-1}, are roughly in accordance with previous studies, while the higher range, 12 cm ka^{-1}, is based on a thick development of the unit seen in the central WAB (Fig. 5b). The observations from the LOMROG seismic data imply that the position of the main depocenter during the late–mid-Eocene shifted towards the center of the basin near LR_2007-01.

Subunit 1c represents a major sedimentary wedge that infills the Amundsen Basin asymmetrically from NW to SE toward the Gakkel Ridge (Figs. 3, 4, and 7). This subunit was deposited between 37–29 Ma corresponding to the late Eocene to mid-Oligocene epochs. Low-angle progradational features are observed, suggesting lateral transport of sediments away from the LR towards the central basin. The evidence for slope instability and mass-transport (Fig. 9b) that appear to correlate with sediment transport over the basement highs (Fig. 9a) suggests that tectonic instability influenced the late Eocene – mid-Oligocene basin development phase. Steeply dipping wedge reflections seen within subunit 1c are interpreted as submarine fan deposits extending from the ridge flank (Fig. 7). Similar features, but more vaguely defined, are seen on other profiles along the LR flank (Fig. 4) and AWI 91097 [*Jokat et al.*, 1995a]. This suggests that sediments were actively eroded from the LR where it merges into the Lincoln Shelf margin. Thus, in most of the profiles, a phase of tectonic instability can be detected in the strata packages at comparable levels of burial.

Jokat et al. [1995a] suggest that the mid-Eocene (46 Ma) marks the onset of LR subsidence to greater depths, shifting the depositional style in the Amundsen Basin from slope-rise to pelagic sedimentation. This may have been accompanied by deposition of biosiliceous ooze deposits with an admixture of terrigenous material along the basin margins. An increase in ice rafted debris from 47 Ma has been related to an early cooling phase and the initiation of sea ice and glacial ice in the Arctic Ocean [*St. John,* 2008; *Stickley et al.*, 2009].

Sedimentary subunits 1b and 1c (mid-Eocene to mid-Oligocene) correspond to the lower half of the 44–18 Ma depositional hiatus inferred in the original study of the ACEX cores [*Backman et al.*, 2008] (Fig. 10). This time gap overlaps the main phase of Eurekan compression in North Greenland, Ellesmere Island, and Svalbard from 55–33 Ma [e.g., *Gion et al.*, 2016; *Oakey and Stephenson*, 2008; *Oakey and Chalmers,* 2012; *Piepjohn et al.*, 2016]. Several recent studies suggest that the Eurekan orogeny affected large parts of the Arctic Ocean [*O'Regan et al*. 2008; *Døssing et al*. 2013; *Døssing et al*. 2014]. In particular, gravity inversion shows that Eurekan compression may have affected the oceanic crust of the Amundsen Basin, the western LR, and below the Lincoln Shelf towards the Morris Jessup Rise, including crustal thickening and uplift of the LR plateau [*Døssing et al*., 2014]. Ensuing erosion from uplifted areas may have been more significant on the shallower parts of the LR closer to the Greenland margin than at the deeper portions lying nearby the ACEX site. The present day depth of LR near Greenland is ~600 m whereas the ACEX site is at 1200 m. Although Eocene reconstructions of paleowater depths exist for the central LR [e.g., *O'Regan et al*. 2008; *Mann et al.*, 2009], there is limited information for the portion of the LR closest to the Lincoln Shelf. Thus, shallow or even subaerial areas near the Lincoln Shelf could have also served as an additional source for erosion and deposition. In the context of the regional tectonic configuration, it is most likely that the sedimentary signatures, e.g. sedimentary wedges, observed within subunit 1b and 1c are linked to compression along the LR associated with Greenland's northward motion into the Arctic Ocean.

The magnetically defined chronology of units 1b-c timing would fit into a model whereby the LR was tectonically active and experienced post-breakup uplift during the late Eocene (Fig. 12) [*O'Regan et al.* 2008; *Minakov and Podladchikov*, 2012; *Døssing et al.* 2014;].

In comparison with the high accumulation rates that characterize the Eocene, units 2 and 3 appear as relatively condensed intervals with inferred sedimentation rates between 2.3-5.0 cm ka^{-1} (Fig. 10). Based on the character of passive infill (e.g., parallel strata with basal onlap toward the LR) it is suggested that these units were deposited primarily by pelagic sedimentation in a relatively low energy environment. Thus, their signature appears associated with a period of tectonic quiescence following the Eurekan compression. The onset of a reduced stress regime along the LR likely ended in the middle-late Oligocene after which the proto-Fram Strait oceanic gateway may have begun to form through in response to trans-extension and subsidence [*Jakobsson et al.*, 2007; *Engen et al.*, 2008].

5.2 Mid-Miocene–late Miocene evolution (unit 4)

The enhanced accumulation of unit 4 along the base of the LR invokes an origin related to oceanographic bottom-currents (Fig. 3a). Although downslope processes, e.g., local submarine fans, may also be considered for this margin-bound depocenter, the lack of sedimentary input sources is conspicuous. Moreover, the buried, asymmetric mound-moat geometries along the ridge flank (Figs. 3a, 4, and 8) and the low-relief mounded accumulations over some of the structural highs (Fig. 9c) are reminiscent of contourite drifts that commonly drape the lower slope of continental margins [*Rebesco et al.*, 2014]. The build-up of contourites reflects enhanced deposition of fine-grained sediments along the fringe of bottom-current pathways that are generally controlled by large-scale meridional overturning circulation. Flow speeds that favor drift accumulation are commonly in the range of 5–15 cm s^{-1}, while erosional elements, e.g., at the base or within juxtaposed moat-channels, imply velocities exceeding 25 cm s^{-1} [*Hernández-Molina et al.*, 2008]. Contourites are widespread within the high-latitude ocean basins, ranging in scale from small patch drifts (10–100 km^2) to giant elongated drifts (>100,000 km^2) [*Faugères and Stow*, 2008; *Rebesco et al.*, 2014]. In the Arctic region of the North Atlantic, slope-controlled contourite drifts are documented along the Western Spitsbergen margin [*Rebesco et al.*, 2013], the eastern Fram Strait [*Howe et al.*, 2008], and the Yermak Plateau [*Mattingsdal et al.*, 2014]. By analogy with these areas of current-induced sedimentation, unit 4 was likely influenced by geostrophic bottom currents flowing along the LR and tracing minor topographical variations within the WAB. Theoretically, this paleo-current system would follow the modern counter-clock wise circulation pattern of the Arctic [*Rudels*, 2012] and thus flow from the Laptev Shelf margin toward Greenland as shown in Fig. 12.

The lack of any robust dating for the horizons bounding unit 4 adds uncertainty to the onset of geostrophic flow responsible for focused sedimentation along the LR. However, since the drift formation is associated with large-scale movement of bottom-waters, thus implying a full-scale ventilation of the Arctic Ocean, unit 4 is likely linked with a deep water connection through Fram Strait gateway. Different timings have been proposed for when this deep-water connection between the North Atlantic and the Arctic Basin became established. *Wolf-Welling et al.* [1996] proposed a late Miocene gateway based on sediment samples. This contrasts with tectonic reconstructions [*Engen et al.*, 2008] and ACEX core data [*Jakobsson et al.*, 2007] that suggest an early Miocene timing. More recent studies based on seismic interpretation studies along the Yermak Plateau that include ties with paleomagnetic and biostratigraphic age constraints from ODP drill sites favor a mid-Miocene age [*Geissler et al.*, 2011; *Mattingsdal et al.*, 2014]. The timing of a late Miocene onset of deep-water circulation in the Arctic Ocean is synchronous with the formation of the major North Atlantic drifts [*Wold*, 1994] and is also recognized as a major phase in sediment drift accumulation in Baffin Bay [*Knutz et al.*, 2015]. Comparing the broadly defined seismic stratigraphic chronology with records from the North Atlantic and Baffin Bay makes a mid-

Miocene age (20–15 Ma) seem most likely for the onset of current-induced deposition along the LR (Fig. 11).

The commencement of the sedimentary drift in unit 4 likely corresponds to a full ventilation of the Amundsen Basin associated with a deep Fram Strait opening. However, as discussed below (5.3) the onset of this regime cannot be affirmed by the ACEX record. The section of reddish heterogenic mudstone above 193 mcd may provide a suitable sedimentary analog to the contourite drifts observed in Unit 4. A paleomagnetic age of 17-18 Ma at the base of this interval provide a minimum age but an older onset, e.g. 20-25 Ma, of a fully ventilated oceanic regime cannot be ruled out [*Geissler et al.*, 2011; *Mattingsdal et al.*, 2014]. The preferred stratigraphic model based on the new data indicate relatively low average sedimentation rates for unit 4 (Fig. 10). This may suggest that the current-induced sedimentation was intermittent and/or that the unit bounding unconformities contain significant depositional gaps (Fig. 5).

5.3 Implications of an alternate age model (ACEX 2)

In the previous sections, the discussion of the seismic-stratigraphic interpretation was within the context of the original age model from the ACEX results. However, the Paleogene chronology of the Arctic Ocean, and in particular the tectonic history leading to the transition from a lake to a full marine setting, was contested by *Poirier and Hillaire-Marcel* [2009, 2011] based on Re-Os isotope analyses. Their alternate age model (ACEX 2) suggests that the transition from an isolated, euxinic lake-stage to a semi-ventilated ocean basin occurred in the lowermost Oligocene at about 36–37 Ma rather than in the early Miocene as proposed by *Jakobsson et al.* [2007]. Following this oceanographic event and a small hiatus (~0.4 Ma), a 5.7 m interval of grey and black colored mudstone was deposited, informally known as the “Zebra unit” (ACEX unit 1/5). Poirier and Hillaire-Marcel [2009, 2001] interpreted this as an estuarine transitional phase when bottom water oxygen levels fluctuated over the LR. While the age of the base of unit 1/5 is constrained, the Os-isotope stratigraphy is inconclusive concerning the duration of the transitional interval. Therefore, uncertainty remains as to when the Arctic Ocean became fully and consistently ventilated. A simple linear interpolation between the Re-Os isochron age at the base of unit 1/5 and the oldest ^{10}Be age (12.31 Ma; *Frank et al.* [2008]) yields an apparent sedimentation rate of approximately 0.18 cm ka^{-1}. However, *Poirier and Hillaire-Marcel* [2011] note that in the absence of terrigenous input such low sedimentations would require much lower ^{187}Os/^{188}O values due to the concurrent influence of global cosmic dust. Thus, higher sedimentation rates within the “Zebra” unit are likely and one or more condensed sections, or hiati, may exist above the onset of estuarine conditions at 36 Ma. In particular, the lithological contact between units 1/4-1/5 at ~193 mcd signifies an abrupt change from oxygen deficient to oxygen rich bottom water conditions [*Moore and the Expedition 302 Scientists*, 2006b].

The geodynamic model by *O’Regan et al.* [2008] and the notion of a delay in ridge subsidence due to compression was criticized by *Chernykh and Krylov* [2017]. Based on a revised seismostratigraphic model for the central Amundsen Basin, the authors argue that the brief hiatus at 36-37 Ma and the low sedimentation rates within unit 1/5 were caused by a sea-level rise due to influx of Atlantic waters. However, the observation of the late Eocene–early Oligocene downlapping wedge extending from the ridge in unit 1c and the presence of a large depocenter in 1b suggests that a substantial terrigenous input in the Amundsen Basin remained prevalent until at least early Oligocene times. This late Eocene–early Oligocene timing would also broadly coincide with a phase of tectonic instability indicated by folding of sedimentary packages in the eastern Amundsen Basin [*Gaina et al.*, 2015] and an observed seismic unconformity along the LR [*Bruvoll et al.*, 2010]. This high volume of terrigenous input would therefore likely match older multi-proxy, geochemical, and sedimentological interpretations linking shallow waters in the central LR to higher depositional rates before the hiatus [*O’Regan et al.*, 2008; *Sangiorgi et al.*, 2008; *März et al.*, 2011].

Poirier and Hillaire-Marcel [2011] argue that a possible marine invasion at 36 Ma reflects basin wide ventilation of the Arctic Ocean via a crustal stretching-related corridor within the proto-Fram Strait. Here, it is questioned whether basin wide ventilation at this stage is consistent with plate-tectonic constraints on the opening of the Fram Strait. Following a prolonged phase of compression during the Eurekan and Svalbardian orogenies from 56–33 Ma [O'Regan et al., 2008], plate reconstructions show that the crust in northeast Greenland and west of Svalbard began to experience trans-extension beginning in the Oligocene around 30 Ma, with major extension following much later [Gion et al., 2016]. This does not fit with opening a seaway connection already at 36 Ma. Seismic refraction data on Svalbard show that present day crust there is 32–33 km thick (Ritzmann et al., 2004) and surface wave dispersion and receiver function analyses show that northern Greenland crust is 30–37 km thick [Gregersen et al., 1988; Dahl-Jensen et al., 2003]. Assuming that the compressionally thickened crust in the proto-Fram Strait was on the order of 35 km thick and that 30 km thick is isostatically at sea level, exceptionally fast and geologically unreasonable strain rates would seem to be required to thin sufficiently to open a significantly wide and deep gateway before the Miocene.

Consequently, the estuarine regime with fluctuating oxygen levels conditions implied by the Zebra zone was most likely controlled by at most a shallow connection across the proto-Fram Strait [*Engen et al.*, 2008]. The regional crustal-tectonic constraints and the seismic-stratigraphic evidence indicating a high sediment supply to the WAB suggests that the estuarine transitional phase (*Poirier and Hillaire-Marcel* [2011]) was associated with vertical adjustments along the LR. This is consistent with the hypothesis of a compressional tectonic regime that delayed the submergence of the LR [*O'Regan et al.*, 2008] although we cannot rule out that other factors, e.g. oceanographic, may have played a role [*Chernykh and Krylov*, 2017].

It is possible that erosion of LR prior to submergence may be linked to the sharp contact between units 1/4 and 1/5 in the ACEX samples. The duration of a hiatus at this level is uncertain but given a depositional rate of 0.18 cm ka^{-1} of the Zebra zone (*Poirier and Hillaire-Marcel* [2011]), the hiatus extends from ~33–17 Ma (ACEX 2 in Fig. 10). However, erosion linked to compression may have been more intense on the shallow ridge segment toward the Lincoln Sea compared to the deeper lying central portions in vicinity of the North Pole. Thus, the ACEX record may not accurately record the depositional changes that we infer for the WAB based on the present seismic data.

5.4 Late Miocene–Quaternary (units 4-6)

Seismic reflection geometries showing present and buried channel features within units 5 and 6 provide evidence for confined and apparently erosive bottom currents trailing the northern margin of the WAB.

5.4.1 Channel-levee development along the Lomonosov Ridge

Erosional features observed in unit 6 and the seafloor horizon below the LR flank include back stepping scarps and channel incision (Fig. 6), suggesting a high energy environment associated with deposition of sand and winnowing/by-pass of fine-grained sediments [*Pickering et al.*, 1995]. The transport of sediments in the fine sand fraction would require average current speeds >30 cm s^{-1}, i.e., far greater than the geostrophic speeds normally associated with oceanographic boundary currents [*McCave and Hall*, 2006]. The development of a prominent basinward levee suggests that the channel morphology was maintained by overbank deposition of muddy sediments carried by suspension currents periodically spilling over the channel pathway. This asymmetry of the channel profile is similar to other high-latitude sediment transfer systems of the northern hemisphere where downslope currents are deflected to the right into the basin due to the pronounced Coriolis effect [e.g., *Menard*, 1955; *Klaucke et al.*, 1998]. The high-amplitude discontinuous seismic facies of unit 6 continues into the basin, implying that the unit corresponds to a period of enhanced current influence on sedimentary deposition and distribution in the WAB. This interpretation is supported by fining-upward sandy facies interpreted as distal turbidite deposits observed in shallow cores [*Fütterer,* 1992; *Svindland and Vorren,* 2002].

It is uncertain when the high-energy depositional phase along the LR began, but it may be associated with a hiatus observed in the in the ACEX cores [*Frank et al.*, 2008] and the onset of Fe-Mn crust formation on the ridge flank [*Knudsen et al*, 2017], suggesting an age of 11.5–8 Ma (Fig. 10). The channelized sedimentary regime observed in units 5 and 6 is thus tentatively correlated to the U 1/1 – U 1/3 interval of the ACEX record, which represents large scale-glaciation of the northern hemisphere [*Zachos et al.*, 2001]. The lower sedimentation rates of the ACEX sequence compared to the Amundsen Basin record reflects the hemipelagic environment of the ridge that is isolated from downslope sources. Based on typical sedimentation rates of high-latitude channel systems influenced by turbidite overbank deposition, sedimentation rates on the thickest part of the levee (unit 6) may be as high as 25 cm ka^{-1} [*Svindland and Vorren,* 2002]. However, average values integrated over longer time scales are likely to be an order of magnitude lower [*Backman et al.*, 2004].

A crucial question relates to the flow mechanisms that generated the channelized seismic pattern and reflection truncation that mark the boundaries of units 5 and 6. The erosive character of the seabed suggests that the dominance of vigorous currents takes place at present, or at least, is a very recent phenomenon. Thus, it could be related to processes occurring during both glacial and interglacial periods. Dilute suspension currents operating on distal submarine fans are conventionally driven by high fine-clastic yields produced by fluvial-deltaic systems [*Kneller and Buckee*, 2000]. The release of suspension driven currents can be triggered by high fluvial discharges forming hyperpycnal plumes [*Parker,* 1982; *Mulder and Syvitski*, 1995]. This latter process is particularly well-described for the Laurentide Fan in the Labarador Sea where sedimentary records show a high frequency of graded beds related to meltwater plumes (“plumites”) [*Piper et al*., 2012]. Radiocarbon dating of these deposits indicate that the discharges were primarily released during deglaciations or major collapse phases of the Laurentide Ice Sheet and related to Heinrich events [*Rashid et al.*, 2003]. However, observations from temperate glacial margin environments are not transferable to the Northern Greenland margin where meltwater production is severely limited by extremely low temperatures and precipitation (mean temperature ranges from -33°C to 0°C and net annual precipitation is typically about 150–200 mm [*Serreze and Barry*, 2005]). Considering the extreme climate condition of the North Greenland–Arctic margin, which is presently dominated by > 2 meter-thick multi-year sea ice [*Lindsay and Schweiger*, 2015], it is difficult to envisage a meltwater driven mechanism as the primary factor for the recent development of channels and channel related deposits.

Based on seismic reflection data collected mainly from drifting ice-stations, *Kristoffersen et al.* [2004] proposed the existence of a submarine fan in the Amundsen Basin. The authors suggest that this fan is associated with the NP-28 channel system and developed during the Pliocene–Pleistocene as a product of enhanced glacial sediment input in the sea passage between the Lincoln Shelf margin and the LR. The seabed morphology and spatial distribution of the NP-28 channel was further characterized by *Boggild and Mosher* [2016] using shallow seismic data. The depocenter geometry of the fan system extending from the Lincoln Shelf is contested by *Døssing et al.* [2014] based on excess sediment thickness mapping that indicate a separation between sediments confined along the LR near the North Pole and sediments further south in vicinity to the North Greenland margin. Thus, even though enhanced glacial sediment delivery to the shelf edge was likely important, other processes have to be considered given the basinal distribution of late Cenozoic depocenters with high accumulation rates and the low potential for glacial meltwater generation.

5.4.2 Brine formation as a mechanism for enhanced sedimentary fluxes

As an alternative to meltwater driven density currents operating on conventional high-latitude fans, the possibility that the channel development within units 5 and 6 are related to dense brines generated from annual sea-ice formation is considered [*Rudels*, 1995]. Modern oceanographic studies suggest that brine formation is an important factor for Arctic deep-water formation, although evidence to constrain these processes and the vertical fluxes in the Arctic Ocean is sparse [*Jones et al.*, 1995; *Haley et al.*, 2008]. Conversely, brine formation linked to cooling and sea-ice production in polynya regions is a well-documented on Antarctic margins where it contributes to the generation of Antarctic bottom water (AABW), e.g. Weddell Sea [*Gill*, 1973; *Smith et al.*, 2010], the Ross Sea [*Assmann et al.*, 2003], the Adélie Coast [*Kusahara et al.*, 2011; *Marsland et al.*, 2004], and East Antarctica [*Ohshima et al.*, 2013]. Density stratification and water mass instability in these regions has also been linked to super-cooling as the brines pass below thick permanent ice shelves at depths >100 m [*Foldvik and Gammelsrød*, 1988]. As the cascades of dense, saline water masses enter the slope regime, energetic bottom currents are produced with speeds recorded of up to 50 cm s^{-1} [*Ohshima et al.*, 2013]. These currents are able to winnow and erode shelf and slope deposits [*Presti et al.*, 2003] and thus may be an important factor in the formation of gullies and channels that are widely observed along the Antarctic margins [*Gales et al.*, 2013].

In the Arctic Ocean, a model-based study by *Backhaus et al.* [1997] invokes sediment plumes triggered by brine release and polynia surface cooling as an important process driving vertical water mass exchange on the Eurasian Arctic margins. The shelf area north of Greenland is a potential source area for cascading brine plumes similar to the processes observed on the Antarctic margins. At the ACEX site, brine-driven water mass circulation has been inferred from radiogenic isotope studies of late Cenozoic material [*Haley et al.*, 2008]. In that study, the Siberian shelf regions are inferred as the main source area of the brines, but since the ridge site is at a depth of intermediate water masses, the geochemical signatures cannot be compared to the deep-water setting of the WAB.

The LOMROG data suggest that the main accumulation area of the Pliocene–Pleistocene package was located in the central parts of the basin, while a secondary depocenter is associated with levee build-up along the NP-28 channel (Figs. 3, 5, and SI Fig. S5). Bathymetric data suggest that the NP-28 channel branches off into the basin before reaching the North Pole [*Boggild and Mosher*, 2016]. The branching, possibly related to levee breaching (avulsion) and Coriolis current deviation, points in the direction of the principal depocenter in the central basin. However, the present data coverage prevents firm conclusions on the regional distribution of transport pathways. It is possible that , rather than being supplied uniformly from the Nares Strait and Lincoln Shelf region, the sedimentary basin infill of units 5 and 6 originated from a broader area of North Greenland and Morris Jessup Rise, transported by dense sediment-laden plumes formed by surface cooling and brine-rejection (Fig. 12). The channelized features seen within unit 5 could potentially form the distal component of fluvial systems active on the North Greenland margin during the Pliocene – early Pleistocene warm periods [*Funder et al.*, 2001]. However, for unit 6, associated with thick Arctic sea-ice and the extreme cooling and major sea-level low-stands of the late Pleistocene, brine-related plumes are suggested as a more feasible mechanism for carrying sediments far into the basin. This process may also be important as a source for Arctic deep-water, thus maintaining the baroclinic pressure gradient that drives southward export of water masses through the Fram Strait [*Rudels*, 1995; *Mauritzen*, 1996; *Rudels et al.*, 2002].

6 Conclusions

Interpretation of new multichannel seismic reflection data is used to constrain the Cenozoic depositional history in the western Amundsen Basin. The study reveals a more detailed picture of the sedimentary packages than previously described [*Jokat et al.*, 1995a; *Kristoffersen et al.*, 2004; *Chernykh and Krylov*, 2011] and provides new insights into bottom current activity and sediment transport in an area that is largely unknown due to the challenges of acquiring data in the high Arctic.

Four main phases of basin development are identified (Fig 12):

1) From the onset of seafloor spreading up to the mid-Oligocene, a small, isolated basin dominated by processes that were tectonically controlled is indicated. The high sedimentation rates in this period are linked to terrestrial material and increased pelagic deposition in a dominantly freshwater environment [*Brinkhuis et al.*, 2006].

   Mass transport and wedging from structural highs and a large depocenter are linked to the Eurekan compression that resulted in uplift and possibly erosion of the Lomonsov Ridge adjacent to the Lincoln Sea.

2) During the late Oligocene to early Miocene, the western Amundsen Basin was marked by a phase of passive infill driven primarily by hemipelagic deposition. We infer that the observed sedimentary signatures are associated with a tectonic quiescent basin and are apparently associated with an estuarine transitional phase of the Arctic Ocean that incurred from about 36 Ma.

3) During the middle Miocene (20-15 Ma), the Amundsen Basin shifted from an isolated basin to an ocean connected to the global meridional ocean circulation system. This phase is demarcated by the commencement of sedimentary drift accumulation controlled by geostrophic currents. We infer this depositional phase to be correlative with the condensed late Miocene section in the ACEX borehole of the central LR.

4) The two uppermost sedimentary units of likely Plio-Pleistocene age are marked by features controlled by erosion and deposition, such as channels, levees and scarps, indicative of a high-energy current processes. The modern and buried channel systems are likely generated by dense water masses cascading from the shelf regions north of Greenland. This suggests that brine production by sea-ice freezing may play a bigger role in the Arctic than previously thought.

Acknowledgments

This work was supported by a scholarship from the Consejo Nacional de Ciencia y Tecnología (CONACYT). Data acquisition was funded by the Continental Shelf Project of the Kingdom of Denmark. Special thanks to Lars Kjærgaard for his assistance with the loading of multichannel seismic reflection data and GEUS-IT for all their technical support. This paper is published with permission from the Geological Survey of Denmark and Greenland. The LOMROG seismic data presented in this paper are permanently archived at the Geological Survey of Denmark and Greenland (GEUS). Information regarding access to data and databases archived at GEUS is available at https://www.geus.dk. The AWI seismic data are owned and archived by the Alfred Wegener Institute (AWI). Information regarding their data can be obtained from the AWI Geophysics Department (https://www.awi.de/en/science/geosciences/geophysics.html).

References

Assmann, K., H. H. Hellmer, and A. Beckmann (2003), Seasonal variation in circulation and water mass distribution on the Ross Sea continental shelf, *Antarctic Science*, *15*(1), 3-11, doi: 10.1017/S0954102003001007.

Backhaus, J. O., H. Fohrmann, J. Kämpf, and A. Rubino (1997), Formation and export of water masses produced in Arctic shelf polynyas — process studies of oceanic convection, *ICES Journal of Marine Science: Journal du Conseil*, *54*(3), 366-382, doi: 10.1006/jmsc.1997.0230.

Backman, J., M. Jakobsson, R. Løvlie, L. Polyak, and L. A. Febo (2004), Is the central Arctic Ocean a sediment starved basin?, *Quaternary Science Reviews*, *23*(11–13), 1435-1454, doi: 10.1016/j.quascirev.2003.12.005.

Backman, J., Moran, K., McInroy, D., and the IODP Expedition 302 Scientists (2005), IODP Expedition 302, Arctic Coring Expedition (ACEX): A First Look at the Cenozoic Paleoceanography of the Central Arctic Ocean, *Sci. Dril*., 1, 12-17, doi:10.2204/iodp.sd.1.02.2005.

Backman, J., et al. (2008), Age model and core-seismic integration for the Cenozoic Arctic Coring Expedition sediments from the LR, *Paleoceanography*, *23*(1), PA1S03, doi: 10.1029/2007pa001476.

Beszczynska-Möller, A., R. A. Woodgate, C. Lee, H. Melling, and M. Karcher (2011), A Synthesis of Exchanges Through the Main Oceanic Gateways to the Arctic Ocean, *Oceanography*, *24*.

Boggild, K., and D. Mosher (2016), Morphological examination of the NP-28 submarine channel-fan complex in the Amundsen Basin, presented at 42nd Coloquium and Annual Meeting, The Atlantic Geoscience Society (AGS), Nova Scotia, 5-6 February.

Brinkhuis, H., et al. (2006), Episodic fresh surface waters in the Eocene Arctic Ocean, *Nature*, *441*(7093), 606-609, doi: 10.1038/nature04692.

Brozena, J. M., V. A. Childers, L. A. Lawver, L. M. Gahagan, R. Forsberg, J. I. Faleide, and O. Eldholm (2003), New aerogeophysical study of the Eurasia Basin and LR: Implications for basin development, *Geology*, *31*(9), 825-828, doi: 10.1130/g19528.1.

Brumley, K., E. L. Miller, A. Konstantinou, M. Grove, K. E. Meisling, and L. A. Mayer (2015), First bedrock samples dredged from submarine outcrops in the Chukchi Borderland, Arctic Ocean, *Geosphere, 11*(1), 76-92, doi: 10.1130/GES01044.1s.

Bruvoll, V., Y. Kristoffersen, B. Coakley, and J. Hopper (2010), Hemipelagic deposits on the Mendeleev and northwestern Alpha submarine Ridges in the Arctic Ocean: acoustic stratigraphy, depositional environment and an inter-ridge correlation calibrated by the ACEX results, *Marine Geophysical Researches*, *31*(3), 149-171, doi: 10.1007/s11001-010-9094-9s.

Burn, C. R. (1994), Permafrost, tectonics, and past and future regional climate change, Yukon and adjacent Northwest Territories, *Canadian Journal of Earth Sciences*, *31*(1), 182-191, doi: 10.1139/e94-015.

Cande, S. C., and D. V. Kent (1992), A new magnetic polarity timescale for the Late Cretaceous and Cenozoic, *Journal of Geophysical Research: Solid Earth*, *97*(B10), 13917-13951, doi: 10.1029/92JB01202s.

Cande, S. C., and D. V. Kent (1995), Revised calibration of the geomagnetic polarity timescale for the late Cretaceous and Cenozoic, *Journal of Geophysical Research: Solid Earth*, *100*(B4), 6093-6095, doi: 10.1029/94JB03098s.

Carmichael, M. J., et al. (2016), A model–model and data–model comparison for the early Eocene hydrological cycle, *Clim. Past*, *12*(2), 455-481, doi: 10.5194/cp-12-455-2016.

Chernykh, A. A., and A. A. Krylov (2011), Sedimentogenesis in the Amundsen Basin from geophysical data and drilling results on the LR, *Doklady Earth Sciences*, *440*(2), 1372-1376, doi: 10.1134/s1028334x11100011.

Chernykh, A. A., and A. A. Krylov (2017), Duration, Causes, and Geodynamic Significance of the Middle Cenozoic Hiatus in Sedimentation in the Near-Polar Part of the LR (Based on IODP-302-ACEX Drilling Data), *Oceanology*, *57*(5), 675-684, doi: 10.1134/S0001437017050058.

Chian, D., H. R. Jackson, D. R. Hutchinson, J. W. Shimeld, G. N. Oakey, N. Lebedeva-Ivanova, Q. Li, R. W. Saltus, and D. C. Mosher (2016), Distribution of crustal types in Canada Basin, Arctic Ocean, *Tectonophysics*, doi: 10.1016/j.tecto.2016.01.038.

Cochran, J. R., M. H. Edwards, and B. J. Coakley (2006), Morphology and structure of the LR, Arctic Ocean, *Geochemistry, Geophysics, Geosystems*, *7*(5), doi: 10.1029/2005gc001114.

Collinson, M. E., J. Barke, J. van der Burgh, J. H. A. van Konijnenburg-van Cittert, C. Heilmann-Clausen, L. E. Howard, and H. Brinkhuis (2010), Did a single species of Eocene Azolla spread from the Arctic Basin to the southern North Sea?, *Review of Palaeobotany and Palynology*, *159*(3–4), 152-165, doi: 10.1016/j.revpalbo.2009.12.001.

Dahl-Jensen, T., T. B. Larsen, I. Woelbern, T. Bach, W. Hanka, R. Kind, S. Gregersen, K. Mosegaard, P. Voss, and O. Gudmundsson (2003), Depth to Moho in Greenland: receiver-function analysis suggests two Proterozoic blocks in Greenland, *Earth and Planetary Science Letters*, *205*(3), 379-393, doi: 10.1016/S0012-821X(02)01080-4s.

Darby, D. A. (2014), Ephemeral formation of perennial sea ice in the Arctic Ocean during the middle Eocene, *Nature Geoscience*, *7*, 210-213, doi: 10.1038/NGEO2068.

DeMets, C., R. G. Gordon, D. F. Argus, and S. Stein (1994), Effect of recent revisions to the geomagnetic reversal time scale on estimates of current plate motions, *Geophysical Research Letters*, *21*(20), 2191-2194, doi: 10.1029/94GL02118.

Dokken, T. M., and E. Jansen (1999), Rapid changes in the mechanism of ocean convection during the last glacial period, *Nature*, *401*(6752), 458-461, doi: 10.1038/46753.

Døssing, A., J. R. Hopper, A. V. Olesen, T. M. Rasmussen, and J. Halpenny (2013a), New aero-gravity results from the Arctic: Linking the latest Cretaceous-early Cenozoic plate kinematics of the North Atlantic and Arctic Ocean, *Geochemistry, Geophysics, Geosystems*, *14*(10), 4044-4065, doi: 10.1002/ggge.20253.

Døssing, A., T. M. Hansen, A. V. Olesen, J. R. Hopper, and T. Funck (2014), Gravity inversion predicts the nature of the Amundsen Basin and its continental borderlands near Greenland, *Earth and Planetary Science Letters*, *408*(0), 132-145, doi: 10.1016/j.epsl.2014.10.011.

Døssing, A., H. R. Jackson, J. Matzka, I. Einarsson, T. M. Rasmussen, A. V. Olesen, and J. M. Brozena (2013b), On the origin of the Amerasia Basin and the High Arctic Large Igneous Province—Results of new aeromagnetic data, *Earth and Planetary Science Letters, 363*(0), 219-230, doi: 10.1016/j.epsl.2012.12.013.

Engen, Ø., J. I. Faleide, and T. K. Dyreng (2008), Opening of the Fram Strait gateway: A review of plate tectonic constraints, *Tectonophysics*, *450*(1–4), 51-69, doi: 10.1016/j.tecto.2008.01.002.

Frank, M., J. Backman, M. Jakobsson, K. Moran, M. O'Regan, J. King, B. A. Haley, P. W. Kubik, and D. Garbe-Schönberg (2008), Beryllium isotopes in central Arctic Ocean sediments over the past 12.3 million years: Stratigraphic and paleoclimatic implications, *Paleoceanography*, *23*(1), PA1S02, doi: 10.1029/2007PA001478.

Faugères, J. C., and D. A. V. Stow (2008), Chapter 14 - Contourite Drifts: Nature, Evolution and Controls, in *Developments in Sedimentology*, edited by M. Rebesco and A. Camerlenghi, pp. 257-288, Elsevier.

Foldvik, A., and T. Gammelsrød (1988), Notes on Southern Ocean hydrography, sea-ice and bottom water formation, *Palaeogeography, Palaeoclimatology, Palaeoecology*, *67*(1–2), 3-17, doi: 10.1016/0031-0182(88)90119-8.

Föllmi, K. B. (2016), Sedimentary condensation, *Earth-Science Reviews*, *152*(1), 143-180, doi: 10.1016/j.earscirev.2015.11.016.

Funder, S., O. Bennike, J. Böcher, C. Israelson, K. S. Petersen, and L. A. Símonarson (2001), Late Pliocene Greenland - The Kap København Formation in North Greenland, pp. 117-134, Bulletin of the Geological Society of Denmark, Copenhagen.

Fütterer, D. (1992), ARCTIC '91: die Expedition ARK-VIII/3 mit FS "Polarstern" 1991 = ARCTIC '91: the expedition ARK-VIII/3 of RV "Polarstern" in 1991, Alfred Wegener Institute for Polar and Marine Research, Bremerhaven.

Gaina, C., A. M. Nikishin, and E. I. Petrov (2015), Ultraslow spreading, ridge relocation and compressional events in the East Arctic region: A link to the Eurekan orogeny?, *Arktos*, *1*(1), 1-11, doi: 10.1007/s41063-015-0006-8.

Gales, J. A., M. Forwick, J. S. Laberg, T. O. Vorren, R. D. Larter, A. G. C. Graham, N. J. Baeten, and H. B. Amundsen (2013), Arctic and Antarctic submarine gullies—A comparison of high latitude continental margins, *Geomorphology*, *201*, 449-461, doi: 10.1016/j.geomorph.2013.07.018.

Geissler, W. H., W. Jokat, and H. Brekke (2011), The Yermak Plateau in the Arctic Ocean in the light of reflection seismic data—implication for its tectonic and sedimentary evolution, *Geophysical Journal International*, *187*(3), 1334-1362, doi: 10.1111/j.1365-246X.2011.05197.x.

Gill, A. E. (1973), Circulation and bottom water production in the Weddell Sea, *Deep Sea Research and Oceanographic Abstracts*, *20*(2), 111-140, doi: 10.1016/0011-7471(73)90048-X.

Gion, A. M., S. E. Williams, and R. D. Müller (2016), A reconstruction of the Eurekan Orogeny incorporating deformation constraints, *Tectonics*, 304-320, doi: 10.1002/2015TC004094.

Glebovsky, V. Y., V. D. Kaminsky, A. N. Minakov, S. A. Merkur'ev, V. A. Childers, and J. M. Brozena (2006), Formation of the Eurasia Basin in the Arctic Ocean as inferred from geohistorical analysis of the anomalous magnetic field, *Geotectonics*, *40*(4), 263-281, doi: 10.1134/s0016852106040029.

Gong et al. 2014, Origin and anatomy of two different types of mass-transport complexes: A 3D seismic case study from the northern South China Sea margin, Mar Petrol Geol 54, 198-215.

Grantz, A., P. E. Hart, and V. A. Childers (2011), Chapter 50 - Geology and tectonic development of the Amerasia and Canada Basins, Arctic Ocean, *Geological Society, London, Memoirs*, *35*(1), 771-799, doi: 10.1144/m35.50.

Gregersen, S., C. Clausen, T. Dahl-Jensen (1988), Crust and upper mantle structure in Greenland, in *Recent Seismological Investigations in Europe, Proceedings of the 19th General Assembly of the ESC*, pp. 467-469, Nauka, Moscow.

Haley, B. A., M. Frank, R. F. Spielhagen, and A. Eisenhauer (2008), Influence of brine formation on Arctic Ocean circulation over the past 15 million years, *Nature Geoscience*, *1*(1), 68-72, doi: 10.1038/ngeo.2007.5.

Heezen, B. C., and M. Ewing (1961), The Mid-Ocean Ridge and its extension through the Arctic Basin, in *Geology of the arctic*, edited by G. O. Raasch, pp. 662-642, University of Toronto Press.

Hegewald, A. and W. Jokat (2013), Relative sea level variations in the Chukchi region – Arctic Ocean – since the late Eocene, *Geophysical Research Letters*, *40*(5), 803-807, doi: 10.1002/grl.50182s.

Hein, J., N. Konstantinova, M. Mikesell, K. Mizell, J. N. Fitzsimmons, P. J. Lam, L. T. Jensen, Y. Xiang, A. Gartman, G. Cherkashov, D. R. Hutchinson, and C. P. Till (2017), Arctic deep water ferromanganese-oxide deposits reflect the unique characteristics of the Arctic Ocean, *Geochemistry, Geophysics, Geosystems*, *18*(11), 3771-3800, doi: 10.1002/2017GC007186s.

Hernández-Molina, F. J., E. Llave, and D. A. V. Stow (2008), Chapter 19 - Continental Slope Contourites, in *Developments in Sedimentology*, edited by M. Rebesco and A. Camerlenghi, pp. 379-408, Elsevier Science, Kidlington, Oxford.

Hopper, J.R., Trinhammer, P., Marcussen, C., and Funck, T., 2012, Acquisition of seismic data in ice filled waters, AGU 2012 Fall Meeting, Abstract C13E-0680.

Howe, J. A., T. M. Shimmield, R. E. X. Harland, and N. Eyles (2008), Late Quaternary contourites and glaciomarine sedimentation in the Fram Strait, *Sedimentology*, *55*(1), 179-200, doi: 10.1111/j.1365-3091.2007.00897.x.

Jakobsson, M., et al. (2007), The early Miocene onset of a ventilated circulation regime in the Arctic Ocean, *Nature*, *447*(7147), 986-990, doi: 10.1038/nature05924.

Jakobsson, M., et al. (2012), The International Bathymetric Chart of the Arctic Ocean (IBCAO) Version 3.0, *Geophysical Research Letters*, *39*(12), doi: 10.1029/2012GL052219.

Jokat, W. (2005), The sedimentary structure of the LR between 88°N and 80°N, *Geophysical Journal International*, *163*(2), 698-726, doi: 10.1111/j.1365-246X.2005.02786.x.

Jokat, W., and U. Micksch (2004), Sedimentary structure of the Nansen and Amundsen basins, Arctic Ocean, *Geophysical Research Letters*, *31*(2), L02603, doi: 10.1029/2003gl018352.

Jokat, W., G. Uenzelmann-Neben, Y. Kristoffersen, and T. M. Rasmussen (1992), LR—A double-sided continental margin, *Geology*, *20*(10), 887-890, doi: 10.1130/0091-7613(1992)020<0887:lradsc>2.3.co;.

Jokat, W., E. Weigelt, Y. Kristoffersen, T. Rasmussen, and T. Schöone (1995a), New insights into the evolution of the LR and the Eurasian Basin, *Geophysical Journal International*, *122*(2), 378-392, doi: 10.1111/j.1365-246X.1995.tb00532.x.

Jokat, W., E. Weigelt, Y. Kristofferseq, T. Rasmussen, and T. Schöne (1995b), New geophysical results from the south-western Eurasian Basin (Morris Jesup Rise, Gakkel Ridge, Yermak Plateau) and the Fram Strait, *Geophysical Journal International*, *123*(2), 601-610, doi: 10.1111/j.1365-246X.1995.tb06874.x.

Jones, E. P., Rudels, B. and Anderson, L.G. (1995), Deep waters of the Arctic Ocean: origins and circulation, *Deep-Sea Research Part I: Oceanographic Research Papers*, *42(5)*, 737-760, doi: 10.1016/0967-0637(95)0013-V.

Kaminski, M. (2007), Faunal constraints for the timing of the Fram Strait opening: The record of deep-water agglutinated foraminifera from IODP Hole M0002A, LR, *IODP UK Newsletter, 32*, 18-20.

Kaminski, M., L. Silye, and S. Kender (2009), Miocene deep-water agglutinated foraminifera from the LR and the opening of the Fram Strait, *Micropaleontology*, *55*(2-3), 117-135.

Klaucke, I., R. Hesse, and W. B. F. Ryan (1998), Seismic stratigraphy of the Northwest Atlantic Mid-Ocean Channel: growth pattern of a mid-ocean channel-levee complex, *Marine and Petroleum Geology*, *15*(6), 575-585, doi: 10.1016/S0264-8172(98)00044-0.

Kneller, B., and C. Buckee (2000), The structure and fluid mechanics of turbidity currents: a review of some recent studies and their geological implications, *Sedimentology*, *47*, 62-94, doi: 10.1046/j.1365-3091.2000.047s1062.x.

Knies, J., J. Matthiessen, C. Vogt, J. S. Laberg, B. O. Hjelstuen, M. Smelror, E. Larsen, K. Andreassen, T. Eidvin, and T. O. Vorren (2009), The Plio-Pleistocene glaciation of the Barents Sea–Svalbard region: a new model based on revised chronostratigraphy, *Quaternary Science Reviews*, *28*(9–10), 812-829, doi: 10.1016/j.quascirev.2008.12.002.

Knudsen, C, Hopper, J.R., Bierman, P.R., Bjerager, M., Funck, T., Ineson, J., Japsen, P., Marcussen, C., Sherlock, S., & Thomsen, T. (2017), Samples from the LR place new constraints on the geological evolution of the Arctic Ocean. In Pease, V., & Coakley, B.J. (eds.) Circum-Arctic Lithosphere Evolution, Geological Society, London, Special Publications, 460, doi: 10.1144/SP460.17.

Knutz, P. C., J. R. Hopper, U. Gregersen, T. Nielsen, and P. Japsen (2015), A contourite drift system on the Baffin Bay–West Greenland margin linking Pliocene Arctic warming to poleward ocean circulation, *Geology*, *43*(10), 907-910, doi: 10.1130/g36927.1.

Kristoffersen, Y., M. Y. Sorokin, W. Jokat, and O. Svendsen (2004), A submarine fan in the Amundsen Basin, Arctic Ocean, *Marine Geology*, *204*(3–4), 317-324, doi: 10.1016/S0025-3227(03)00373-6.

Kusahara, K., H. Hasumi, and G. D. Williams (2011), Dense shelf water formation and brine-driven circulation in the Adélie and George V Land region, *Ocean Modelling*, *37*(3–4), 122-138, doi: 10.1016/j.ocemod.2011.01.008.

Lawver, L. A., and Scotese, C.R. (1990), A review of tectonic models for the evolution of the Canada Basin, in *The Arctic Ocean Region*, edited by A. Grantz, Johnson, L., and Sweeney, J.F., pp. 593-617, Geological Society of America, The Geology of North America, Boulder, Colorado.

Lindsay, R., and A. Schweiger (2015), Arctic sea ice thickness loss determined using subsurface, aircraft, and satellite observations, *The Cryosphere*, *9*(1), 269-283, doi: 10.5194/tc-9-269-2015.

Lykke-Andersen, H., Funck, T., Hopper, J.R., Trinhammer, P., Marcussen, C., Gunvald, A. K., & Jørgensen, E. V., 2010. Seismic Acquisition Report - LOMROG 2009. Danmarks and Grønlands Geologiske Undersøgelse Rapport, 2010/53, 73pp. (excl. appendices).

Mann, U., J. Knies, S. Chand, W. Jokat, R. Stein, and J. Zweigel (2009), Evaluation and modelling of Tertiary source rocks in the central Arctic Ocean, *Marine and Petroleum Geology*, *26*(8), 1624-1639, doi: 10.1016/j.marpetgeo.2009.01.008.

Marcussen, C., Vangkilde-Pedersen, T., Lykke-Andersen, H., Trinhammer, P., Funck, T., Dahl-Jensen, T., & Forsberg, R., 2008. Seismic Acquisition Report - LOMROG 2007. Danmarks and Grønlands Geologiske Undersøgelse Rapport 2008/77, 82pp (excl. appendices).

Marsland, S. J., N. L. Bindoff, G. D. Williams, and W. F. Budd (2004), Modeling water mass formation in the Mertz Glacier Polynya and Adélie Depression, East Antarctica, *Journal of Geophysical Research: Oceans*, *109*, C11003, doi: 10.1029/2004JC002441.

Mattingsdal, R., J. Knies, K. Andreassen, K. Fabian, K. Husum, K. Grøsfjeld, and S. De Schepper (2014), A new 6 Myr stratigraphic framework for the Atlantic–Arctic Gateway, *Quaternary Science Reviews, 92*, 170-178, doi: 10.1016/j.quascirev.2013.08.022.

Mauritzen, C. (1996), Production of dense overflow waters feeding the North Atlantic across the Greenland-Scotland Ridge. Part 1: Evidence for a revised circulation scheme, *Deep Sea Research Part I: Oceanographic Research Papers, 43*(6), 769-806, doi: 10.1016/0967-0637(96)00037-4.

McCave, I. N., and I. R. Hall (2006), Size sorting in marine muds: Processes, pitfalls, and prospects for paleoflow-speed proxies, *Geochemistry, Geophysics, Geosystems*, *7*(10), Q10N05, doi: 10.1029/2006GC001284.

McKenzie, D. (1978), Some remarks on the development of sedimentary basins, *Earth and Planetary Science Letters*, *40*(1), 25-32, doi: 10.1016/0012-821X(78)90071-7.

McNeil, D. H. (1990), Tertiary Marine Events of the Beaufort-Mackenzie Basin and Correlation of Oligocene to Pliocene Marine Outcrops in Arctic North America, *Arctic*, *43*(4), 301-313.

Menard, H. W. (1955), Deep-sea channels, topography, and sedimentation, *AAPG Bulletin*, *39*(2), 236-255.

Mitchum Jr., R. M., P. R. Vail, and J. B. Sangree (1997), Seismic stratigraphy and global changes of sea level, Part 6: stratigraphic interpretation of seismic reflection patterns in depositional sequences, in *Seismic Stratigraphy - Applications to Hydrocarbon Exploration*, edited by C. Paynton, pp. 117-133, AAPG Memoir, Tulsa.

Minakov, A. N., and Y. Y. Podladchikov (2012), Tectonic subsidence of the LR, *Geology*, *40*(2), 99-102, doi: 10.1130/g32445.1.

Moore, T. C., and the Expedition 302 Scientists (2006a), Sedimentation and subsidence history of the LR. In Backman, J., Moran, K., McInroy, D.B., Mayer, L.A., and the Expedition 302 Scientists. *Proc. IODP*, 302: Edinburgh (Integrated Ocean Drilling Program Management International, Inc.), doi: 10.2204/iodp.proc.302.105.2006

Moore, T. C., and the Expedition 302 Scientists (2006b), Sites M0001 – M0004. In Backman, J., Moran, K., McInroy, D.B., Mayer, L.A., and the Expedition 302 Scientists. *Proc. IODP*, 302: Edinburgh (Integrated Ocean Drilling Program Management International, Inc.), doi: 10.2204/iodp.proc.302.104.2006

Moran, K., et al. (2006), The Cenozoic palaeoenvironment of the Arctic Ocean, *Nature*, *441*(7093), 601-605, doi: 10.1038/nature04800.

Morozov, A. F., O. V. Petrov, S. P. Shokalsky, S. N. Kashubin, A. A. Kremenetsky, M. Yu. Shkatov, V. D. Kaminsky, E. A. Gusev, G. E. Grikurov, P. V. Rekant, S. S. Shevchenko, S. A. Sergeev, V. V. Shatov (2013), New geological data explaining the nature of the Central Arctic rises, *Regional Geology and Metallogeny*, 53, 34-55.

Mulder, T., and J. P. M. Syvitski (1995), Turbidity Currents Generated at River Mouths during Exceptional Discharges to the World Oceans, *The Journal of Geology*, *103*(3), 285-299, doi: doi:10.1086/629747.

März, C., C. Vogt, B. Schnetger, and H. -J. Brumsack (2011), Variable Eocene-Miocene sedimentation processes and bottom water redox conditions in the Central Arctic Ocean (IODP Expedition 302), *Earth and Planetary Science Letters, 310*(3), 526-537, doi: 10.1016/j.epsl. 2011.08.025s.

O'Regan, M., K. Moran, J. Backman, M. Jakobsson, F. Sangiorgi, H. Brinkhuis, R. Pockalny, A. Skelton, C. Stickley, N. Koç, H.-J. Brumsack, and D. Willard (2008), Mid-Cenozoic tectonic and paleoenvironmental setting of the central Arctic Ocean, *Paleoceanography, 23*(1), PA1S20, doi: 10.1029/2007PA001559.

O'Regan, M., C.J. Williams, K.E. Frey, and M. Jakobsson (2011), A synthesis of the long-term paleoclimatic evolution of the Arctic. *Oceanography*, *24*(3), doi: 10.5670/oceanog.2011.57.

O'Regan, M., K. Moran, C. D. P. Baxter, J. Cartwright, C. Vogt, and M. Kölling (2010), Towards ground truthing exploration in the central Arctic Ocean: a Cenozoic compaction history from the LR, *Basin Research*, *22*(2), 215-235, doi: 10.1111/j.1365-2117.2009.00403.x.

Oakey, G. N., and R. Stephenson (2008), Crustal structure of the Innuitian region of Arctic Canada and Greenland from gravity modelling: implications for the Palaeogene Eurekan orogen, *Geophysical Journal International*, *173*(3), 1039-1063, doi: 10.1111/j.1365-246X.2008.03784.x.

Oakey, G. N., and J. A. Chalmers (2012), A new model for the Paleogene motion of Greenland relative to North America: Plate reconstructions of the Davis Strait and Nares Strait regions between Canada and Greenland, *Journal of Geophysical Research: Solid Earth*, *117*, B10401, doi: 10.1029/2011JB008942.

Ogg, J. G. (2012), Chapter 5 - Geomagnetic Polarity Time Scale, in *The Geologic Time Scale*, edited by F. M. Gradstein, J. G. Ogg, M. D. Schmitz and G. M. Ogg, pp. 85-113, Elsevier, Boston.

Ohshima, K. I., et al. (2013), Antarctic Bottom Water production by intense sea-ice formation in the Cape Darnley polynya, *Nature Geosci*, *6*(3), 235-240, doi: 10.1038/ngeo1738.

Ostenso, N. A., and R. J. Wold (1977), A seismic and gravity profile across the Arctic Ocean Basin, *Tectonophysics*, *37*(1), 1-24, doi: 10.1016/0040-1951(77)90036-1.

Pagani, M., N. Pedentchouk, M. Huber, A. Sluijs, S. Schouten, H. Brinkhuis, J. S. Sinninghe Damsté, G. R. Dickens, and the Expedition 302 Scientists (2006), Arctic hydrology during global warming at the Palaeocene/Eocene thermal maximum. *Nature*, *442*(598), 671-675, doi: 10.1038/nature05043.

Parker, G. (1982), Conditions for the ignition of catastrophically erosive turbidity currents, *Marine Geology*, *46*(3), 307-327, doi: 10.1016/0025-3227(82)90086-X.

Parsons, B., and Sclater, J.G. (1977), An analysis of the variation of ocean floor bathymetry and heat flow with age, *Journal of Geophysical Research, 82*, 803-827, doi: 10.1029/JB082i005p00803

Pickering, K. T., J. D. Clark, R. D. A. Smith, R. N. Hiscott, F. Ricci Lucchi, and N. H. Kenyon (1995), Architectural element analysis of turbidite systems, and selected topical problems for sand-prone deep-water systems, in *Atlas of Deep Water Environments: Architectural style in turbidite systems*, edited by K. T. Pickering, R. N. Hiscott, N. H. Kenyon, F. Ricci Lucchi and R. D. A. Smith, pp. 1-10, Springer Netherlands, Dordrecht.

Piepjohn, K., W. von Gosen, and F. Tessensohn (2016), The Eurekan deformation in the Arctic: an outline, *Journal of the Geological Society*, *173*(6), 1007-1024, doi: 10.1144/jgs2016-081.

Piper, D. J. W., M. E. Deptuck, D. C. Mosher, J. E. H. Clarke, and S. Migeon (2012), Erosional and Depositional Features of Glacial Meltwater Discharges on the Eastern Canadian Continental Margin, in *Application of the Principles of Seismic Geomorphology to Continental Slope and Base-of-Slope Systems*, edited by B. E. Prather, M. E. Deptuck, D. Mohring, B. V. Hoorn and R. B. Wynn, pp. 61-80, SEPM Society for Sedimentary Geology.

Poirier, A., and C. Hillaire-Marcel (2009), Os-isotope insights into major environmental changes of the Arctic Ocean during the Cenozoic, *Geophysical Research Letters*, *36* (11), L11602, doi:10.1029/2009GL037422.

Poirier, A., and C. Hillaire-Marcel (2011), Improved Os-isotope stratigraphy of the Arctic Ocean, *Geophysical Research Letters*, *38*(14), L14607, doi:10.1029/2011GL047953.

Poselov, V., V. Butsenki, A. Chernykh, V. Glebovsky, H. R. Jackson, D. P. Potter, G. Oakey, J. Shimeld, and C. Marcussen (2014), The structural integrity of the LR withhe North American and Siberian continental margins, paper presented at International Conference on Arctic Margins VI, Fairbanks, Alaska, May 2011.

Presti, M., L. De Santis, M. Busetti, and P. T. Harris (2003), Late Pleistocene and Holocene sedimentation on the George V Continental Shelf, East Antarctica, *Deep Sea Research Part*

II: Topical Studies in Oceanography, *50*(8–9), 1441-1461, doi: 10.1016/S0967-0645(03)00068-7.

Rashid, H., R. Hesse, and D. J. W. Piper (2003), Origin of unusually thick Heinrich layers in ice-proximal regions of the northwest Labrador Sea, *Earth and Planetary Science Letters*, *208*(3–4), 319-336, doi: 10.1016/S0012-821X(03)00030-X.

Rebesco, M., F. J. Hernández-Molina, D. Van Rooij, and A. Wåhlin (2014), Contourites and associated sediments controlled by deep-water circulation processes: State-of-the-art and future considerations, *Marine Geology*, *352*, 111-154, doi: 10.1016/j.margeo.2014.03.011.

Rebesco, M., A. Wåhlin, J. S. Laberg, U. Schauer, A. Beszczynska-Möller, R. G. Lucchi, R. Noormets, D. Accettella, Y. Zarayskaya, and P. Diviacco (2013), Quaternary contourite drifts of the Western Spitsbergen margin, *Deep Sea Research Part I: Oceanographic Research Papers*, *79*, 156-168, doi: 10.1016/j.dsr.2013.05.013.

Riefstahl, F., S. Estrada, W. H. Geissler, W. Jokat, R. Stein, H. Kämpf, P. Dulski, R. Naumann, and C. Spiegel (2013), Provenance and characteristics of rocks from the Yermak Plateau, Arctic Ocean: Petrographic, geochemical and geochronological constraints, *Marine Geology*, *343*, 125-145, doi: 10.1016/j.margeo.2013.06.009.

Ritzmann, O., W. Jokat, W. Czuba, A. Guterch, R. Mjelde, and Y. Nishimura (2004), A deep seismic transect from Hovgård Ridge to northwestern Svalbard across the continental-ocean transition: a sheared margin study, *Geophysical Journal International*, *157*(2), 683-702, doi: 10.1111/j.1365-246X.2004.02204.xs.

Roest, W. R., and S. P. Srivastava (1989), Sea-floor spreading in the Labrador Sea: A new reconstruction, *Geology*, *17*(11), 1000-1003, doi: 10.1130/0091-7613(1989)017<1000:sfsitl>2.3.co;2.

Rudels, B. (1995), The Thermohaline Circulation of the Arctic Ocean and the Greenland Sea, *Philosophical Transactions: Physical Sciences and Engineering*, *352*(1699), 287-299.

Rudels, B. (2012), Arctic Ocean circulation and variability - advection and external forcing encounter constraints and local processes, *Ocean Sci.*, *8*(2), 261-286, doi: 10.5194/os-8-261-2012.

Rudels, B., and H. Friedrich (2000), The transformations of Atlantic water in the Arctic Ocean and their significance for the freshwater budget, in *The Freshwater Budget of the Arctic Ocean*, edited by L. L. Lewis, E. P. Jones, P. Lemke, T. D. Prowse and P. Wadhams, pp. 503-532, Kluwer Academic Publishers, the Netherlands.

Rudels, B., E. Fahrbach, J. Meincke, G. Budéus, and P. Eriksson (2002), The East Greenland Current and its contribution to the Denmark Strait overflow, *ICES Journal of Marine Science*, *59*(6), 1133-1154, doi: 10.1006/jmsc.2002.1284.

Russell, S.M., 1999, A magnetic study of the West Iberia and conjugate rifted continental margins: Constraints on rift-to-drift process, Ph.D. Thesis, University of Durham, UK. 278 pages

Sangiorgi, F., H.-J. Brumsack, D. A. Willard, S. Schouten, C. E. Stickley, M. O'Regan, G.-J. Reichart, J. S. Sinninghe Damsté, and H. Brinkhuis (2008), A 26 million year gap in the central Arctic record at the greenhouse-icehouse transition: Looking for clues, *Paleoceanography*, *23*(1), PA1S04, doi: 10.1029/2007pa001477.

Sclater, J. G., R. N. Anderson, and M. L. Bell (1971), Elevation of ridges and evolution of the central eastern Pacific, *Journal of Geophysical Research*, *76*(32), 7888-7915, doi: 10.1029/JB076i032p07888.

Serreze, M. C., and R. G. Barry (2005), Arctic ocean–sea ice–climate interactions, in *The Arctic Climate System:*, edited, pp. 177-207, Cambridge University Press, Cambridge.

Smith, J. A., C.-D. Hillenbrand, C. J. Pudsey, C. S. Allen, and A. G. C. Graham (2010), The presence of polynyas in the Weddell Sea during the Last Glacial Period with implications for the reconstruction of sea-ice limits and ice sheet history, *Earth and Planetary Science Letters*, *296*(3–4), 287-298, doi: 10.1016/j.epsl.2010.05.008.

Speelman, E. N., et al. (2009), The Eocene Arctic Azolla bloom: environmental conditions, productivity and carbon drawdown, *Geobiology*, *7*(2), 155-170, doi: 10.1111/j.1472-4669.2009.00195.x.

St. John, K. (2008), Cenozoic ice-rafting history of the central Arctic Ocean: Terrigenous sands on the LR, *Paleoceanography*, *23*(1), PA1S05, doi: 10.1029/2007PA001483.

Stein, R. (2007), Upper Cretaceous/lower Tertiary black shales near the North Pole: Organic-carbon origin and source-rock potential, *Marine and Petroleum Geology*, *24*(2), 67-73, doi: 10.1016/j.marpetgeo.2006.10.002.

Stein, R., B. Boucsein, and H. Meyer (2006), Anoxia and high primary production in the Paleogene central Arctic Ocean: First detailed records from LR, *Geophysical Research Letters*, *33* (18), L18606, doi: 10.1029/2006GL026776.

Stein, R., P. Weller, J. Backman, H. Brinkhuis, K. Moran, and H. Pälike (2014), Chapter 3.2 - Cenozoic Arctic Ocean Climate History : Some Highlights from the Integrated Ocean Drilling Program Arctic Coring Expedition, in *Developments in Marine Geology*, edited by R. Stein, D. Blackman, F. Inagaki, and H. -C. Larsen, pp. 259-293, Elsevier.

Stein, R., K. Fahl, M. Schreck, G. Knorr, F. Niessen, M. Forwick, C. Gebhardt, L. Jensen, M. Kaminski, A. Kopf, J. Matthiessen, W. Jokat, and G. Lohmann (2016), Evidence for ice-free summers in the late Miocene central Arctic Ocean, *Nature Communications*, *7*, 11148, doi: 10.1038/ncomms11148.

Stickley, C. E., K. St John, N. Koç, R. W. Jordan, S. Passchier, R. B. Pearce, and L. E. Kearns (2009), Evidence for middle Eocene Arctic sea ice from diatoms and ice-rafted debris, *Nature*, *460*, 376-380, doi: 10.1038/nature08163.

Svindland, K. T., and T. O. Vorren (2002), Late Cenozoic sedimentary environments in the Amundsen Basin, Arctic Ocean, *Marine Geology*, *186*(3–4), 541-555, doi: 10.1016/S0025-3227(02)00197-4.

Sweeney, J. F., J. R. Weber, and S. M. Blasco (1982), Structure of the Arctic Continental ridges in the Arctic Ocean: Lorex constraints, *Tectonophysics*, *89*(1), 217-237, doi: 10.1016/0040-1951(82)90039-7.

Talwani, M., and O. Eldholm (1977), Evolution of the Norwegian-Greenland Sea, *Geological Society of America Bulletin*, *88*(7), 969-999, doi: 10.1130/0016-7606(1977)88<969:eotns>2.0.co;2.

Thompson, B., J. Nilsson, J. Nycander, M. Jakobsson, and K. Döös (2010), Ventilation of the Miocene Arctic Ocean: An idealized model study, *Paleoceanography*, *25*(4), doi: 10.1029/2009PA001883s.

Tomczak, M., and J. S. Godfrey (1994), CHAPTER 7 - Arctic oceanography; the path of North Atlantic Deep Water, in *Regional Oceanography*, edited by M. Tomczak and J. S. Godfrey, pp. 89-111, Pergamon, Amsterdam.

Vail, P. R., R. M. Mitchum, and S. Thompson (1977), Seismic stratigraphy and global changes of sea level, Part 3: Relative changes of sea level from coastal onlap, in *Seismic Stratigraphy - Applications to Hydrocarbon Exploration*, edited by C. Paynton, pp. 63-81, AAPG Memoir, Tulsa.

van der Burgh, J., M. E. Collinson, J. H. A. van Konijnenburg-van Cittert, J. Barke, and H. Brinkhuis (2013), The freshwater fern Azolla (Azollaceae) from Eocene Arctic and Nordic Sea sediments: New species and their stratigraphic distribution, *Review of Palaeobotany and Palynology*, *194*, 50-68, doi: 10.1016/j.revpalbo.2013.02.002.

Varming, T., Funck, T., Hopper, J.R., Trinhammer, P., Ejlertsen, S., Rödel, L., Schiling, J., Kvist-Lassen, T., Rasmussen, M.L., Ugelvig, S., & Marcussen, C. 2012. Seismic Acquisition Report - LOMROG 2012. Danmarks and Grønlands Geologiske Undersøgelse Rapport 2012/120, 77pp (excl. appendices).

Vogt, P. R., P. T. Taylor, L. C. Kovacs, and G. L. Johnson (1979), Detailed aeromagnetic investigation of the Arctic Basin, *Journal of Geophysical Research: Solid Earth*, *84*(B3), 1071-1089, doi: 10.1029/JB084iB03p01071.

Weigelt, E., W. Jokat, and D. Franke (2014), Seismostratigraphy of the Siberian Sector of the Arctic Ocean and adjacent Laptev Sea Shelf, *Journal of Geophysical Research: Solid Earth*, *119*(7), 5275-5289, doi: 10.1002/2013jb010727.

White, J. M., T. A. Ager, D. P. Adam, E. B. Leopold, G. Liu, H. Jetté, and C. E. Schweger (1997), An 18 million year record of vegetation and climate change in northwestern Canada and Alaska: tectonic and global climatic correlates, *Palaeogeography, Palaeoclimatology, Palaeoecology*, *130*(1–4), 293-306, doi: 10.1016/S0031-0182(96)00146-0.

Wold, C. N. (1994), Cenozoic sediment accumulation on drifts in the northern North Atlantic, *Paleoceanography*, *9*(6), 917-941, doi: 10.1029/94PA01438.

Wolf-Welling, T. C. W., M. Cremer, S. O'Connell, A. Winkler, and J. Thiede (1996), Cenozoic Arctic Gateway Paleoclimate Variability: Indications from Changes in Coarse-Fraction Composition, in *Proceedings of the Ocean Drilling Program, 151 Scientific Results*, International Ocean Discovery Program (IODP).

Woodgate, R. (2013), Arctic Ocean Circulation: Going Around At the Top Of the World, *Nature Education Knowledge*, *4(8):8.*

Zachos, J. C., G. R. Dickens, and R. E. Zeebe (2008), An early Cenozoic perspective on greenhouse warming and carbon-cycle dynamics, *Nature*, *451*(7176), 279-283, doi: 10.1038/nature06588.

Zachos, J. C., M. Pagani, L. Sloan, E. Thomas, and K. Billups (2001), Trends, Rhythms, and Aberrations in Global Climate 65 Ma to Present, *Science*, *292*(5517), 686-693, doi: 10.1126/science.1059412.

Zelt, C. A., and R. B. Smith (1992), Seismic traveltime inversion for 2-D crustal velocity structure, *Geophysical Journal International*, *108*(1), 16-34, doi: 10.1111/j.1365-246X.1992.tb00836.xs.

	LOMROG I	LOMROG II	LOMROG III
Source	1 Sercel G and 1 Sercel GI gun	1 Sercel G and 1 Sercel GI gun	2*Sercel G-Gun
Chamber volume	605 cu. inch	605 cu. inch	1040 cu. inch
Gun pressure	200 bar (3000 psi)	180 bar (2600 psi)	180 bar (2600 psi)
Nominal tow depth	20 m	20 m	20 m
Streamer	Geometrics GeoEel	Geometrics GeoEel	Geometrics GeoEel
Length of tow cable	43 m	43 m	30 m
Total no. of groups	48 / 40 / 32 / 24	32 / 40	32
Group interval	6.25	6.25 m	6.25 m
Nominal Tow Depth	20 m	20 m	20 m

Table 1. Summary of Key Acquisition Parameters during LOMROG I through III

Table 1. Summary of the key acquisition parameters during the LOMROG cruises. The data quality was enhanced by a basic processing sequence that included band pass filtering, spectral shaping filtering, spike and noise burst editing, f-k filtering, static corrections, trace equalization, shot-mixing, stacking, and velocity migrations.

Table 2. Parameters Used for Calculating Sediment Rates

AB Unit	Age of top horizon	Thickness, TWT	Velocity (km s^{-1})
Unit 6	-	100–200 m (125–250 ms)	1.54–1.6
Unit 5	2-4 Ma[a]	150–300 m (160–320 ms)	1.9–2.0
Unit 4	8–11.5 Ma	120–182 m (125–190 ms)	1.9–2.0
Unit 3	15–20 Ma	130–270 m (125–260 ms)	2.0–2.4
Unit 2b	Younger than C8y < 25 Ma.	140–310 m (120–270 ms)	2.1–2.4
Unit 2a	C12o–18y 27.5 ± 2.5 Ma	190–430 m (150–300 ms)	2.5–2.8
Unit 1b	C18o–15y 37.5 ± 2.5 Ma	470–910 m (375–700 ms)	2.6–2.9
Unit 1a	C21y–20o 44.5 ± 1.5 Ma	1500 m (925 ms)	3.1–3.2

[a] Based on estimated sedimentation rates.

Table 2. Chronology, thickness, and velocity ranges used for calculating sediment rates in this study. Only basinal thicknesses were used for calculating sediment rates while sections influenced by tectonic factors (e.g., thin sediments above basement ridges) were omitted. Locations of key sonobuoys used for the velocity estimates are shown in Fig. 2. The velocity modeling and sonobuoy data is presented in the supplemental material. Ages are calibrated according to the timescale of *Ogg* [2012] except for unit 6.

Figure Captions

Figure 1. Bathymetry of the Amundsen Basin and surrounding areas in the Arctic Ocean. Yellow lines: LOMROG multichannel seismic reflection data collected in 2007, 2009, and 2012. White lines: seismic reflection data from ARCTIC'91 [*Jokat et al*., 1995]. Purple line: seismic reflection data from AMORE 2001 [*Jokat and Micksch*, 2004]. Black lines: seismic reflection lines from NP-28 [*Fütterer*, 1992] and Arlis-II [*Ostenso and Wold*, 1977]. Red lines and white rectangles: seismic reflection segments featured in this paper. Green lines: major sediment pathways from *Boggild and Mosher* [2016]. Filled red circle: location of IODP 302 (ACEX). Filled red square: location of coring station from PS87/2014 [*Stein et al.*, 2016]. The bathymetry is based on the IBCAO grid v.3 [*Jakobsson et al.*, 2012]. Abbreviations: BS – Barents Shelf; CB – Canada Basin; ESS – East Siberian Shelf; EAB – Eastern Amundsen Basin; EI – Ellesmere Island; FS – Fram Strait; KS – Kara Shelf; LVS – Laptev Shelf; LS – Lincoln Shelf; NS – Nares Strait; RU – Russia; SAT – St. Anna Trough; WAB – Western Amundsen Basin; YP – Yermak Plateau.

Figure 2. Magnetic anomaly map from *Brozena et al.* [2003] used to determine the ages of the stratigraphic units in this study. Orange lines: normal polarity chrons. The "y" and "o" refer to the young and old side of the anomalies respectively. Yellow lines: LOMROG multichannel seismic reflection data collected in 2007, 2009, and 2012. The seismic lines are labeled "xx-yy", where "xx" refers to the year the data were collected and "yy" refers to the profile number. White lines: seismic reflection data from ARCTIC'91 [*Jokat et al.*, 1995a]. The seismic lines are labeled "A91-yyy", where "A91" refers to "AWI1991," and "yyy" refers to the profile number. Purple line: seismic reflection data from AMORE 2001 [*Jokat and Micksch*, 2004]. Filled light blue stars: position where the top horizon of subunit 1a onlaps the oceanic basement. Filled dark blue stars: position where the top horizon of subunit 1b onlaps the oceanic basement. Filled orange stars: position where the top horizon of subunit 1c onlaps the oceanic basement. Filled white star: position where the top horizon of unit 2 onlaps the oceanic basement. Filled green circles: deployment position of sonobuoys used in this study.

Figure 3. Three seismic transects crossing the Amundsen Basin with line names shown along the top axis (see Fig. 1 and 2 for line positions). Key seismic horizons interpreted: oceanic basement – black; top subunit 1a – light blue; top subunit 1b – dark blue; top subunit 1c – orange; top subunit 2 – white; top unit 3 – red; top unit 4 – yellow; top unit 5 – green; top unit 6 – seabed. Red circles: positions where the horizons onlap the oceanic basement (see Fig. 2). Gray dashed line: estimated thermal subsidence curve of the seafloor according to plate cooling models [*Parsons and Slater, 1977*].

Figure 4. Seismic profile LOMROG2009-11 crossing the LR flank into the Amundsen Basin. Horizon colors same as in Fig. 3. A 1D-velocity column modeled from the refraction data is shown.

Figure 5. Detail of channel segment developed within unit 6 (see position in Fig. 4). The channel system is characterized by terraced surfaces back-stepping towards the ridge flank. Note the prominent development of the basinward channel levee influenced by growth faults and asymmetric mounded depositional features seen within units 4 and 5. Unit 5 is divided into two subunits (a-b).

Figure 6. Detail from Fig. 4 showing erosion within unit 5 interpreted as a buried channel segment (turquoise dot-dash horizon). The buried channel is about 7 km wide and shows a stepwise incision with a preferential levee accumulation in a basinward direction similar to the modern channel.

Figure 7. Detail from Fig. 4 displaying a thick sedimentary wedge developed within subunit 1c and fault-bounded against the LR. The depositional body is characterized by an irregular surface with discontinuous seismic reflections that appear to offlap and downlap top subunit 1b (dark blue horizon).

Figure 8. Detail from profile LOMROG2009-10 crossing the LR flank and the Amundsen Basin.

Figure 9a-c. Detailed images from Fig. 3c and Fig. S5 (supplementary material) showing structural influence on strata development and sedimentation patterns. a: strata dip changes in unit 3 along a basement structure (indicated by blue arrows). An upward decrease in dip of onlapping strata from 30 – 0 degrees is observed. b: Example of mass-movements within subunit 2a related to slope instability and structural faulting along the flanks of a sub-basin (internal horizons shown in red and purple colors). c: Asymmetric mounded features seen within unit 4 (purple and light green hatchured markers) inferred as contourite drift deposits formed along a fault-bounded topographic high.

Figure 10. Seismic-stratigraphic units and horizon ages defined in the western Amundsen Basin compared to previous basin studies and the ACEX borehole stratigraphy. The numbers shown are the inferred sedimentation rates (cm ka^{-1}). Color-coding indicates the four interpreted depositional environments discussed in the text. Magenta horizons and colored stars: aeromagnetic dated boundaries (see also Fig. 2). Yellow horizons: boundaries inferred from oceanographic considerations. Dark blue horizons: boundaries inferred from estimated sedimentation rates. Light blue horizons: cosmogenic dated boundaries *[Frank et al*., 2008*]*. Geomagnetic polarity timescales based on *Cande and Kent* [1992] (left), *Cande and Kent* [1995] (middle), and *Ogg* [2012] (right). Black: normal polarity chrons. White: reversed polarity chrons. Abbreviations: CK92 – *Cande and Kent* [1992]; CK95 – *Cande and Kent* [1995]; O12 – *Ogg* [2012]; CK [2011]– *Chernykh and Krylov* [2011].

Figure 11. Line drawing of profile LOMROG2009-11 (Figs. 4-7) with inferred depositional environments and horizon ages. Main sedimentary pathways are indicated by green arrows. Ages for units are derived from ties to the magnetic anomaly interpretation of *Brozena et al.* [2003]. Color-coding same as Fig. 10.

Figure 12. Conceptual scenarios illustrating the gross depositional evolution in the western Amundsen Basin since the mid-Eocene. The panels show kinematic evolution of key features using present day contours. Top: middle Eocene (about 45 Ma) modified from *Døssing et al.* [2013a]. The main faults of the Eurekan compression and main crustal discontinuities/transforms (dashed/dotted lines) are shown. Pink arrow indicates the direction of Greenland motion. Black arrows indicate seafloor spreading; Red/brown arrows indicate sediment transport from possible source areas. Middle: Mid- to late Miocene (about 20 Ma). Blue arrows indicate potential pathway of geostrophic currents along the base of slope. bottom: Plio-Pleistocene scenario. Green arrows indicate channel pathways linked to brine formation and dense shelf water cascades. The Plio-Pleistocene depocenter (units 5 and 6) in the central basin is marked in gray. Abbreviations: GR - Gakkel Ridge; LR - LR; LRP - LR Plateau; MJR - Morris Jessup Rise; NB - Nansen Basin; YP - Yermak Plateau; WAB - western Amundsen Basin

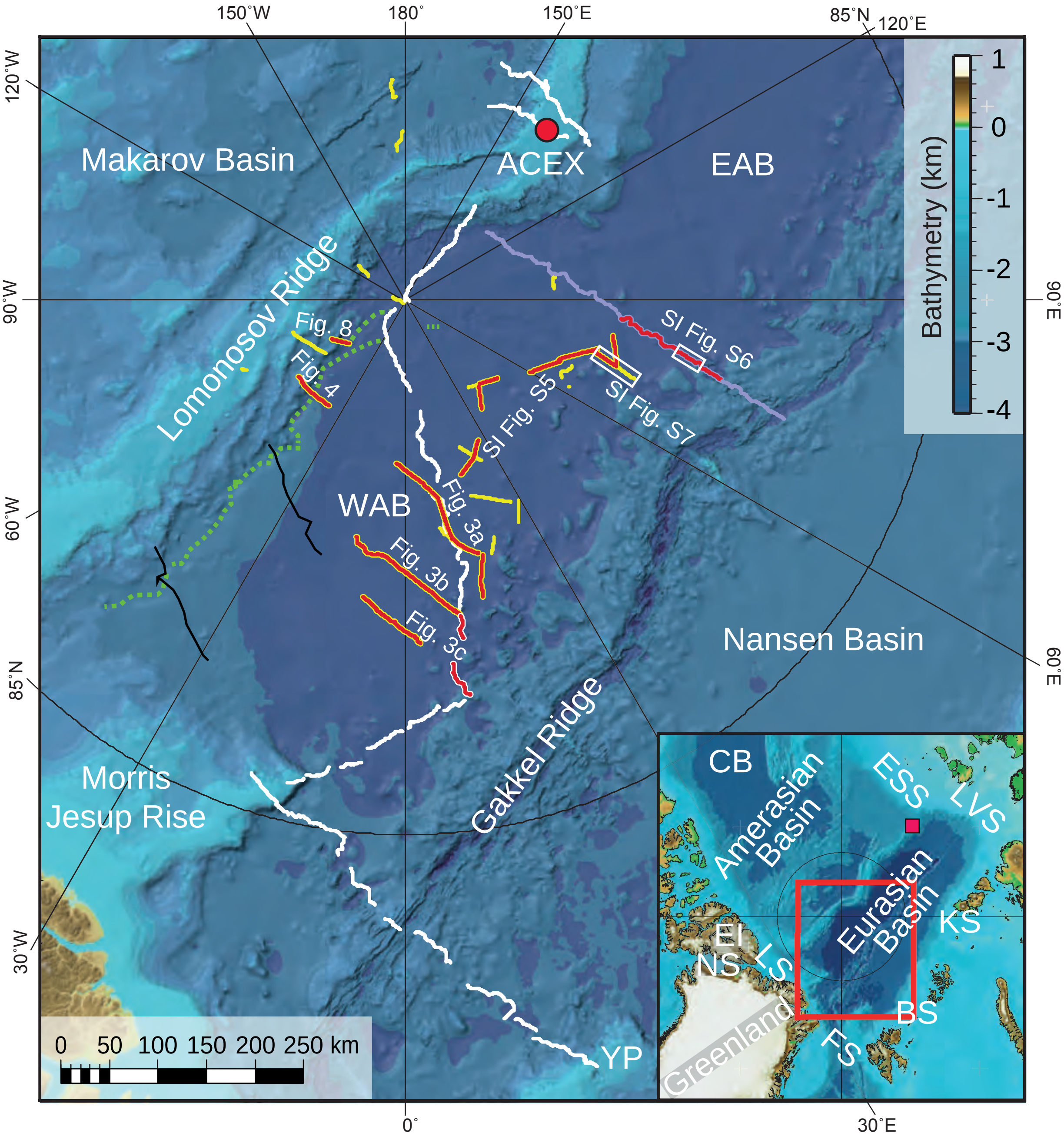

150˚W
180˚
150˚E
85˚N
120˚E
120˚W
90˚W
60˚W
85˚N
30˚W
0˚
30˚E
60˚E
90˚E
Makarov Basin
ACEX
EAB
Lomonosov Ridge
Fig. 8
Fig. 4
SI Fig. S6
SI Fig. S5
SI Fig. S7
WAB
Fig. 3a
Fig. 3b
Fig. 3c
Nansen Basin
Gakkel Ridge
Morris
Jesup Rise
YP
0 50 100 150 200 250 km
Bathymetry (km)
1
0
-1
-2
-3
-4
CB
Amerasian
Basin
ESS
LVS
Eurasian
Basin
KS
EI
NS
LS
BS
FS
Greenland

Fig. 1

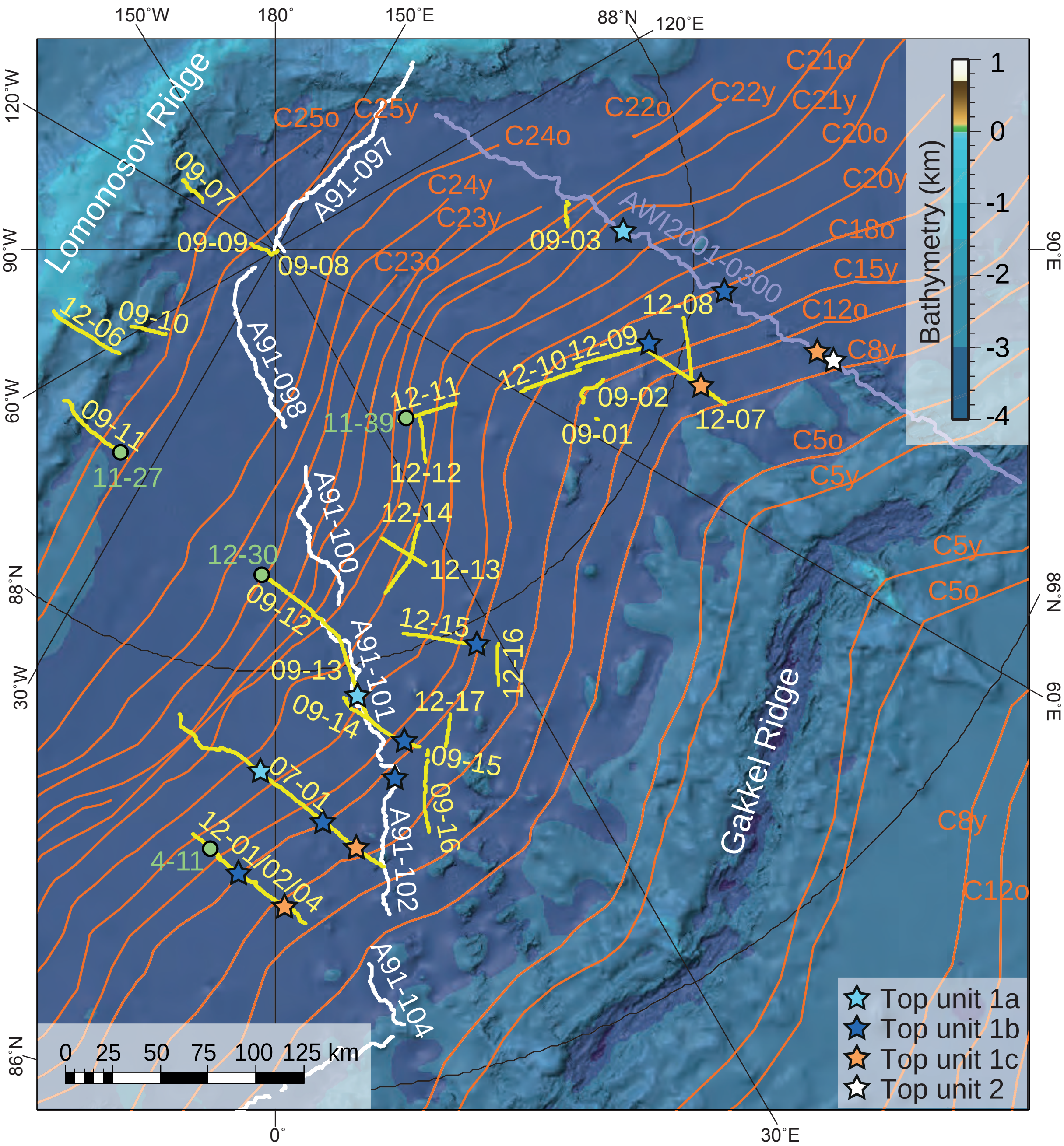

Lomonosov Ridge
Gakkel Ridge
AWI2001-0300
A91-097
A91-098
A91-100
A91-101
A91-102
A91-104
Bathymetry (km)
Top unit 1a
Top unit 1b
Top unit 1c
Top unit 2
0 25 50 75 100 125 km

Fig. 2

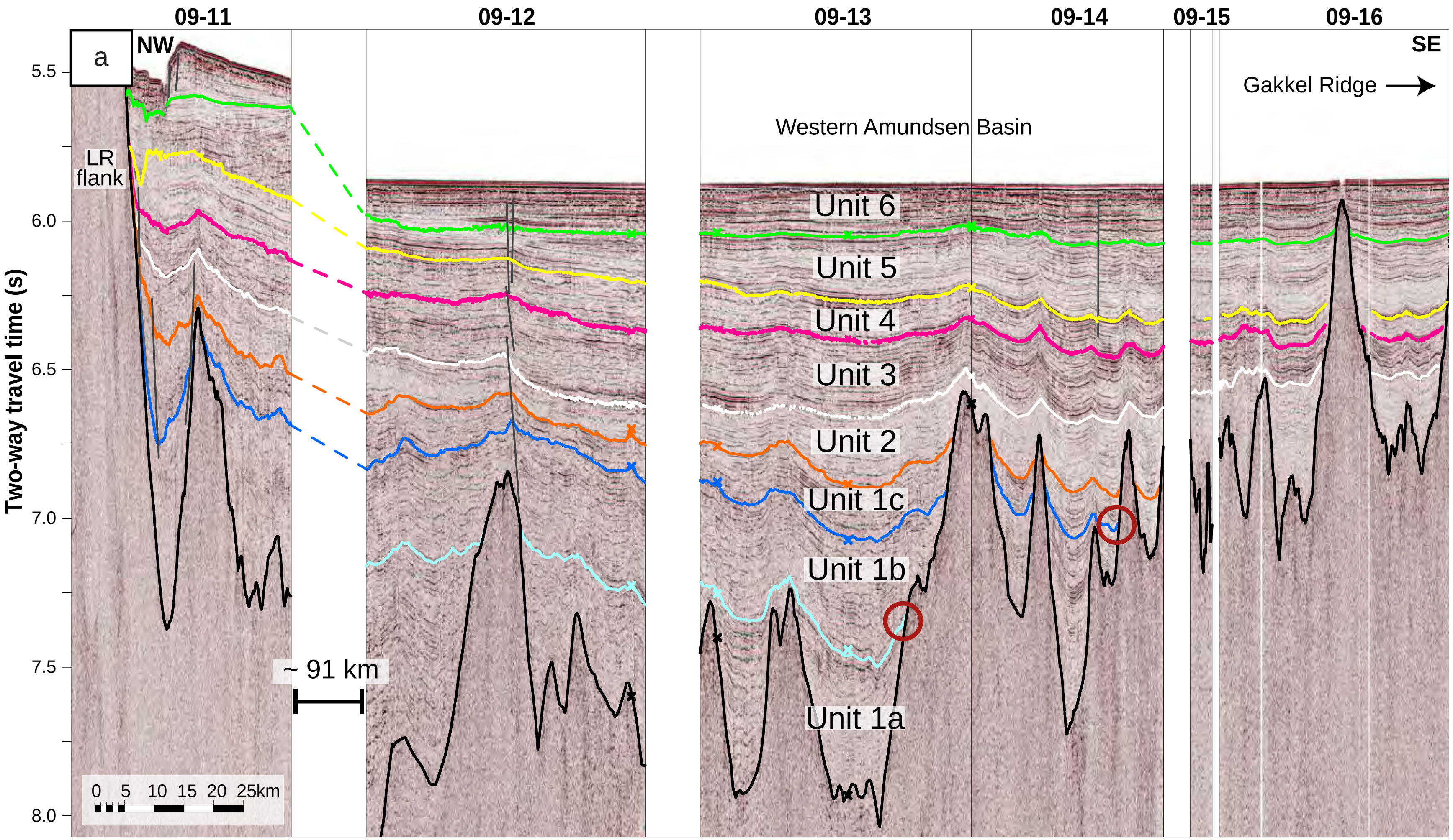
a
NW
SE
09-11
09-12
09-13
09-14
09-15
09-16
Gakkel Ridge
Western Amundsen Basin
LR flank
Two-way travel time (s)
5.5
6.0
6.5
7.0
7.5
8.0
Unit 6
Unit 5
Unit 4
Unit 3
Unit 2
Unit 1c
Unit 1b
Unit 1a
~ 91 km
0 5 10 15 20 25km

Fig. 3a

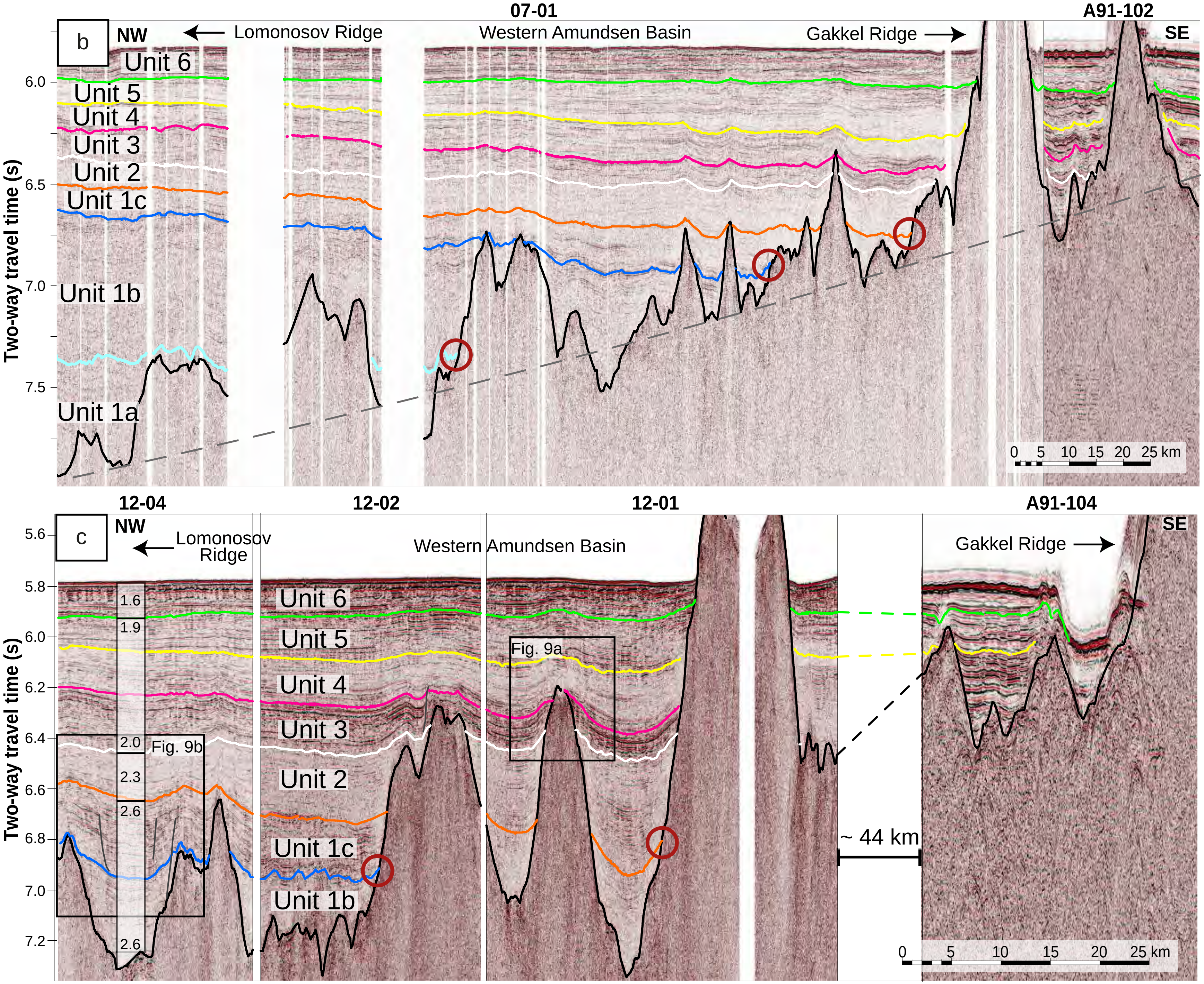

07-01
A91-102
b
NW
Lomonosov Ridge
Western Amundsen Basin
Gakkel Ridge
SE
Unit 6
Unit 5
Unit 4
Unit 3
Unit 2
Unit 1c
Unit 1b
Unit 1a
Two-way travel time (s)
6.0
6.5
7.0
7.5
0 5 10 15 20 25 km
12-04
12-02
12-01
A91-104
c
NW
Lomonosov Ridge
Western Amundsen Basin
Gakkel Ridge
SE
Unit 6
Unit 5
Unit 4
Unit 3
Unit 2
Unit 1c
Unit 1b
Fig. 9a
Fig. 9b
1.6
1.9
2.0
2.3
2.6
2.6
~ 44 km
Two-way travel time (s)
5.6
5.8
6.0
6.2
6.4
6.6
6.8
7.0
7.2
0 5 10 15 20 25 km

Fig. 3bc

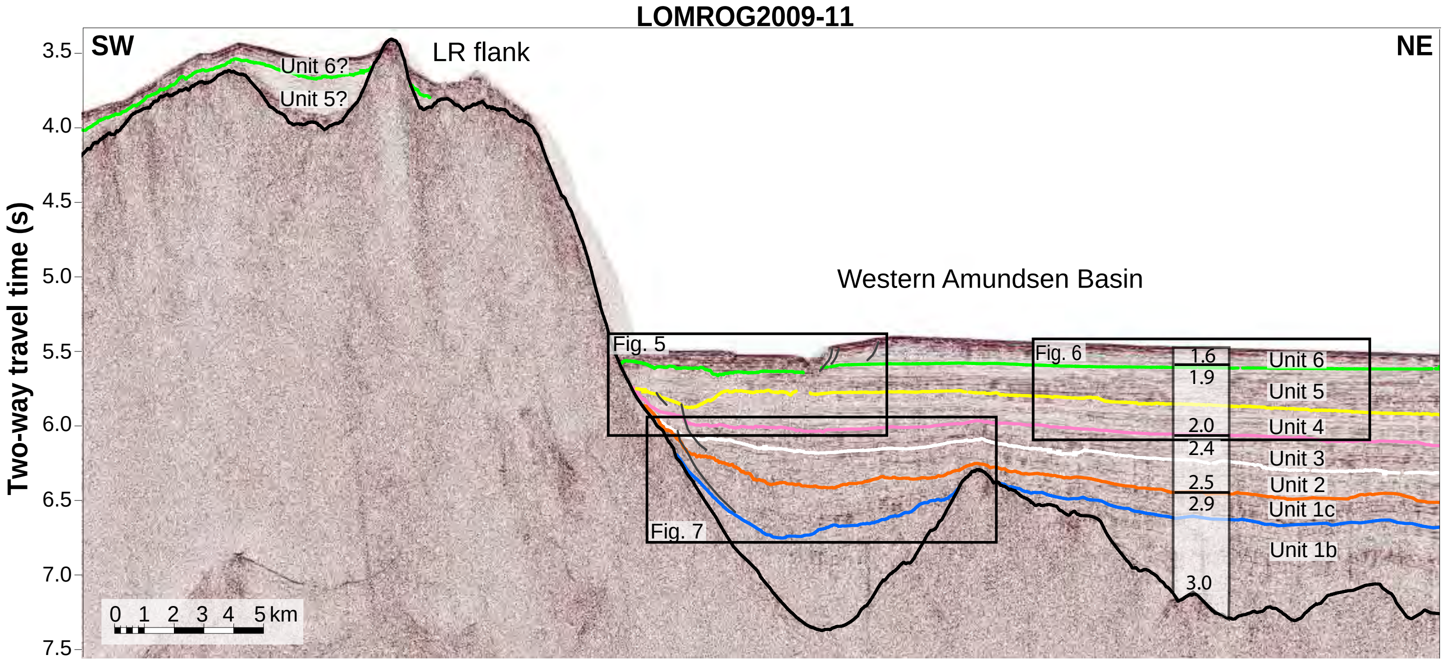

LOMROG2009-11
SW
NE
LR flank
Unit 6?
Unit 5?
Western Amundsen Basin
Two-way travel time (s)
3.5
4.0
4.5
5.0
5.5
6.0
6.5
7.0
7.5
0 1 2 3 4 5 km
Fig. 5
Fig. 6
Fig. 7
1.6
1.9
2.0
2.4
2.5
2.9
3.0
Unit 6
Unit 5
Unit 4
Unit 3
Unit 2
Unit 1c
Unit 1b

Fig. 4

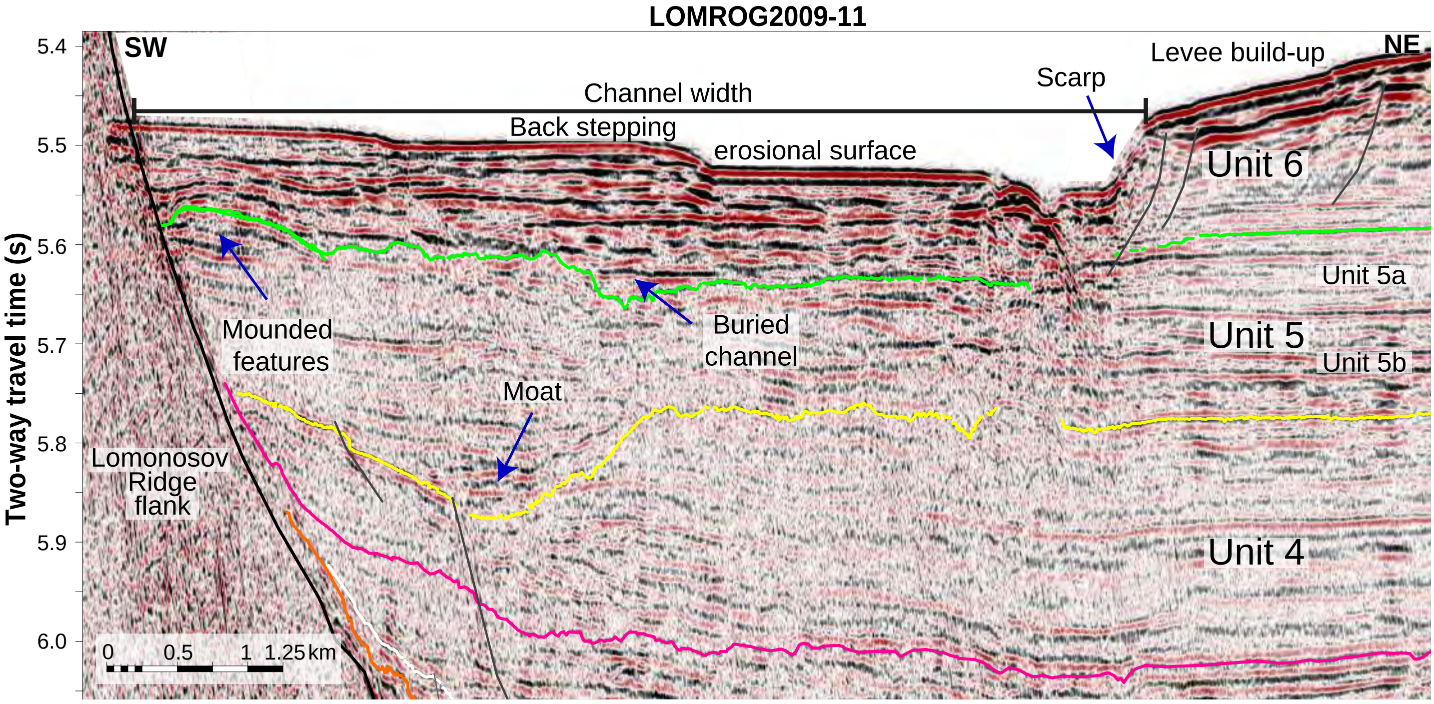
LOMROG2009-11
SW
NE
Channel width
Back stepping
erosional surface
Scarp
Levee build-up
Unit 6
Unit 5a
Unit 5
Unit 5b
Unit 4
Mounded
features
Buried
channel
Moat
Lomonosov
Ridge
flank
Two-way travel time (s)
5.4
5.5
5.6
5.7
5.8
5.9
6.0
0
0.5
1
1.25 km

Fig. 5

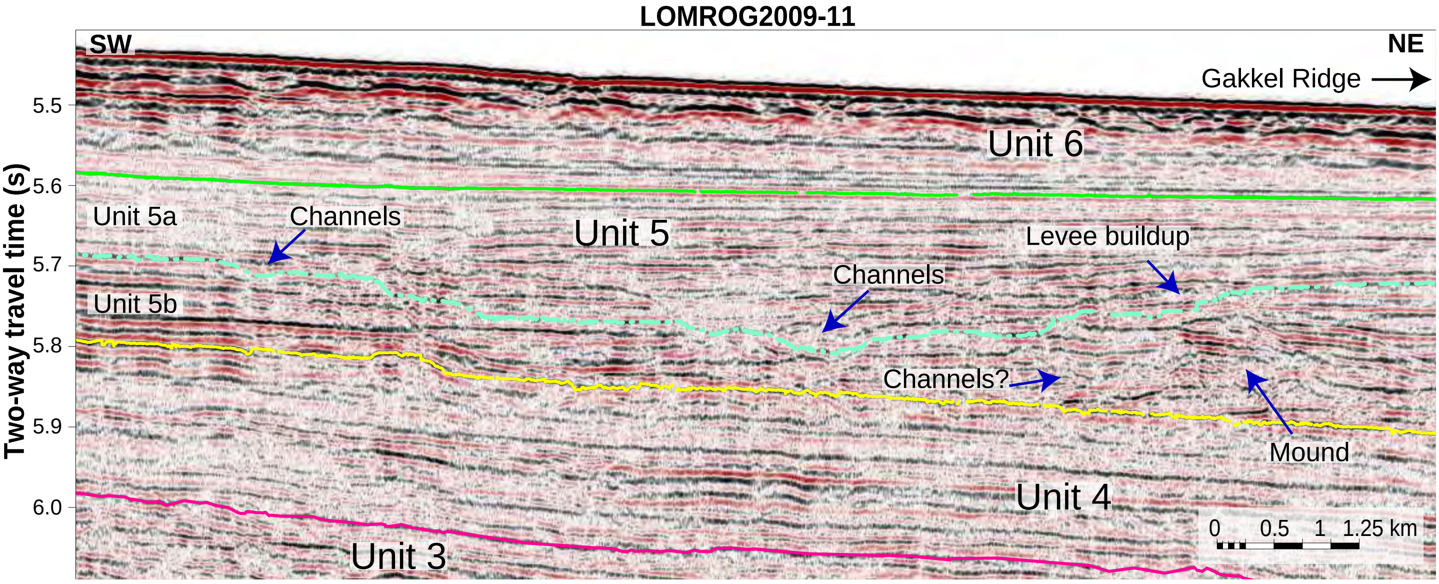
LOMROG2009-11
SW
NE
Gakkel Ridge
Two-way travel time (s)
5.5
5.6
5.7
5.8
5.9
6.0
Unit 6
Unit 5a
Channels
Unit 5
Levee buildup
Channels
Unit 5b
Channels?
Mound
Unit 4
Unit 3
0
0.5
1
1.25 km

Fig. 6

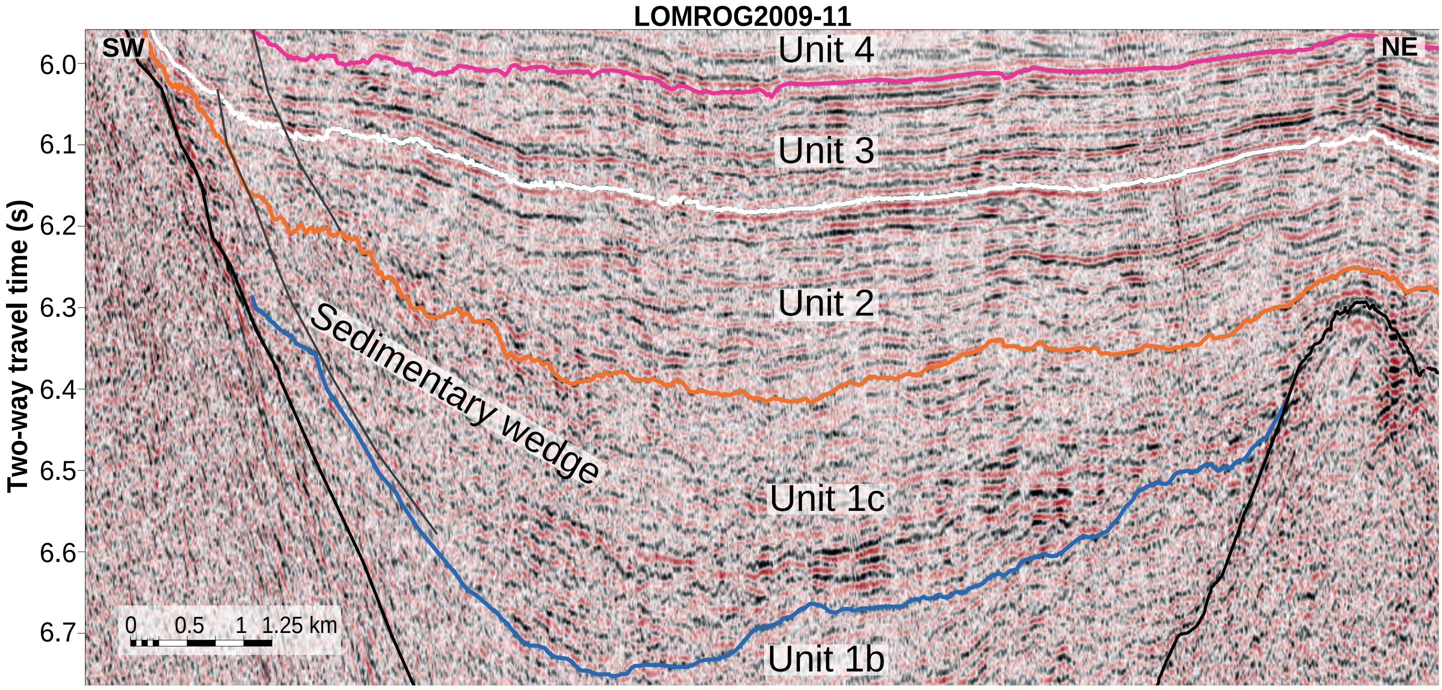

LOMROG2009-11
SW
NE
Unit 4
Unit 3
Unit 2
Sedimentary wedge
Unit 1c
Unit 1b
Two-way travel time (s)
6.0
6.1
6.2
6.3
6.4
6.5
6.6
6.7
0 0.5 1 1.25 km

Fig. 7

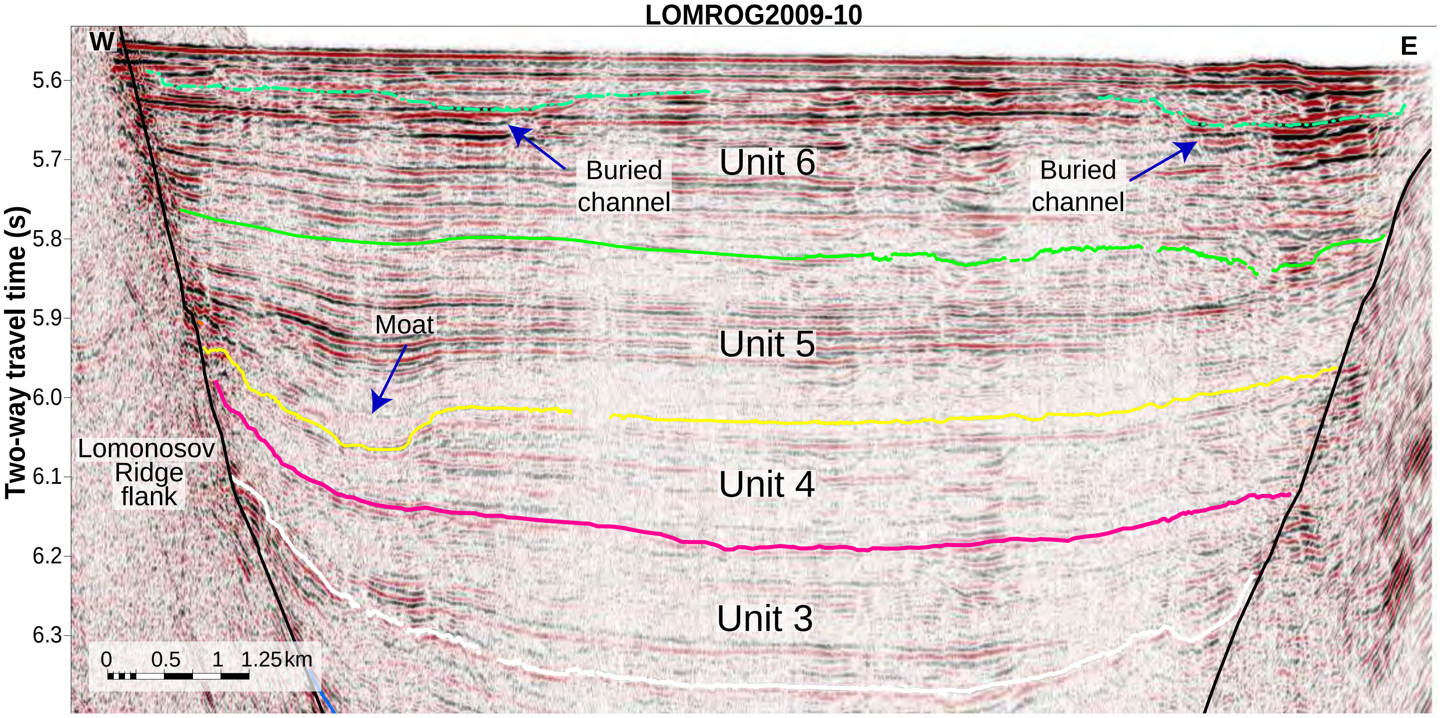

LOMROG2009-10
W
E
Two-way travel time (s)
5.6
5.7
5.8
5.9
6.0
6.1
6.2
6.3
Buried channel
Buried channel
Unit 6
Unit 5
Unit 4
Unit 3
Moat
Lomonosov Ridge flank
0 0.5 1 1.25 km

Fig. 8

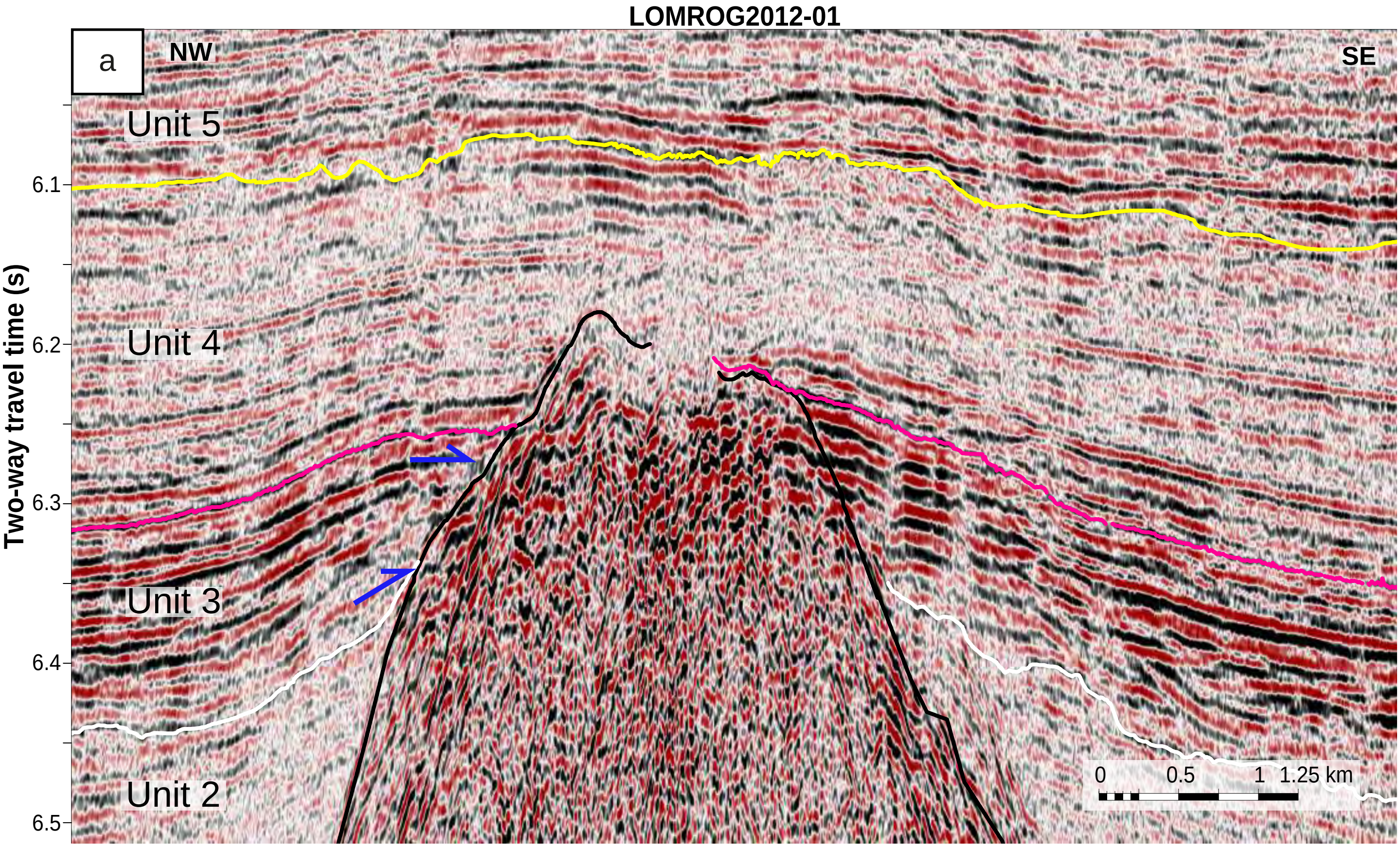
LOMROG2012-01
a
NW
SE
Unit 5
Unit 4
Unit 3
Unit 2
Two-way travel time (s)
6.1
6.2
6.3
6.4
6.5
0
0.5
1
1.25 km

Fig. 9a

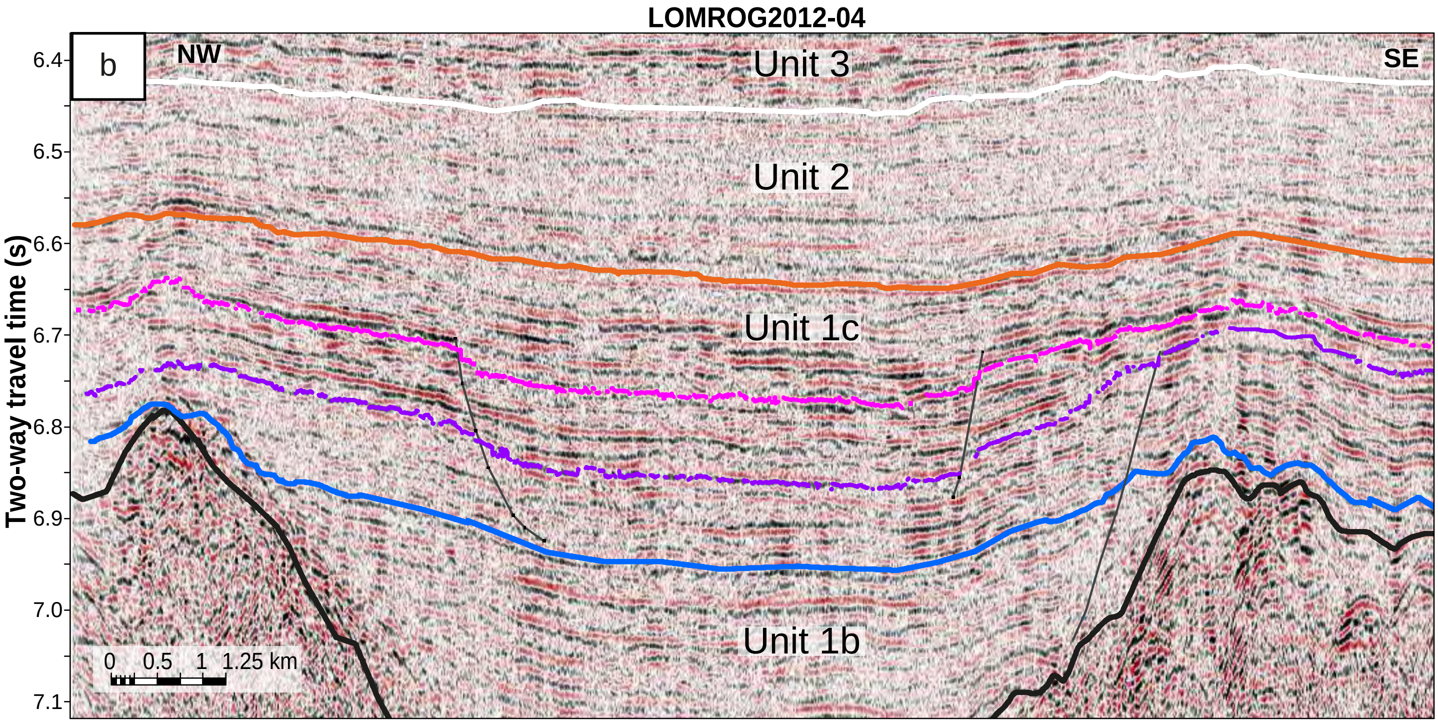
LOMROG2012-04
b
NW
SE
Unit 3
Unit 2
Unit 1c
Unit 1b
Two-way travel time (s)
6.4
6.5
6.6
6.7
6.8
6.9
7.0
7.1
0 0.5 1 1.25 km

Fig. 9b

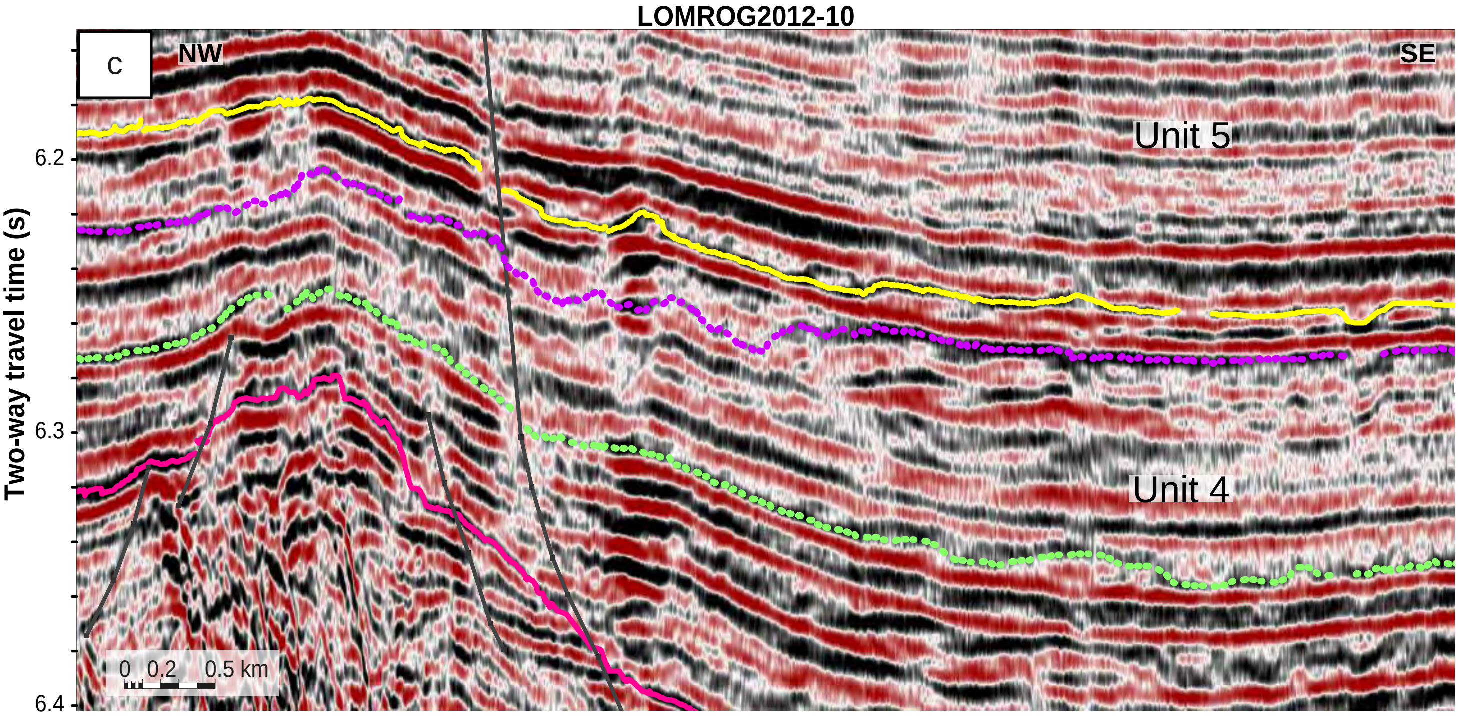
LOMROG2012-10
c
NW
SE
Unit 5
Unit 4
Two-way travel time (s)
6.2
6.3
6.4
0 0.2 0.5 km

Fig. 9c

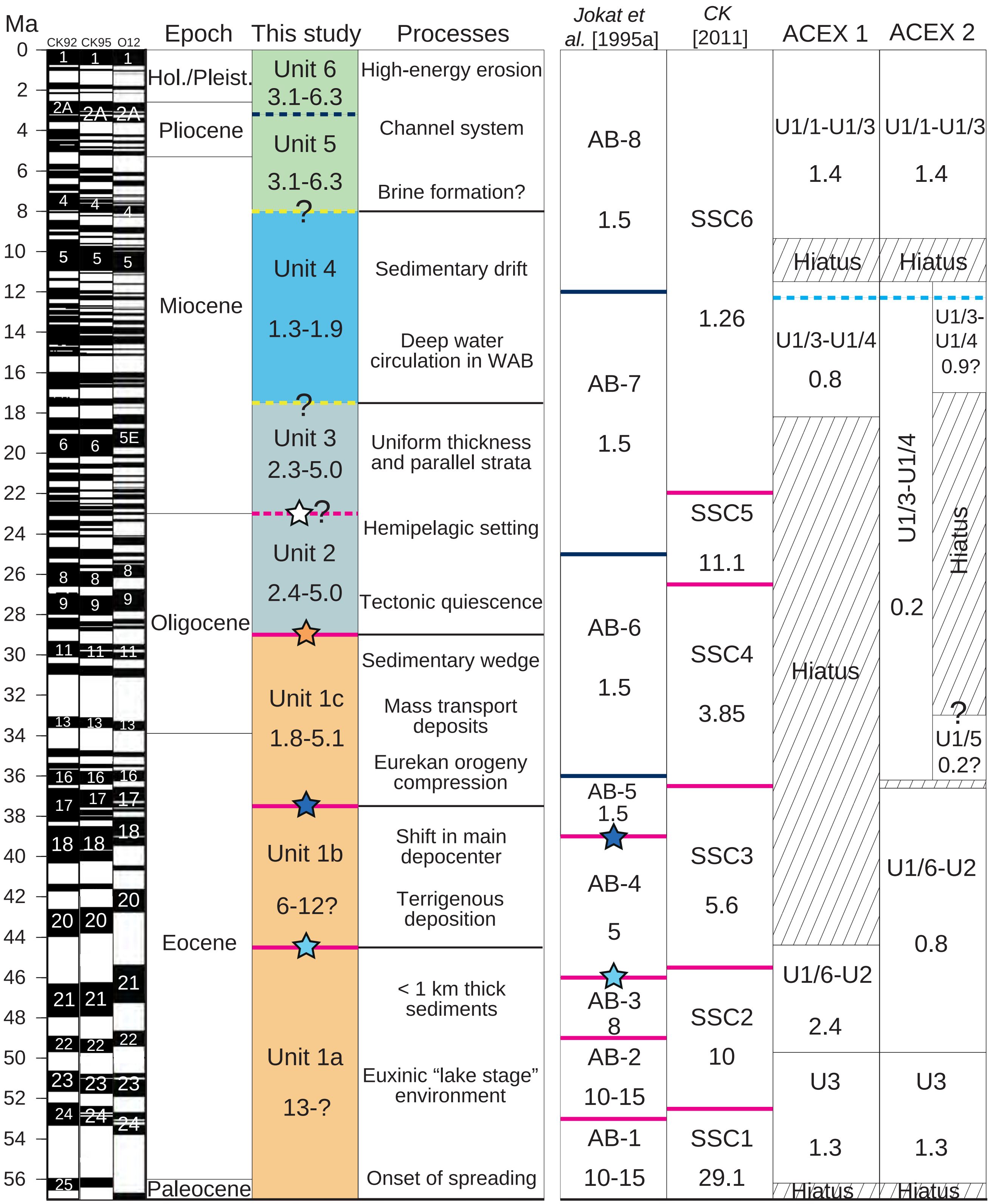

Ma
CK92 CK95 O12
Epoch
This study
Processes
Jokat et al. [1995a]
CK [2011]
ACEX 1
ACEX 2
Hol./Pleist.
Pliocene
Miocene
Oligocene
Eocene
Paleocene
Unit 6
3.1-6.3
Unit 5
3.1-6.3
Unit 4
1.3-1.9
Unit 3
2.3-5.0
Unit 2
2.4-5.0
Unit 1c
1.8-5.1
Unit 1b
6-12?
Unit 1a
13-?
High-energy erosion
Channel system
Brine formation?
Sedimentary drift
Deep water circulation in WAB
Uniform thickness and parallel strata
Hemipelagic setting
Tectonic quiescence
Sedimentary wedge
Mass transport deposits
Eurekan orogeny compression
Shift in main depocenter
Terrigenous deposition
< 1 km thick sediments
Euxinic “lake stage” environment
Onset of spreading
AB-8
1.5
AB-7
1.5
AB-6
1.5
AB-5
1.5
AB-4
5
AB-3
8
AB-2
10-15
AB-1
10-15
SSC6
1.26
SSC5
11.1
SSC4
3.85
SSC3
5.6
SSC2
10
SSC1
29.1
U1/1-U1/3
1.4
Hiatus
U1/3-U1/4
0.8
Hiatus
U1/6-U2
2.4
U3
1.3
Hiatus
U1/1-U1/3
1.4
Hiatus
U1/3-U1/4
0.9?
U1/3-U1/4
0.2
Hiatus
U1/5
0.2?
U1/6-U2
0.8
U3
1.3
Hiatus

Fig. 10

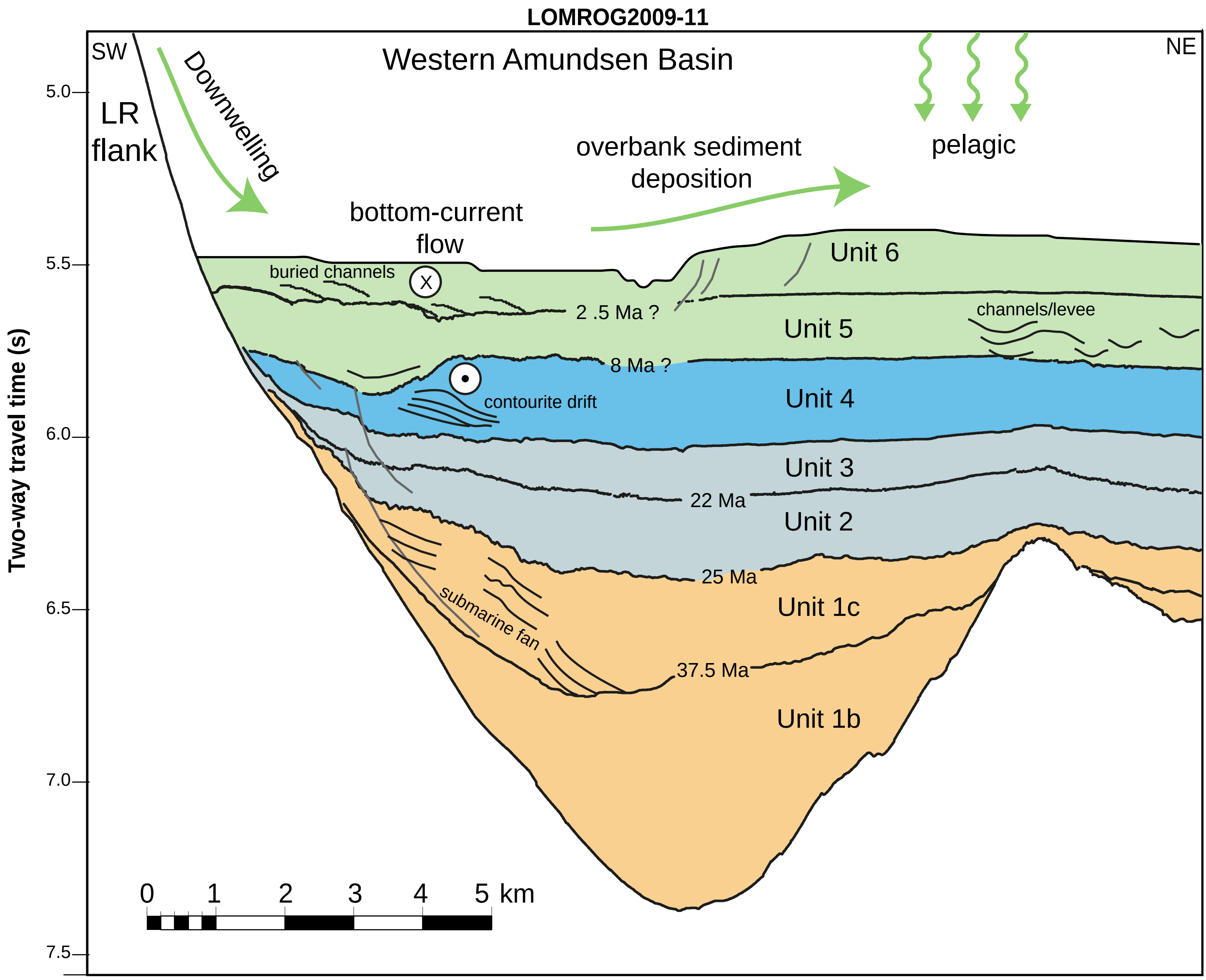
LOMROG2009-11
SW
NE
Western Amundsen Basin
LR
flank
Downwelling
overbank sediment
deposition
pelagic
bottom-current
flow
buried channels
Unit 6
2 .5 Ma ?
Unit 5
channels/levee
8 Ma ?
Unit 4
contourite drift
Unit 3
22 Ma
Unit 2
25 Ma
Unit 1c
submarine fan
37.5 Ma
Unit 1b
0
1
2
3
4
5 km
Two-way travel time (s)
5.0
5.5
6.0
6.5
7.0
7.5

Fig. 11

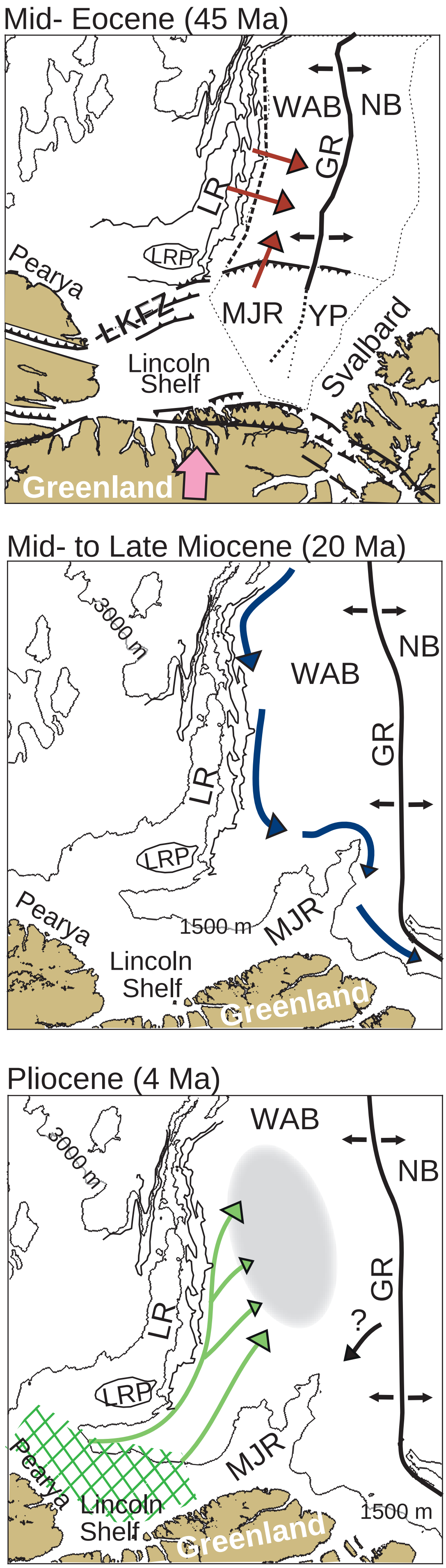
Mid- Eocene (45 Ma)
WAB
NB
GR
LR
LRP
Pearya
KFZ
MJR
YP
Svalbard
Lincoln Shelf
Greenland
Mid- to Late Miocene (20 Ma)
3000 m
NB
WAB
GR
LR
LRP
Pearya
1500 m
MJR
Lincoln Shelf
Greenland
Pliocene (4 Ma)
WAB
3000 m
NB
GR
?
LR
LRP
MJR
Pearya
Lincoln Shelf
1500 m
Greenland

Fig. 12

AGU PUBLICATIONS

Paleoceanography and Paleoclimatology

Supporting Information for

Depositional Evolution of the Amundsen Basin, Arctic Ocean: paleoceanographic and tectonic implications

Carlos F. Castro [1,2*], Paul C. Knutz [1], John R. Hopper [1], and Thomas Funck [1]

[1] Geological Survey of Denmark and Greenland, Øster Voldgade 10, 1350 Copenhagen K, Denmark
[2] Niels Bohr Institute, University of Copenhagen, Copenhagen, Denmark

Contents of this file

Introduction

Text S1 provides additional acquisition and processing details concerning the LOMROG surveys acquired in 2007, 2009, and 2012.

Figures S1 to S4 present the two-dimensional velocity models of four sonobuoys acquired along the seismic lines of two LOMROG expeditions (GEUS-LOMROG2009 and GEUS-LOMROG2012). In addition, the ray coverage for each sonobuoy is shown to illustrate how individual layers in the velocity model are constrained by data. Record sections of the sonobuoys are shown to allow judgement on the data quality and the interpretation of the seismic phases.

The models are divided into as many as eight distinct layers: the water column, up to six sedimentary layers (Sediment 1 through Sediment 6 from top to bottom), and the basement. Seismic phases labelled in the figures are refractions within the sedimentary layers (P_{S1} through P_{S6} from top to bottom), reflections from the base of the six sedimentary layers ($P_{S1}P$ through $P_{S6}P$), and a refraction in the basement (P_g). In addition, all stations recorded a reflection from the seafloor and the direct water wave between the sonobuoys and the shots.

Figure S5 presents a long seismic transect crossing the western Amundsen Basin. The seismic transect zigzags between profiles from LOMROG expeditions 2009 and 2012, and the AMORE 2001 expedition [*Jokat and Micksch*, 2004] (see Figs. 1 and 2 for line positions). The data processing is described in the main text (Ch. 3). For a description of the seismic stratigraphy, see Ch 4.1 of the main text.

Figures S6 and S7 display detailed chronostratigraphic pinchouts of key horizons (see Figs. 1 and 2 for transect positions and ages).

Text S1.

Because the speed of an icebreaker is highly variable and the actual sail line in ice can deviate greatly from the planned sail line, it is difficult to shoot reliably on distance. In 2007, the shot interval was set to 25 m with continual corrections to the sail line, which proved cumbersome. In addition, the variable ship speed led to problems with lost shot-triggers when the gun array was insufficiently pressurized (ship speed too fast), or with compressor shutdowns and restarts when the array became over-pressured (ship speed too slow). Because of the difficulties with shooting on distance, the 2009 survey and 2012 surveys were shot on time. When shooting on time, it is necessary to randomize the actual shot time around the desired time interval to prevent multiple energy from previous shots from stacking coherently. The trigger system software was not programmed to do this and modifications were necessary. These modifications were not complete before the 2009 survey, which was therefore shot on a constant time of 12 s. Because of the relatively small array and deep water of Amundsen Basin, multiples from previous shots proved to be only a minor problem, though some caution should still be exercised in interpreting the 2009 data since weak energy from the second primary multiple could still be present in the stacked sections. In 2012, data were acquired with a randomized time interval of 14 s ± 1s.

The data processing was essentially the same for each survey. With the short streamer, processing options are limited. However, the difficult acquisition environment results in several problems that were addressed in the processing sequence. Three problems in particular compromised the data quality that had to be addressed. The deep towing depth resulted in some problems with the frequency content of the data that was partly addressed with spectral shaping filters. The ice breaking operation itself caused tugging and stress on the streamer, generating strong linear noise that was effectively suppressed with *f-k* filtering. Finally, the tow depth of both the source and receivers was highly inconsistent because of the variable speed and ice breaking operation. Gun and cable statics are essential for the stacking. In some cases, the depth transducers either broke down during acquisition or were not functioning correctly. It was necessary to carefully quality control the depth transducer data and in some cases, manually pick static corrections for each shot and receiver.

The final processing sequence consisted of: bandpass filter; spectral shaping filter; spike and noise burst editing; shot gather *f-k* filter and resample to 2 ms; geometry, including gun and cable statics; trace equalization and trace mixing; midpoint sort and stack. At the typical depth of the Amundsen Basin, the moveout of the seafloor arrival over 300 m is only a few ms, so velocity analysis and moveout correction prior to stack were ignored. The final stacks still had some residual noise burst problems. Therefore, an automatic gain control was applied to reduce their amplitude relative to surrounding energy prior to migration. Partial post-stack migration was done with water velocity, primarily to help suppress diffracted energy from the rough basement topography.

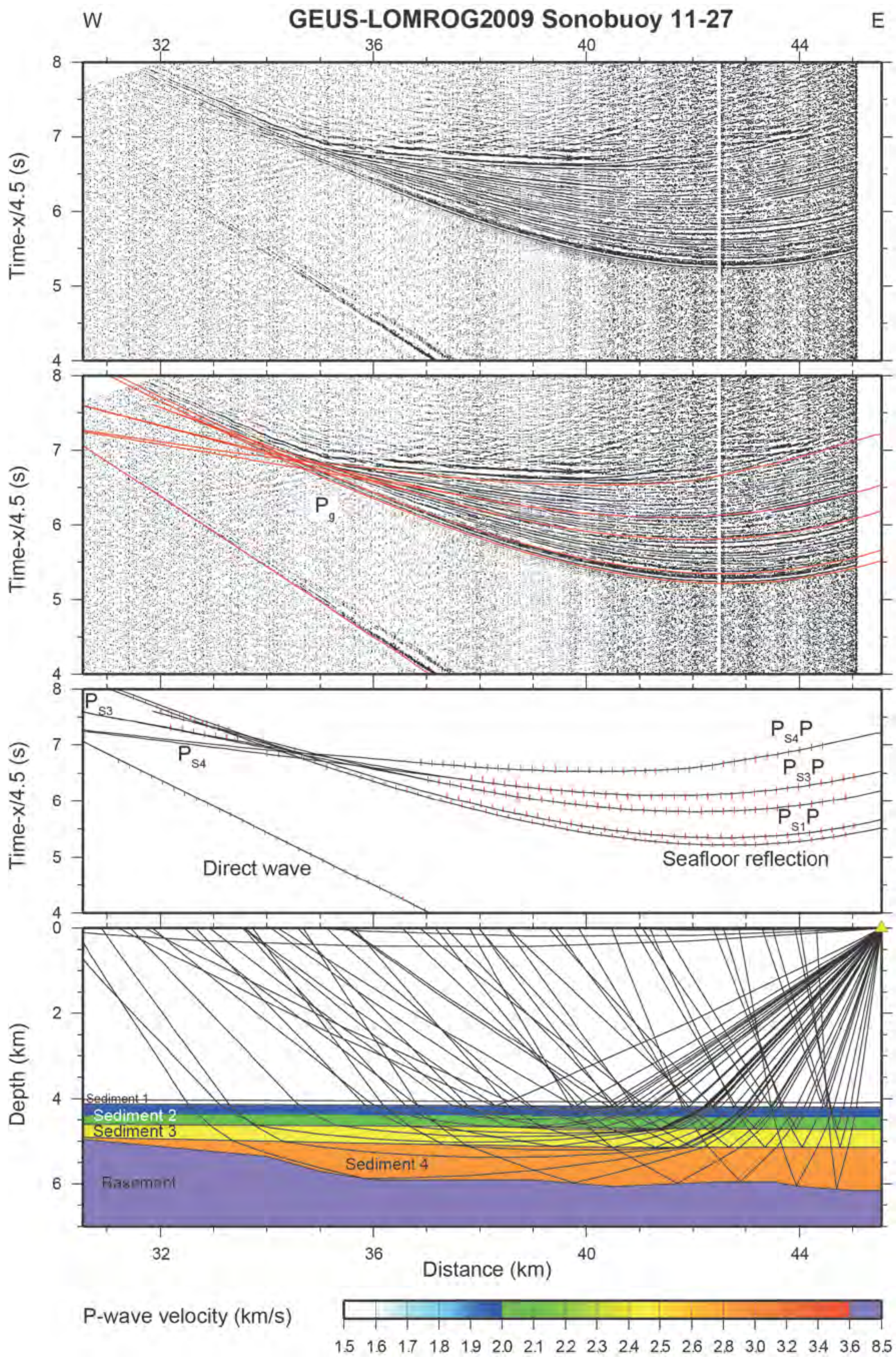

W
GEUS-LOMROG2009 Sonobuoy 11-27
E
Time-x/4.5 (s)
Pg
PS3
PS4
PS4P
PS3P
PS1P
Direct wave
Seafloor reflection
Depth (km)
Sediment 1
Sediment 2
Sediment 3
Sediment 4
Basement
Distance (km)
P-wave velocity (km/s)
1.5 1.6 1.7 1.8 1.9 2.0 2.1 2.2 2.3 2.4 2.5 2.6 2.8 3.0 3.2 3.4 3.6 8.5

Figure S1. Record section and ray tracing for sonobuoy 11-27 on line GEUS-LOMROG2009-11. The upper two panels show the record section with and without the calculated travel times (red lines). The lower two panels show the observed (red vertical bars with heights representing pick uncertainty) and calculated travel times (solid lines) (top), and the ray paths through the velocity model (bottom). The yellow triangle marks the location of the sonobuoy. All travel times are displayed with a reduction velocity of 4.5 km s^{-1}.

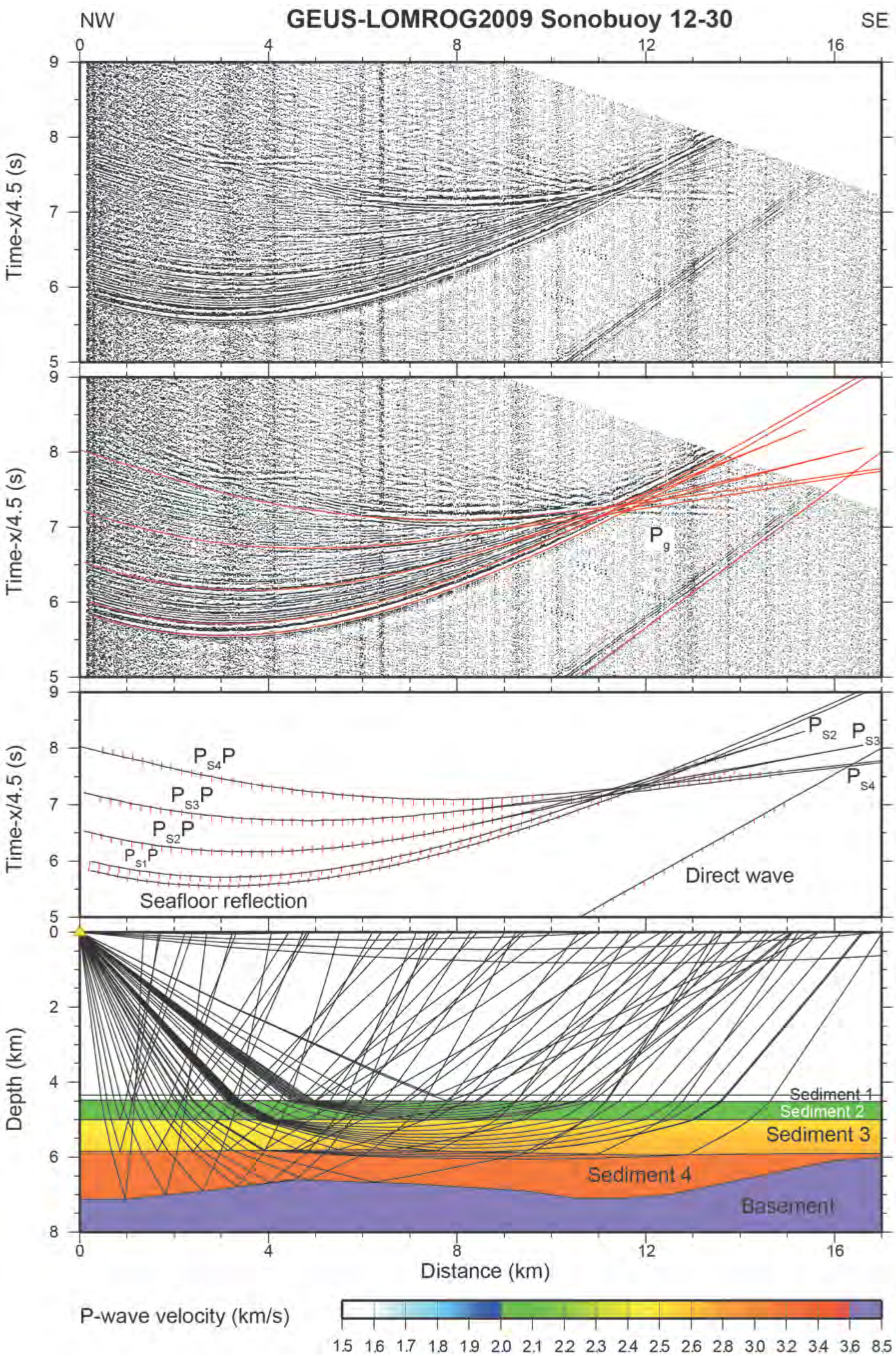
NW
GEUS-LOMROG2009 Sonobuoy 12-30
SE
Time-x/4.5 (s)
Pg
PS4P
PS3P
PS2P
PS1P
Seafloor reflection
Direct wave
PS2
PS3
PS4
Depth (km)
Sediment 1
Sediment 2
Sediment 3
Sediment 4
Basement
Distance (km)
P-wave velocity (km/s)
1.5 1.6 1.7 1.8 1.9 2.0 2.1 2.2 2.3 2.4 2.5 2.6 2.8 3.0 3.2 3.4 3.6 8.5

Figure S2. Record section and ray tracing for sonobuoy 12-30 on line GEUS-LOMROG2009-12. The upper two panels show the record section with and without the calculated travel times (red lines). The lower two panels show the observed (red vertical bars with heights representing pick uncertainty) and calculated travel times (solid lines) (top), and the ray paths through the velocity model (bottom). The yellow triangle marks the location of the sonobuoy. All travel times are displayed with a reduction velocity of 4.5 km s^{-1}.

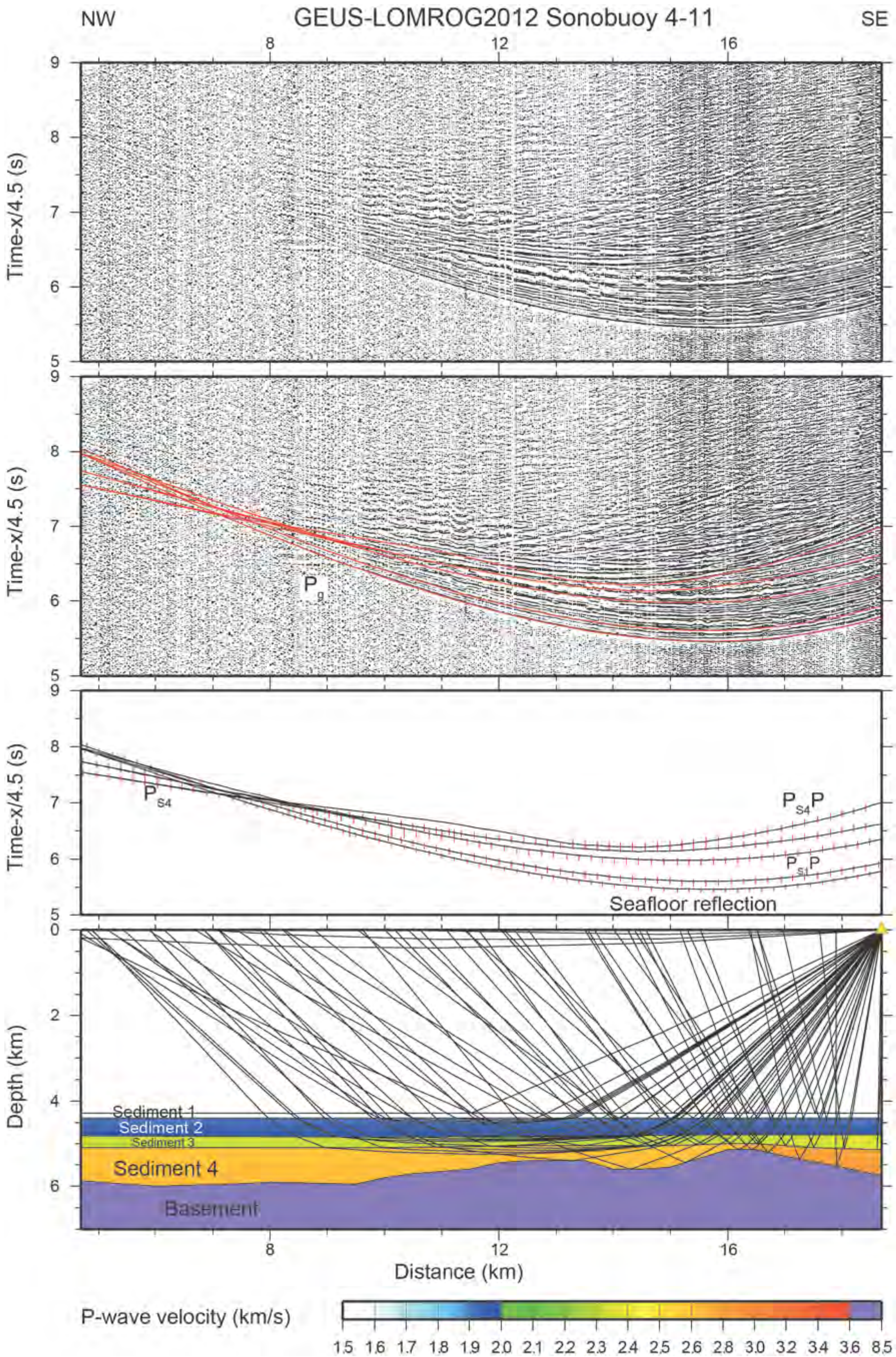

NW
GEUS-LOMROG2012 Sonobuoy 4-11
SE
Time-x/4.5 (s)
Pg
PS4
PS4P
PS1P
Seafloor reflection
Depth (km)
Sediment 1
Sediment 2
Sediment 3
Sediment 4
Basement
Distance (km)
P-wave velocity (km/s)
1.5 1.6 1.7 1.8 1.9 2.0 2.1 2.2 2.3 2.4 2.5 2.6 2.8 3.0 3.2 3.4 3.6 8.5

Figure S3. Record section and ray tracing for sonobuoy 4-11 on line GEUS-LOMROG2012-04. The upper two panels show the record section with and without the calculated travel times (red lines). The lower two panels show the observed (red vertical bars with heights representing pick uncertainty) and calculated travel times (solid lines) (top), and the ray paths through the velocity model (bottom). The yellow triangle marks the location of the sonobuoy. All travel times are displayed with a reduction velocity of 4.5 km s^{-1}.

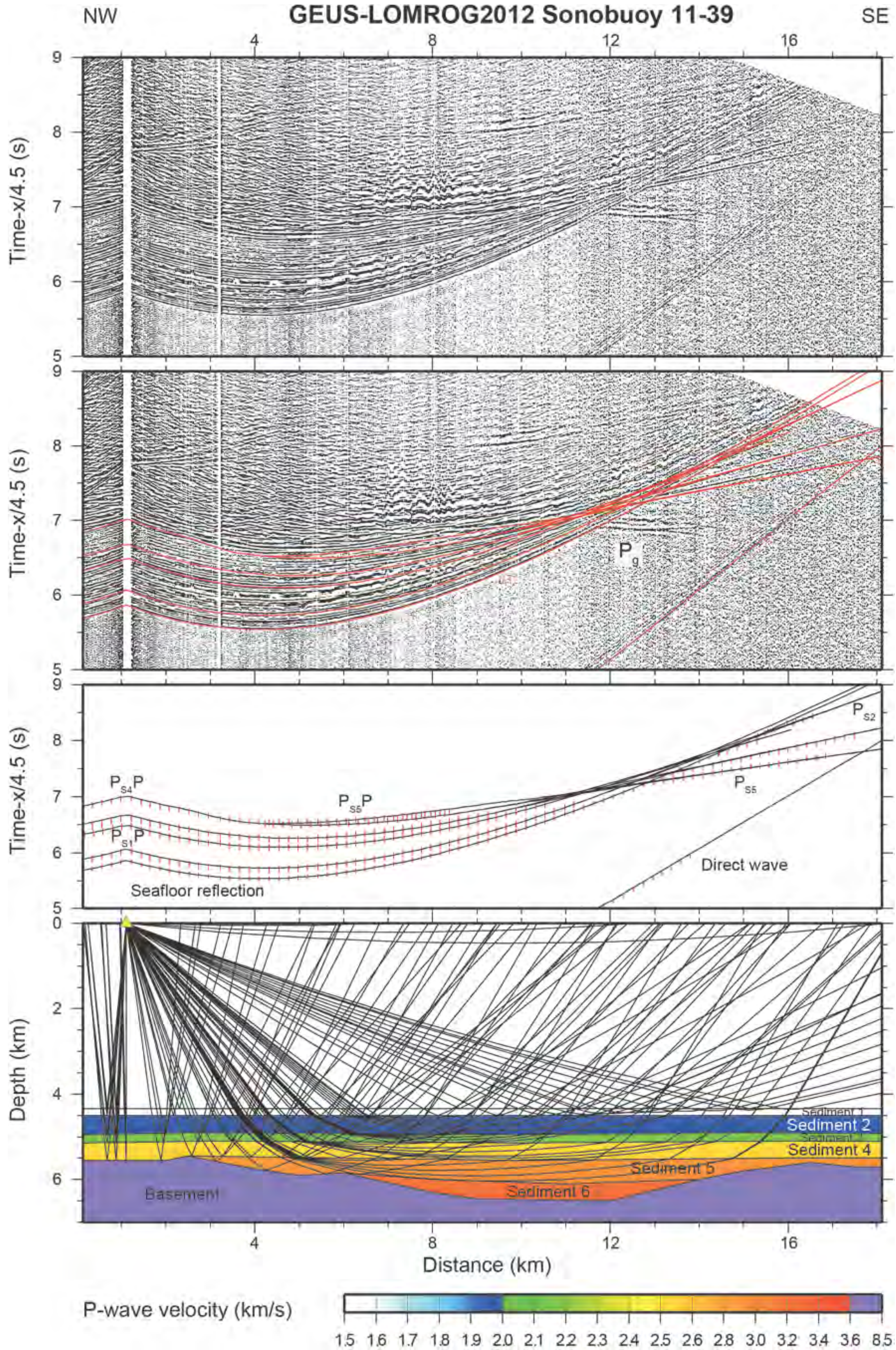

NW
GEUS-LOMROG2012 Sonobuoy 11-39
SE
Time-x/4.5 (s)
Pg
PS4P
PS5P
PS1P
PS2
PS5
Direct wave
Seafloor reflection
Depth (km)
Sediment 1
Sediment 2
Sediment 3
Sediment 4
Sediment 5
Sediment 6
Basement
Distance (km)
P-wave velocity (km/s)

Figure S4. Record section and ray tracing for sonobuoy 11-39 on line GEUS-LOMROG2012-11. The upper two panels show the record section with and without the calculated travel times (red lines). The lower two panels show the observed (red vertical bars with heights representing pick uncertainty) and calculated travel times (solid lines) (top), and the ray paths through the velocity model (bottom). The yellow triangle marks the location of the sonobuoy. All travel times are displayed with a reduction velocity of 4.5 km s^{-1}.

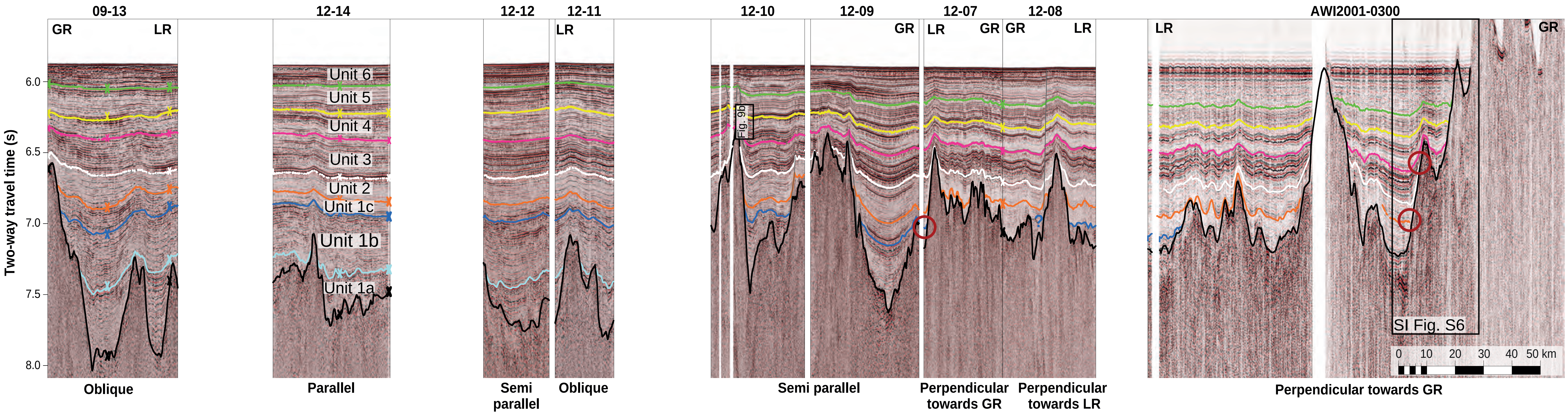

09-13
12-14
12-12
12-11
12-10
12-09
12-07
12-08
AWI2001-0300
GR
LR
Two-way travel time (s)
6.0
6.5
7.0
7.5
8.0
Unit 6
Unit 5
Unit 4
Unit 3
Unit 2
Unit 1c
Unit 1b
Unit 1a
Fig. 9b
SI Fig. S6
0 10 20 30 40 50 km
Oblique
Parallel
Semi parallel
Oblique
Semi parallel
Perpendicular towards GR
Perpendicular towards LR
Perpendicular towards GR

Figure S5. Seismic transect zigzagging the western Amundsen Basin with line names shown along the top axis (see Fig. 1 and 2 for line positions). Line flows relative to the magnetic isochrons are displayed along the bottom axis. Key seismic horizons interpreted: oceanic basement – black; top subunit 1a – light blue; top subunit 1b – dark blue; top subunit 1c – orange; top unit 2 – white; top unit 3 – red; top unit 4 – yellow; top unit 5 – green; top unit 6 – seabed.

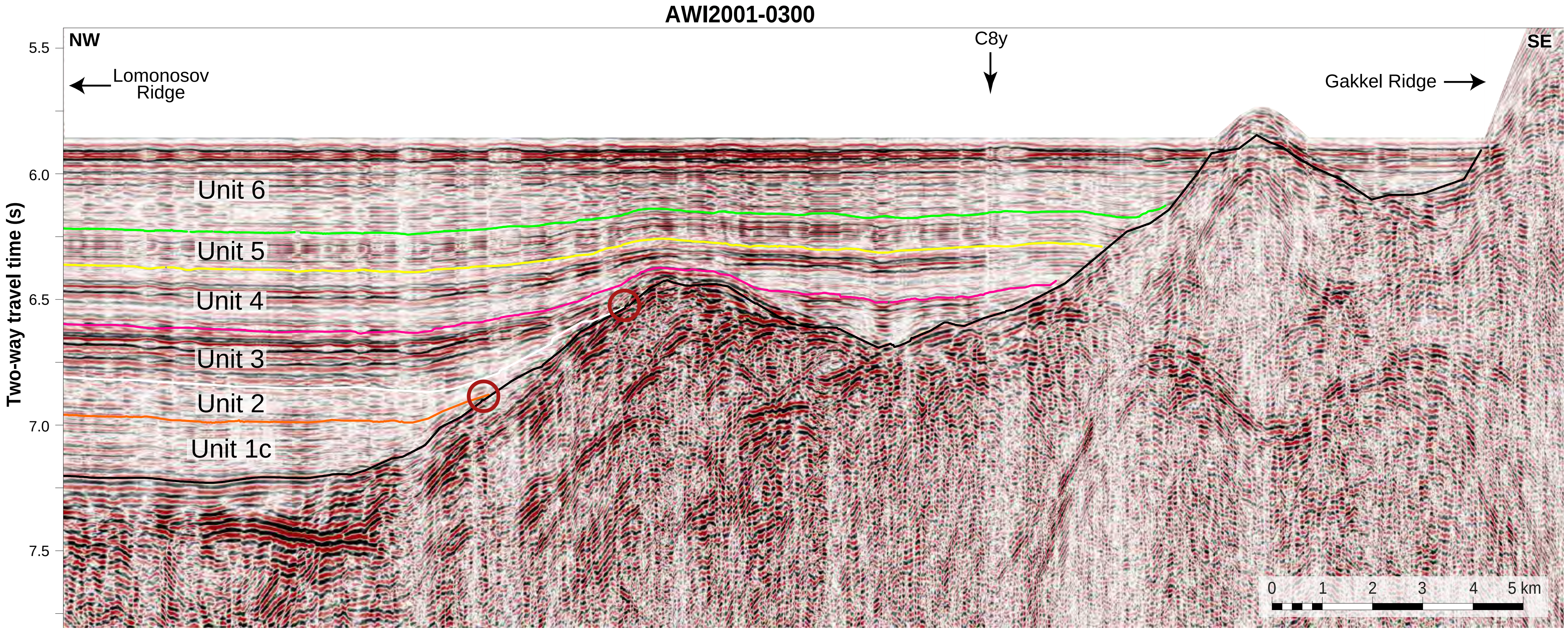
AWI2001-0300
NW
SE
C8y
Lomonosov Ridge
Gakkel Ridge
Two-way travel time (s)
5.5
6.0
6.5
7.0
7.5
Unit 6
Unit 5
Unit 4
Unit 3
Unit 2
Unit 1c
0
1
2
3
4
5 km

Figure S6. Detail from Figure S5 showing the chronostratigraphic pinchouts for subunit 1c and unit 2. The pinchout for unit 2 cannot be traced any further along the profile due to the shallow regional bathymetry beyond C8y. Red circles: positions where the horizons onlap the oceanic basement (see Fig. 2).

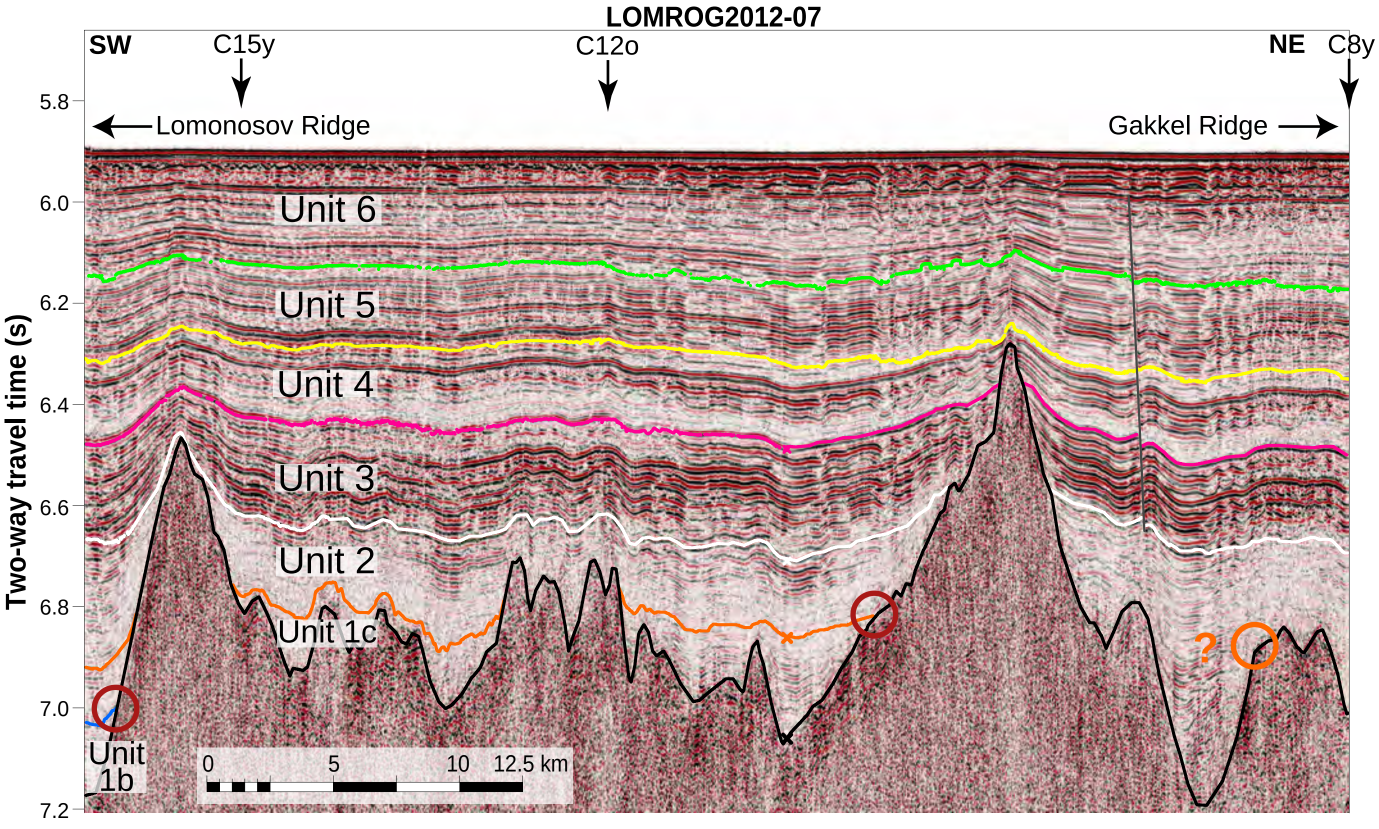

LOMROG2012-07
SW
C15y
C12o
NE
C8y
Lomonosov Ridge
Gakkel Ridge
Two-way travel time (s)
5.8
6.0
6.2
6.4
6.6
6.8
7.0
7.2
Unit 6
Unit 5
Unit 4
Unit 3
Unit 2
Unit 1c
Unit 1b
?
0
5
10
12.5 km

Figure S7. Seismic profile GEUS-LOMROG2012-07 crossing the western Amundsen Basin between Chrons C18o and C8y (see Fig. 1 and 2 for line position). The large thickness observed in unit 2 at C8y suggests that the true chronostratigraphic pinchout for unit 2 lies beyond magnetic isochron C8y. Horizon colors same as in Figure S5. Red circles: positions where the horizons onlap the oceanic basement (see Fig. 2).

Chapter IV

Future Studies

In standard marine survey operations in open water, seismic refraction data are typically recorded by deploying ocean bottom seismometers (OBS) at the seafloor. A seismic source – usually an air gun towed behind the acquisition vessel – is used to generate sound waves propagating through the upper 10-50 km of the Earth's strata. Once the shooting is complete, the anchor from the OBS is released and the OBS is able to rise to the surface for recovery. In areas with permanent sea ice cover, however, this method is not possible since the rising instruments risk being trapped beneath the ice [*Riddell-Dixon*, 2017]. Instead, floating expendable sonobuoys are deployed to record the seismic signals. Sonobuoys, however, have significant setbacks. As opposed to an OBS, sonobuoys are free to drift in the prevailing ocean currents, record smaller ranges, and have decreased signal-to-noise ratios [*Bruguier and Minshull*, 1996]. In addition, their exact position is unknown unless they are equipped with a navigation device (e.g., GPS).

In recent decades, the increasing melting of the polar ice sheets has contributed to a significant change in global sea levels and oceanic conditions [*Shepherd et al*., 2012]. The increasing accessibility to the Arctic waters would thus enable seismic investigations to deploy instrumentation according to modern standards. This accessibility would also extend to seismic reflection data acquisitions, where hydrophone streamers are kept short in ice-covered waters in order to reduce risk of damage and permit a rapid deployment and recovery.

For the P-wave velocity models in this study (Chapter II), refraction/wide-angle reflection seismic data, multichannel seismic data, gravity data, and other geophysical information were used to constrain the models as best as possible; however, more parameters could have been included:

1) Incorporating S-waves would allow us to calculate Poisson's ratio to further constrain crustal compositions. P-wave velocities and Poisson's ratios may be compared for a range of various crustal rock types [e.g., *Hyndman,* 1979; *Holbrook et al*., 1992] and improve the interpretation of the basement layer in some segments of the Amundsen Basin. Given that the seismic data show some evidence for S-waves (e.g., sonobuoy 60, see Appendix), it is therefore suggested to explore this possibility.
2) Synthetic seismograms enable us to theoretically calculate traveltimes and amplitudes of the wave propagation through the velocity model. From this information seismogram modelling can be used to mimic refraction effects on wide-angle seismic attributes [*Nowack and Stacky*, 2002], compare them with the record section, and make improvements to the model. This is particularly helpful for constraining velocity gradients since the synthetic seismograms will show how far the seismic energy travelled and would therefore help us minimize some of this uncertainty.

As part of the objectives during the LOMROG expeditions, the seismic refraction and reflection data were collected in areas with a predicted thick sedimentary cover. This was done by acquiring the data along pronounced gravity lows in the Amundsen Basin (Chapter II, Fig. 7). Assuming isostatic compensation throughout the crust, the acquired refraction profiles are expected to display thinner crust when compared to areas marked by gravity highs. Future studies could therefore focus on seismic transects crossing both gravity highs and lows to 1) check whether the gravity highs are associated with possible seamounts or crust underlain by serpentinized mantle; and 2) 3) to obtain a more complete overview of the variations within the crust over time and space.

The presence of an oceanic layer 2 and 3 along transect 1 is different than previous observations along the Gakkel Ridge where only an oceanic layer 2 is recognized. This suggests that there is a spatial and temporal variation in crustal accretion process at the ridge. In order to check this, however, transect 1 should ideally be extended towards the Nansne Basin, crossing the Sparsely Magmatic Zone within the Amundsen Basin and the Nansen Basin, and ending in older crust at the Nansen Basin.

Transect 1 is also located close to one of the many prominent basement ridges that extend perpendicularly from the axis of the Gakkel Ridge (Chapter III, Fig. 2). The ridges are distinct from one another and have been suggested to be associated primarily to either a tectonic origin [*Michael et al*., 2003; *Cochran et al*., 2003], a volcanic one, or a combination of both [*Schmidt-Aursch and Jokat*, 2016]. Unfortunately, limited velocity information is available for these ridges. A refraction profile parallel to the spreading axis and crossing these ridges could thus provide some further velocity constraints and hopefully more information regarding their crustal character and origin.

For the stratigraphic model (Chapter III), the approach to use the age horizons according to pinch out patterns along crust that is known to have significant relief comes with uncertainties that need to be considered (see Chapter III, 4.2). Ideally, drilling and coring would allow proper dating of the key horizons, but this is difficult and expensive in the Arctic. The model derived here will certainly need revision if we are ever able to recover cores from the Amundsen Basin. However, a pre-condition for justifying drilling is to do the best possible interpretation of the available data so that testable hypotheses can be put forward, as we have done here. In the absence of good stratigraphic coverage and deep borehole data, correlation to magnetic anomalies remains the only, and widely used, method for estimating ages of sedimentary successions in the Eurasia Basin (e.g., *Jokat et al*. [1995a] and *Chernykh and Kyrlov* [2011] for the Amundsen Basin; *Engen et al*. [2009] for the Nansen Basin).

Profile 09-11 located next to the Lomonosov Ridge flank (Chapter III, Fig. 2) suggests that the enhanced accumulation of unit 4 along the base of the Lomonosov Ridge is related to the onset of oceanographic bottom-currents that likely formed in response to the opening of the

Fram Strait. The lack of any robust dating, however, adds uncertainty to the onset of geostrophic flow responsible for focused sedimentation along the Lomonosov Ridge. Ideally, drilling along profile 09-11 could provide some ground truth to this hypothesis. Alternatively, the results presented for the stratigraphic model also allow the possibility to contemplate processes that have been important for sedimentary delivery but have never been considered before. In particular, the observed Plio-Pleistocene cascading plumes, possibly from brine formation, imply that alternate channels and/or gullies close to the shelf area north of Greenland could have influenced deep circulation in the western Amundsen Basin. Since the data coverage is limited in this region as evidenced by the sparse mapping and available crossings from the Lomonosov Ridge, more investigations are needed to verify this hypothesis and further constrain the Cenozoic history of the Amundsen Basin. Our interpretations in our stratigraphic model should therefore serve as a useful tool for testable hypotheses in the future.

References

Backman, J., M. Jakobsson, R. Løvlie, L. Polyak, and L. A. Febo (2004), Is the central Arctic Ocean a sediment starved basin?, Quaternary Science Reviews, 23(11–13), 1435-1454, doi: 10.1016/j.quascirev.2003.12.005s.

Backman, J., Moran, K., McInroy, D., and the IODP Expedition 302 Scientists (2005), IODP Expedition 302, Arctic Coring Expedition (ACEX): A First Look at the Cenozoic Paleoceanography of the Central Arctic Ocean, *Sci. Dril*., 1, 12-17, doi:10.2204/iodp.sd.1.02.2005.

Bruguier, N. J., and T. A. Minshull (1997), Accurate Modelling of Sonobuoy Refraction Data to Determine Velocity Variations in Oceanic Crust, *Marine Geophysical Researches*, *19*(1), 25-36, doi: 10.1023/a:1004249108479s.

Brozena, J. M., V. A. Childers, L. A. Lawver, L. M. Gahagan, R. Forsberg, J. I. Faleide, and O. Eldholm (2003), New aerogeophysical study of the Eurasia Basin and Lomonosov Ridge: Implications for basin development, Geology, 31(9), 825-828, doi: 10.1130/g19528.1s.

Brumley, K., E. L. Miller, A. Konstantinou, M. Grove, K. E. Meisling, and L. A. Mayer (2015), First bedrock samples dredged from submarine outcrops in the Chukchi Borderland, Arctic Ocean, Geosphere, 11(1), 76-92, doi: 10.1130/GES01044.1s.

Chernykh, A. A., and A. A. Krylov (2011), Sedimentogenesis in the Amundsen Basin from geophysical data and drilling results on the Lomonosov Ridge, Doklady Earth Sciences, 440(2), 1372-1376, doi: 10.1134/s1028334x11100011s.

Cochran, J. R., G. J. Kurras, M. H. Edwards, and B. J. Coakley (2003), The Gakkel Ridge: Bathymetry, gravity anomalies, and crustal accretion at extremely slow spreading rates, *Journal of Geophysical Research: Solid Earth*, *108*(B2), doi: doi:10.1029/2002JB001830s.

DeMets, C., R. G. Gordon, D. F. Argus, and S. Stein (1994), Effect of recent revisions to the geomagnetic reversal time scale on estimates of current plate motions, Geophysical Research Letters, 21(20), 2191-2194, doi: 10.1029/94GL02118s.

Dick, H. J. B., J. Lin, and H. Schouten (2003), An ultraslow-spreading class of ocean ridge, Nature, 426(6965), 405-412.

Døssing, A., J. R. Hopper, A. V. Olesen, T. M. Rasmussen, and J. Halpenny (2013), New aero-gravity results from the Arctic: Linking the latest Cretaceous-early Cenozoic plate kinematics of the North Atlantic and Arctic Ocean, Geochemistry, Geophysics, Geosystems, 14(10), 4044-4065, doi: 10.1002/ggge.20253s.

Døssing, A., T. M. Hansen, A. V. Olesen, J. R. Hopper, and T. Funck (2014), Gravity inversion predicts the nature of the Amundsen Basin and its continental borderlands near Greenland, Earth and Planetary Science Letters, 408(0), 132-145, doi: 10.1016/j.epsl.2014.10.011s.

Ehlers, B.-M., and W. Jokat (2009), Subsidence and crustal roughness of ultra-slow spreading ridges in the northern North Atlantic and the Arctic Ocean, Geophysical Journal International, 177(2), 451-462, doi: 10.1111/j.1365-246X.2009.04078.xs.

Engen, Ø., J. A. Gjengedal, J. I. Faleide, Y. Kristoffersen, and O. Eldholm (2009), Seismic stratigraphy and sediment thickness of the Nansen Basin, Arctic Ocean, Geophysical Journal International, 176(3), 805-821, doi: 10.1111/j.1365-246X.2008.04028.xs.

Hirth, G., and S. Guillot (2013), Rheology and Tectonic Significance of Serpentinite, Elements, 9(2), 107-113, doi: 10.2113/gselements.9.2.107s.

Holbrook, W. S., W. D. Mooney, and N. I. Christensen (1992), The seismic velocity structure of the deep continental crust, 43.

Hyndman, R. D. (1979), Poisson's Ratio in the Oceanic Crust – a Review, in Developments in Geotectonics, edited by C. E. Keen, pp. 321-333, Elsevier.
Jakobsson, M., et al. (2007), The early Miocene onset of a ventilated circulation regime in the Arctic Ocean, Nature, 447(7147), 986-990, doi: 10.1038/nature05924s.
Jokat, W., and U. Micksch (2004), Sedimentary structure of the Nansen and Amundsen basins, Arctic Ocean, Geophysical Research Letters, 31(2), L02603, doi: 10.1029/2003gl018352s.
Jokat, W., and M. C. Schmidt-Aursch (2007), Geophysical characteristics of the ultraslow spreading Gakkel Ridge, Arctic Ocean, Geophysical Journal International, 168(3), 983-998, doi: 10.1111/j.1365-246X.2006.03278.xs.
Jokat, W., M. Ickrath, and J. O'Connor (2013), Seismic transect across the Lomonosov and Mendeleev Ridges: Constraints on the geological evolution of the Amerasia Basin, Arctic Ocean, Geophysical Research Letters, 40(19), 5047-5051, doi: 10.1002/grl.50975s.
Jokat, W., E. Weigelt, Y. Kristofferseq, T. Rasmussen, and T. Schöne (1995a), New geophysical results from the south-western Eurasian Basin (Morris Jesup Rise, Gakkel Ridge, Yermak Plateau) and the Fram Strait, Geophysical Journal International, 123(2), 601-610, doi: 10.1111/j.1365-246X.1995.tb06874.xs.
Jokat, W., E. Weigelt, Y. Kristoffersen, T. Rasmussen, and T. Schöone (1995b), New insights into the evolution of the Lomonosov Ridge and the Eurasian Basin, Geophysical Journal International, 122(2), 378-392, doi: 10.1111/j.1365-246X.1995.tb00532.xs.
Jokat, W., O. Ritzmann, M. C. Schmidt-Aursch, S. Drachev, S. Gauger, and J. Snow (2003), Geophysical evidence for reduced melt production on the Arctic ultraslow Gakkel mid-ocean ridge, Nature, 423(6943), 962-965, doi: http://www.nature.com/nature/journal/v423/n6943/suppinfo/nature01706_S1.htmls.
Jonathan E. Snow | Department of Geosciences, U. o. H., Houston, TX, USA, and M. S. I. Henrietta N. Edmonds | The University of Texas at Austin, Port Aransas, TX, USA (2007), Ultraslow-Spreading Ridges: Rapid Paradigm Changes Oceanography, 20.
Kandilarov, A., R. Mjelde, K. Okino, and Y. Murai (2008), Crustal structure of the ultra-slow spreading Knipovich Ridge, North Atlantic, along a presumed amagmatic portion of oceanic crustal formation, Marine Geophysical Researches, 29(2), 109-134, doi: 10.1007/s11001-008-9050-0s.
Kandilarov, A., H. Landa, R. Mjelde, R. Pedersen, K. Okino, and Y. Murai (2010), Crustal structure of the ultra-slow spreading Knipovich Ridge, North Atlantic, along a presumed ridge segment center, Marine Geophysical Researches, 31(3), 173-195, doi: 10.1007/s11001-010-9095-8s.
Klingelhöfer, F., L. Géli, L. Matias, N. Steinsland, and J. Mohr (2000), Crustal structure of a super-slow spreading centre: a seismic refraction study of Mohns Ridge, 72° N, Geophysical Journal International, 141(2), 509-526, doi: 10.1046/j.1365-246x.2000.00098.xs.
Knudsen, C., J. R. Hopper, P. R. Bierman, M. Bjerager, T. Funck, P. F. Green, J. R. Ineson, P. Japsen, C. Marcussen, S. C. Sherlock and T. B. Thomsen (2017), Samples from the Lomonosov Ridge place new constraints on the geological evolution of the Arctic Ocean, Geological Society, London, Special Publications, 460, 18 August 2017, doi: 10.1144/SP460.17.
McKenzie, D. & Bickle, M.J. 1988: The volume and composition of melt generated by extension of the lithosphere. Journal of Petrology 29 (3), 625-679.
Michael, P. J., et al. (2003), Magmatic and amagmatic seafloor generation at the ultraslow-spreading Gakkel ridge, Arctic Ocean, Nature, 423(6943), 956-961.
Moran, K., et al. (2006), The Cenozoic palaeoenvironment of the Arctic Ocean, Nature, 441(7093), 601-605, doi: 10.1038/nature04800s.

Nowack R.L., Stacy S.M. (2002) Synthetic Seismograms and Wide-angle Seismic Attributes from the Gaussian Beam and Reflectivity Methods for Models with Interfaces and Velocity Gradients. In: Pšenčík I., Červený V. (eds) Seismic Waves in Laterally Inhomogeneous Media. Pageoph Topical Volumes. Birkhäuser, Basel, https://doi.org/10.1007/978-3-0348-8146-3_4.

Riddell-Dixon, Elizabeth M. (2017), *Breaking the Ice: Canada, Sovereignty, and the Arctic Extended Continental Shelf*. 2 nd edition, University of Toronto, Dundurn, 343 pp.

Schmidt-Aursch, M. C., and W. Jokat (2016), 3D gravity modelling reveals off-axis crustal thickness variations along the western Gakkel Ridge (Arctic Ocean), Tectonophysics, doi: http://dx.doi.org/10.1016/j.tecto.2016.03.021s.

Shepherd, A., et al. (2012), A Reconciled Estimate of Ice-Sheet Mass Balance, Science, 338(6111), 1183-1189, doi: 10.1126/science.1228102s.

Snow, J.E., and H.N. Edmonds. 2007. Ultraslow-spreading ridges: Rapid paradigm changes. *Oceanography* 20(1):90–101, https://doi.org/10.5670/oceanog.2007.83.

White, R. S., T. A. Minshull, M. J. Bickle, and C. J. Robinson (2001), Melt Generation at Very Slow-Spreading Oceanic Ridges: Constraints from Geochemical and Geophysical Data, *Journal of Petrology*, *42*(6), 1171-1196, doi: 10.1093/petrology/42.6.1171s.

Appendix

This appendix contains the sonobuoy record sections used during the LOMROG III expedition. Each record is displayed in four panels: the raw record section, the record section overlayed with the computed travel times, the travel time picks overlayed by the calculated travel times, and the raypath diagram along the model. The sonobuoy record section are ordered after their deployment position. For the exact location of the sonobuoys, please refer to Chapter II, Fig. 2.

Figure Captions:

Left page. Raw record section (top) and record section with computed travel times (bottom) for sonobuoy. The vertical scale for the record sections is the travel time using a reduction velocity of 6.8 km/s, and the horizontal scale is the shot-receiver distance (offset).

Right page Observed and calculated travel times (top) and ray path diagram (bottom) for sonobuoy. The vertical scale (top) is the travel time using a reduction velocity of 6.8 km/s and the vertical scale (bottom) is the depth in km. The horizontal scale for both panels is the distance along the velocity model. Pick uncertainties of the observed travel times are indicated by the heights of the vertical bars in red.

LOMROG 2012 - Station 1

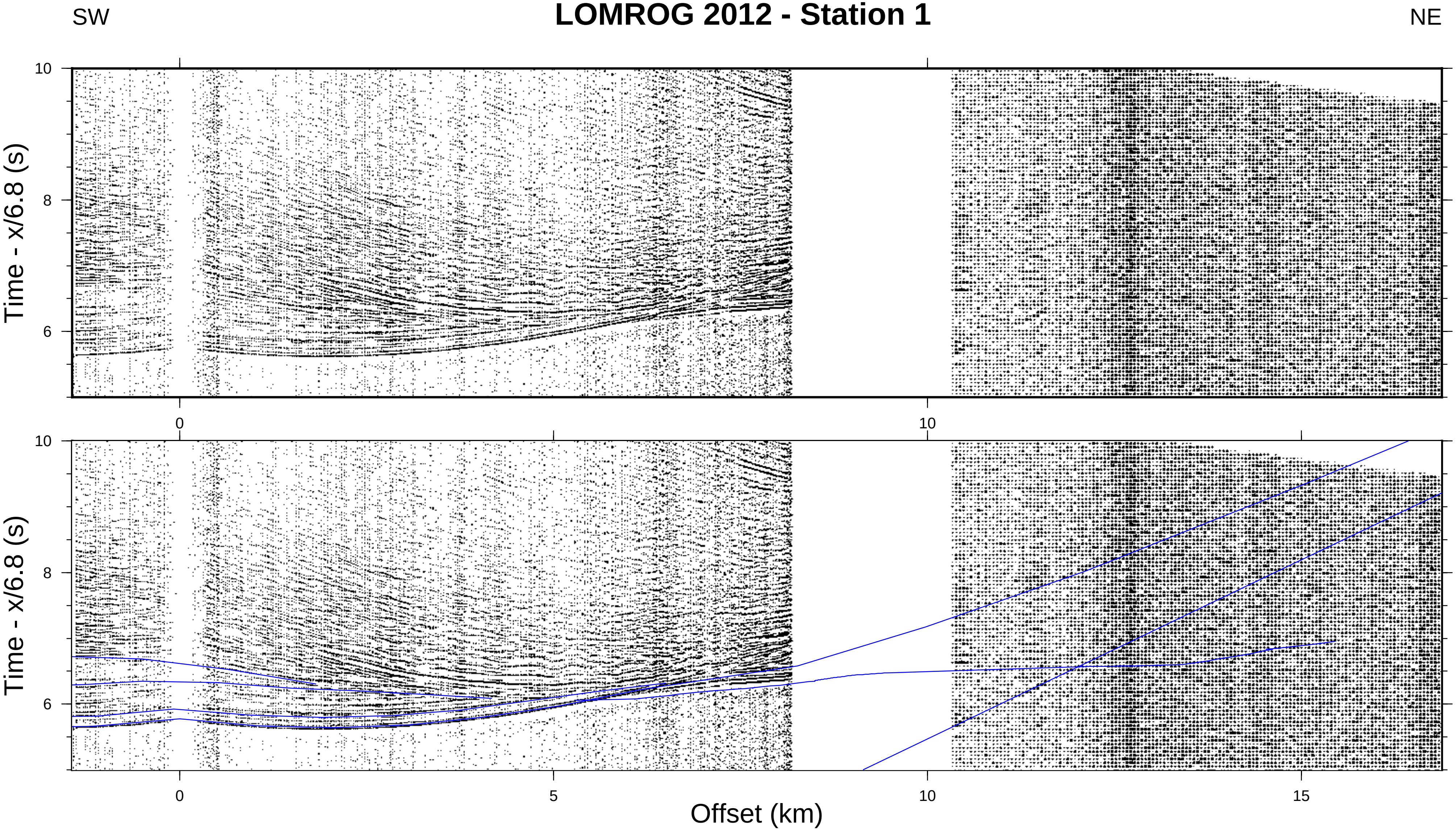

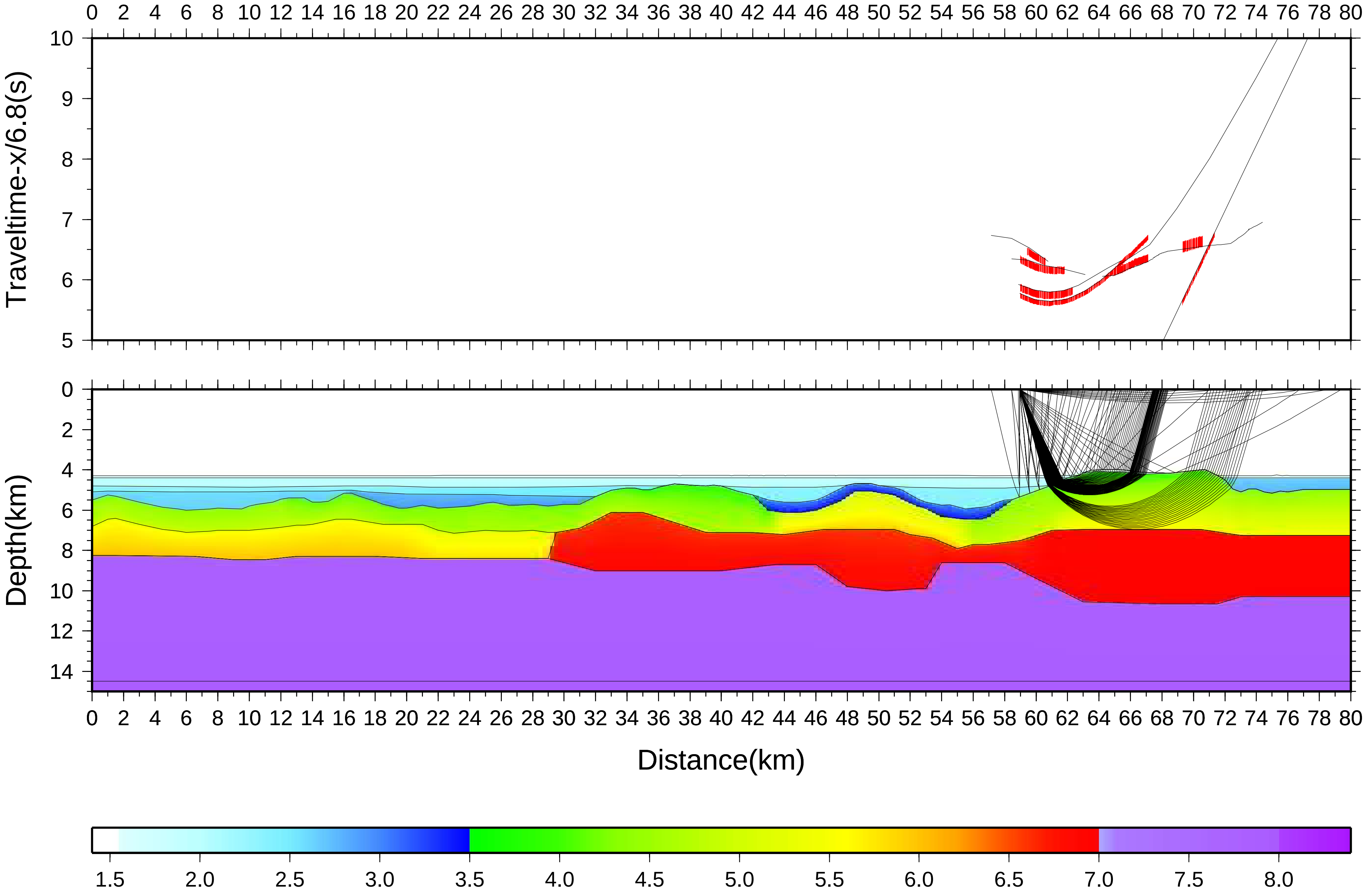

Traveltime-x/6.8(s)
Depth(km)
Distance(km)
0 2 4 6 8 10 12 14 16 18 20 22 24 26 28 30 32 34 36 38 40 42 44 46 48 50 52 54 56 58 60 62 64 66 68 70 72 74 76 78 80
1.5 2.0 2.5 3.0 3.5 4.0 4.5 5.0 5.5 6.0 6.5 7.0 7.5 8.0

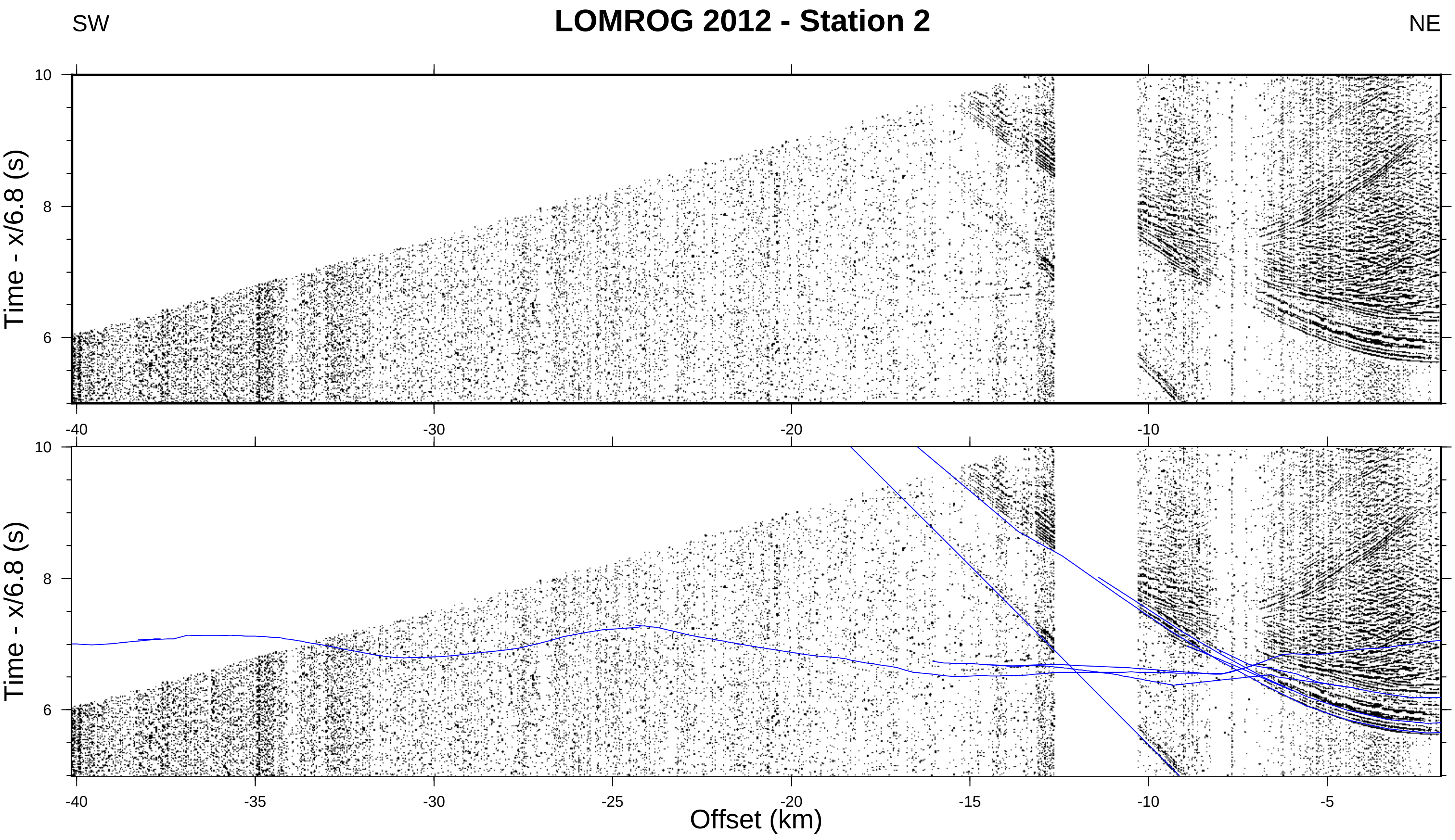
SW
LOMROG 2012 - Station 2
NE
Time - x/6.8 (s)
10
8
6
-40
-35
-30
-25
-20
-15
-10
-5
Offset (km)

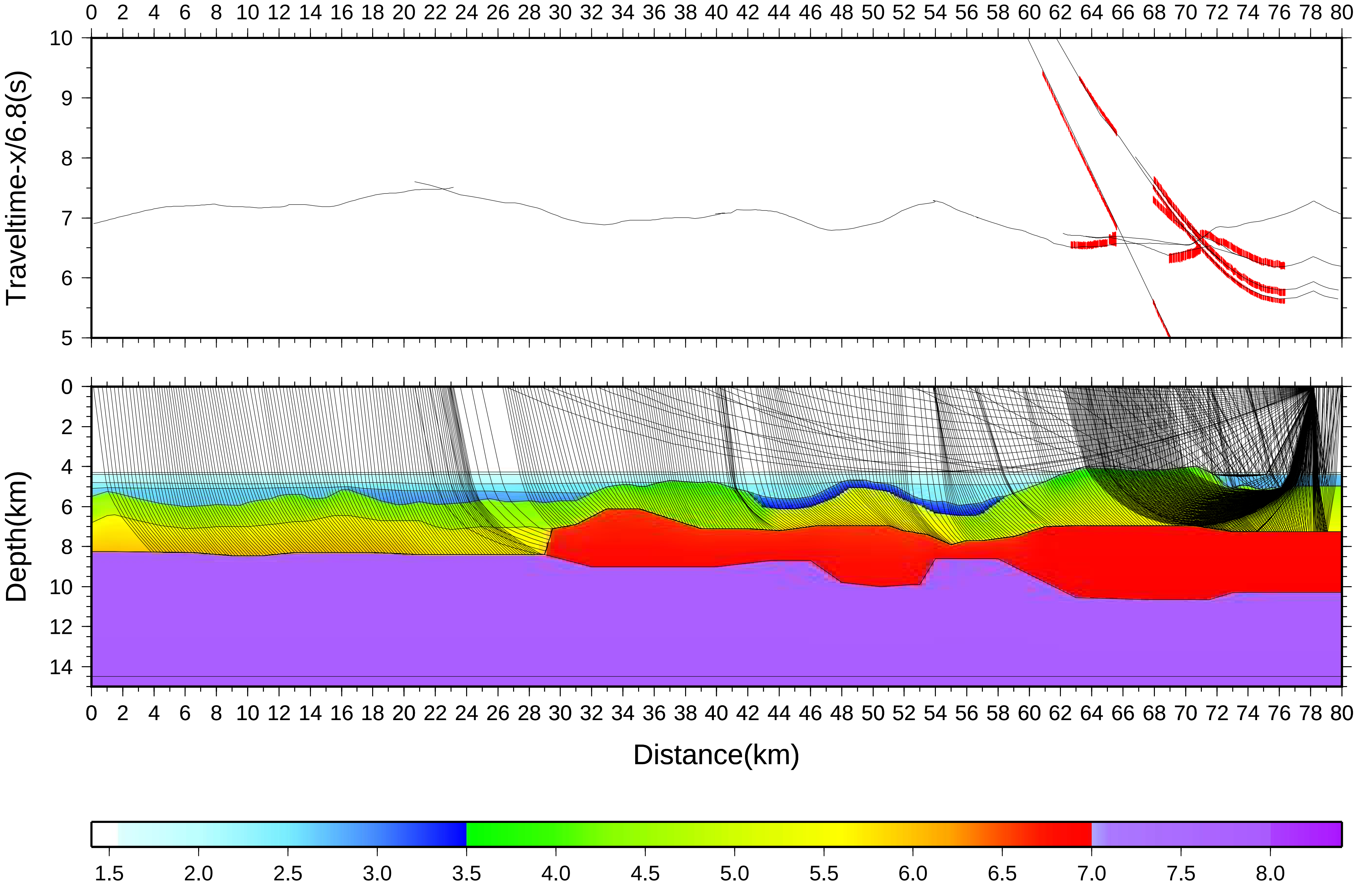

Traveltime-x/6.8(s)
Depth(km)
Distance(km)
1.5
2.0
2.5
3.0
3.5
4.0
4.5
5.0
5.5
6.0
6.5
7.0
7.5
8.0

LOMROG 2012 - Station 2 (drift)

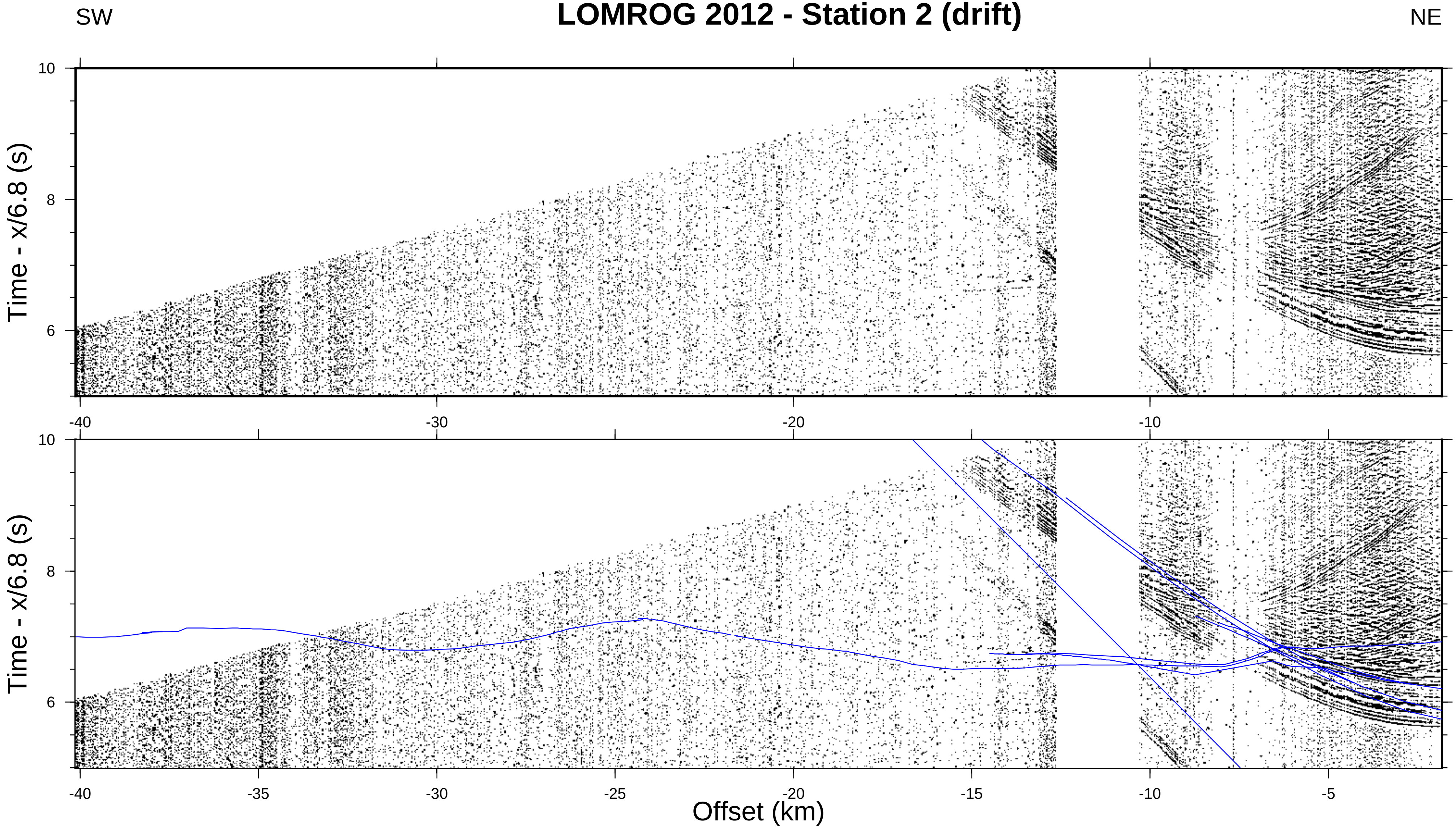

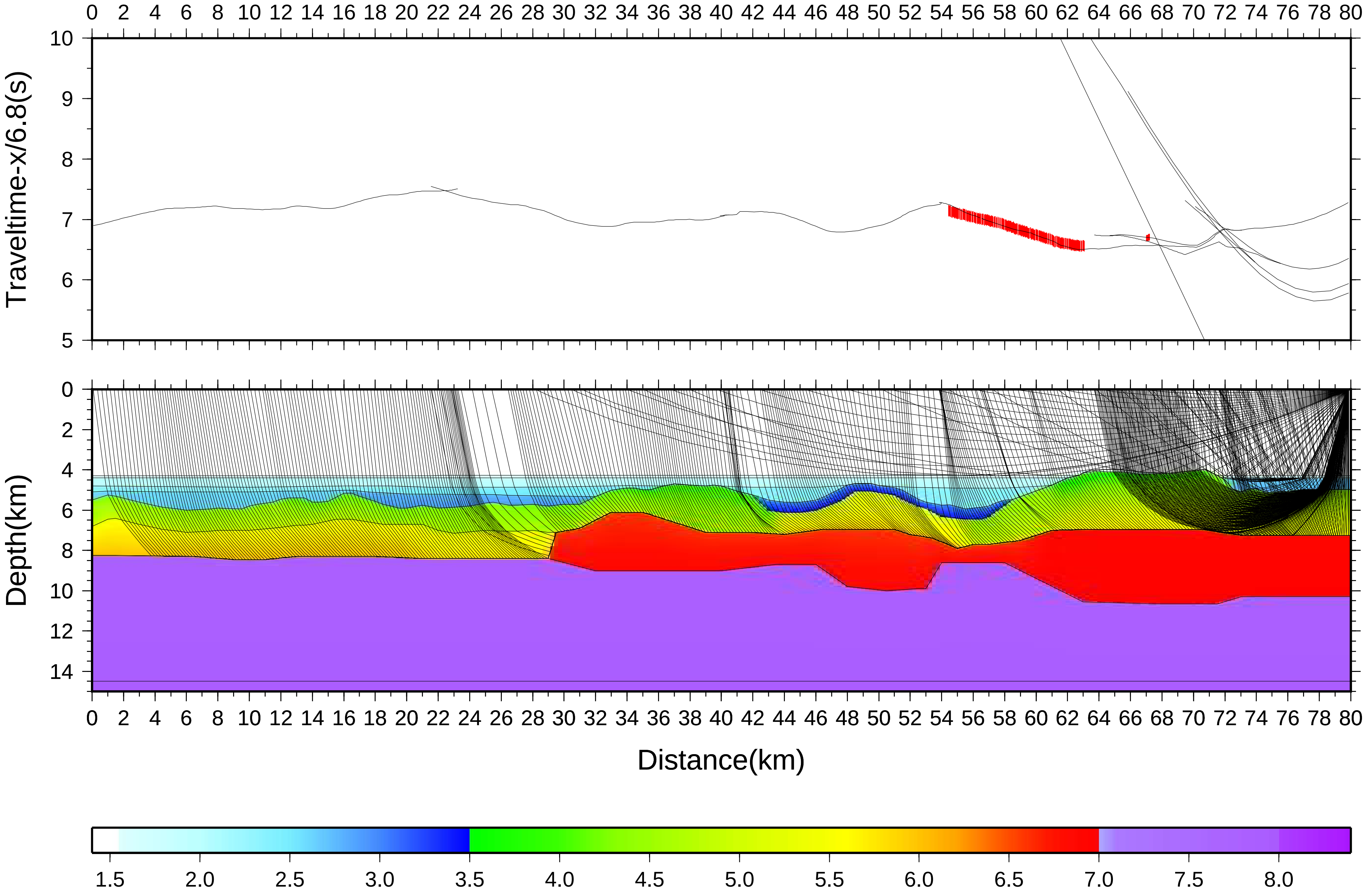

Traveltime-x/6.8(s)
Depth(km)
Distance(km)

LOMROG 2012 - Station 3

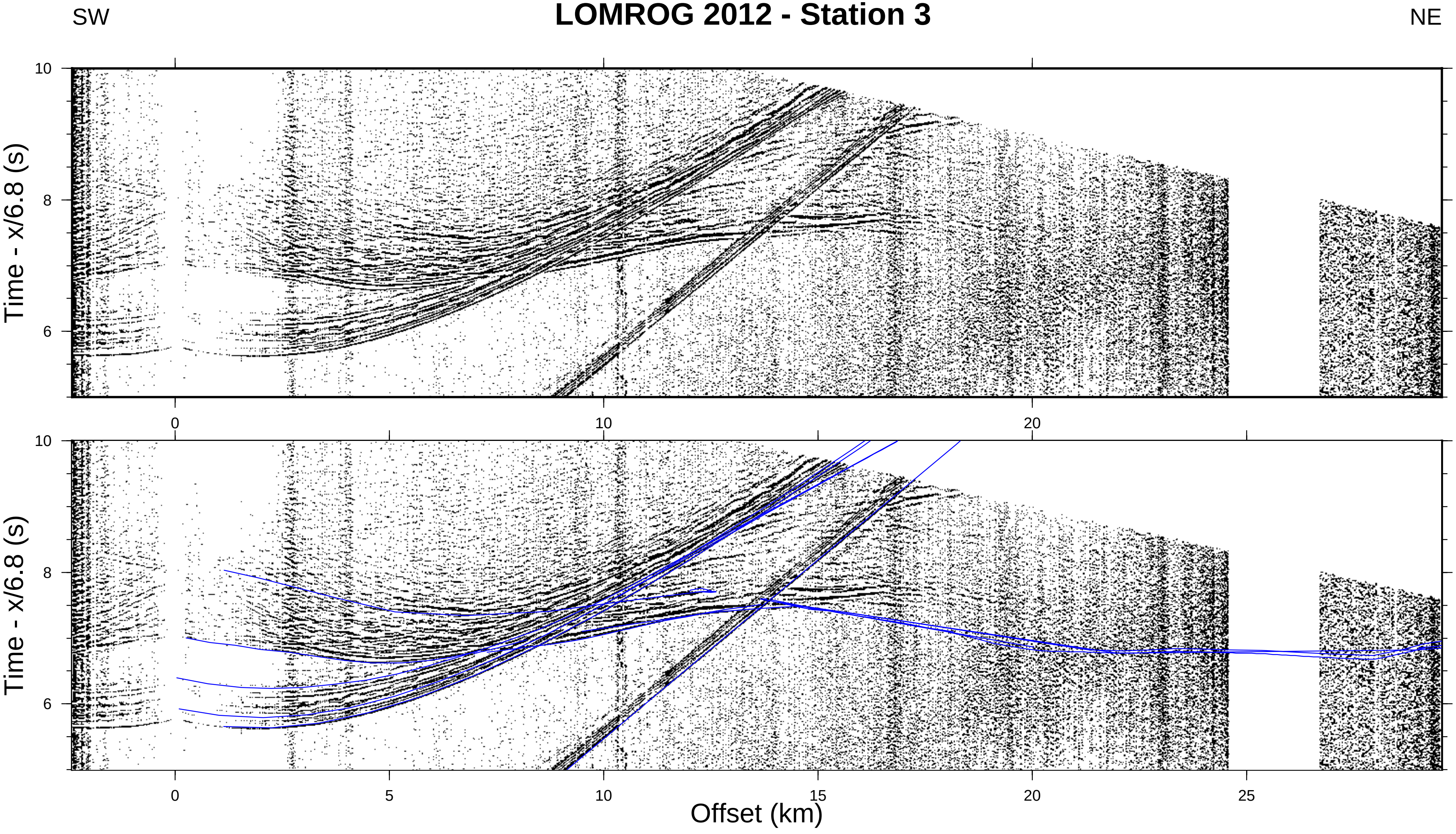

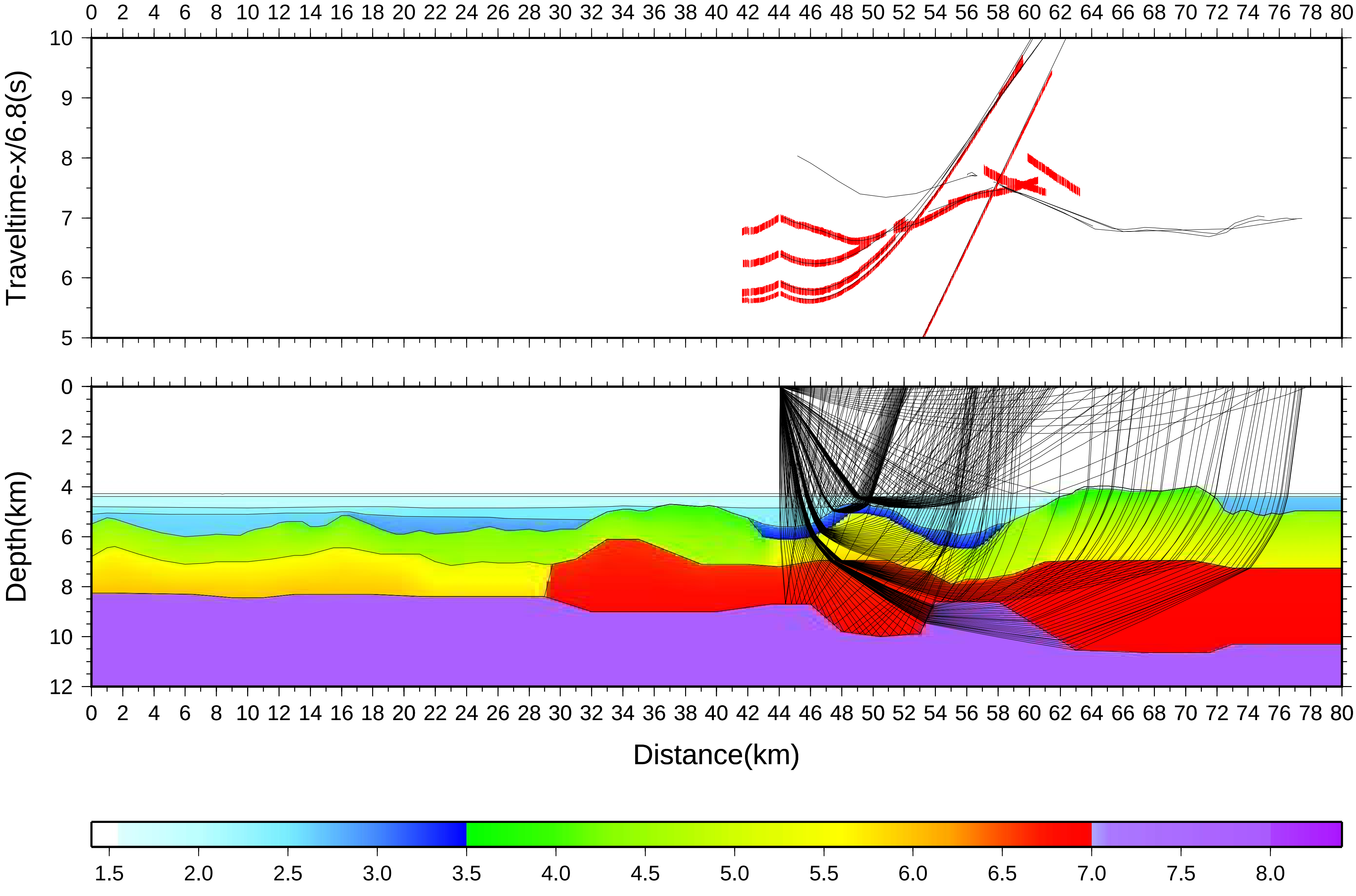

Traveltime-x/6.8(s)
Depth(km)
Distance(km)
0 2 4 6 8 10 12 14 16 18 20 22 24 26 28 30 32 34 36 38 40 42 44 46 48 50 52 54 56 58 60 62 64 66 68 70 72 74 76 78 80
1.5 2.0 2.5 3.0 3.5 4.0 4.5 5.0 5.5 6.0 6.5 7.0 7.5 8.0

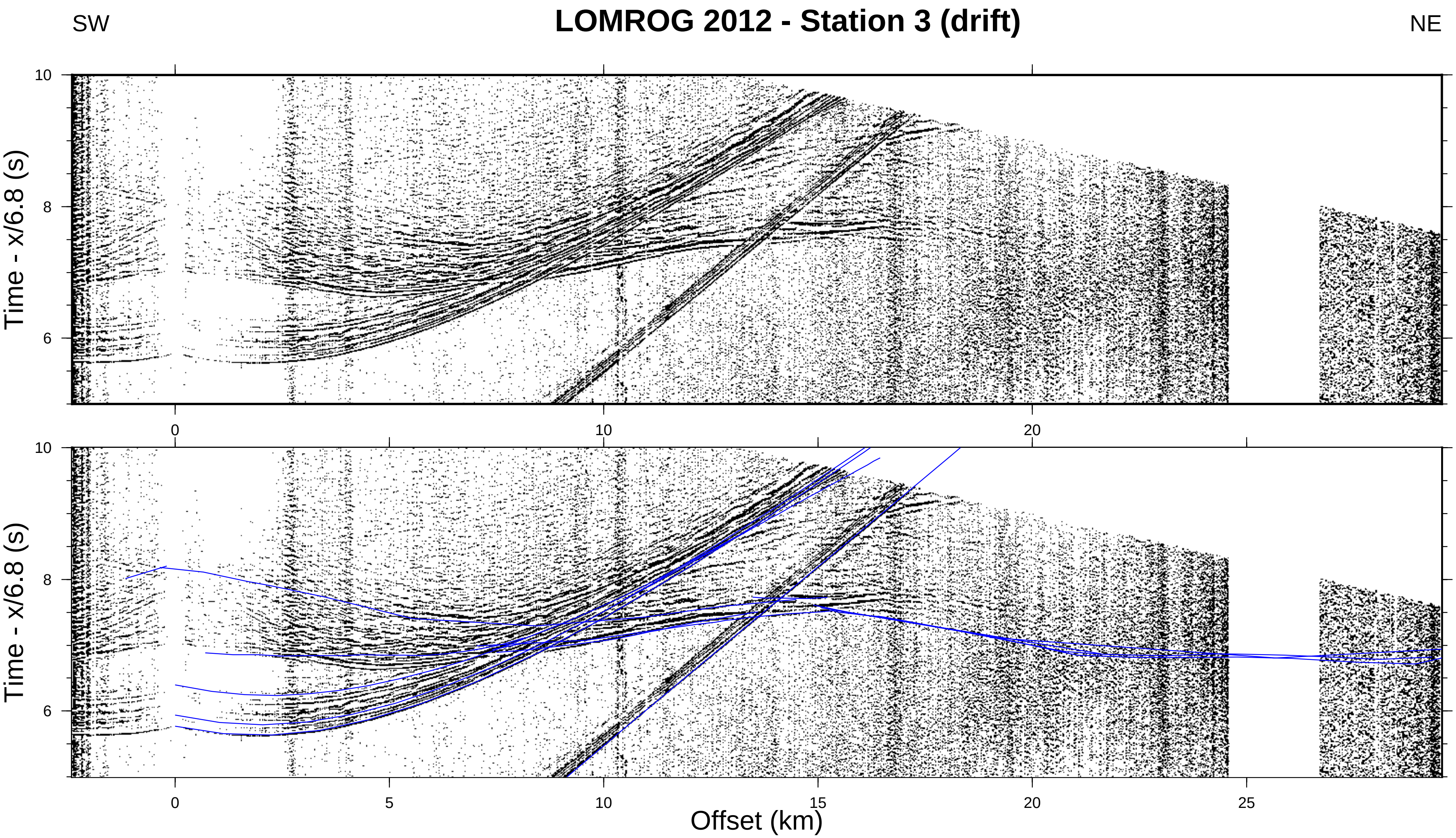
SW
LOMROG 2012 - Station 3 (drift)
NE
Time - x/6.8 (s)
10
8
6
0
10
20
Time - x/6.8 (s)
10
8
6
0
5
10
15
20
25
Offset (km)

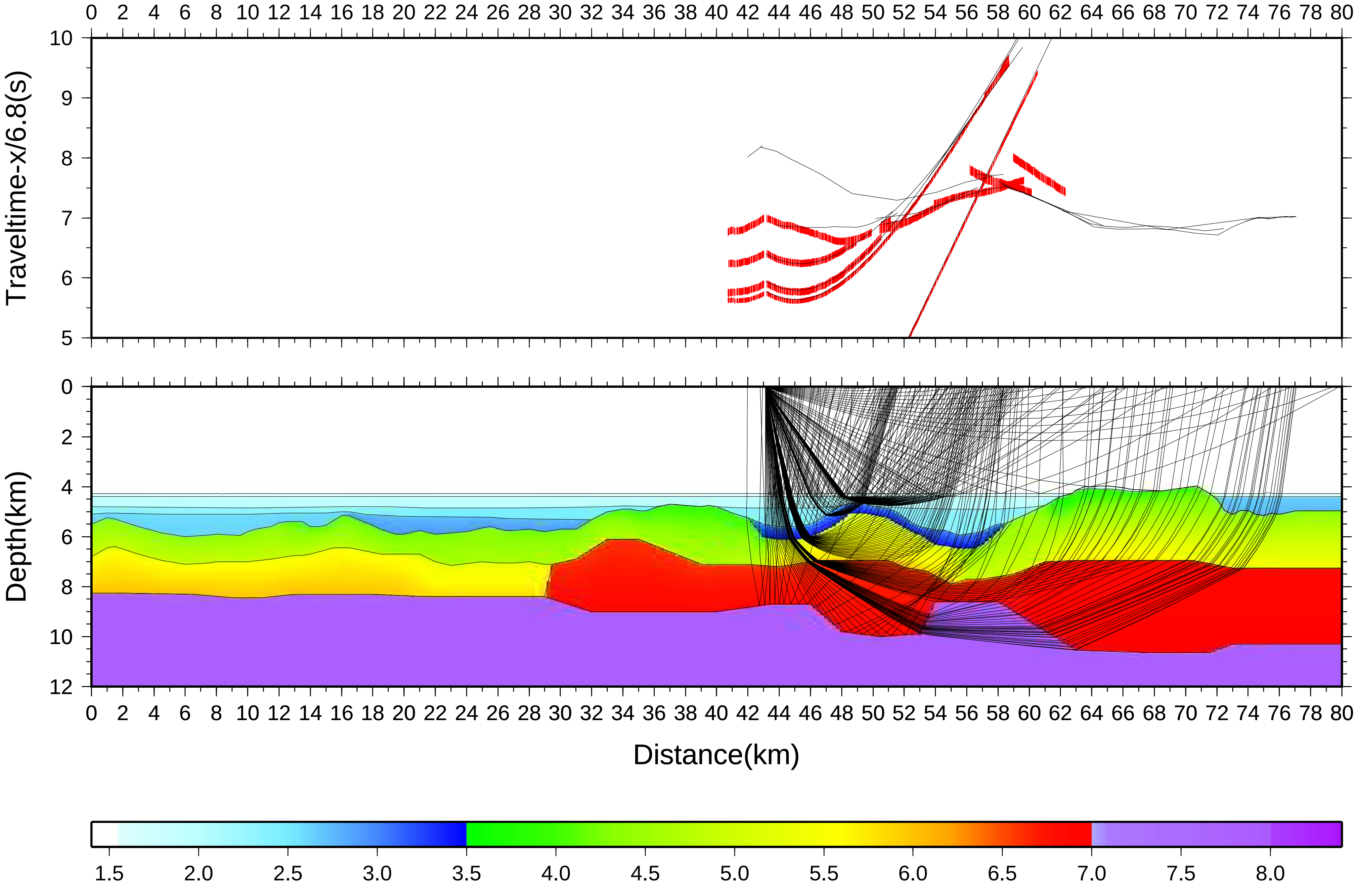

Traveltime-x/6.8(s)
Depth(km)
Distance(km)
0 2 4 6 8 10 12 14 16 18 20 22 24 26 28 30 32 34 36 38 40 42 44 46 48 50 52 54 56 58 60 62 64 66 68 70 72 74 76 78 80
10 9 8 7 6 5
0 2 4 6 8 10 12
1.5 2.0 2.5 3.0 3.5 4.0 4.5 5.0 5.5 6.0 6.5 7.0 7.5 8.0

LOMROG 2012 - Station 5

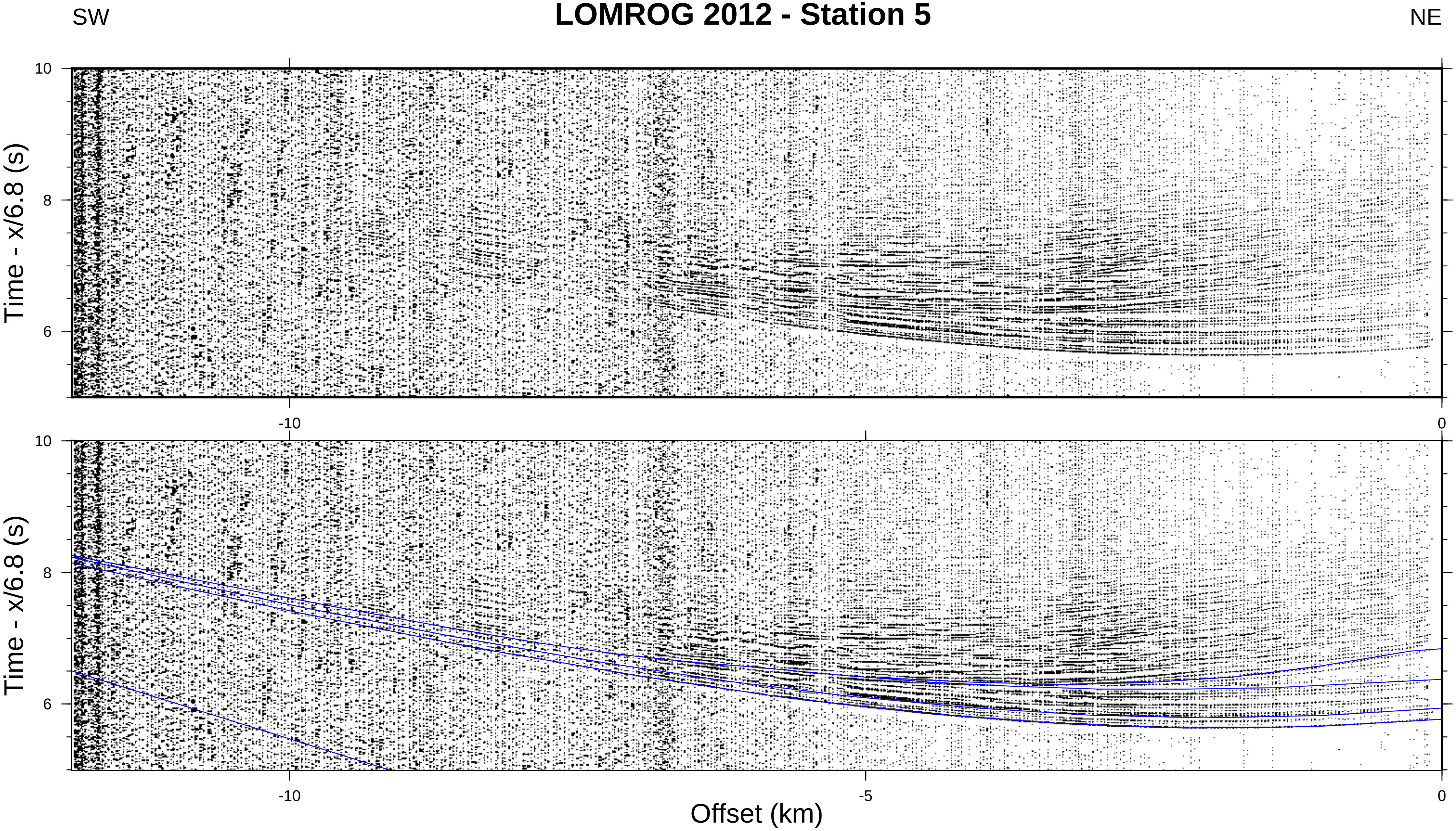

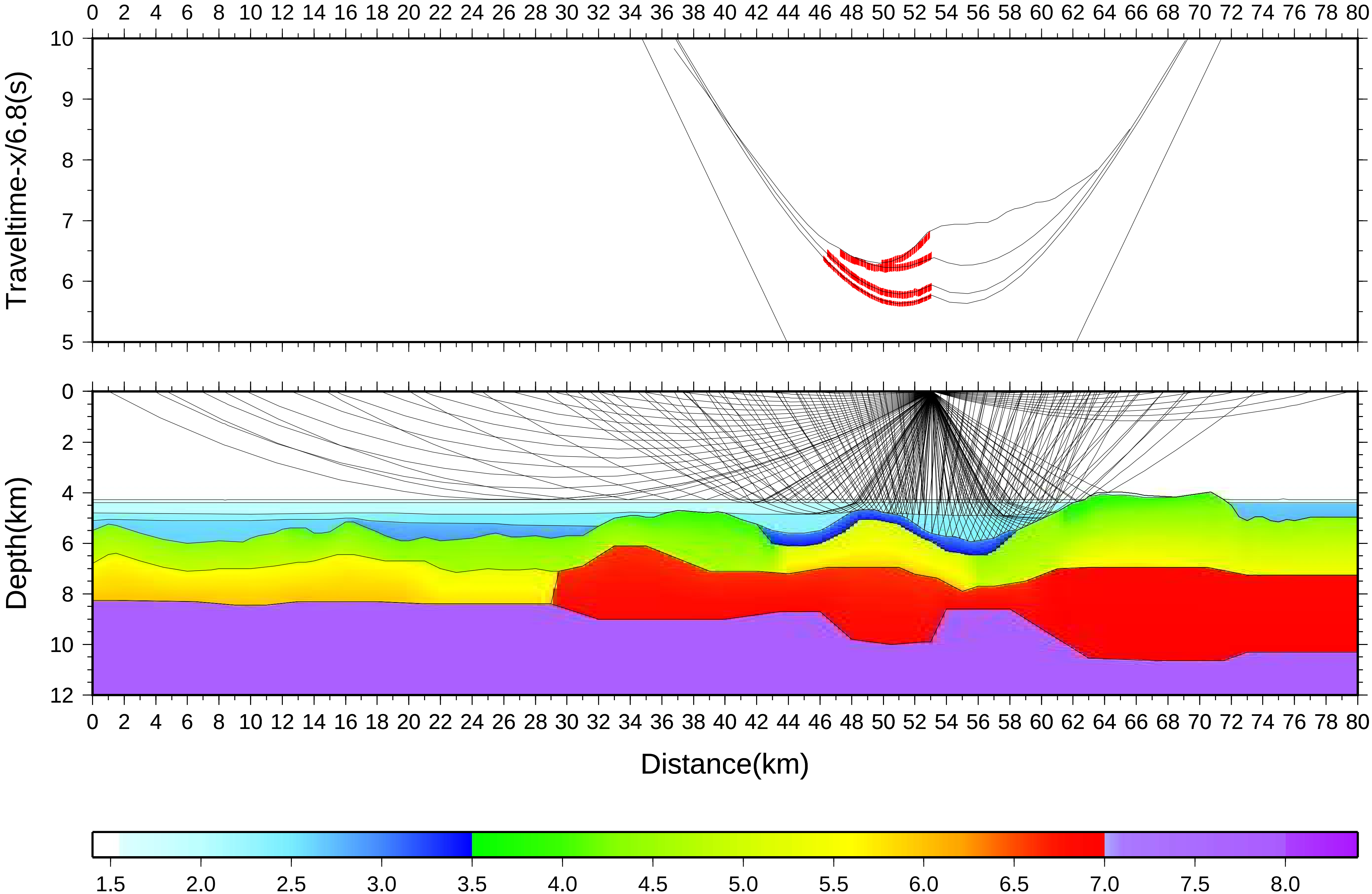

Traveltime-x/6.8(s)
Depth(km)
Distance(km)
0 2 4 6 8 10 12 14 16 18 20 22 24 26 28 30 32 34 36 38 40 42 44 46 48 50 52 54 56 58 60 62 64 66 68 70 72 74 76 78 80
1.5 2.0 2.5 3.0 3.5 4.0 4.5 5.0 5.5 6.0 6.5 7.0 7.5 8.0

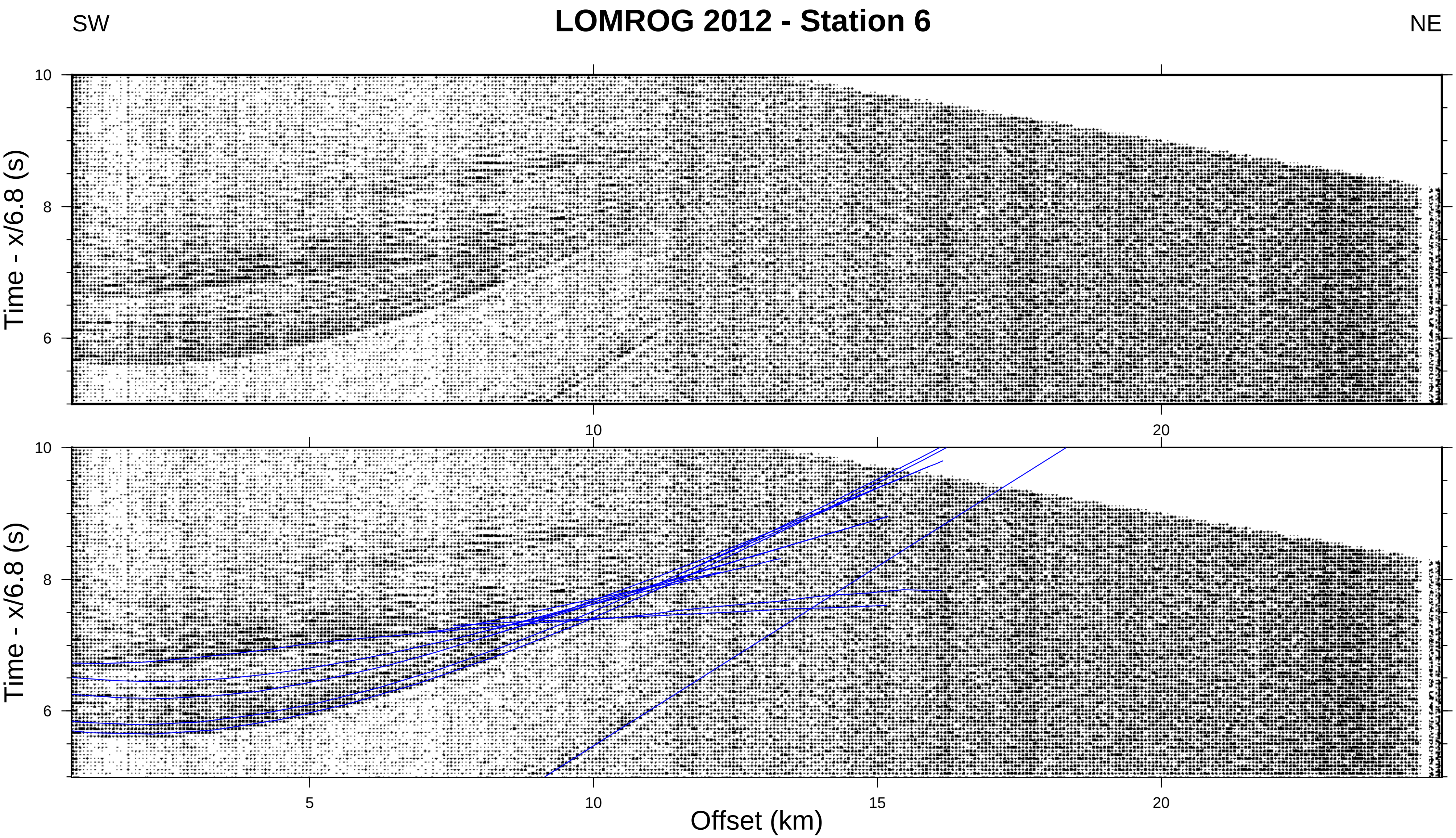

SW
LOMROG 2012 - Station 6
NE
Time - x/6.8 (s)
10
8
6
10
20
Time - x/6.8 (s)
10
8
6
5
10
15
20
Offset (km)

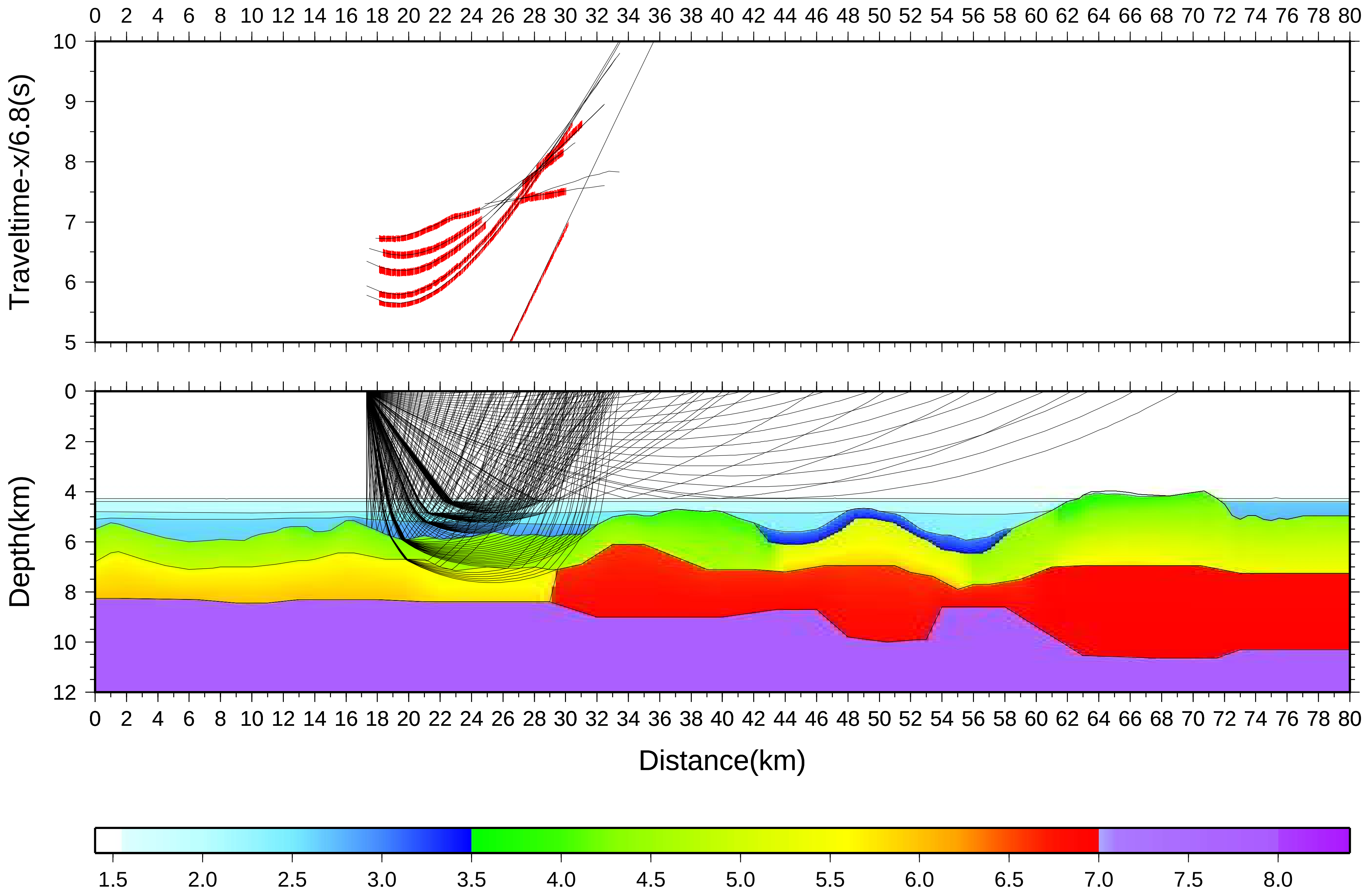

0 2 4 6 8 10 12 14 16 18 20 22 24 26 28 30 32 34 36 38 40 42 44 46 48 50 52 54 56 58 60 62 64 66 68 70 72 74 76 78 80
Traveltime-x/6.8(s)
5 6 7 8 9 10
Depth(km)
0 2 4 6 8 10 12
Distance(km)
1.5 2.0 2.5 3.0 3.5 4.0 4.5 5.0 5.5 6.0 6.5 7.0 7.5 8.0

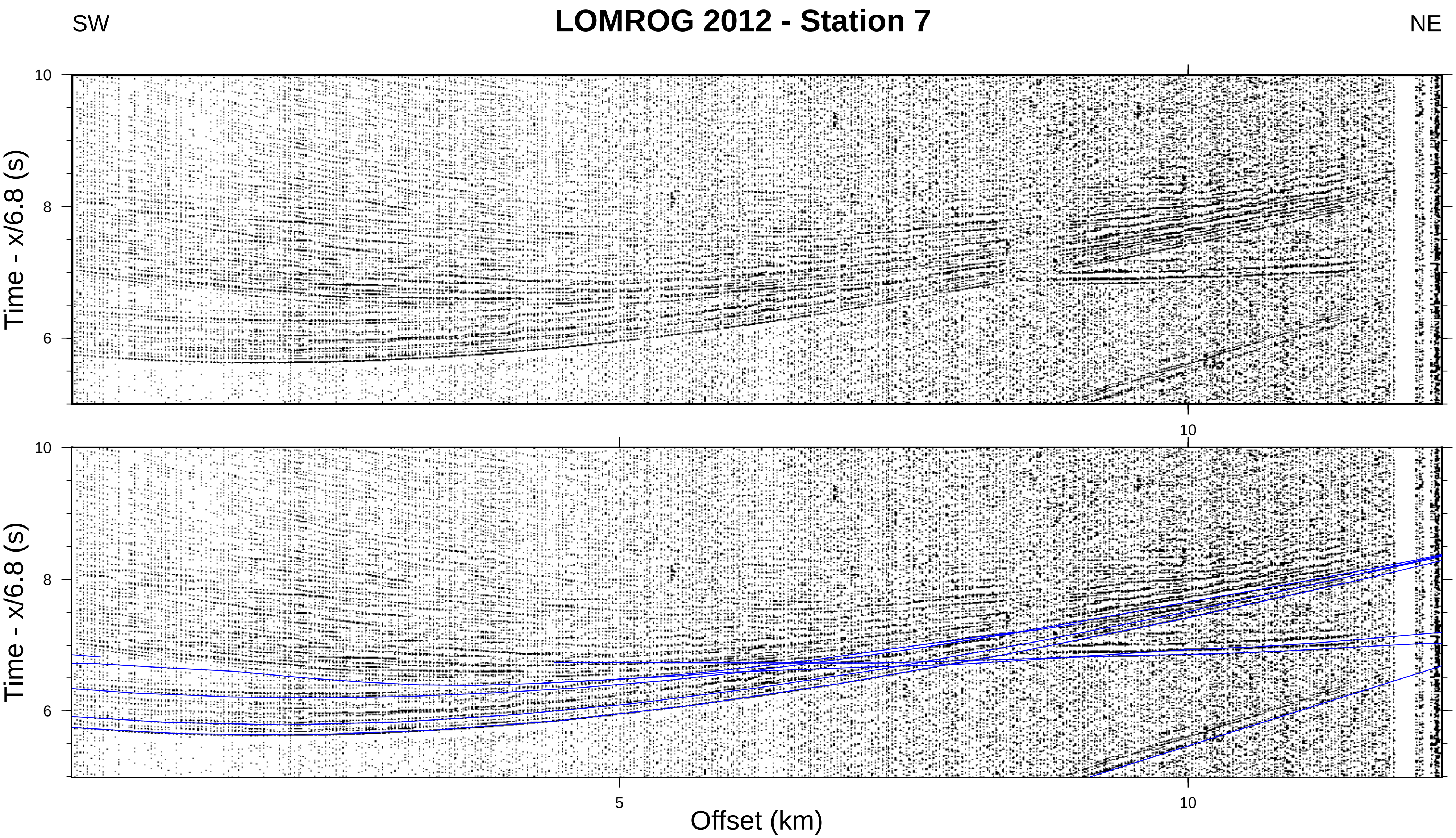
SW
LOMROG 2012 - Station 7
NE
Time - x/6.8 (s)
10
8
6
10
Time - x/6.8 (s)
10
8
6
5
10
Offset (km)

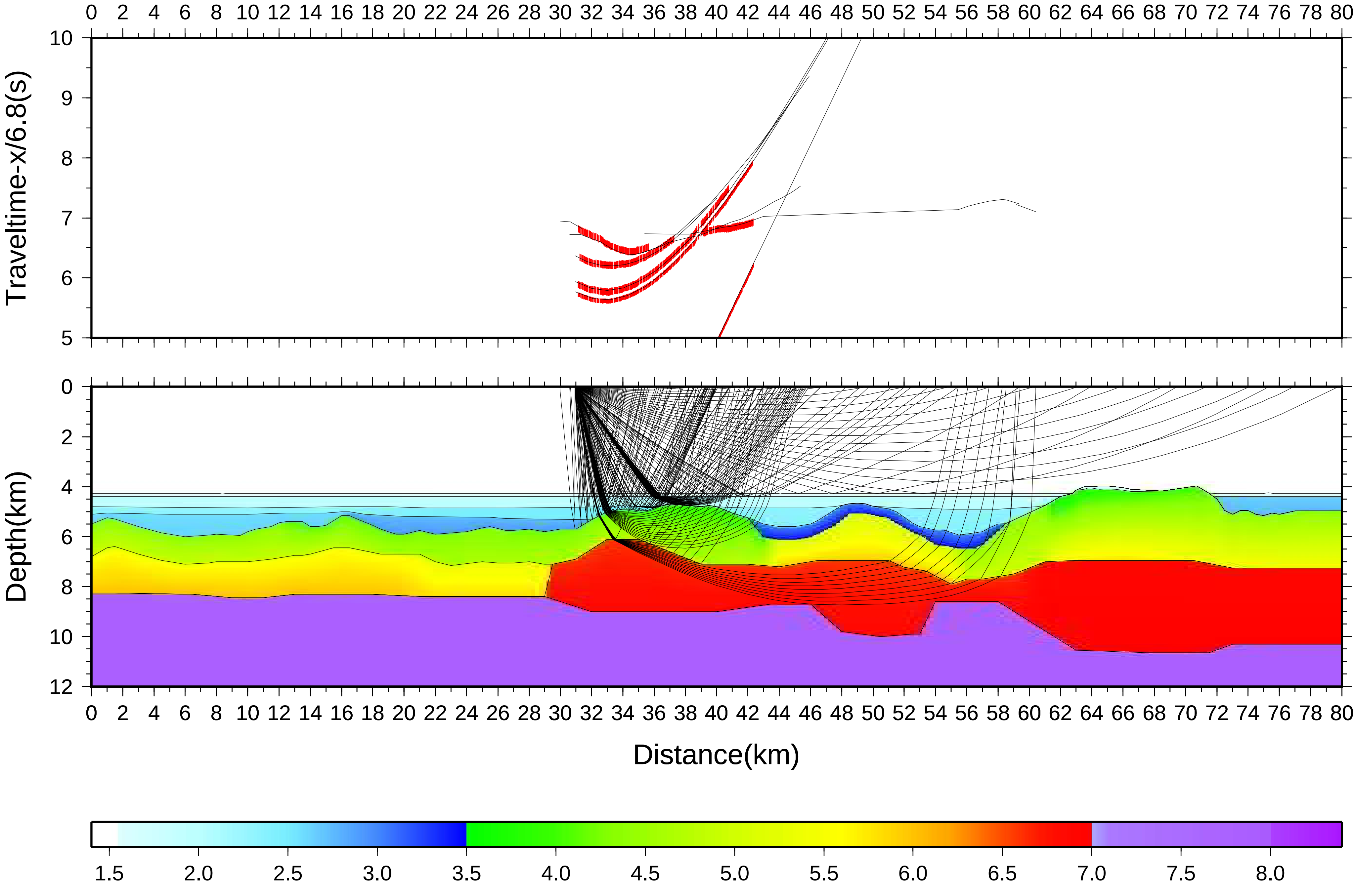
Traveltime-x/6.8(s)
Depth(km)
Distance(km)
0 2 4 6 8 10 12 14 16 18 20 22 24 26 28 30 32 34 36 38 40 42 44 46 48 50 52 54 56 58 60 62 64 66 68 70 72 74 76 78 80
1.5 2.0 2.5 3.0 3.5 4.0 4.5 5.0 5.5 6.0 6.5 7.0 7.5 8.0

LOMROG 2012 - Station 8

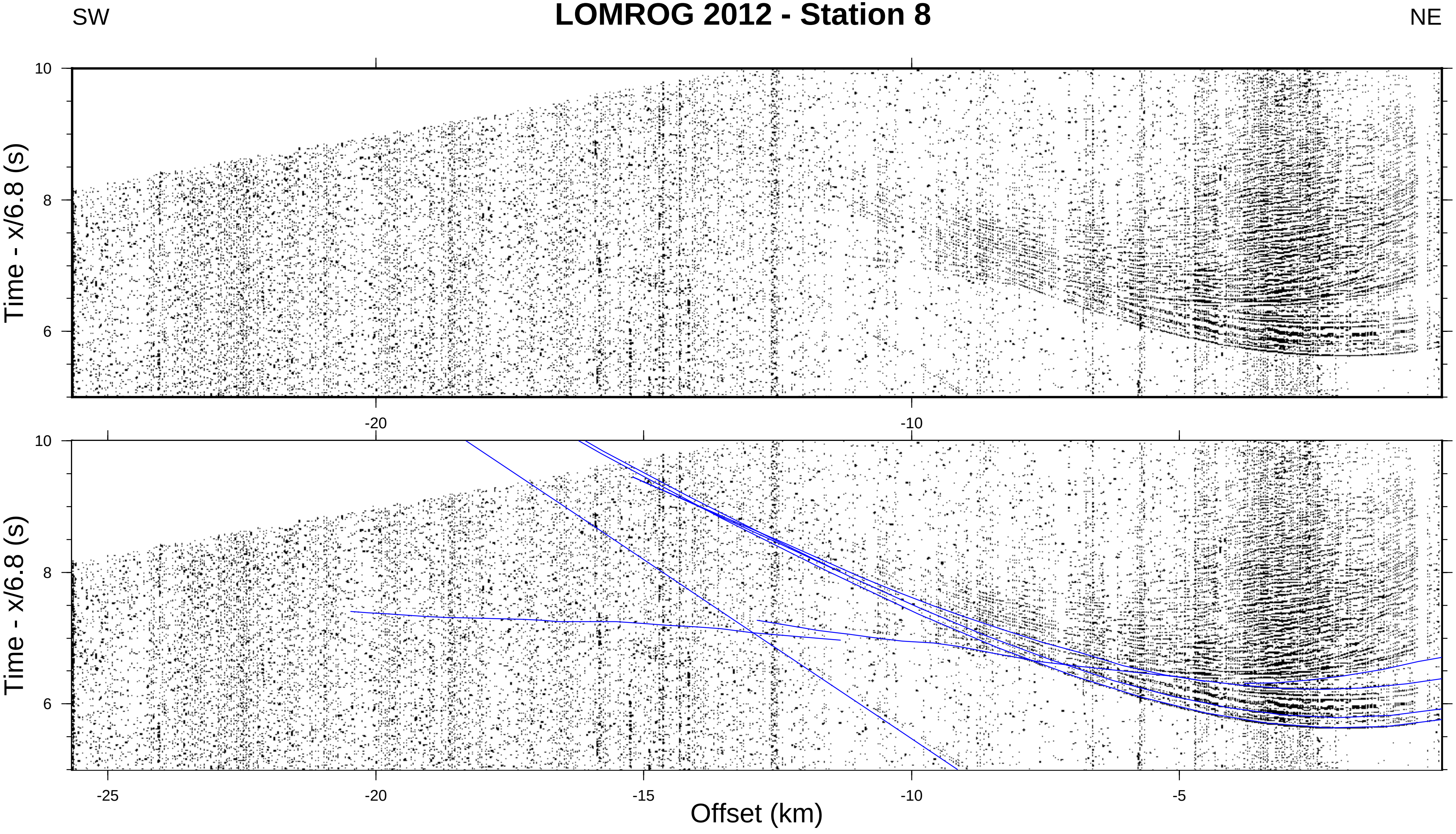

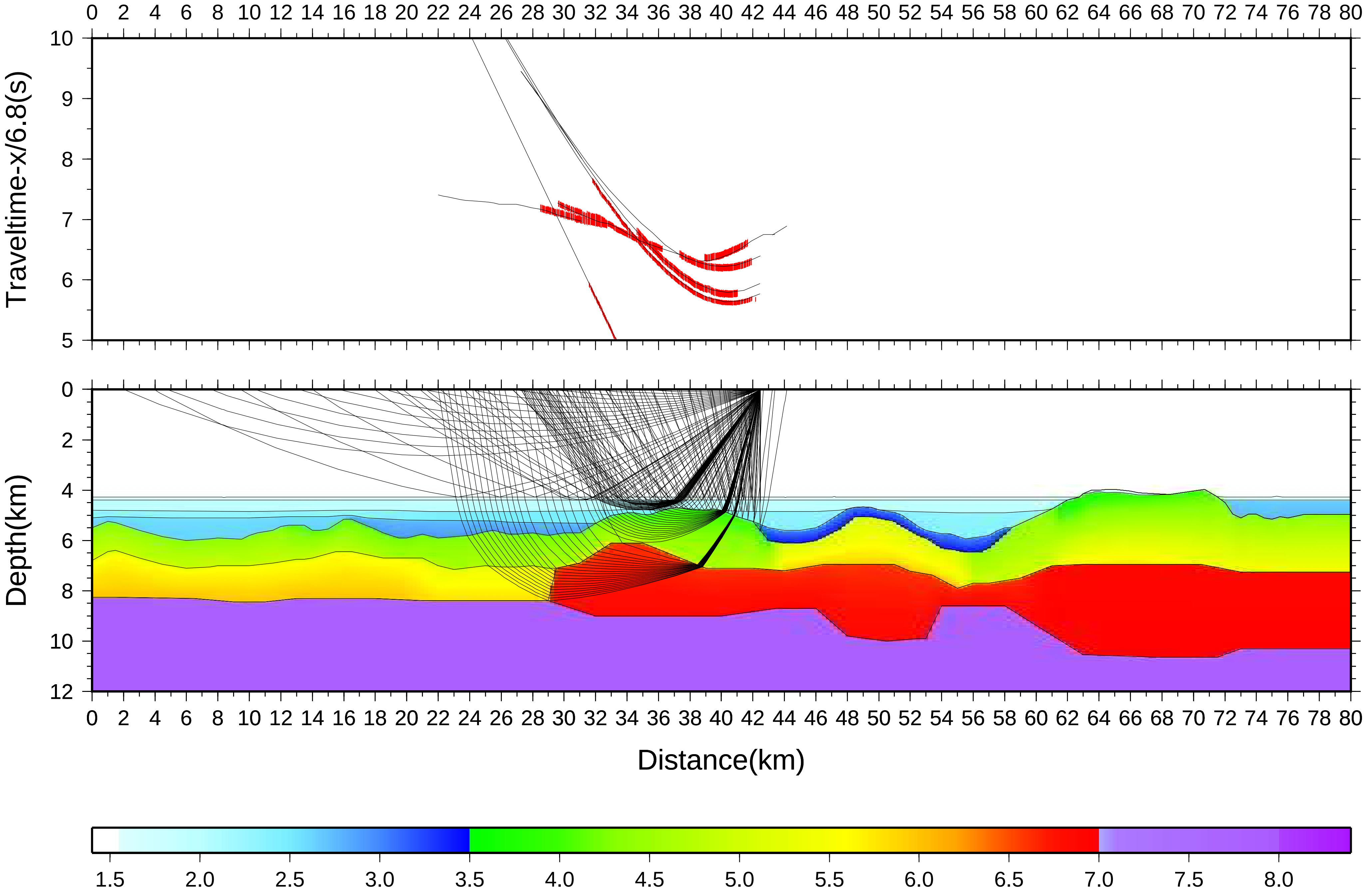

Traveltime-x/6.8(s)
Depth(km)
Distance(km)
1.5
2.0
2.5
3.0
3.5
4.0
4.5
5.0
5.5
6.0
6.5
7.0
7.5
8.0

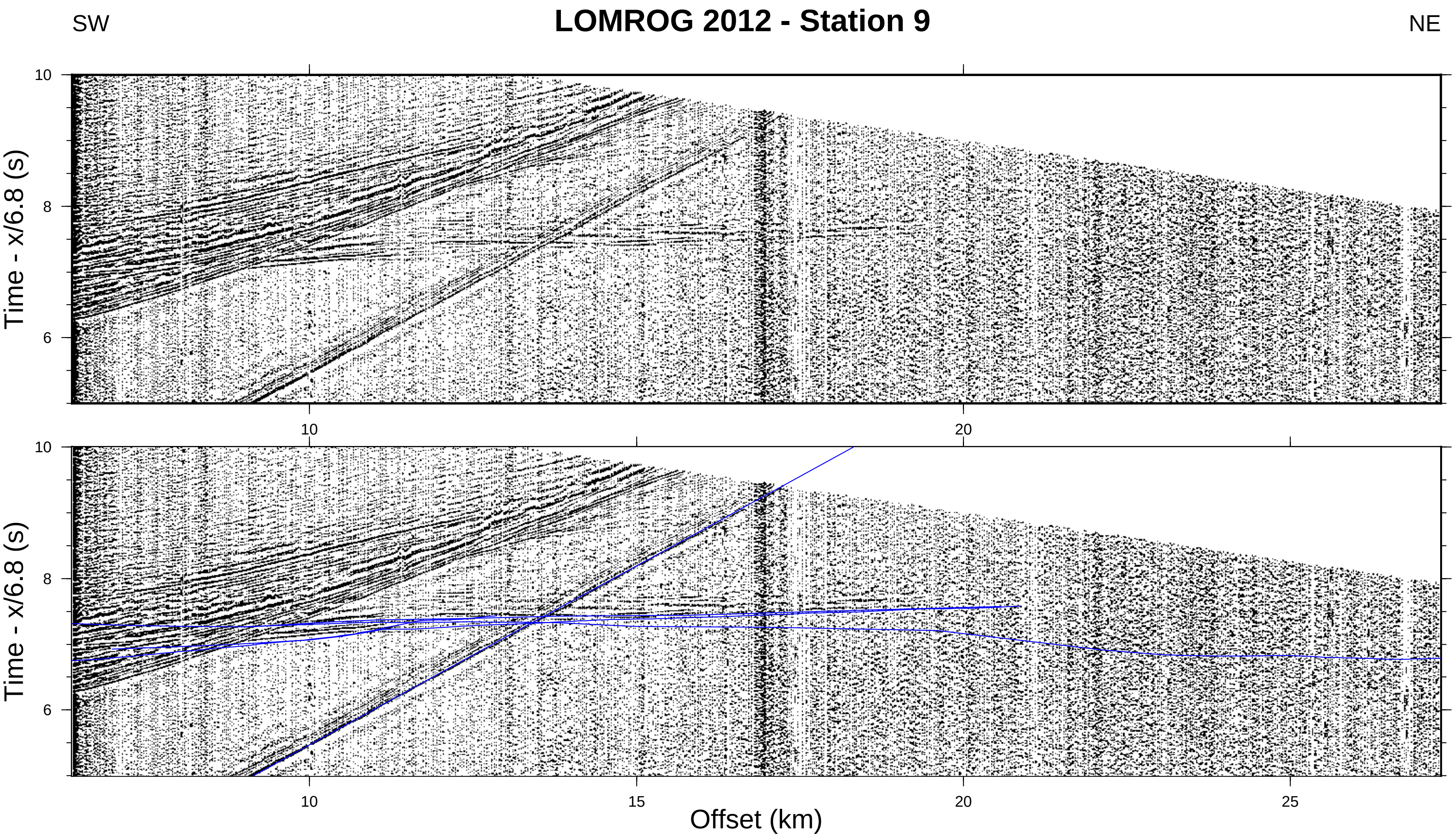
SW
LOMROG 2012 - Station 9
NE
Time - x/6.8 (s)
10
8
6
Time - x/6.8 (s)
10
8
6
10
15
20
25
Offset (km)

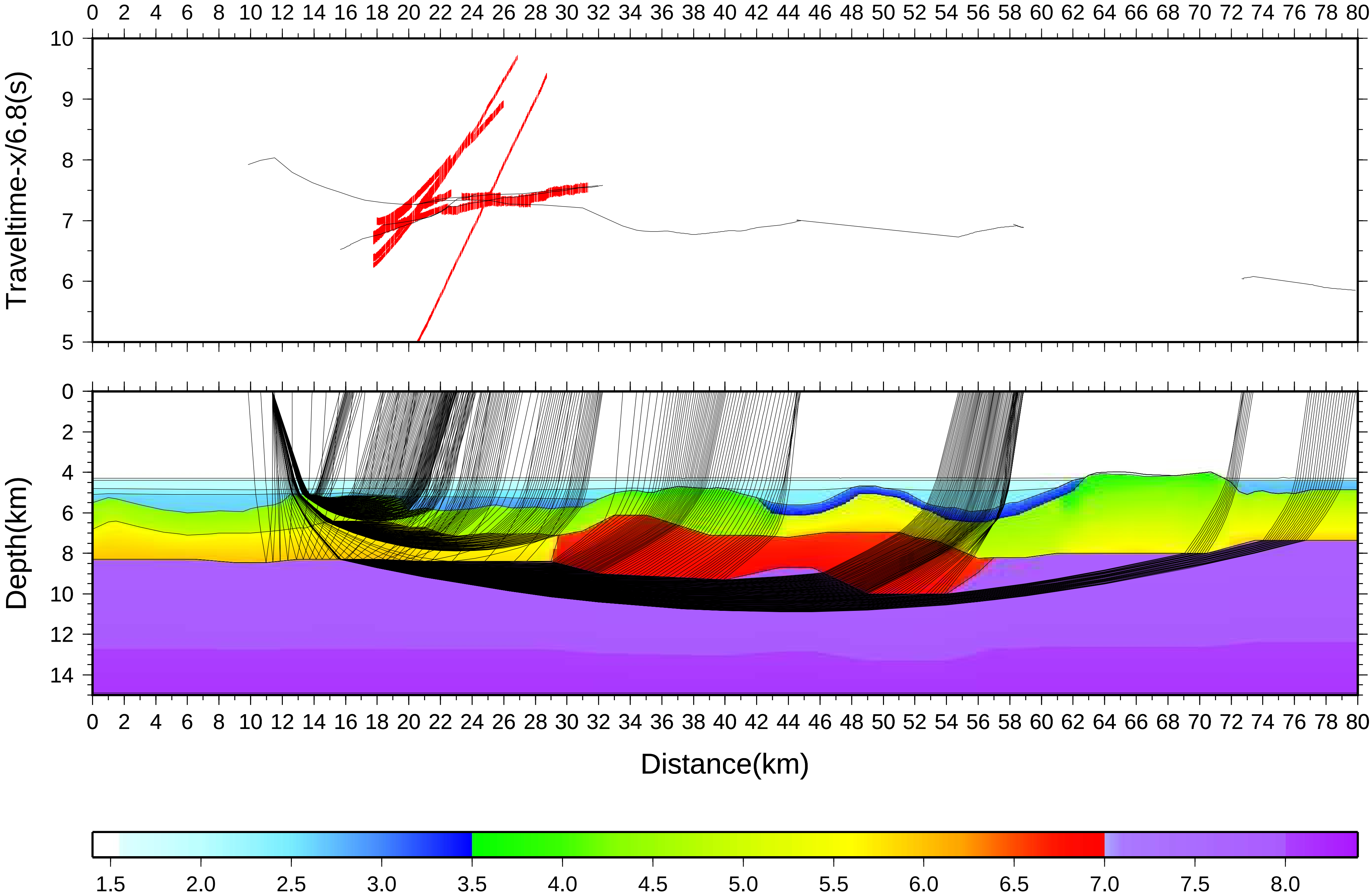
Traveltime-x/6.8(s)
Depth(km)
Distance(km)
0 2 4 6 8 10 12 14 16 18 20 22 24 26 28 30 32 34 36 38 40 42 44 46 48 50 52 54 56 58 60 62 64 66 68 70 72 74 76 78 80
1.5 2.0 2.5 3.0 3.5 4.0 4.5 5.0 5.5 6.0 6.5 7.0 7.5 8.0

LOMROG 2012 - Station 10

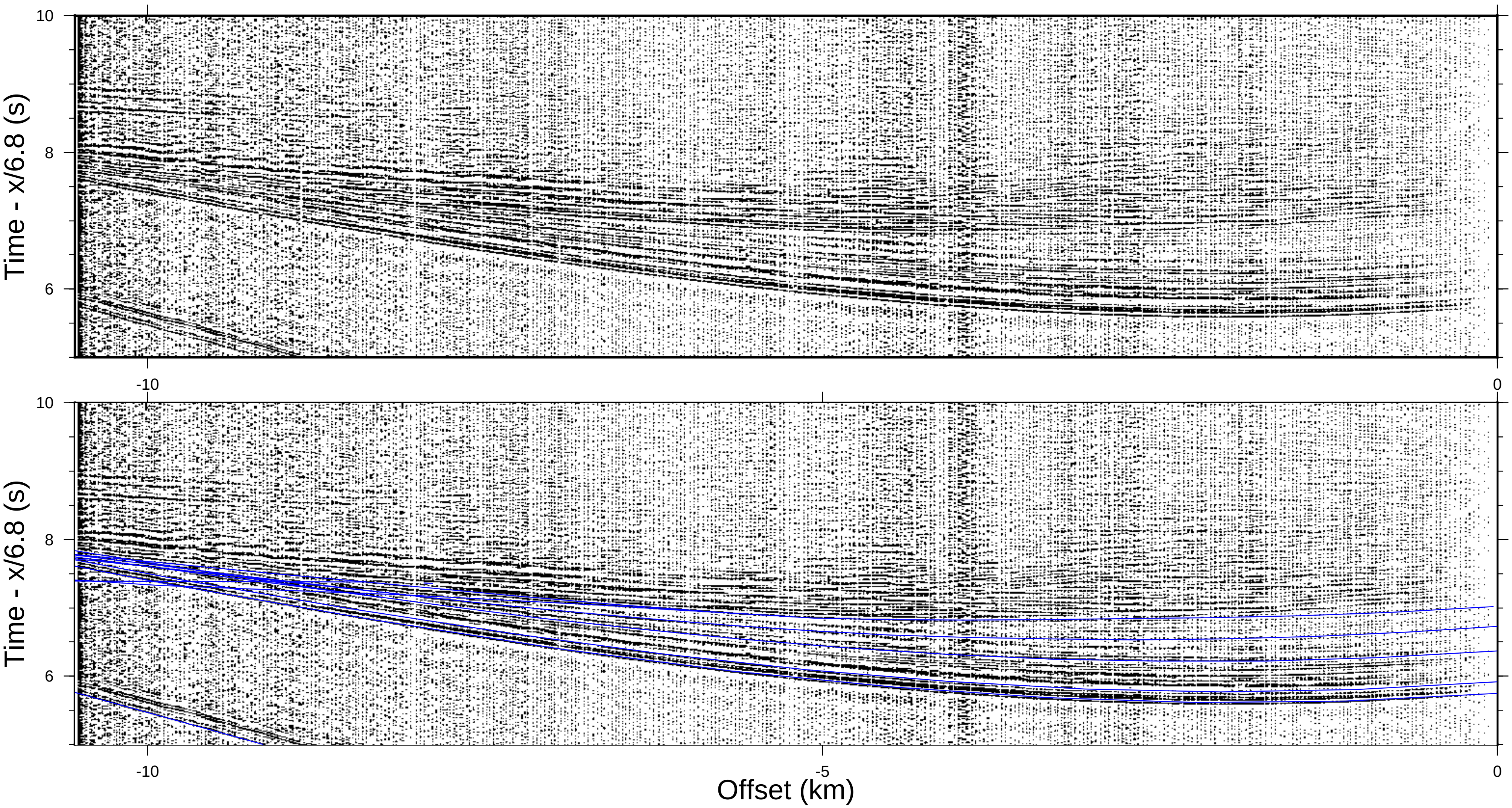

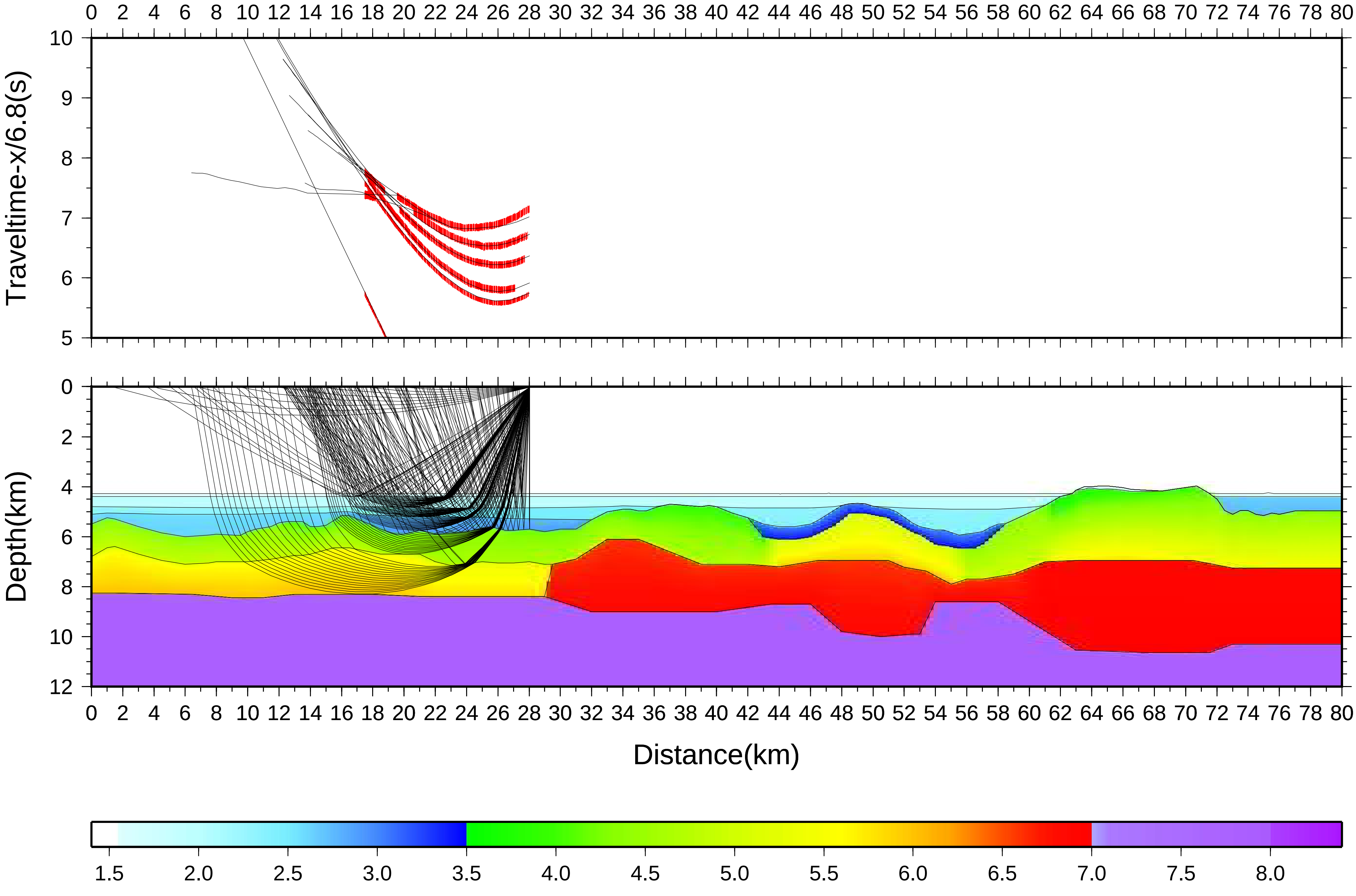

Traveltime-x/6.8(s)
Depth(km)
Distance(km)
1.5
2.0
2.5
3.0
3.5
4.0
4.5
5.0
5.5
6.0
6.5
7.0
7.5
8.0

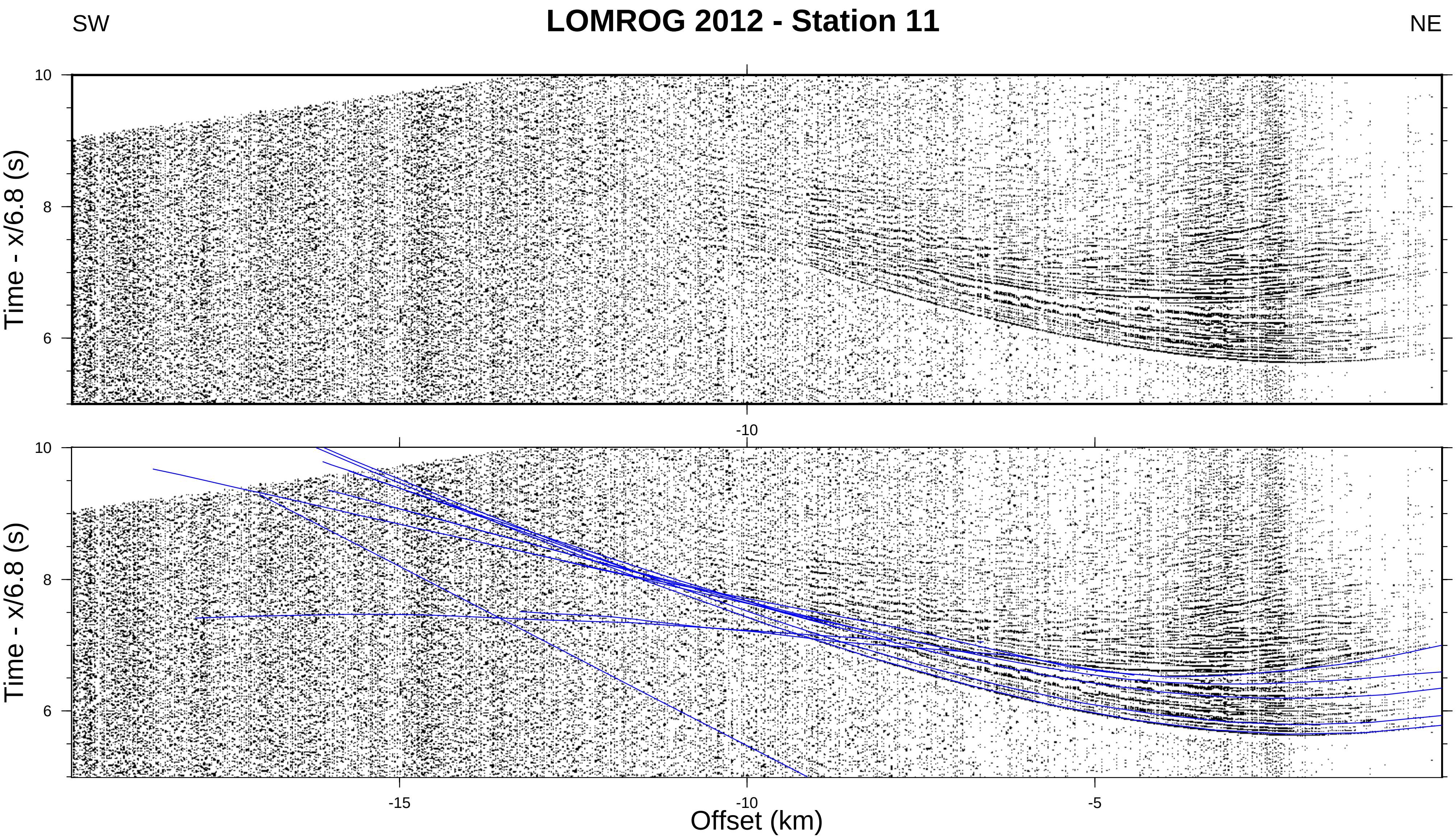
SW
LOMROG 2012 - Station 11
NE
10
8
6
Time - x/6.8 (s)
-10
10
8
6
Time - x/6.8 (s)
-15
-10
-5
Offset (km)

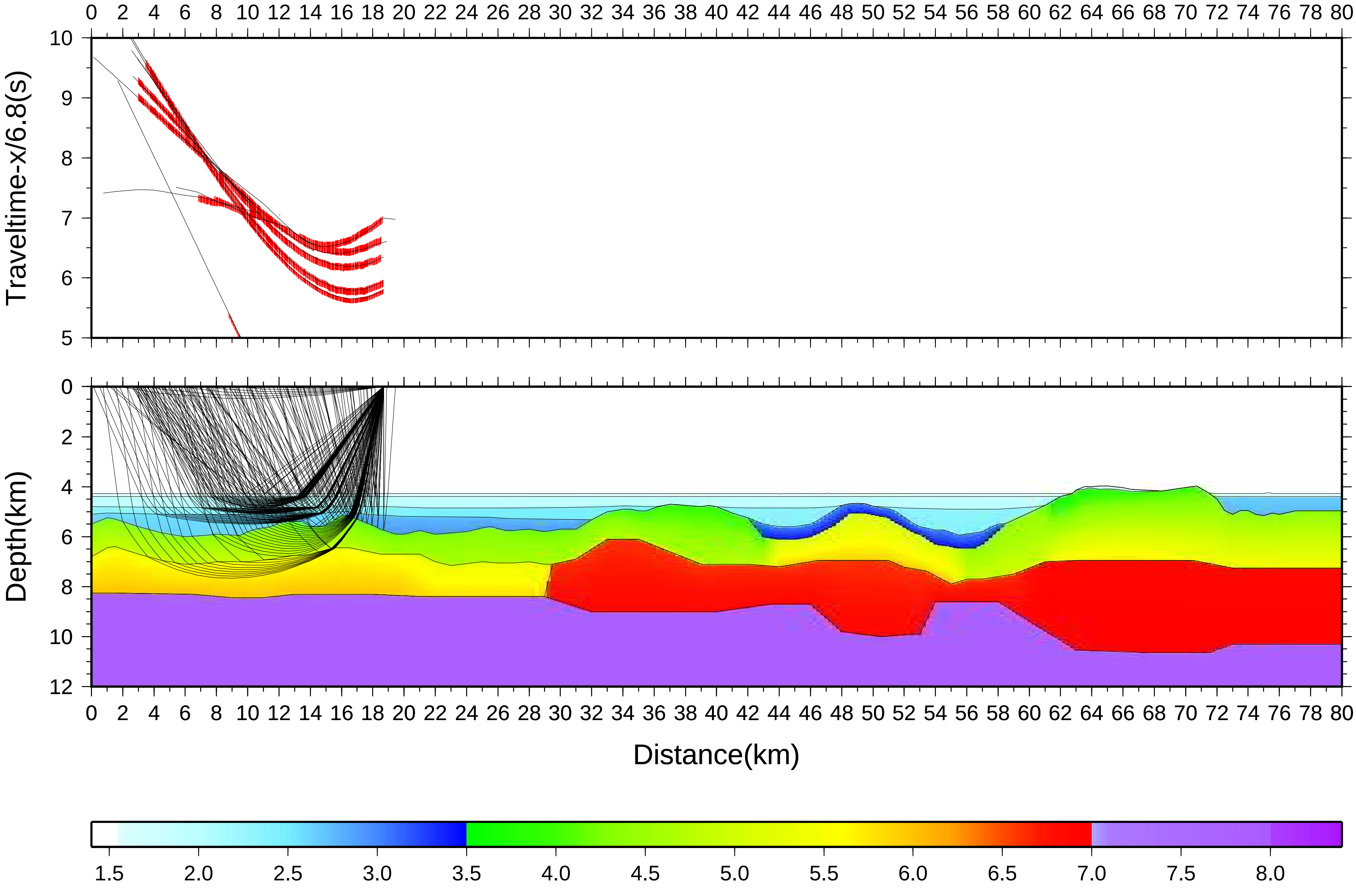
Traveltime-x/6.8(s)
Depth(km)
Distance(km)
1.5
2.0
2.5
3.0
3.5
4.0
4.5
5.0
5.5
6.0
6.5
7.0
7.5
8.0

LOMROG 2012 - Station 19

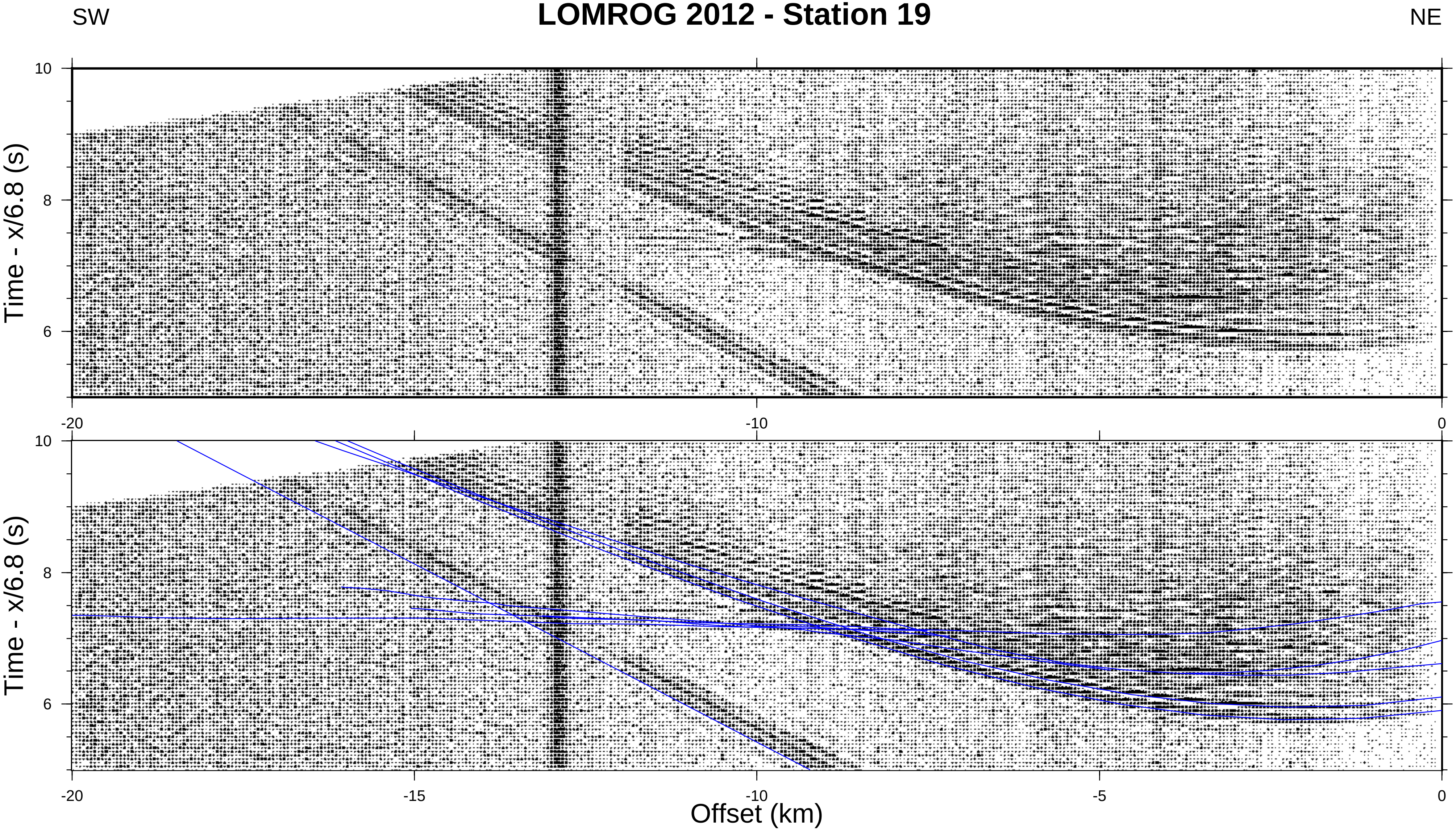

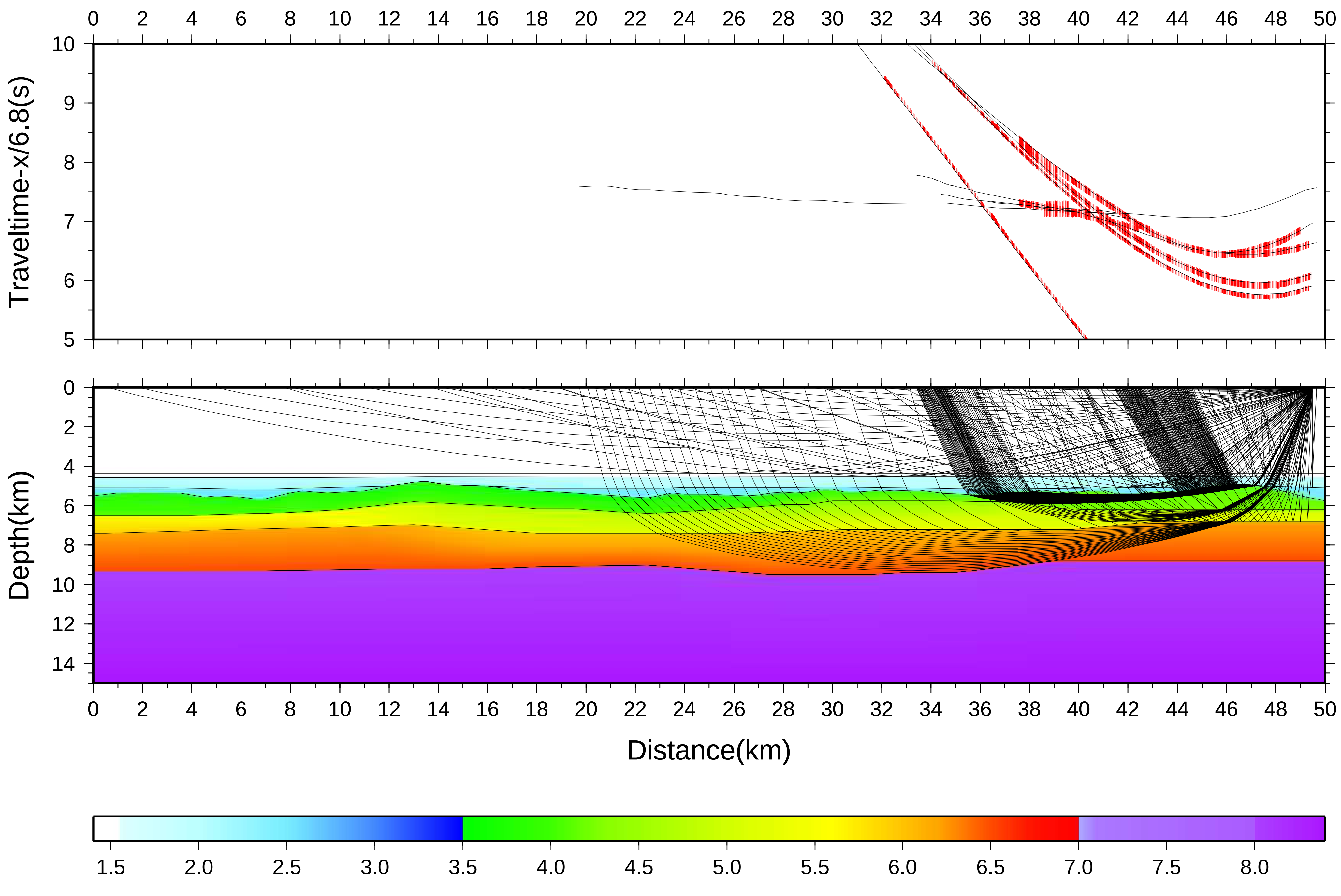

Traveltime-x/6.8(s)
Depth(km)
Distance(km)
0 2 4 6 8 10 12 14 16 18 20 22 24 26 28 30 32 34 36 38 40 42 44 46 48 50
10 9 8 7 6 5
0 2 4 6 8 10 12 14
1.5 2.0 2.5 3.0 3.5 4.0 4.5 5.0 5.5 6.0 6.5 7.0 7.5 8.0

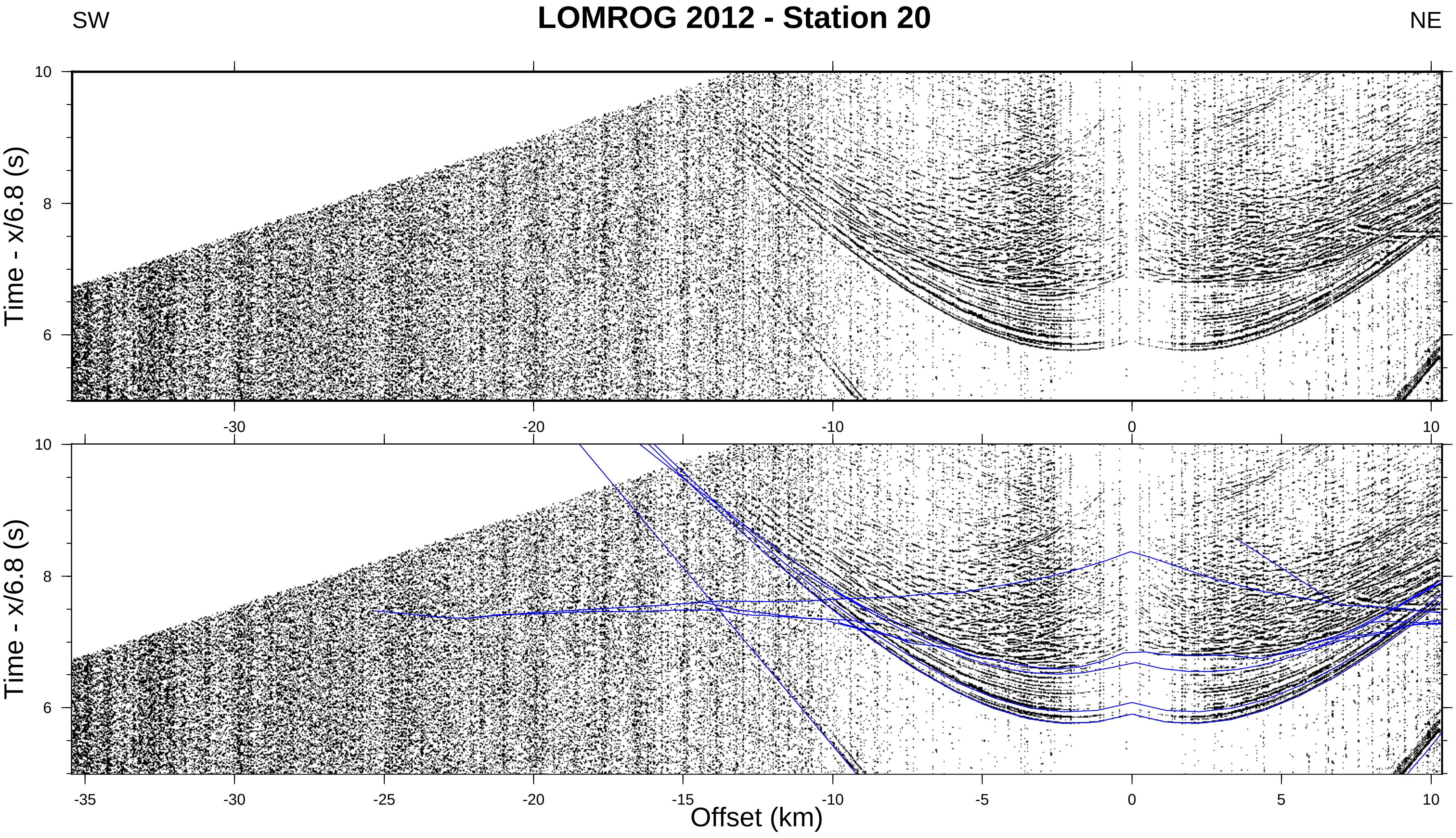
SW
LOMROG 2012 - Station 20
NE
Time - x/6.8 (s)
10
8
6
-30
-20
-10
0
10
Time - x/6.8 (s)
10
8
6
-35
-30
-25
-20
-15
-10
-5
0
5
10
Offset (km)

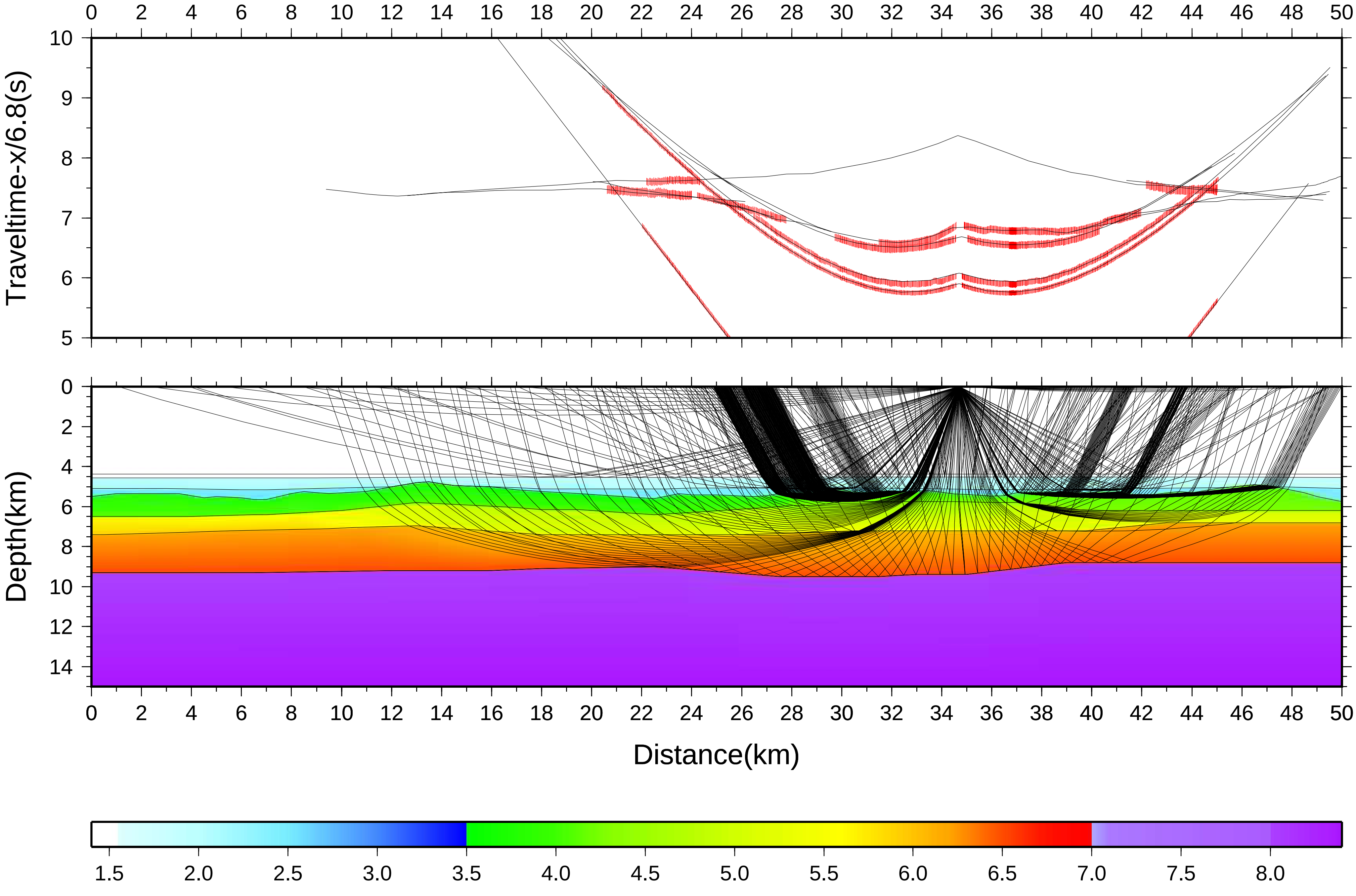
Traveltime-x/6.8(s)
Depth(km)
Distance(km)
0 2 4 6 8 10 12 14 16 18 20 22 24 26 28 30 32 34 36 38 40 42 44 46 48 50
1.5 2.0 2.5 3.0 3.5 4.0 4.5 5.0 5.5 6.0 6.5 7.0 7.5 8.0

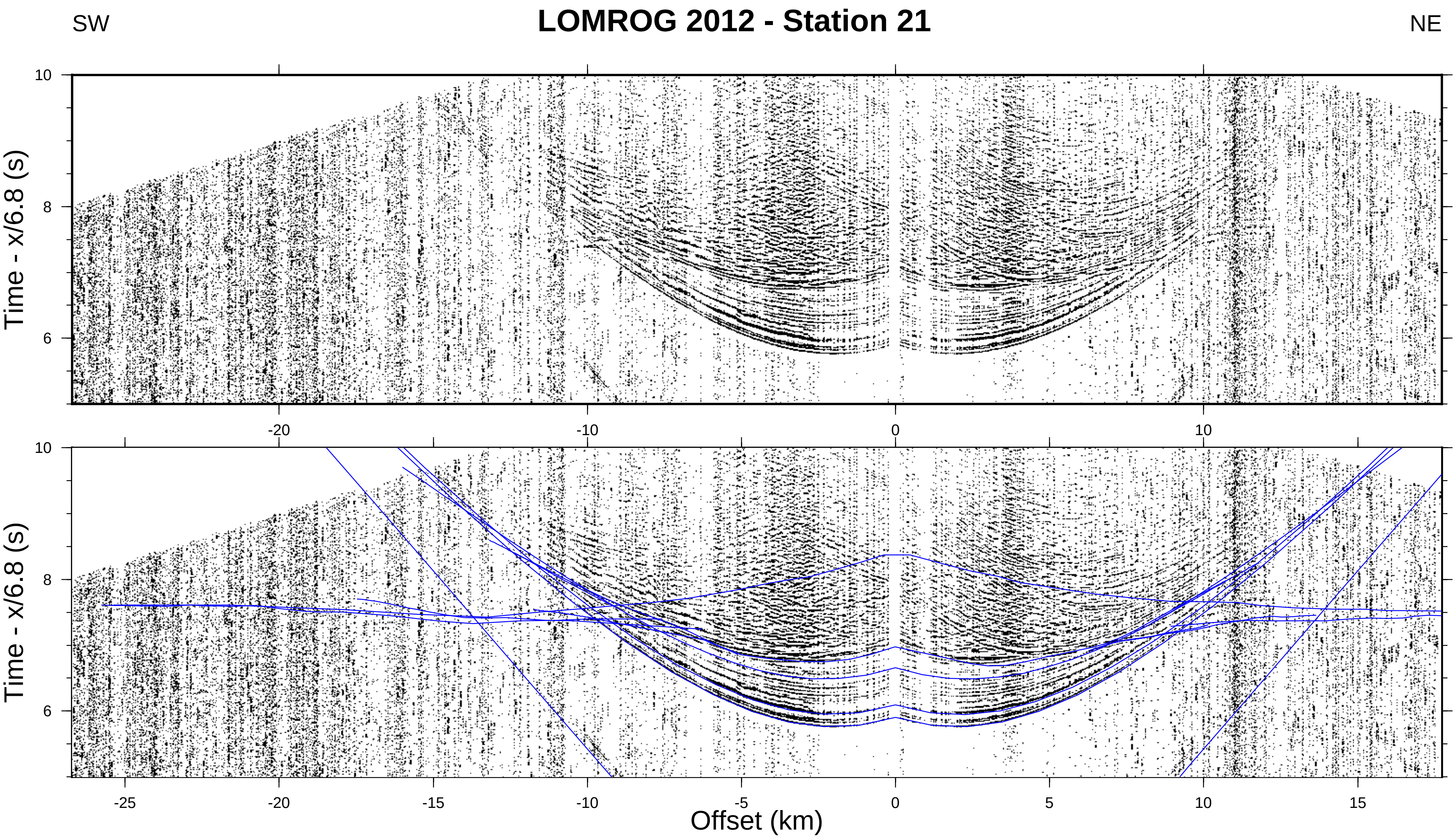
SW
LOMROG 2012 - Station 21
NE
Time - x/6.8 (s)
Offset (km)
10
8
6
-25
-20
-15
-10
-5
0
5
10
15

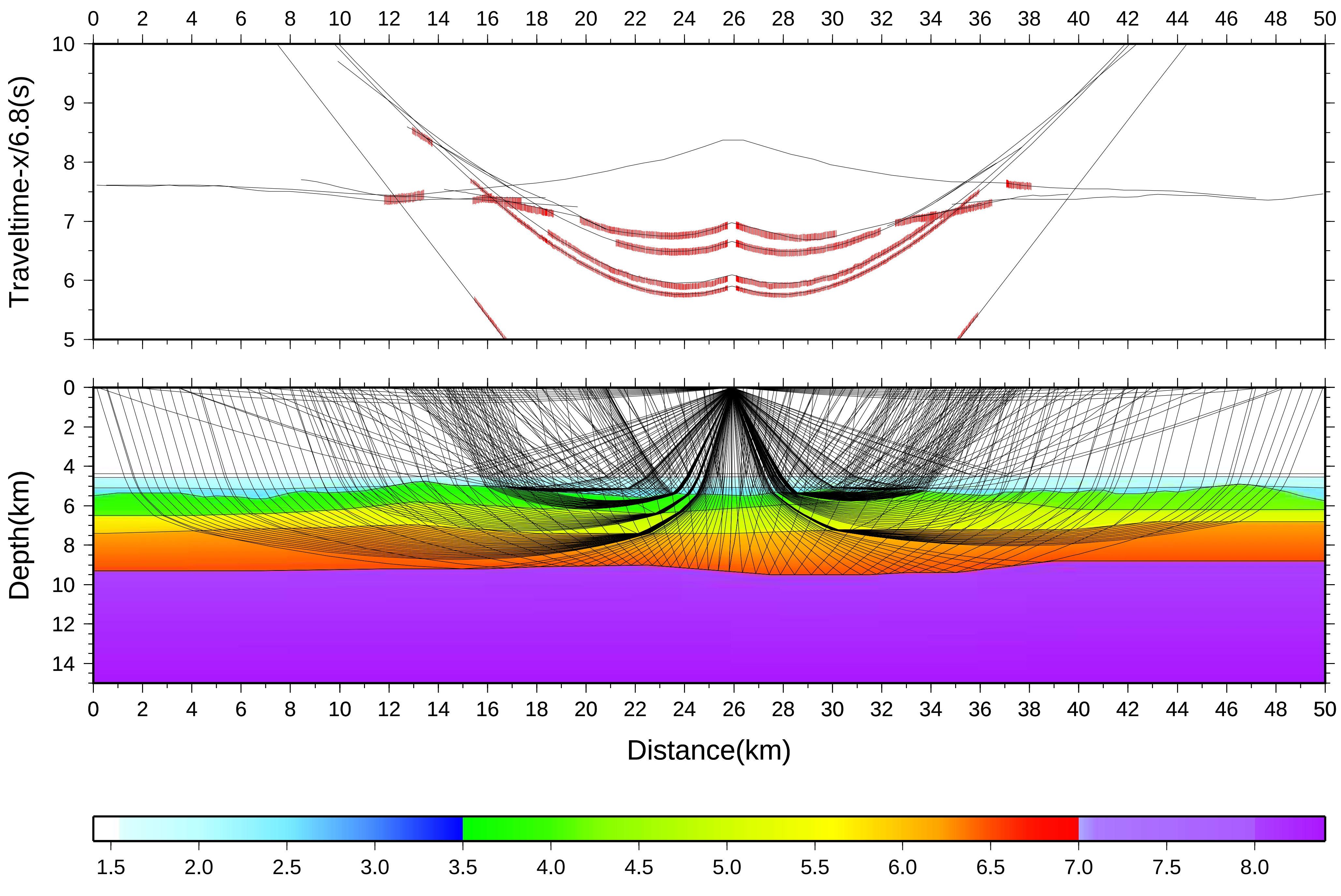

Traveltime-x/6.8(s)
Depth(km)
Distance(km)
0 2 4 6 8 10 12 14 16 18 20 22 24 26 28 30 32 34 36 38 40 42 44 46 48 50
1.5 2.0 2.5 3.0 3.5 4.0 4.5 5.0 5.5 6.0 6.5 7.0 7.5 8.0

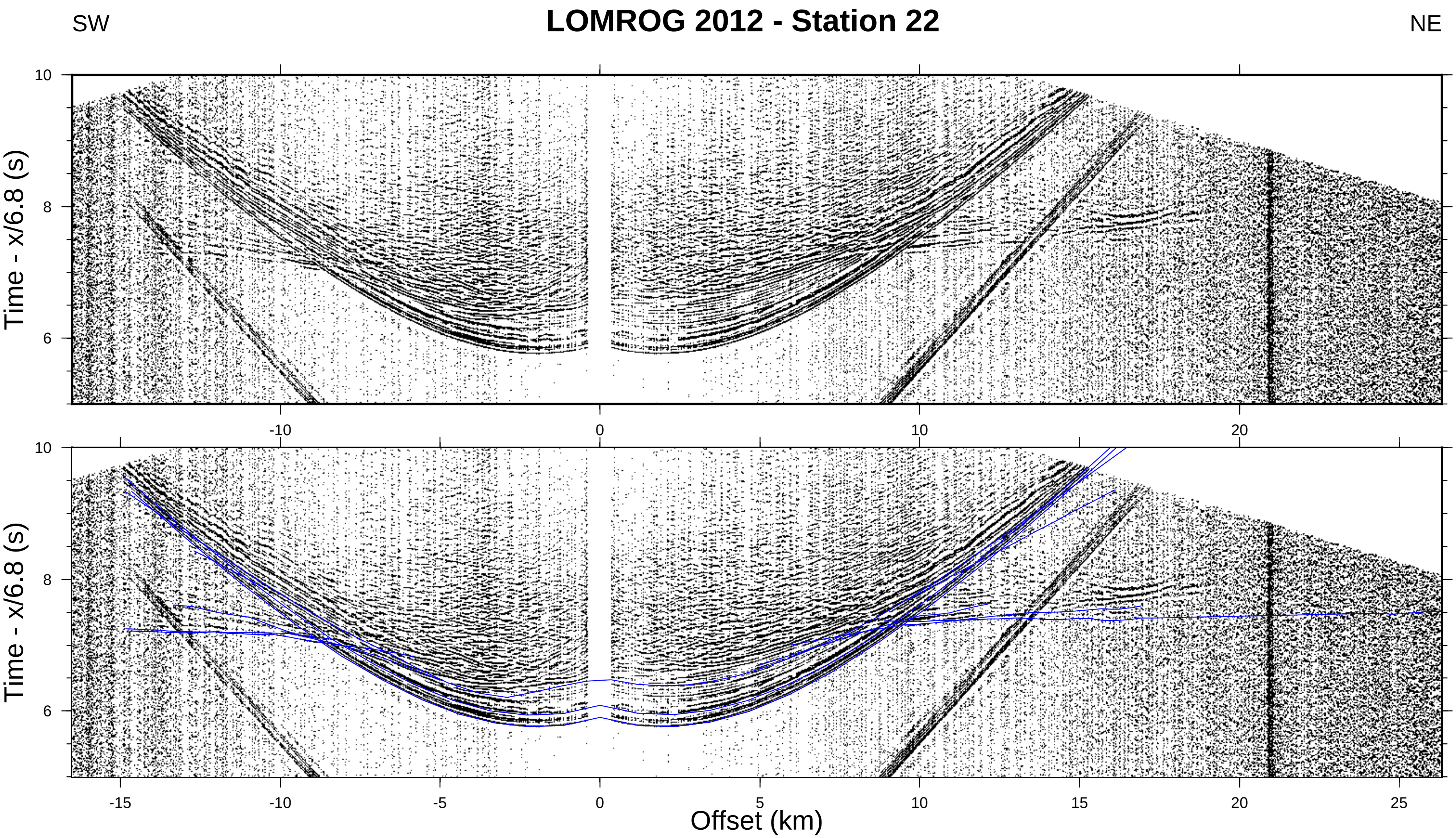
SW
LOMROG 2012 - Station 22
NE
Time - x/6.8 (s)
10
8
6
-10
0
10
20
Time - x/6.8 (s)
10
8
6
-15
-10
-5
0
5
10
15
20
25
Offset (km)

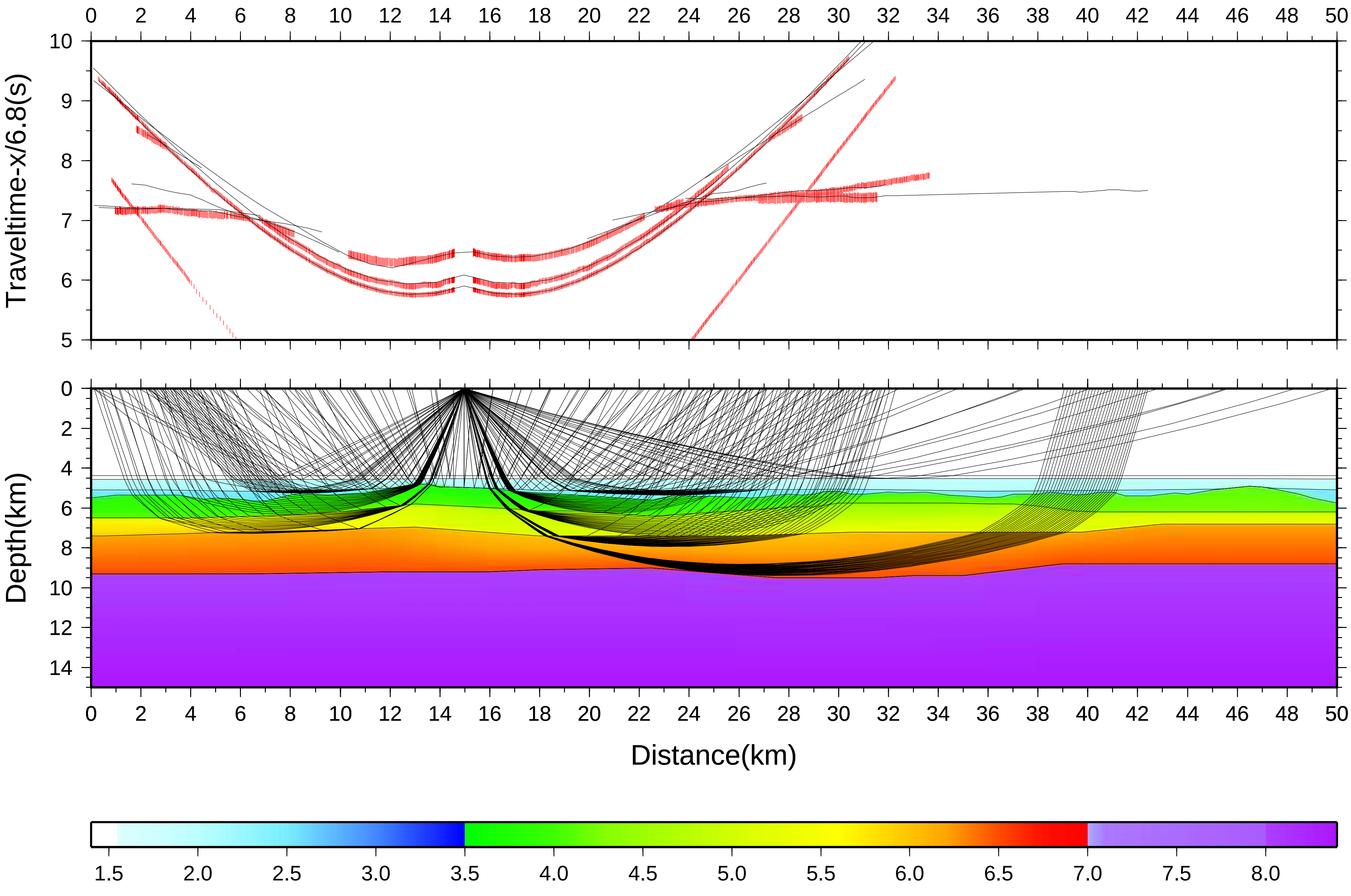

Traveltime-x/6.8(s)
Depth(km)
Distance(km)
0 2 4 6 8 10 12 14 16 18 20 22 24 26 28 30 32 34 36 38 40 42 44 46 48 50
1.5 2.0 2.5 3.0 3.5 4.0 4.5 5.0 5.5 6.0 6.5 7.0 7.5 8.0

LOMROG 2012 - Station 23

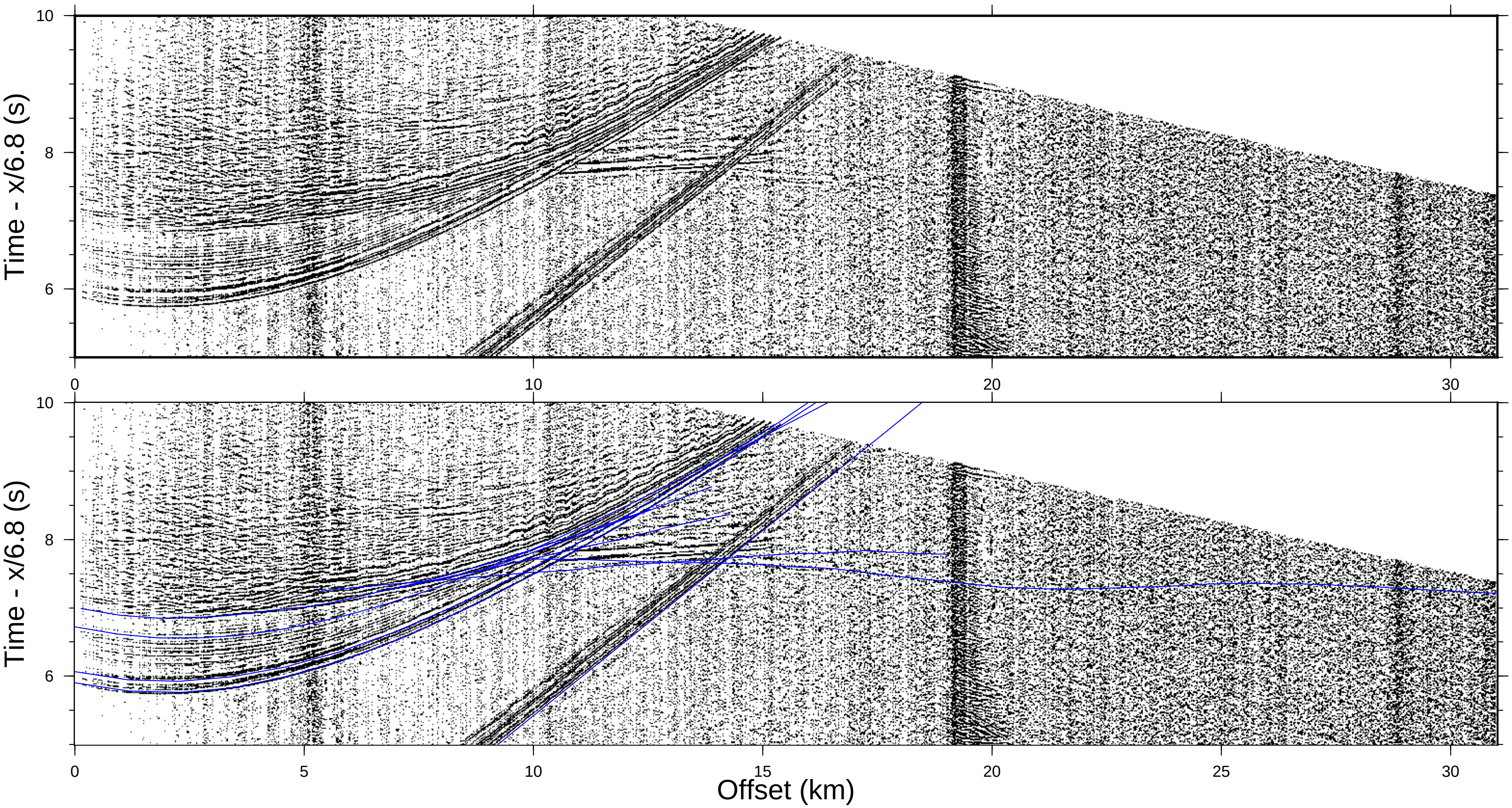

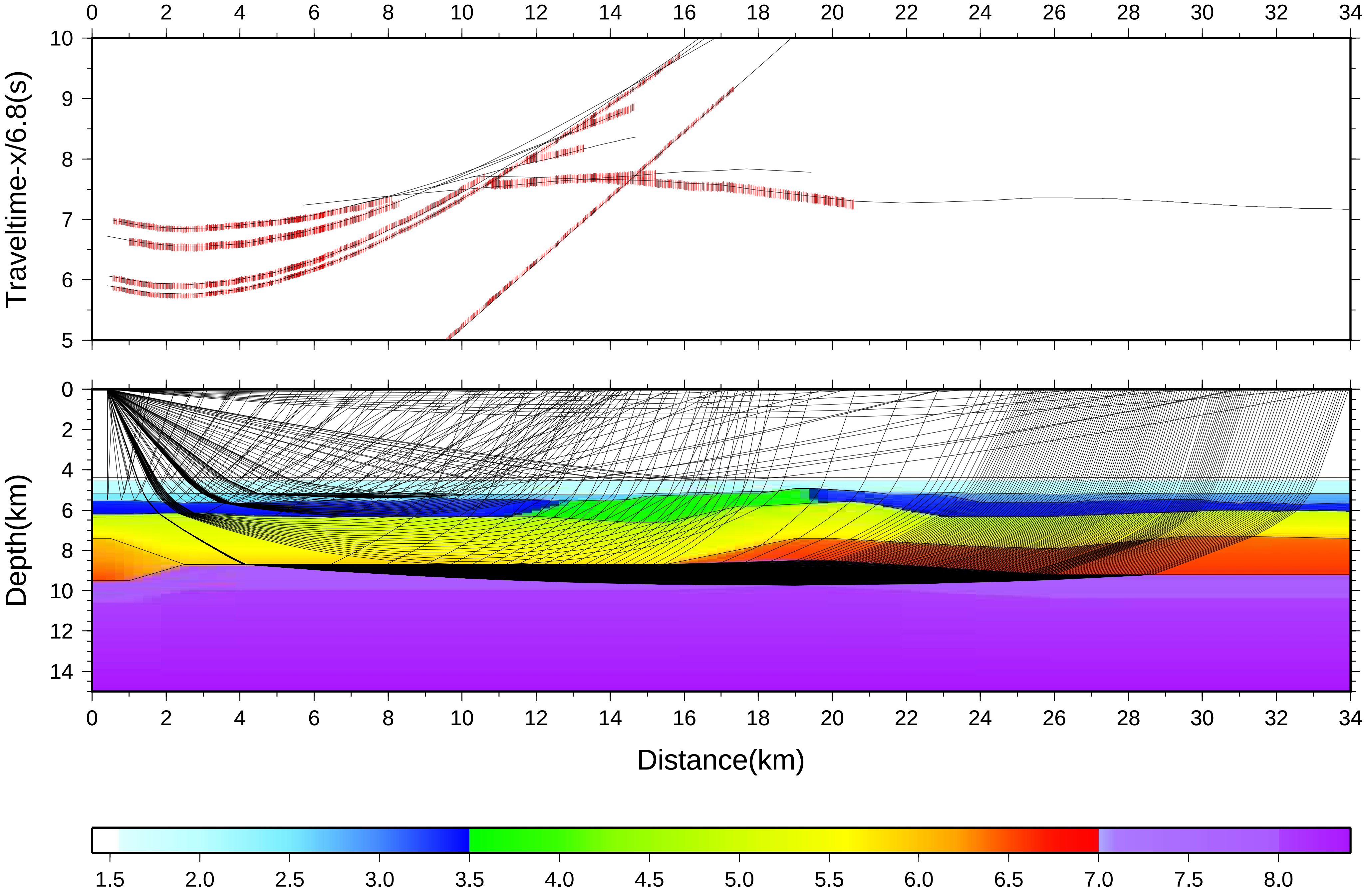
Traveltime-x/6.8(s)
Depth(km)
Distance(km)
0 2 4 6 8 10 12 14 16 18 20 22 24 26 28 30 32 34
1.5 2.0 2.5 3.0 3.5 4.0 4.5 5.0 5.5 6.0 6.5 7.0 7.5 8.0

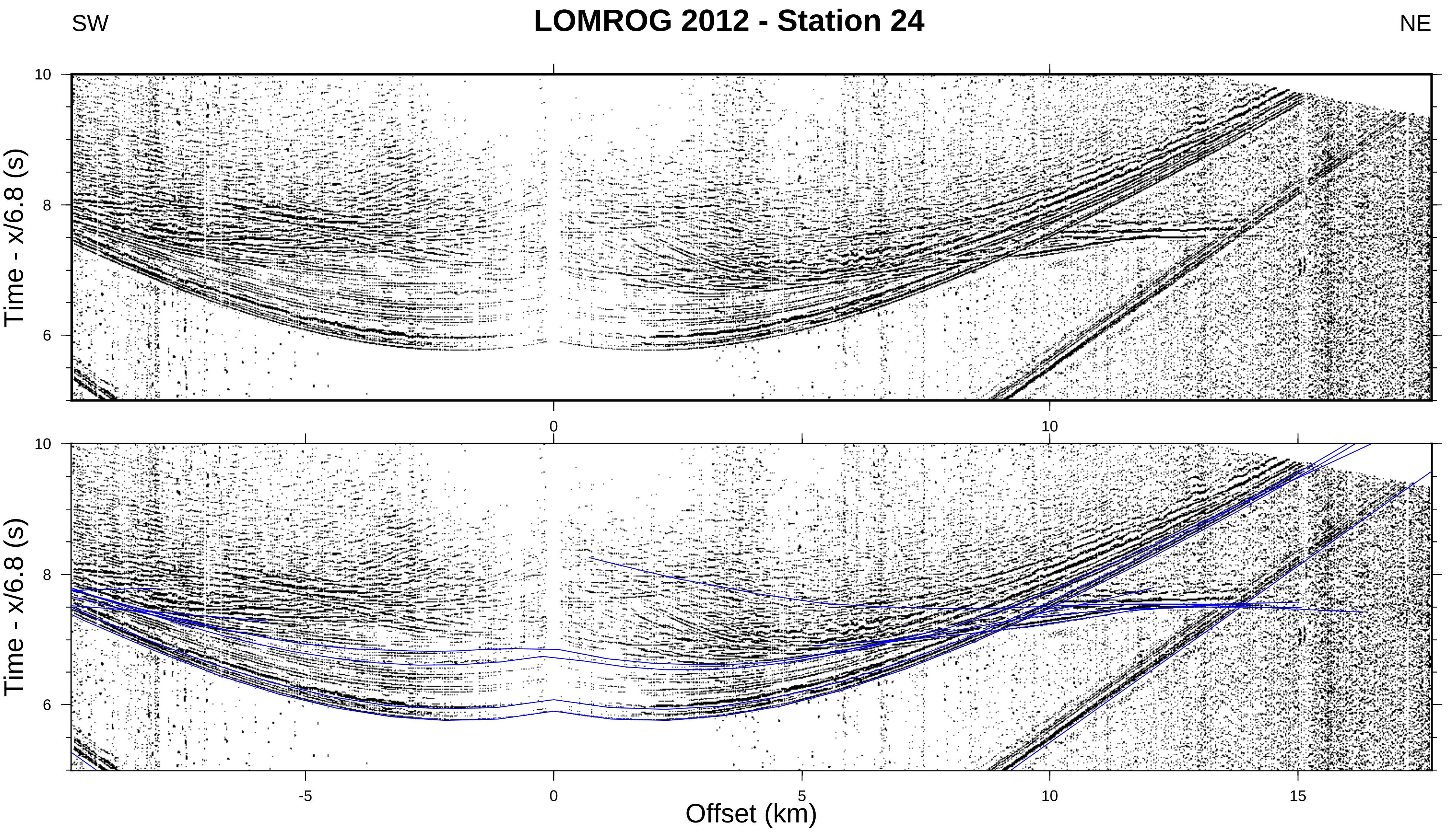

SW
LOMROG 2012 - Station 24
NE
Time - x/6.8 (s)
10
8
6
0
10
Time - x/6.8 (s)
10
8
6
-5
0
5
10
15
Offset (km)

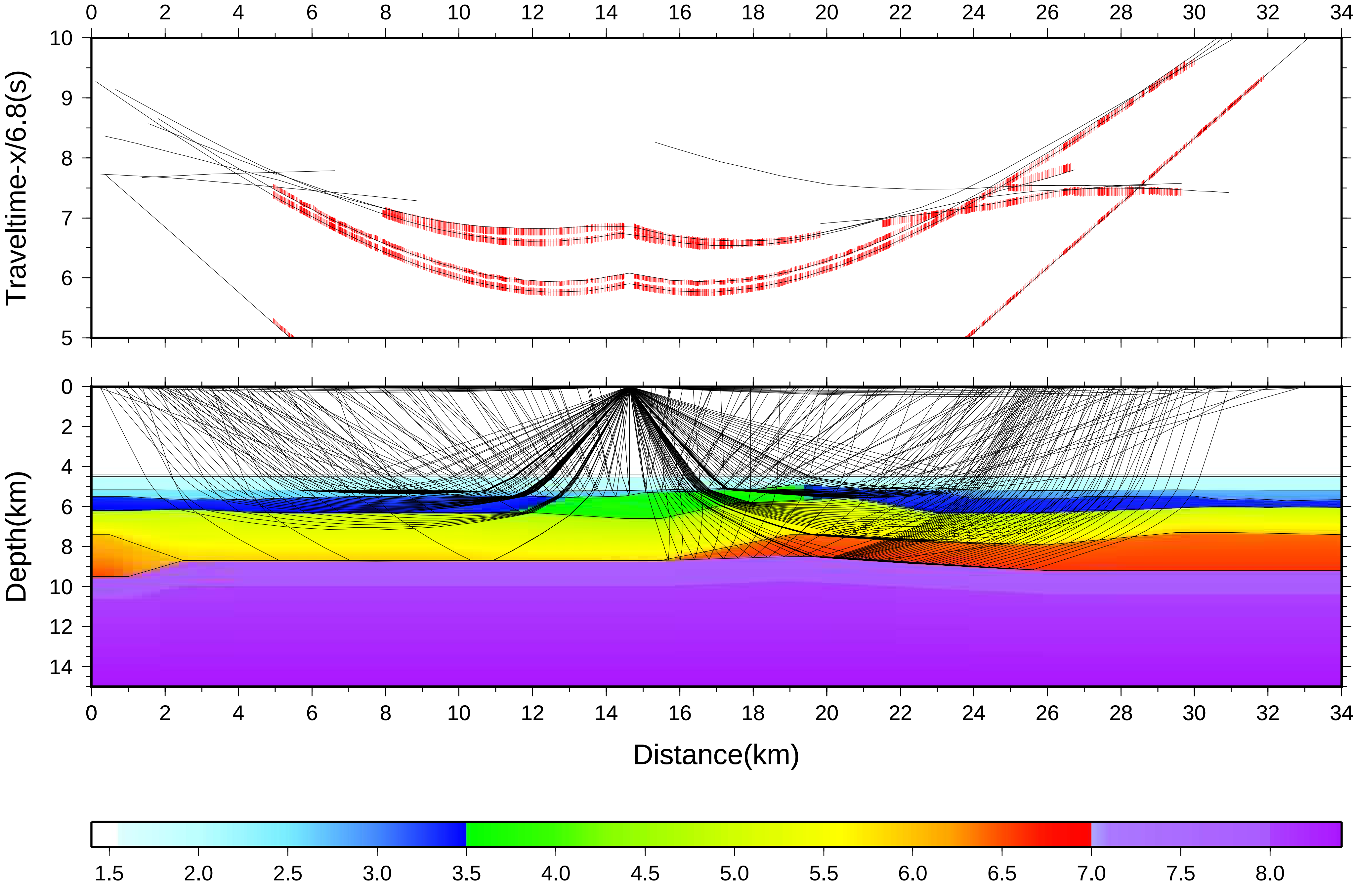

Traveltime-x/6.8(s)
Depth(km)
Distance(km)
0 2 4 6 8 10 12 14 16 18 20 22 24 26 28 30 32 34
10 9 8 7 6 5
0 2 4 6 8 10 12 14
1.5 2.0 2.5 3.0 3.5 4.0 4.5 5.0 5.5 6.0 6.5 7.0 7.5 8.0

LOMROG 2012 - Station 25

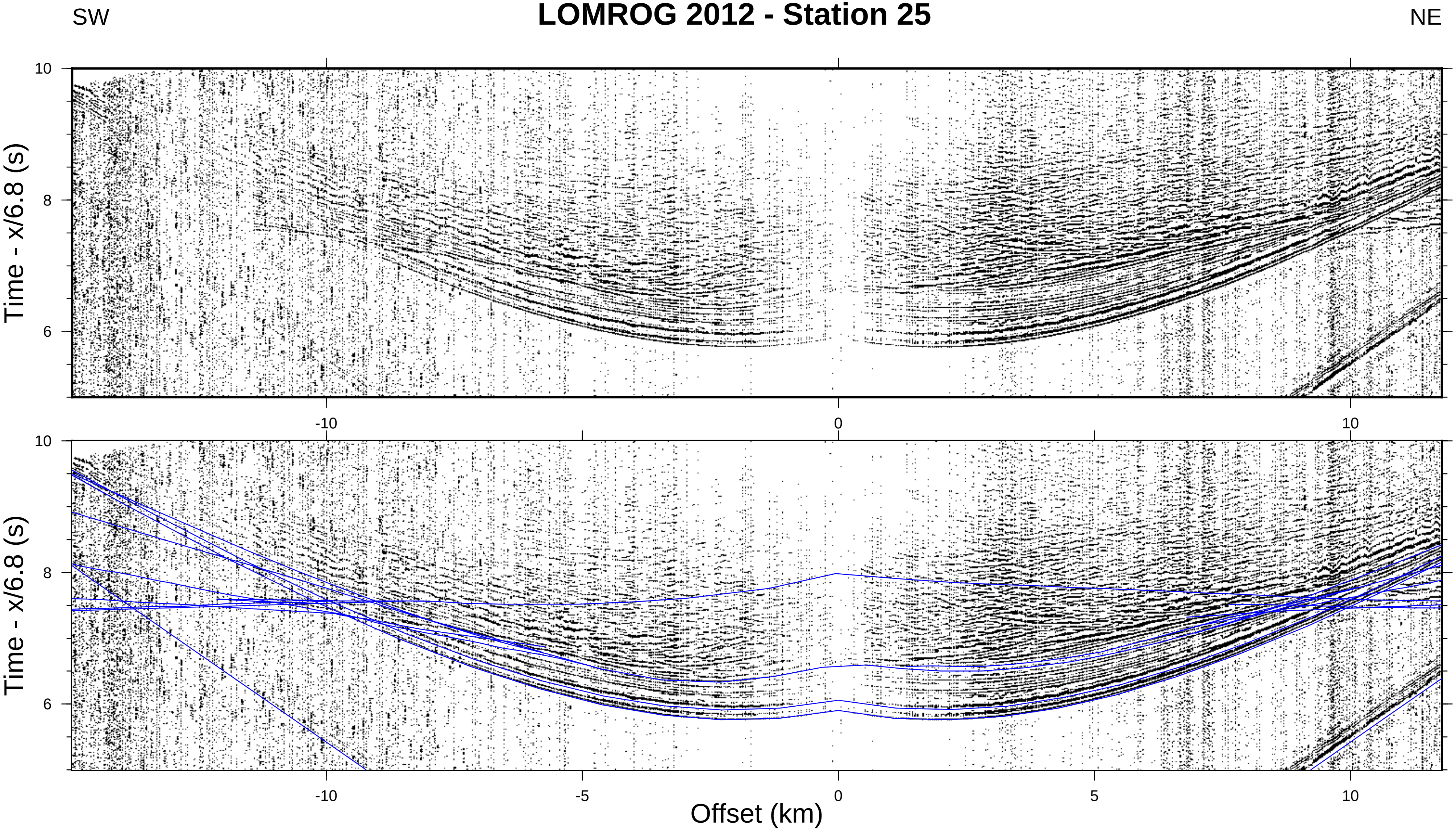

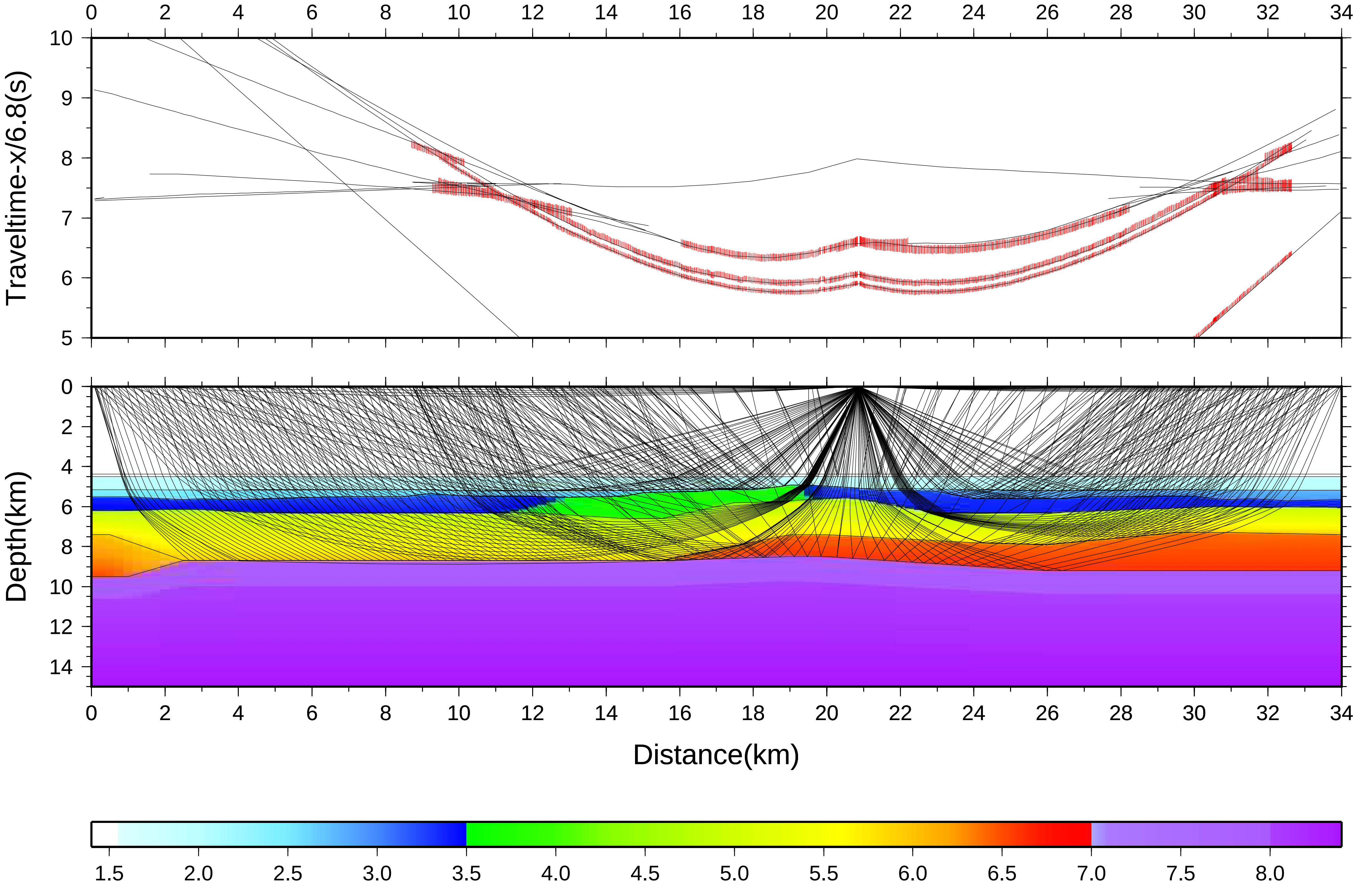

Traveltime-x/6.8(s)
Depth(km)
Distance(km)
0 2 4 6 8 10 12 14 16 18 20 22 24 26 28 30 32 34
1.5 2.0 2.5 3.0 3.5 4.0 4.5 5.0 5.5 6.0 6.5 7.0 7.5 8.0

LOMROG 2012 - Station 26

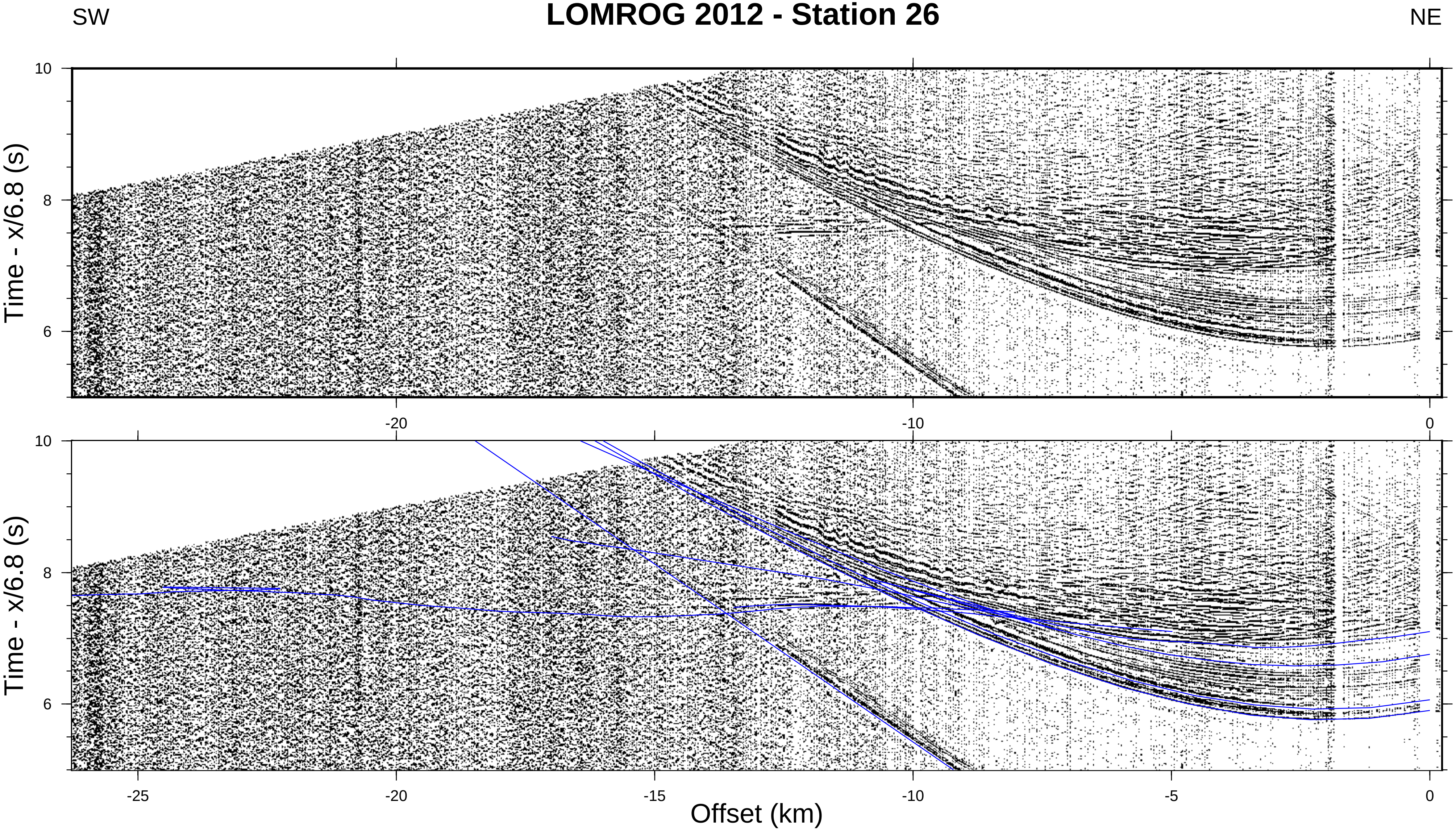

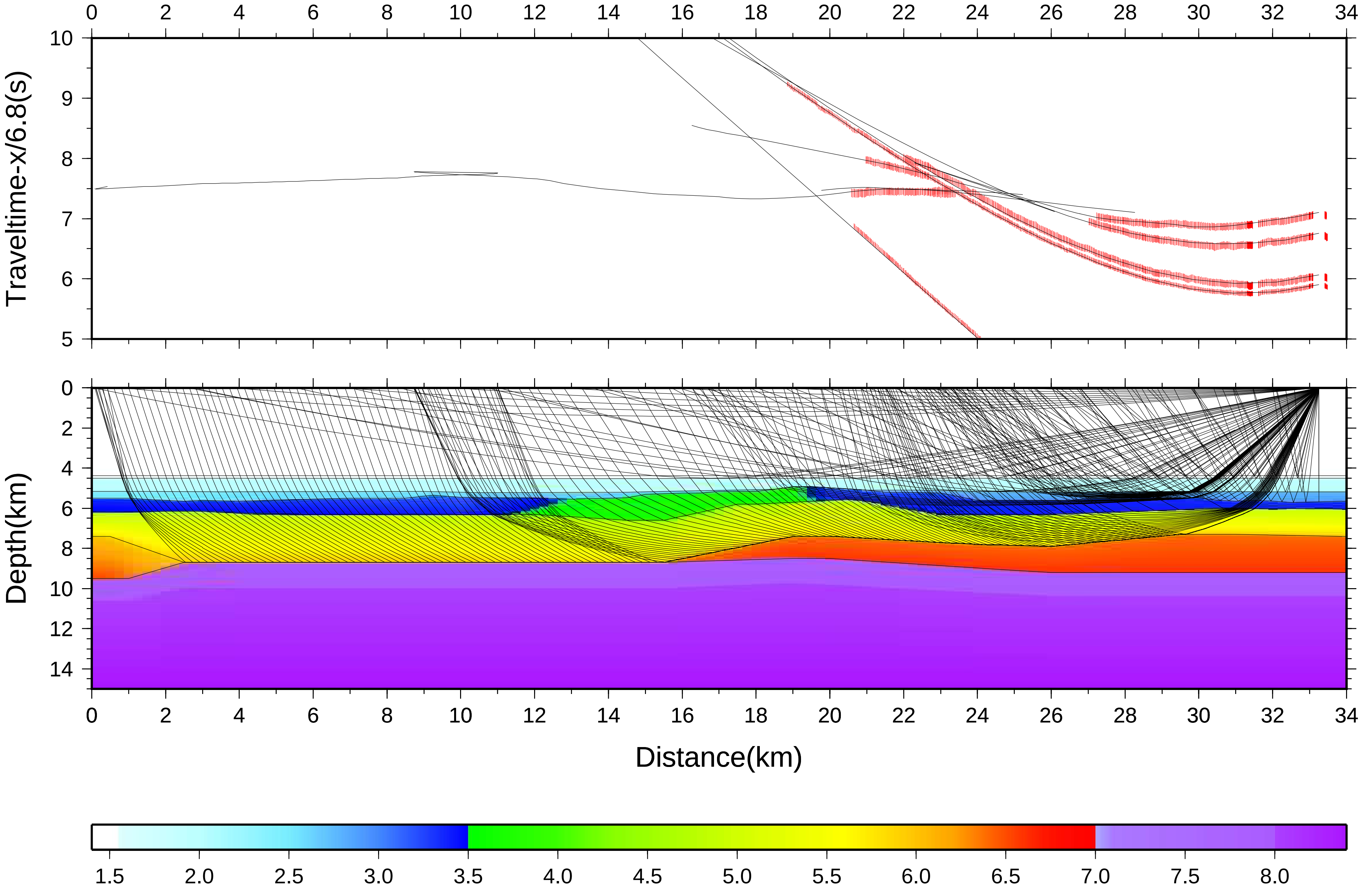

Traveltime-x/6.8(s)
Depth(km)
Distance(km)

LOMROG 2012 - Station 27

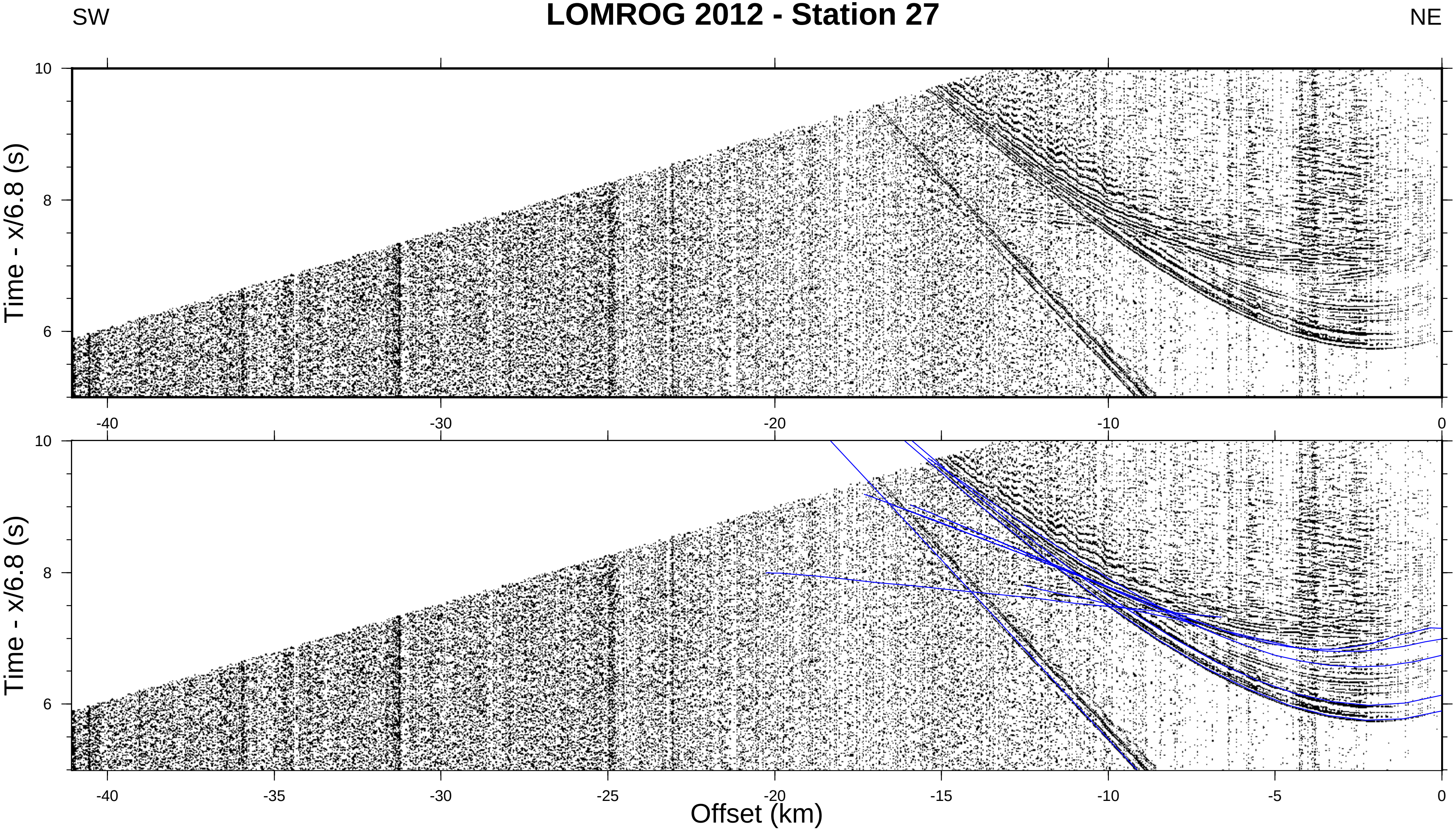

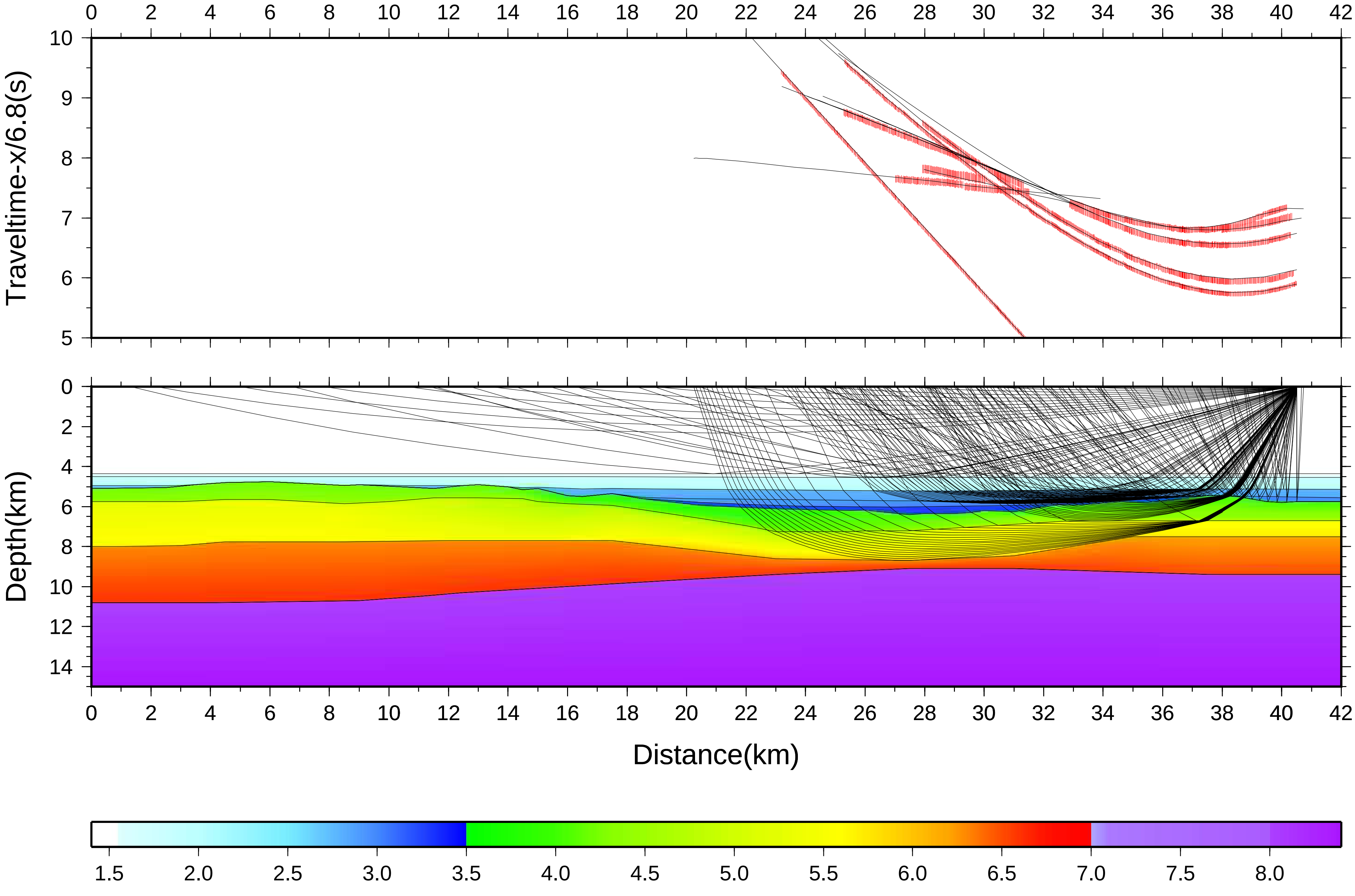

Traveltime-x/6.8(s)
Depth(km)
Distance(km)
0 2 4 6 8 10 12 14 16 18 20 22 24 26 28 30 32 34 36 38 40 42
10 9 8 7 6 5
0 2 4 6 8 10 12 14
1.5 2.0 2.5 3.0 3.5 4.0 4.5 5.0 5.5 6.0 6.5 7.0 7.5 8.0

LOMROG 2012 - Station 28

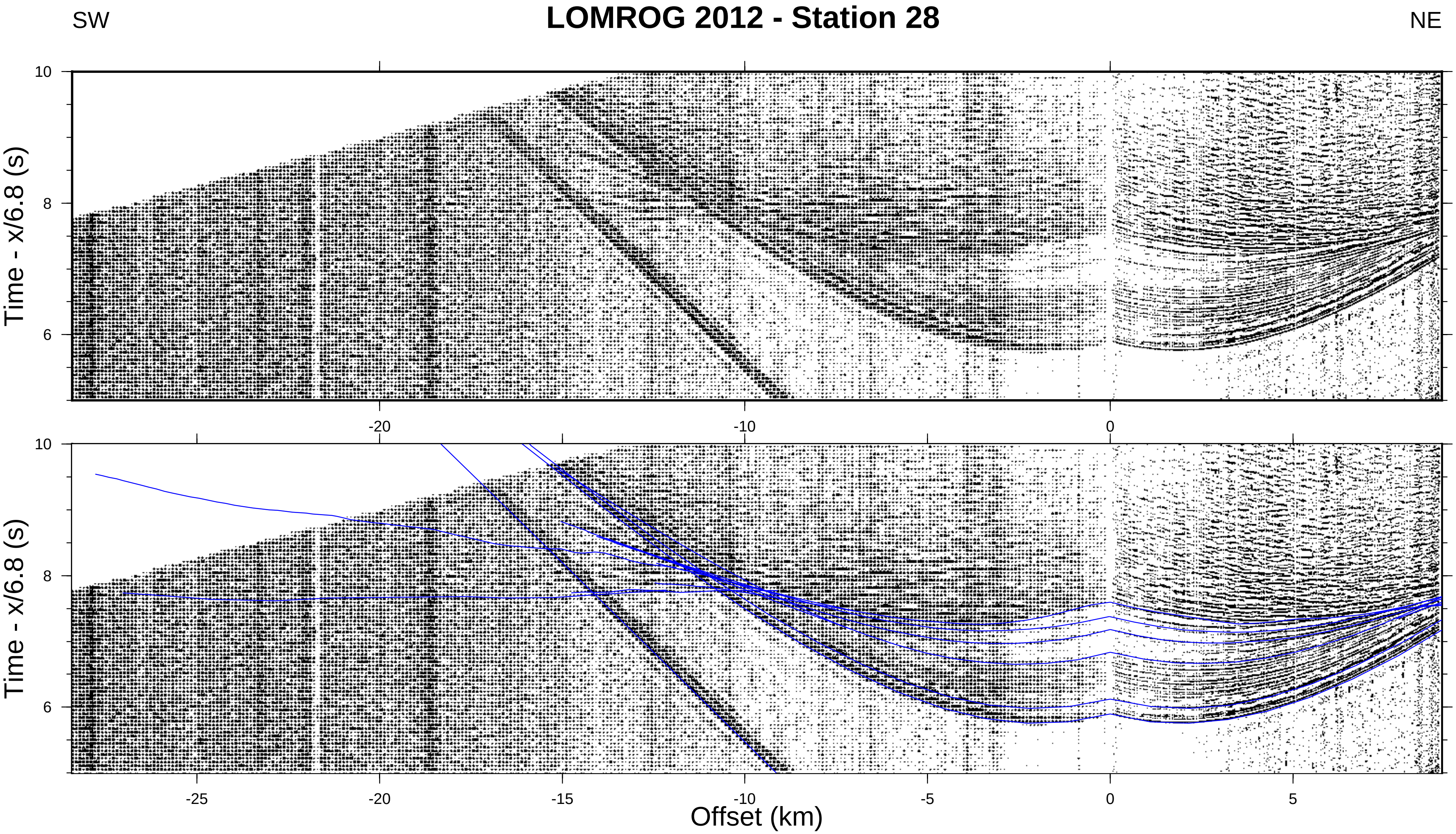

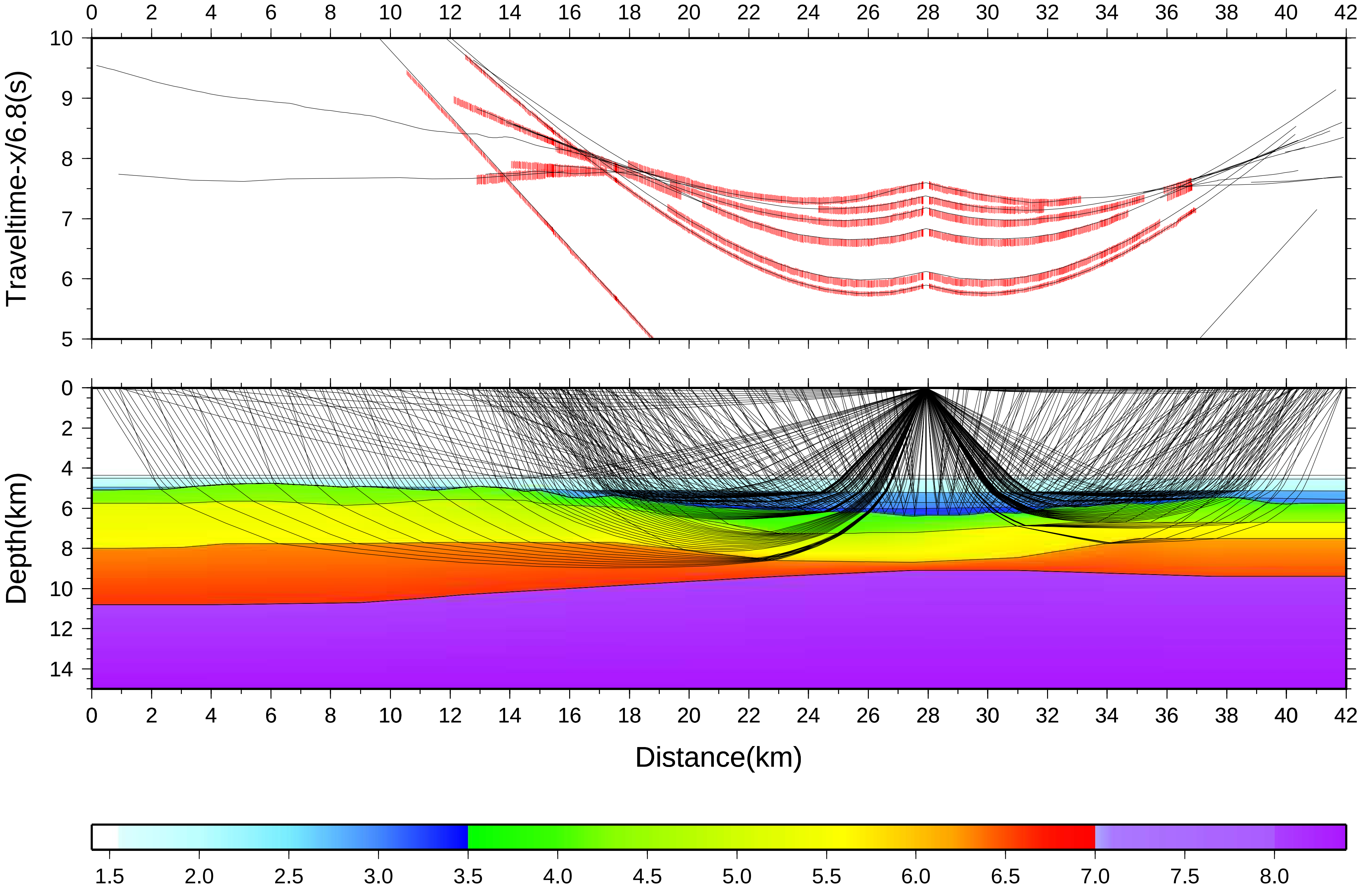
Traveltime-x/6.8(s)
Depth(km)
Distance(km)
1.5
2.0
2.5
3.0
3.5
4.0
4.5
5.0
5.5
6.0
6.5
7.0
7.5
8.0

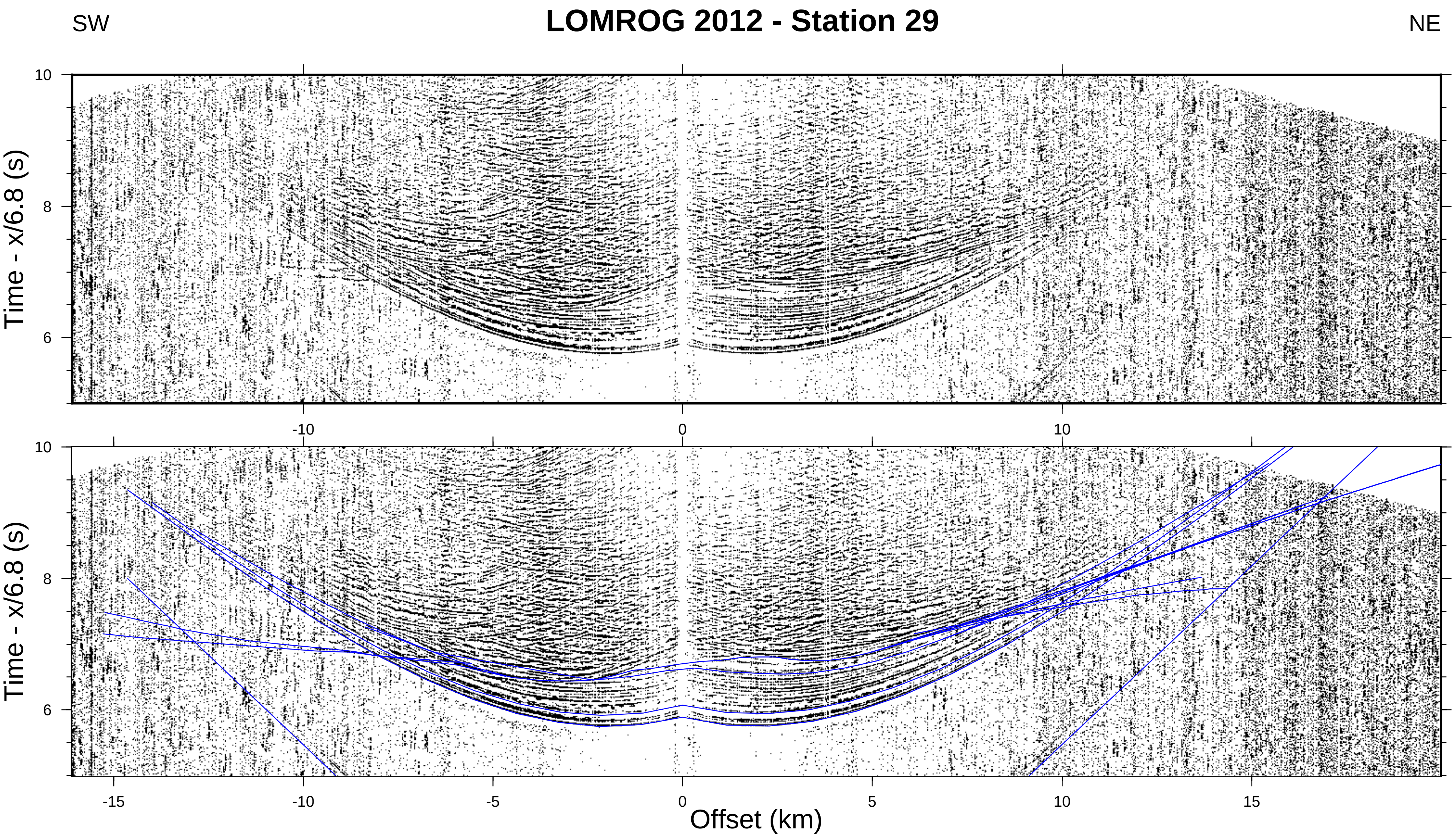

SW
LOMROG 2012 - Station 29
NE
Time - x/6.8 (s)
10
8
6
-10
0
10
Time - x/6.8 (s)
10
8
6
-15
-10
-5
0
5
10
15
Offset (km)

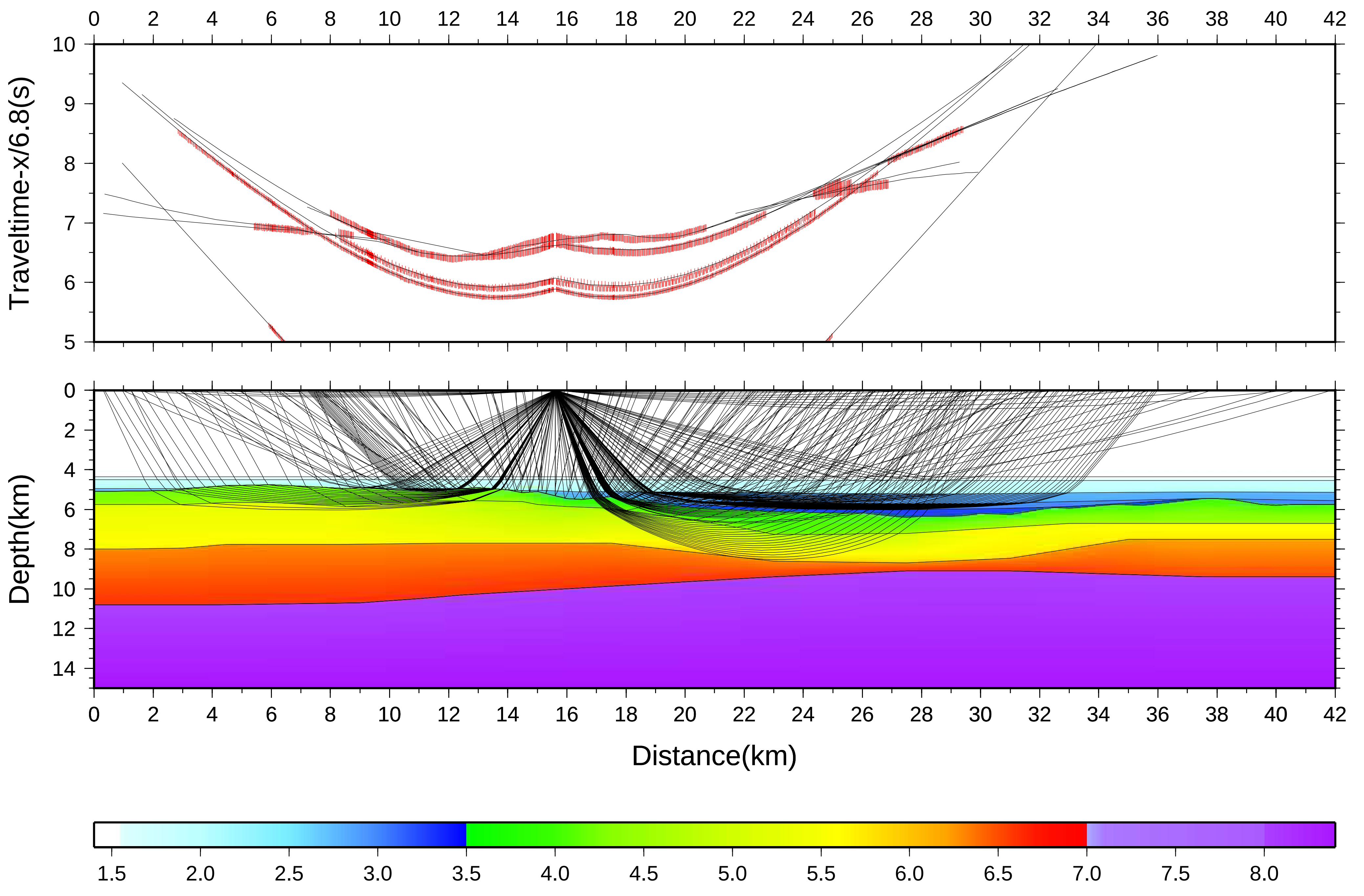

Traveltime-x/6.8(s)
Depth(km)
Distance(km)
0
2
4
6
8
10
12
14
16
18
20
22
24
26
28
30
32
34
36
38
40
42
5
6
7
8
9
10
1.5
2.0
2.5
3.0
3.5
4.0
4.5
5.0
5.5
6.0
6.5
7.0
7.5
8.0

LOMROG 2012 - Station 30

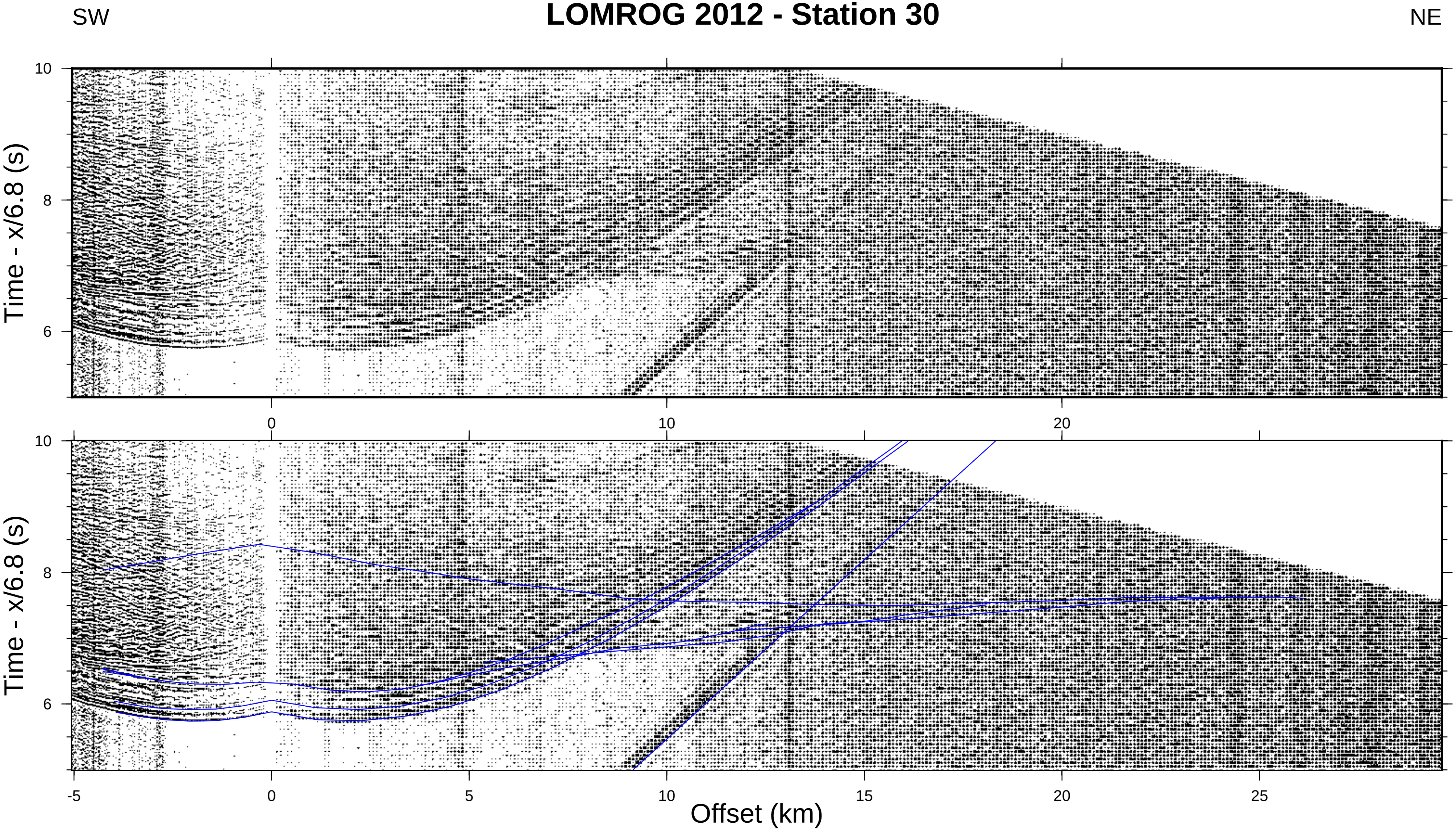

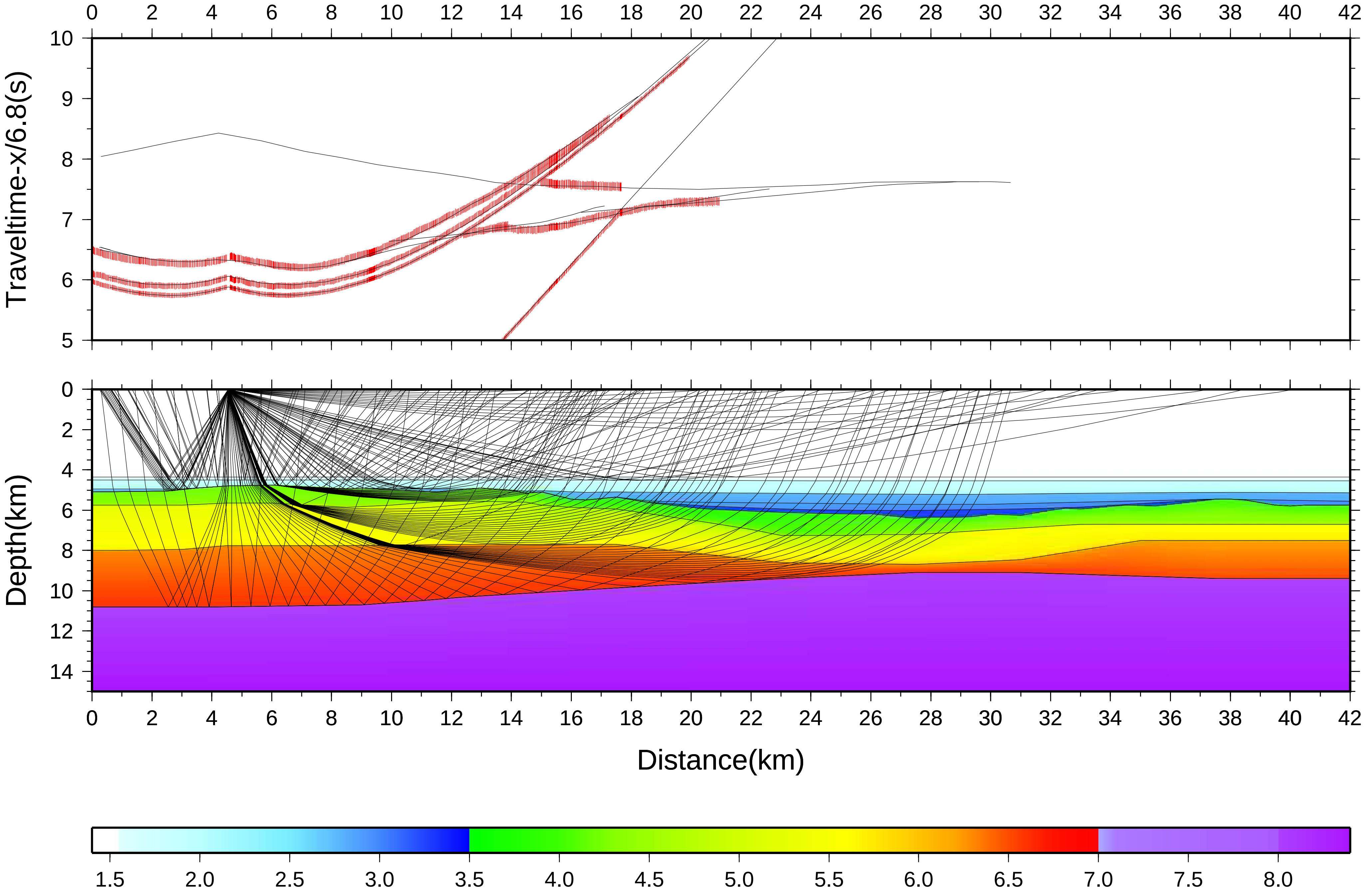

Traveltime-x/6.8(s)
Depth(km)
Distance(km)
0 2 4 6 8 10 12 14 16 18 20 22 24 26 28 30 32 34 36 38 40 42
5 6 7 8 9 10
0 2 4 6 8 10 12 14
1.5 2.0 2.5 3.0 3.5 4.0 4.5 5.0 5.5 6.0 6.5 7.0 7.5 8.0

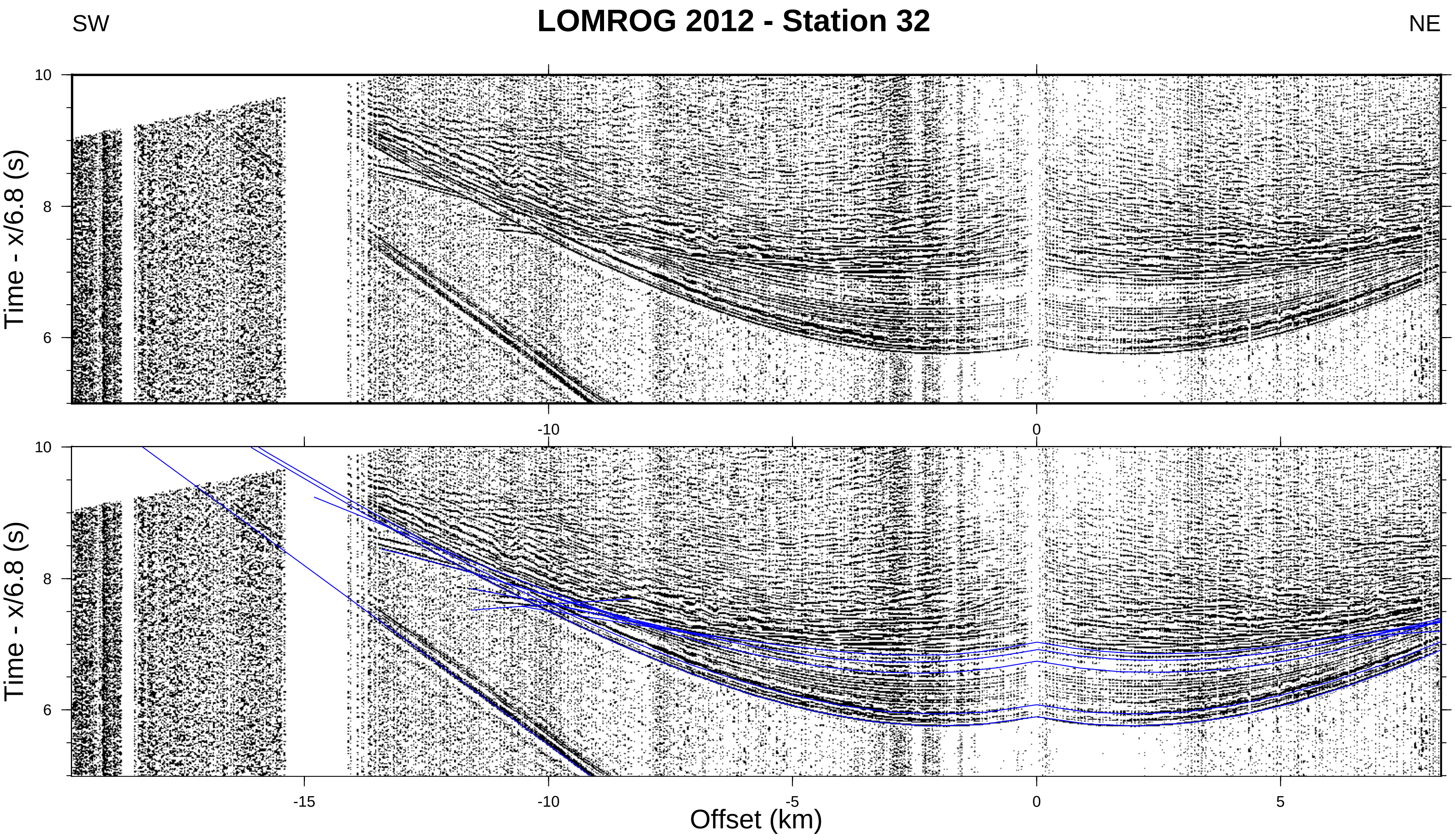
SW
LOMROG 2012 - Station 32
NE
Time - x/6.8 (s)
10
8
6
-10
0
Time - x/6.8 (s)
10
8
6
-15
-10
-5
0
5
Offset (km)

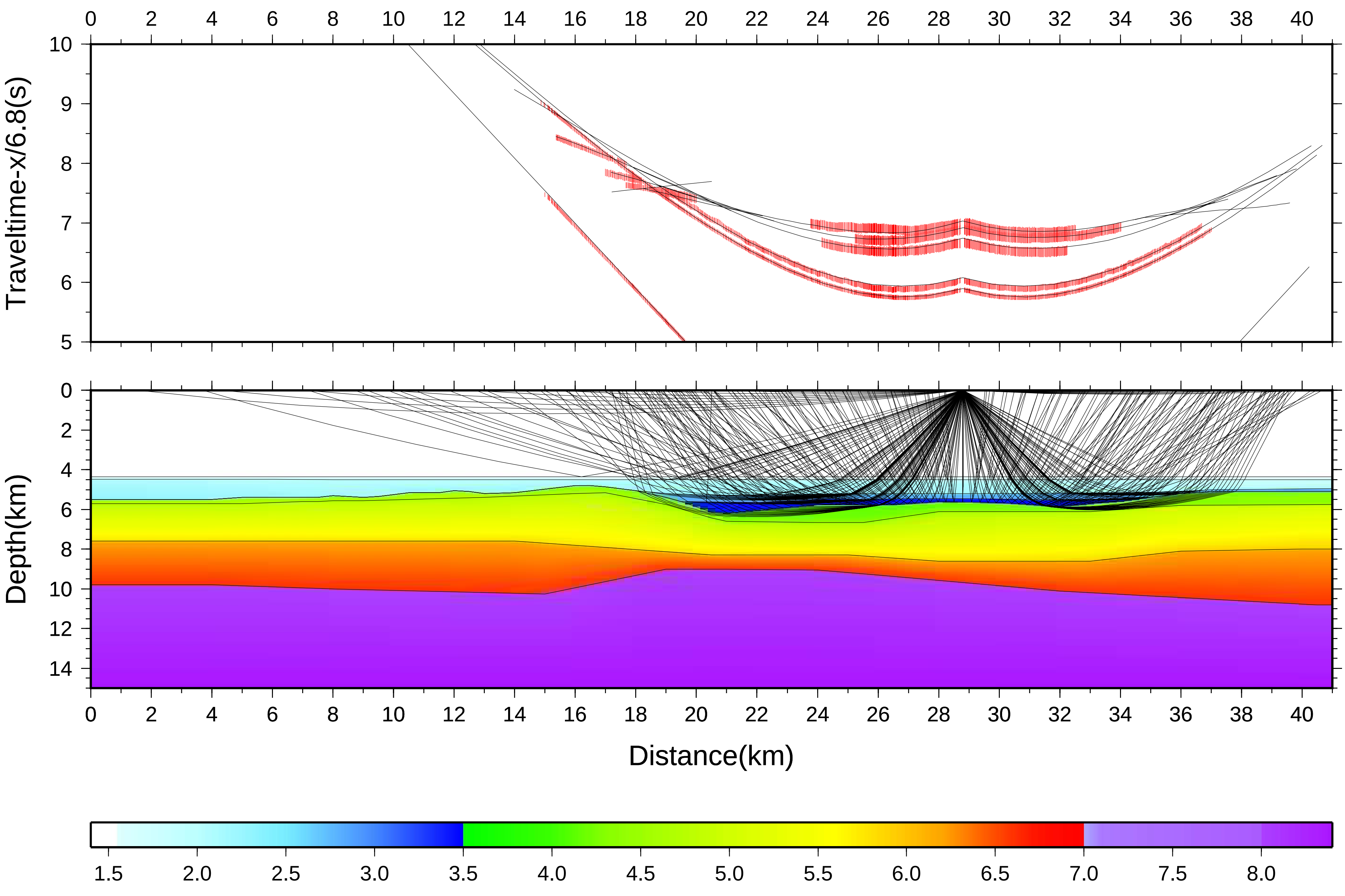

Traveltime-x/6.8(s)
Depth(km)
Distance(km)
0 2 4 6 8 10 12 14 16 18 20 22 24 26 28 30 32 34 36 38 40
10 9 8 7 6 5
0 2 4 6 8 10 12 14
1.5 2.0 2.5 3.0 3.5 4.0 4.5 5.0 5.5 6.0 6.5 7.0 7.5 8.0

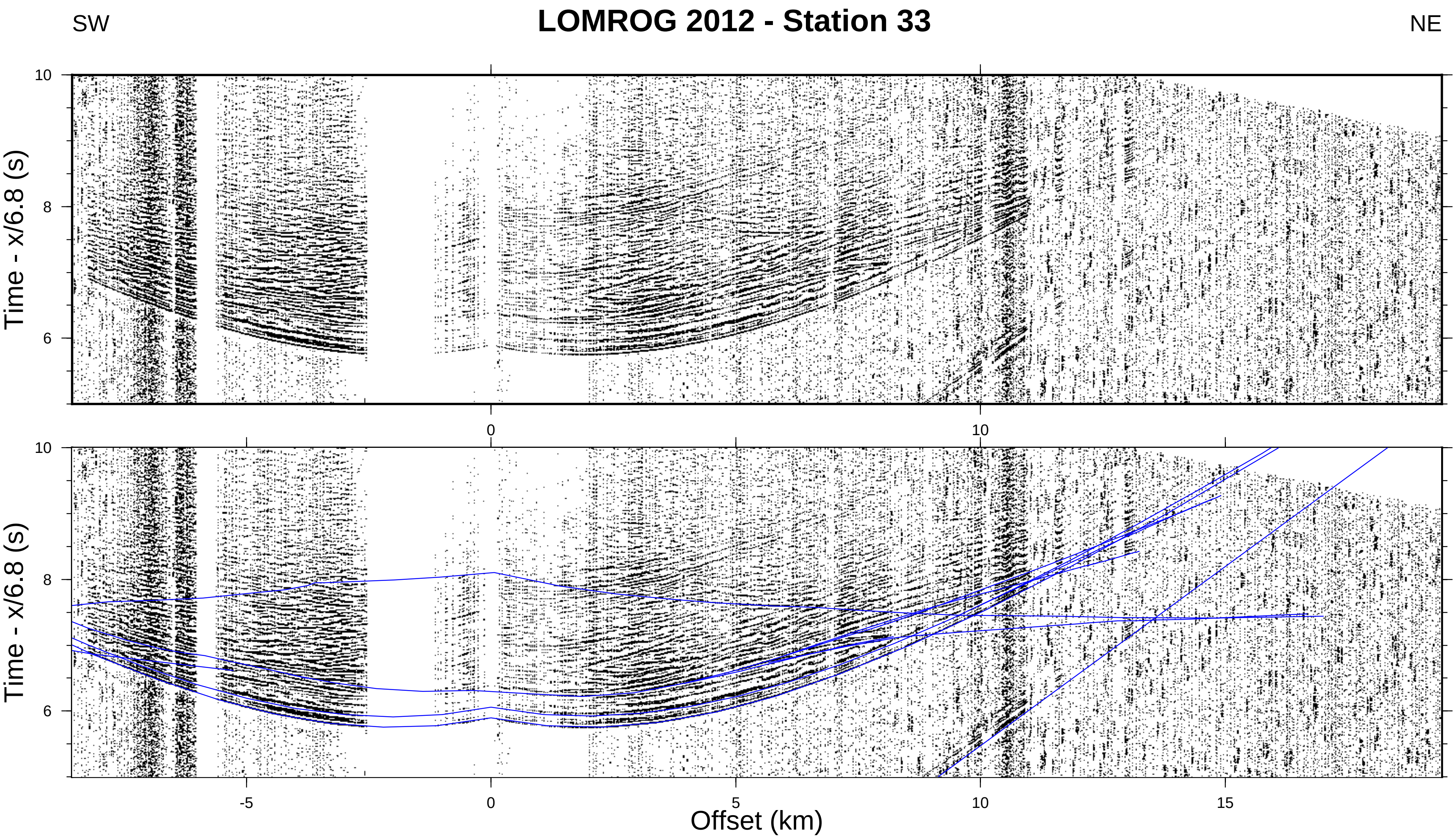
SW
LOMROG 2012 - Station 33
NE
Time - x/6.8 (s)
10
8
6
0
10
Time - x/6.8 (s)
10
8
6
-5
0
5
10
15
Offset (km)

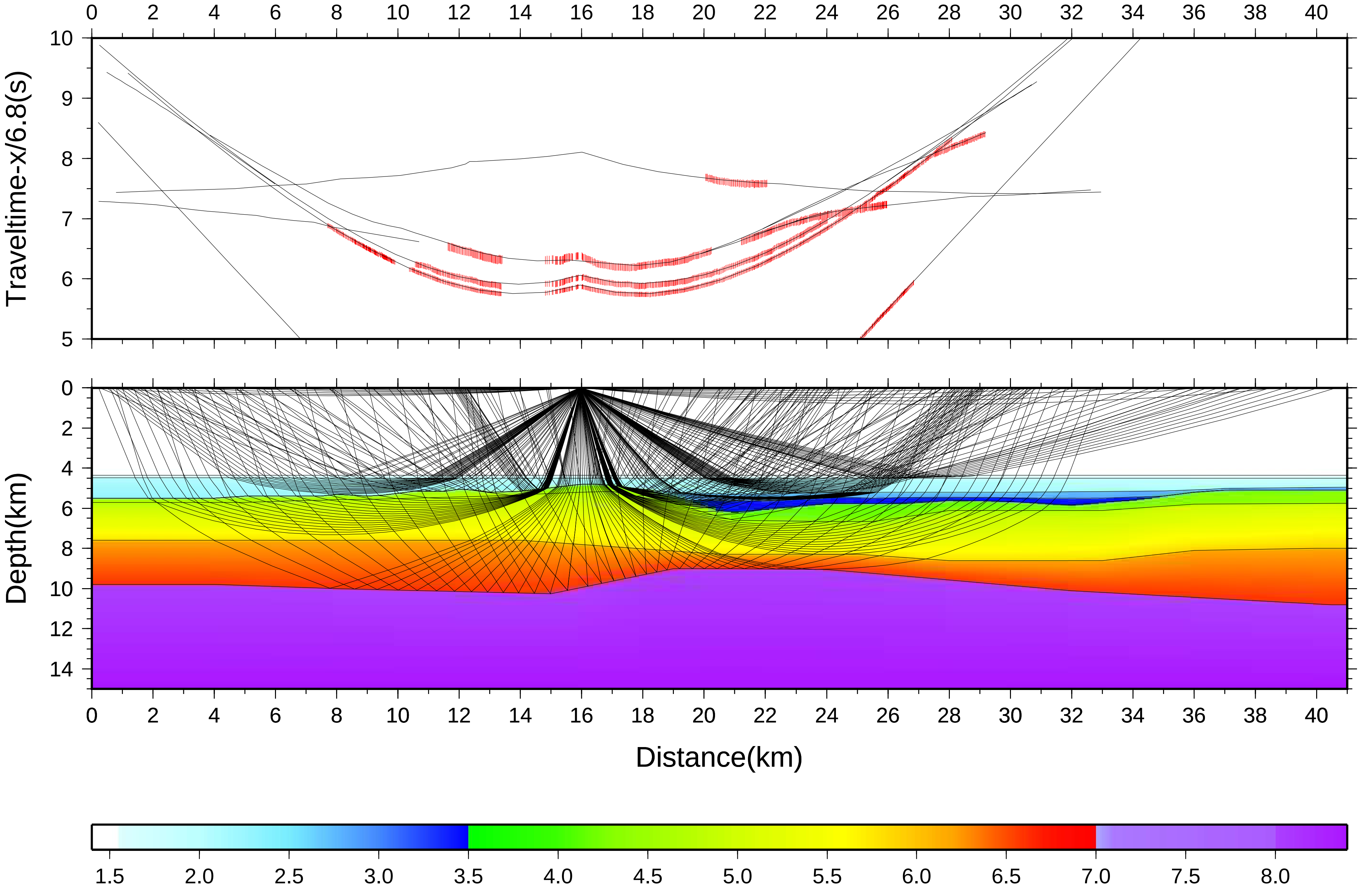

Traveltime-x/6.8(s)
Depth(km)
Distance(km)
0
2
4
6
8
10
12
14
16
18
20
22
24
26
28
30
32
34
36
38
40
10
9
8
7
6
5
1.5
2.0
2.5
3.0
3.5
4.0
4.5
5.0
5.5
6.0
6.5
7.0
7.5
8.0

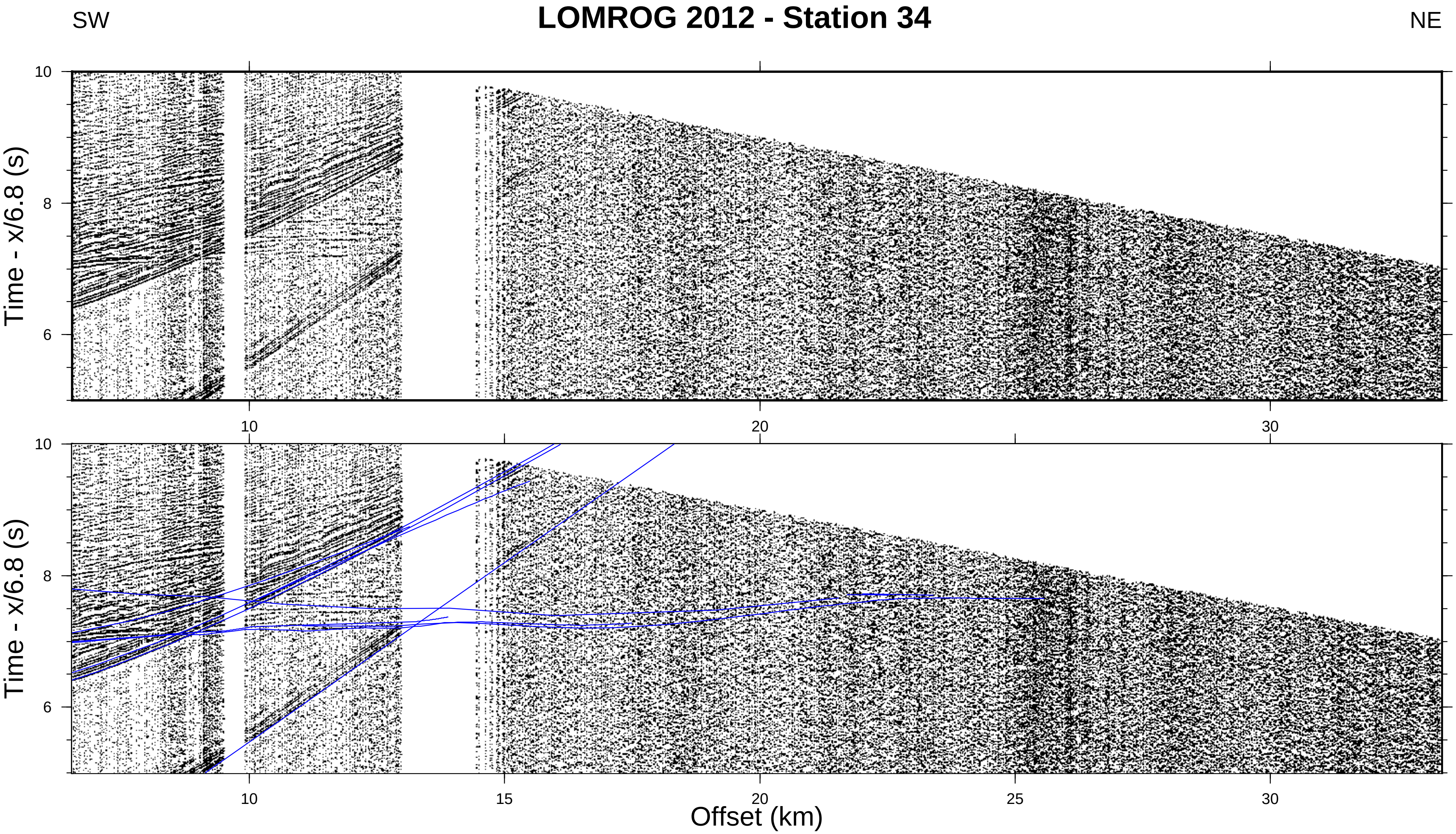
SW
LOMROG 2012 - Station 34
NE
Time - x/6.8 (s)
Time - x/6.8 (s)
10
8
6
10
20
30
10
8
6
10
15
20
25
30
Offset (km)

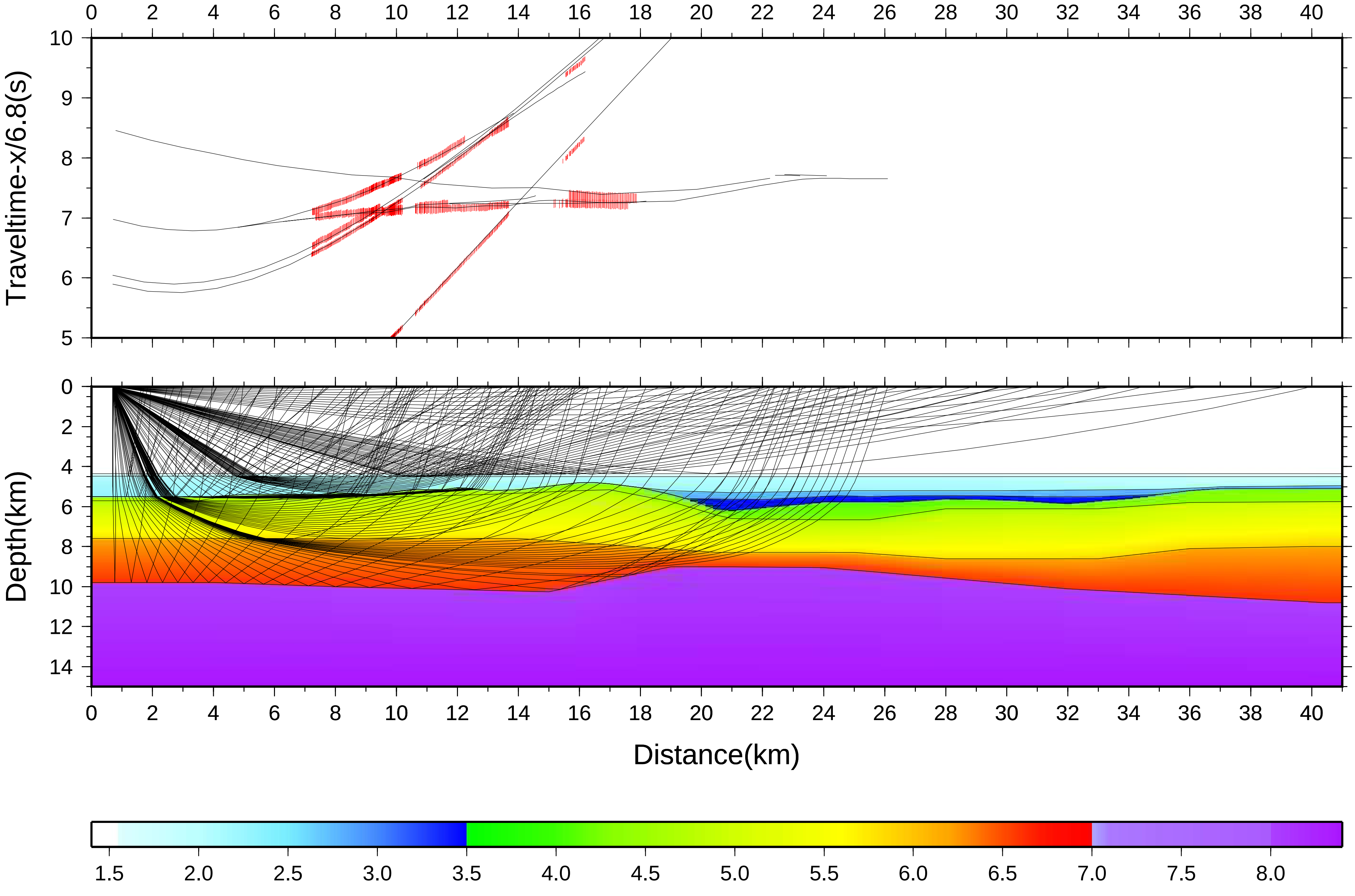

Traveltime-x/6.8(s)
Depth(km)
Distance(km)
0 2 4 6 8 10 12 14 16 18 20 22 24 26 28 30 32 34 36 38 40
10 9 8 7 6 5
0 2 4 6 8 10 12 14
1.5 2.0 2.5 3.0 3.5 4.0 4.5 5.0 5.5 6.0 6.5 7.0 7.5 8.0

LOMROG 2012 - Station 37

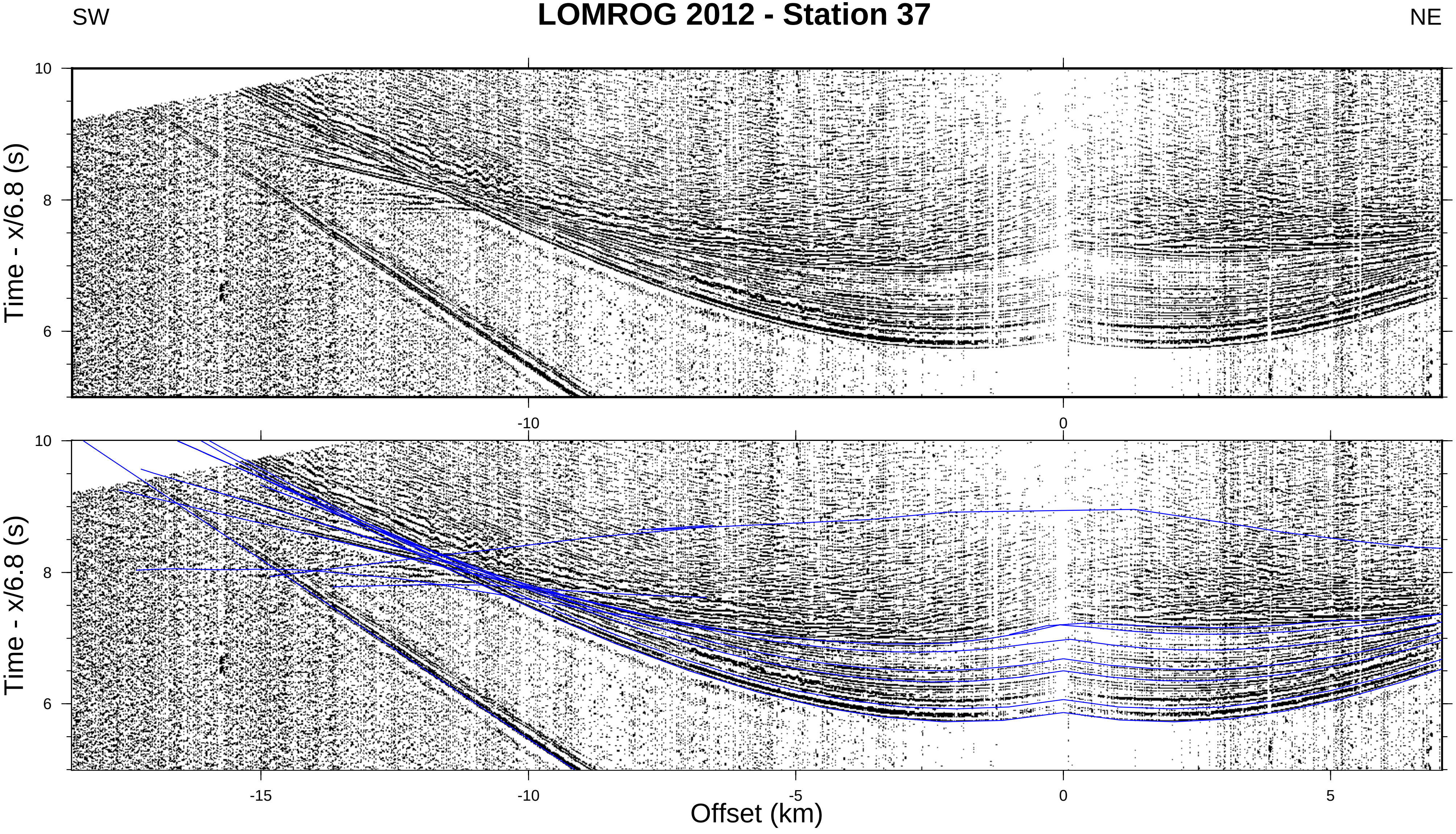

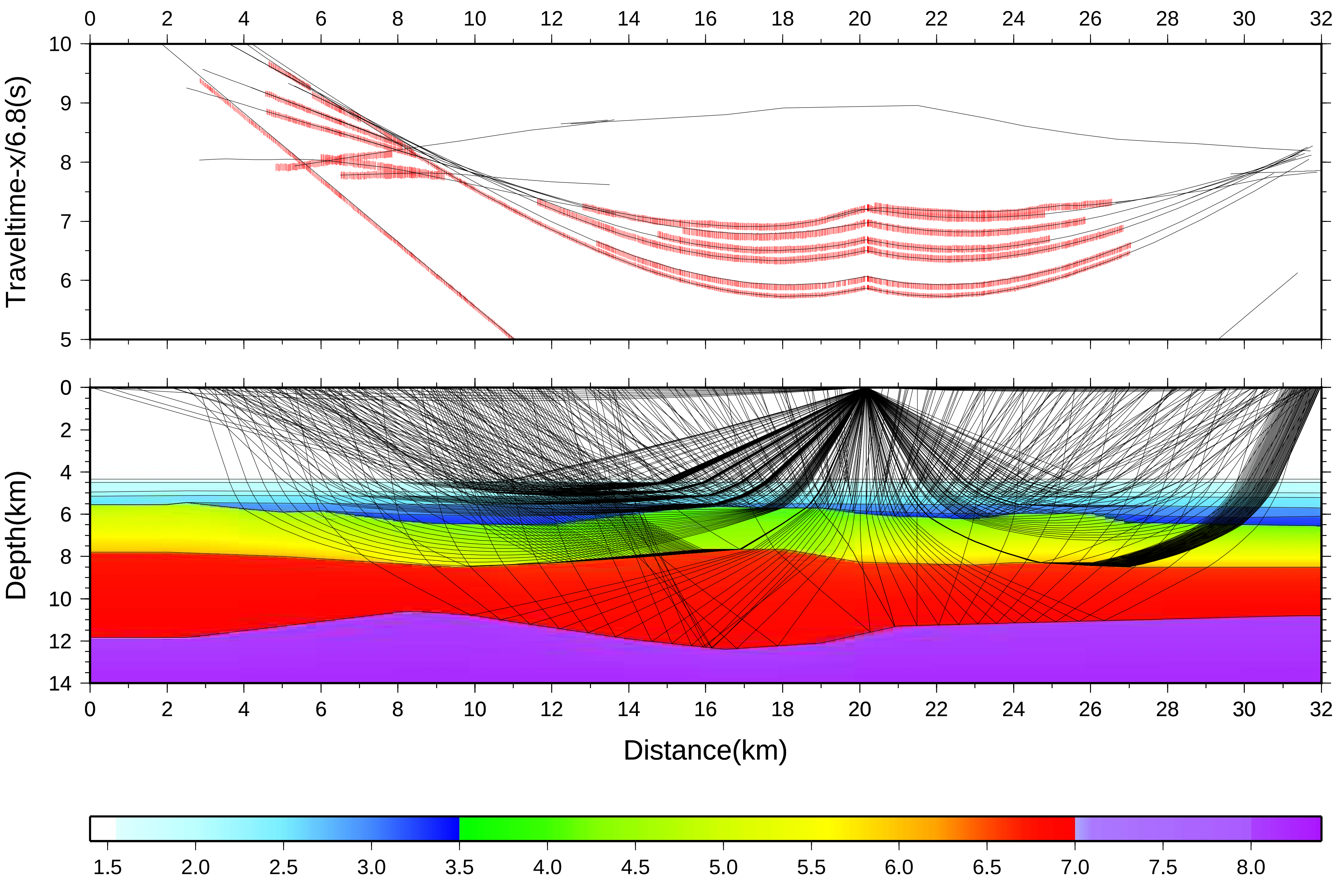

Traveltime-x/6.8(s)
Depth(km)
Distance(km)
0 2 4 6 8 10 12 14 16 18 20 22 24 26 28 30 32
10 9 8 7 6 5
0 2 4 6 8 10 12 14
1.5 2.0 2.5 3.0 3.5 4.0 4.5 5.0 5.5 6.0 6.5 7.0 7.5 8.0

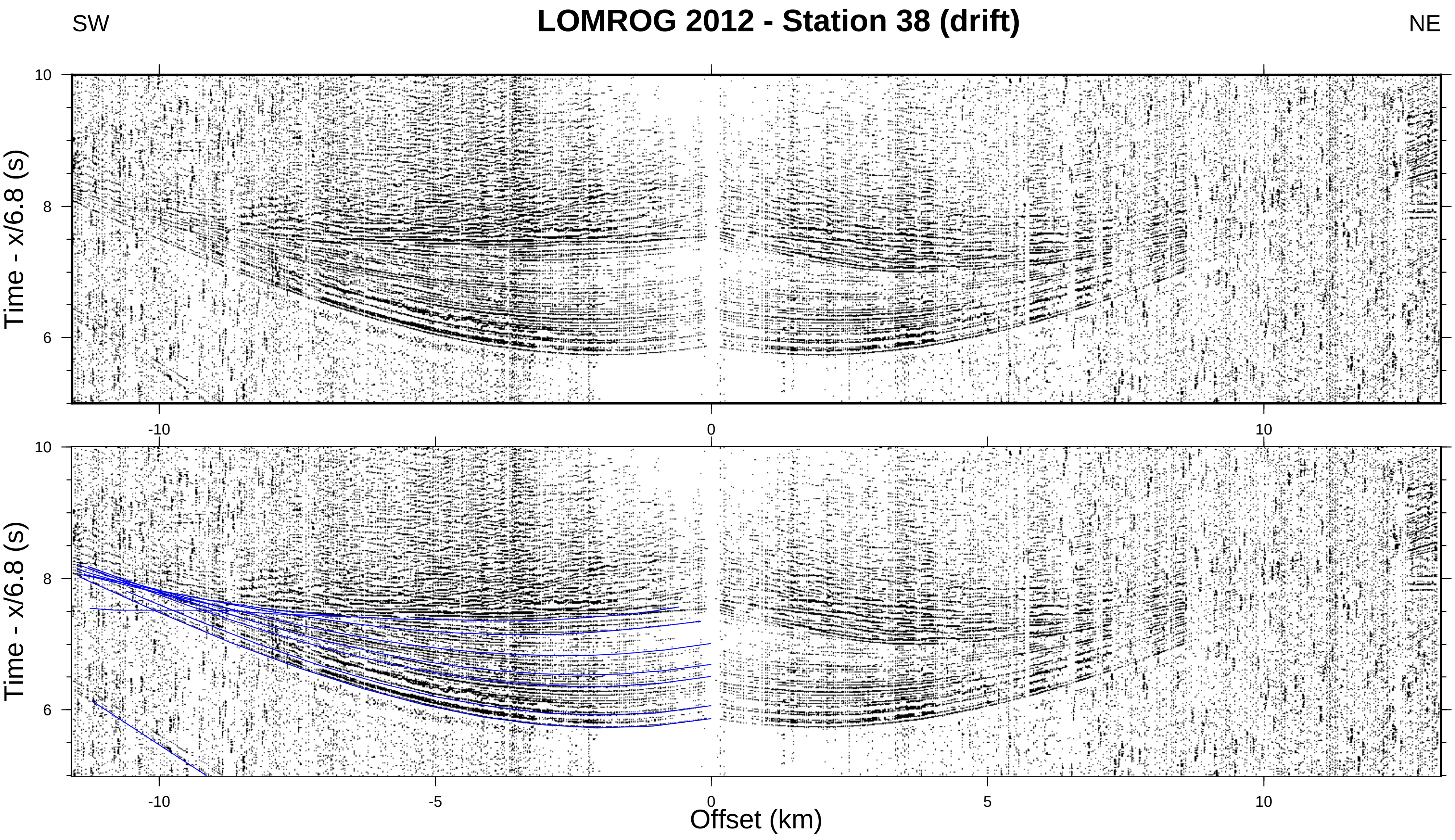
SW
LOMROG 2012 - Station 38 (drift)
NE
Time - x/6.8 (s)
10
8
6
-10
0
10
Time - x/6.8 (s)
10
8
6
-10
-5
0
5
10
Offset (km)

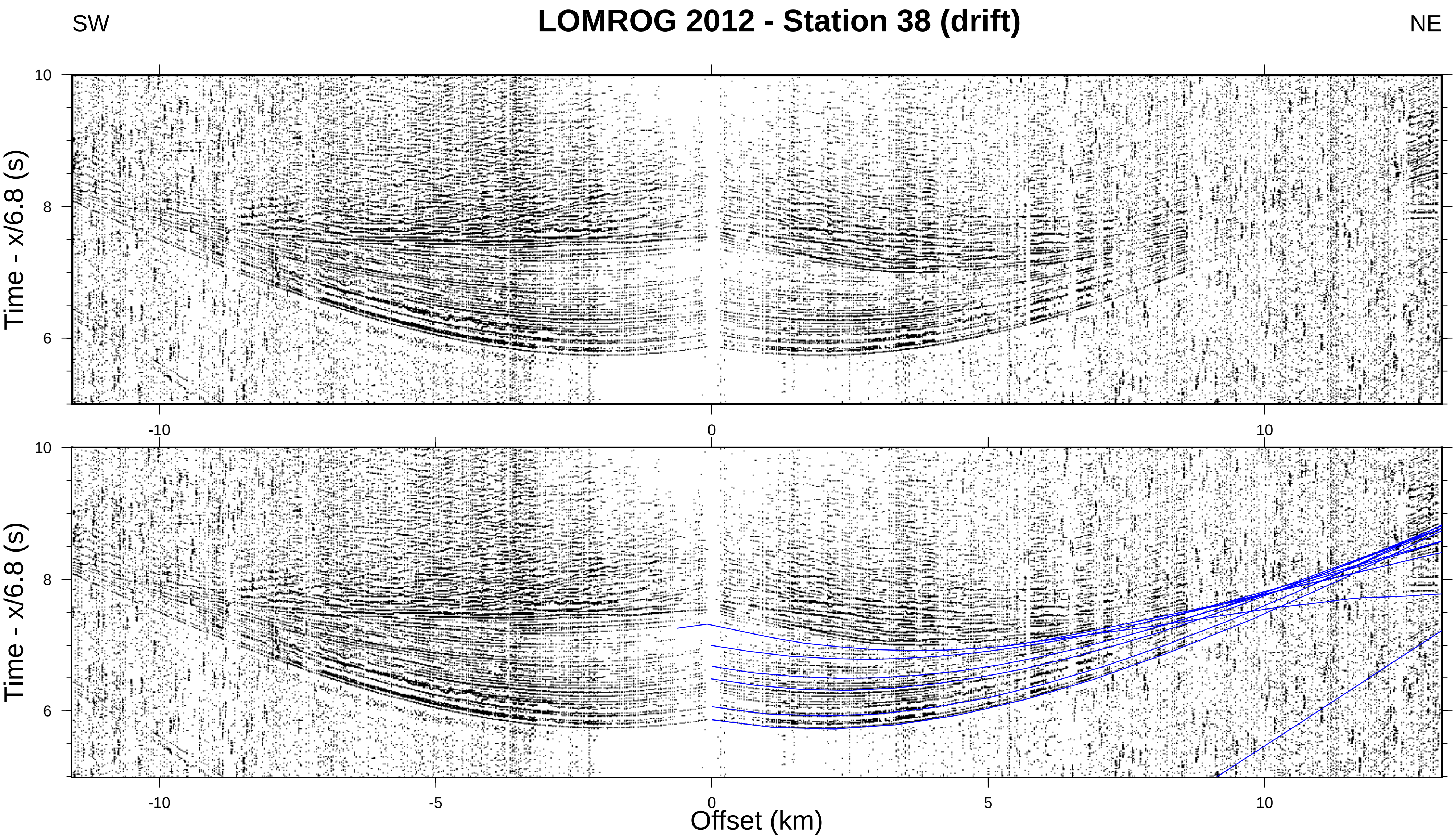

LOMROG 2012 - Station 38 (drift)
SW
NE
Time - x/6.8 (s)
10
8
6
-10
0
10
-5
5
Offset (km)

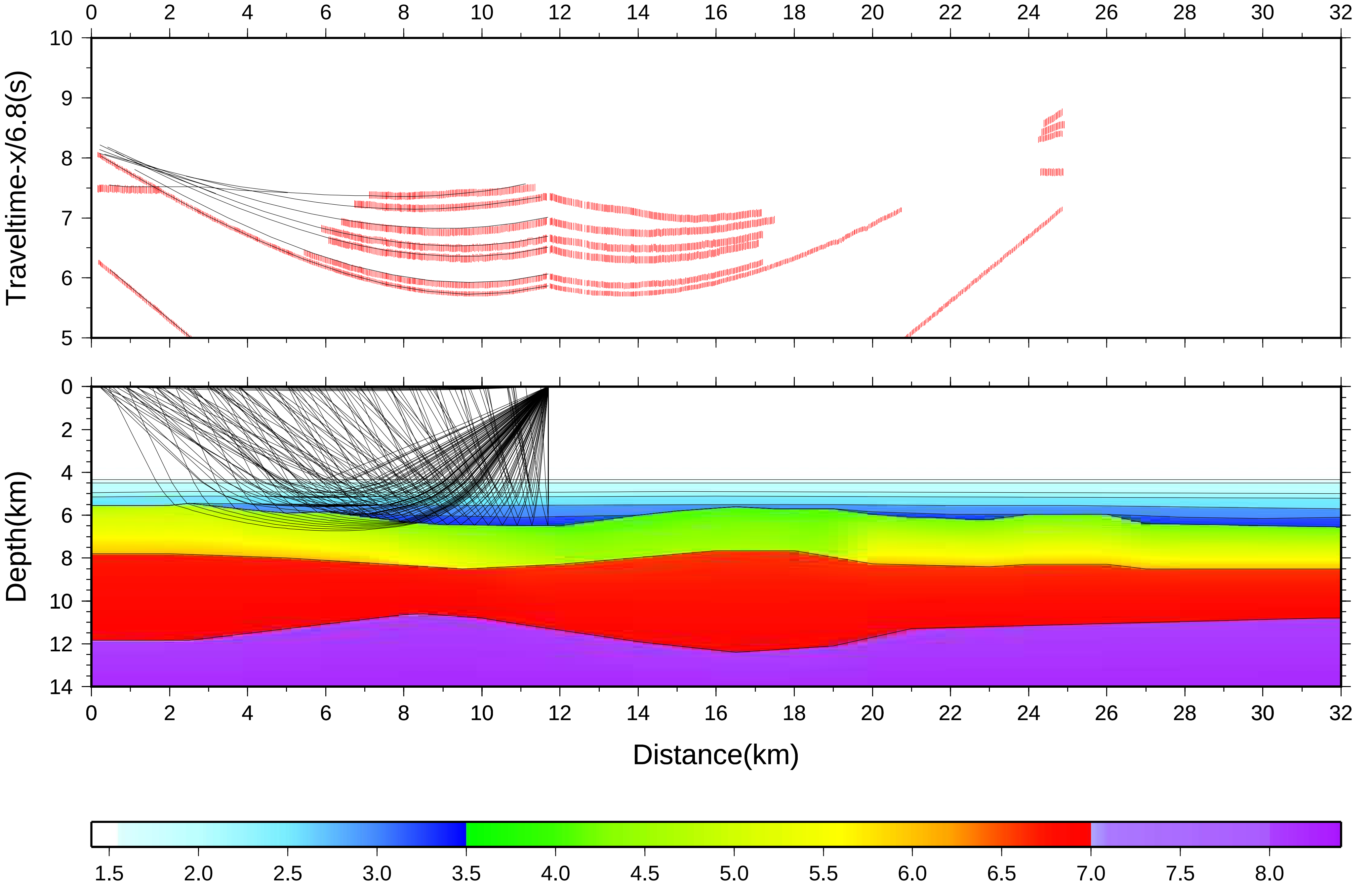

Traveltime-x/6.8(s)
Depth(km)
Distance(km)
0 2 4 6 8 10 12 14 16 18 20 22 24 26 28 30 32
10 9 8 7 6 5
0 2 4 6 8 10 12 14
1.5 2.0 2.5 3.0 3.5 4.0 4.5 5.0 5.5 6.0 6.5 7.0 7.5 8.0

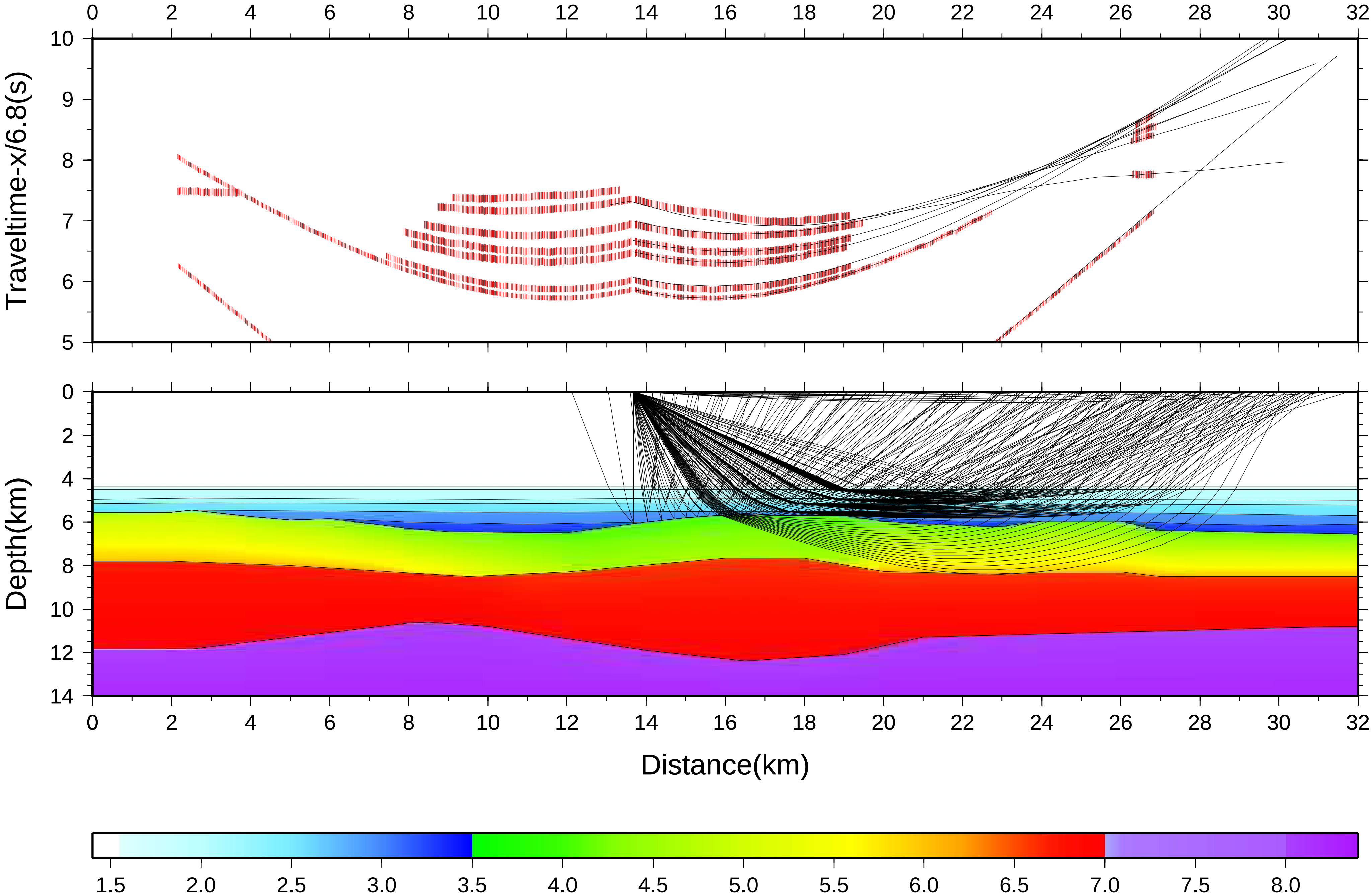

Traveltime-x/6.8(s)
Depth(km)
Distance(km)
1.5
2.0
2.5
3.0
3.5
4.0
4.5
5.0
5.5
6.0
6.5
7.0
7.5
8.0

LOMROG 2012 - Station 39

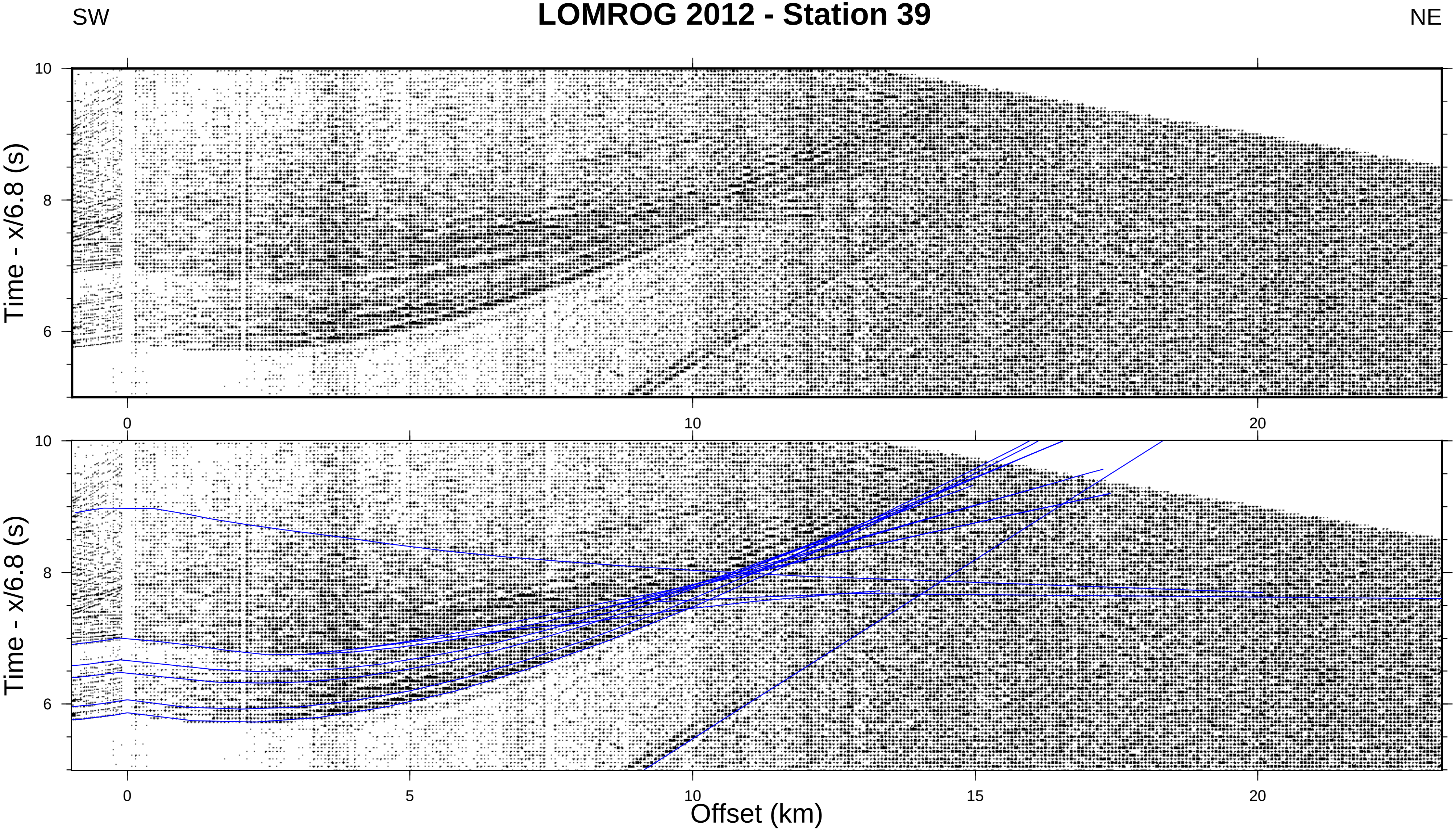

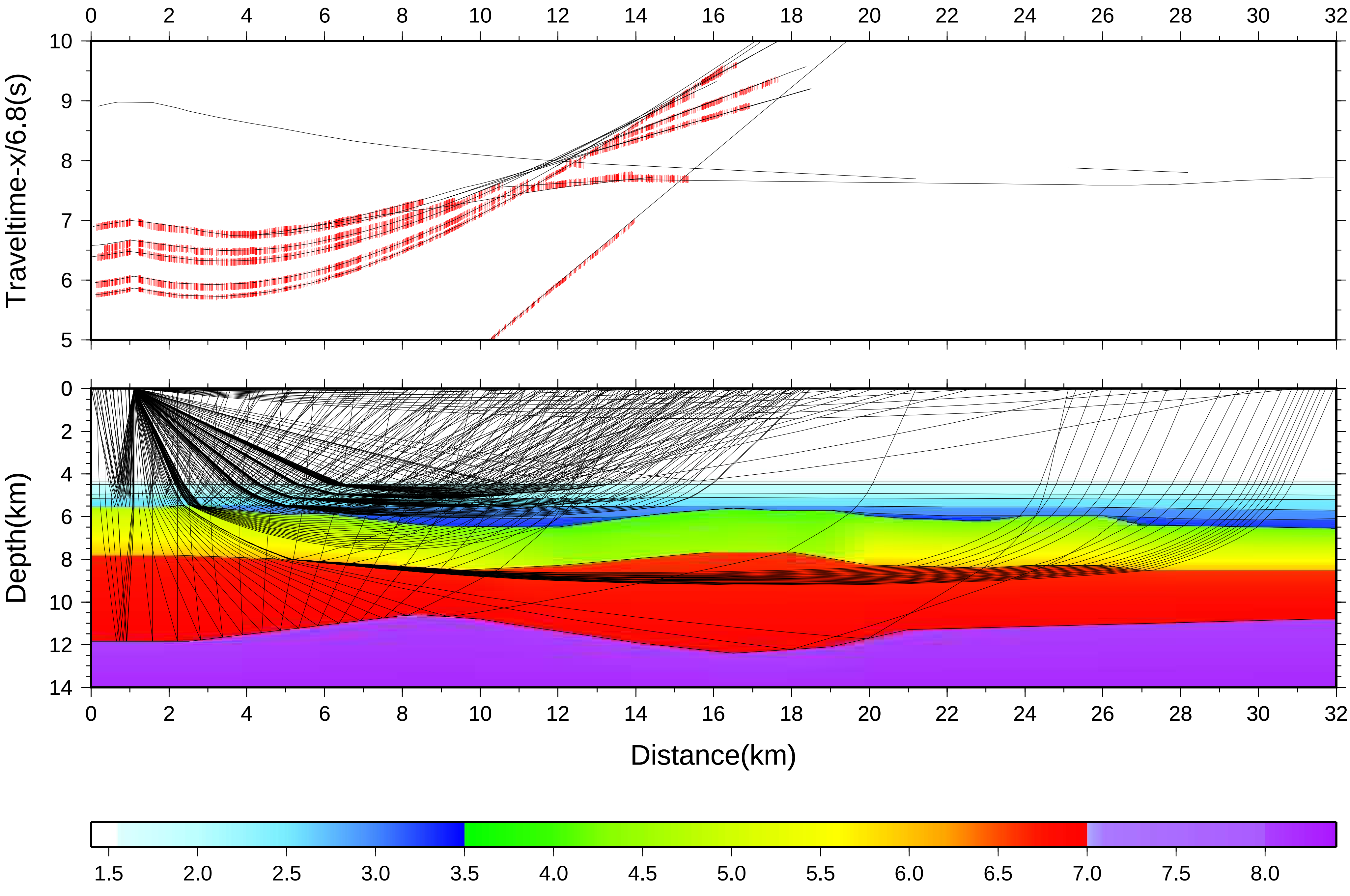
Traveltime-x/6.8(s)
Depth(km)
Distance(km)
0 2 4 6 8 10 12 14 16 18 20 22 24 26 28 30 32
1.5 2.0 2.5 3.0 3.5 4.0 4.5 5.0 5.5 6.0 6.5 7.0 7.5 8.0

LOMROG 2012 - Station 40

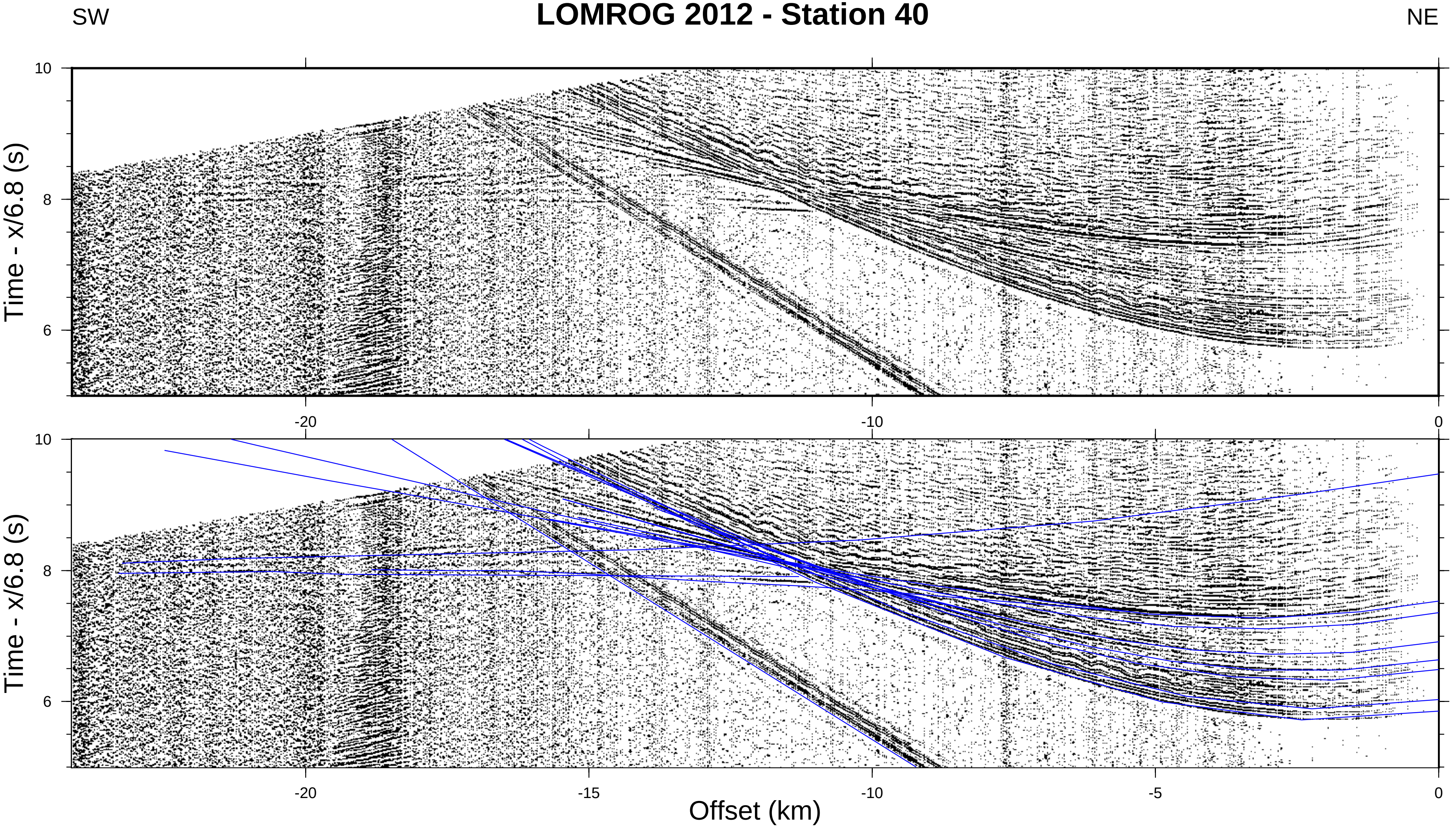

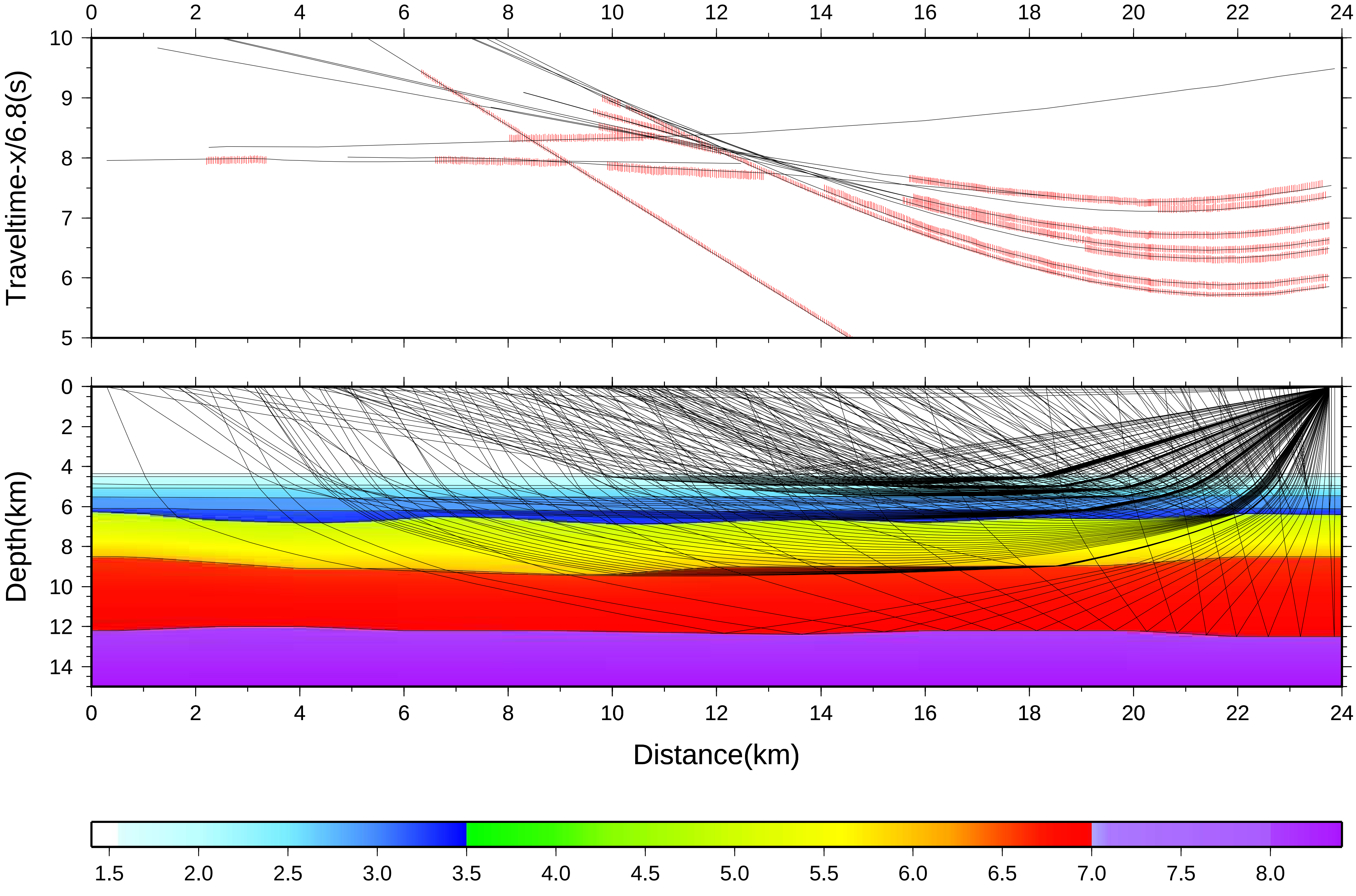

Traveltime-x/6.8(s)
Depth(km)
Distance(km)
0
2
4
6
8
10
12
14
16
18
20
22
24
5
6
7
8
9
10
1.5
2.0
2.5
3.0
3.5
4.0
4.5
5.0
5.5
6.0
6.5
7.0
7.5
8.0

LOMROG 2012 - Station 41

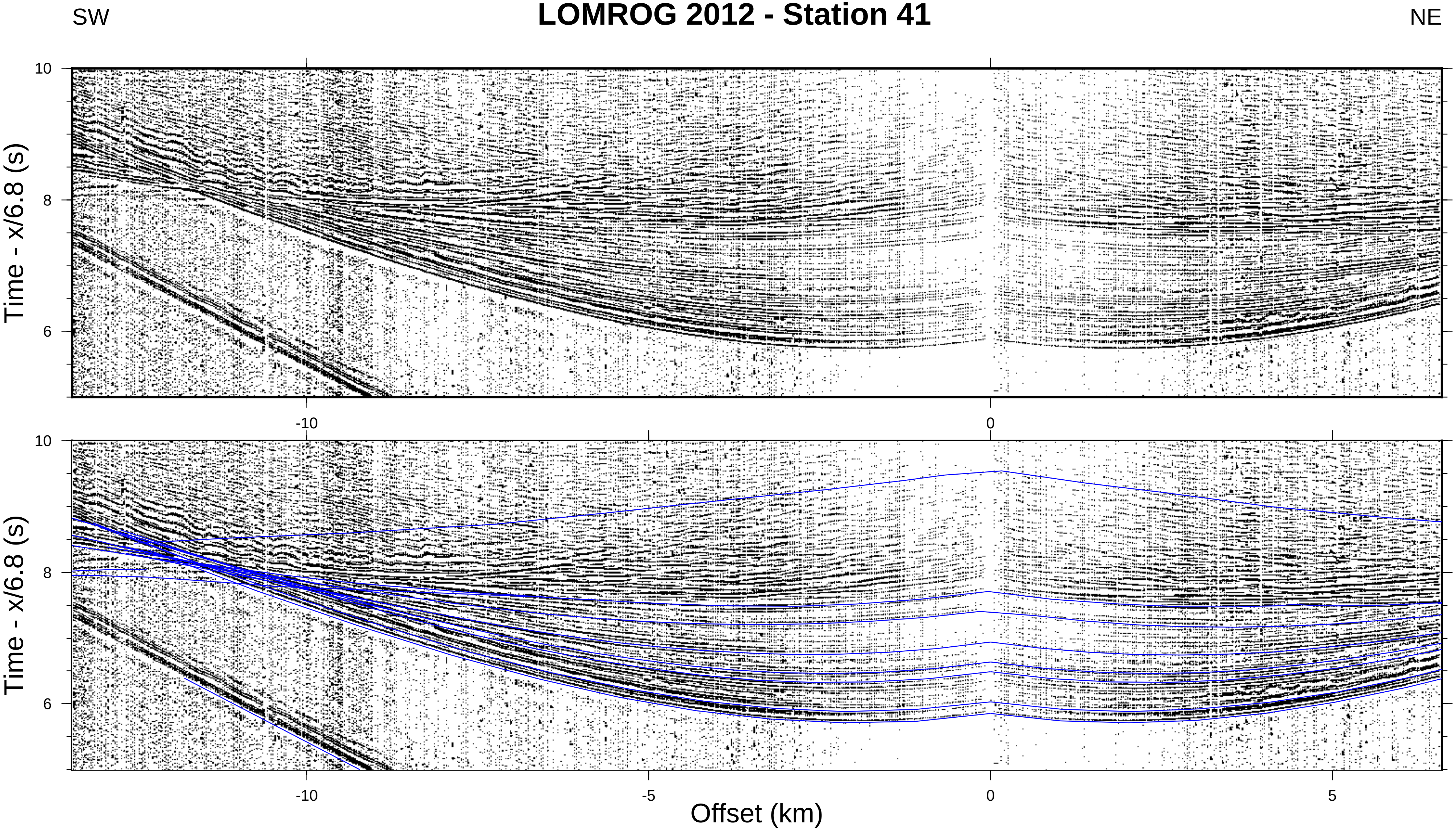

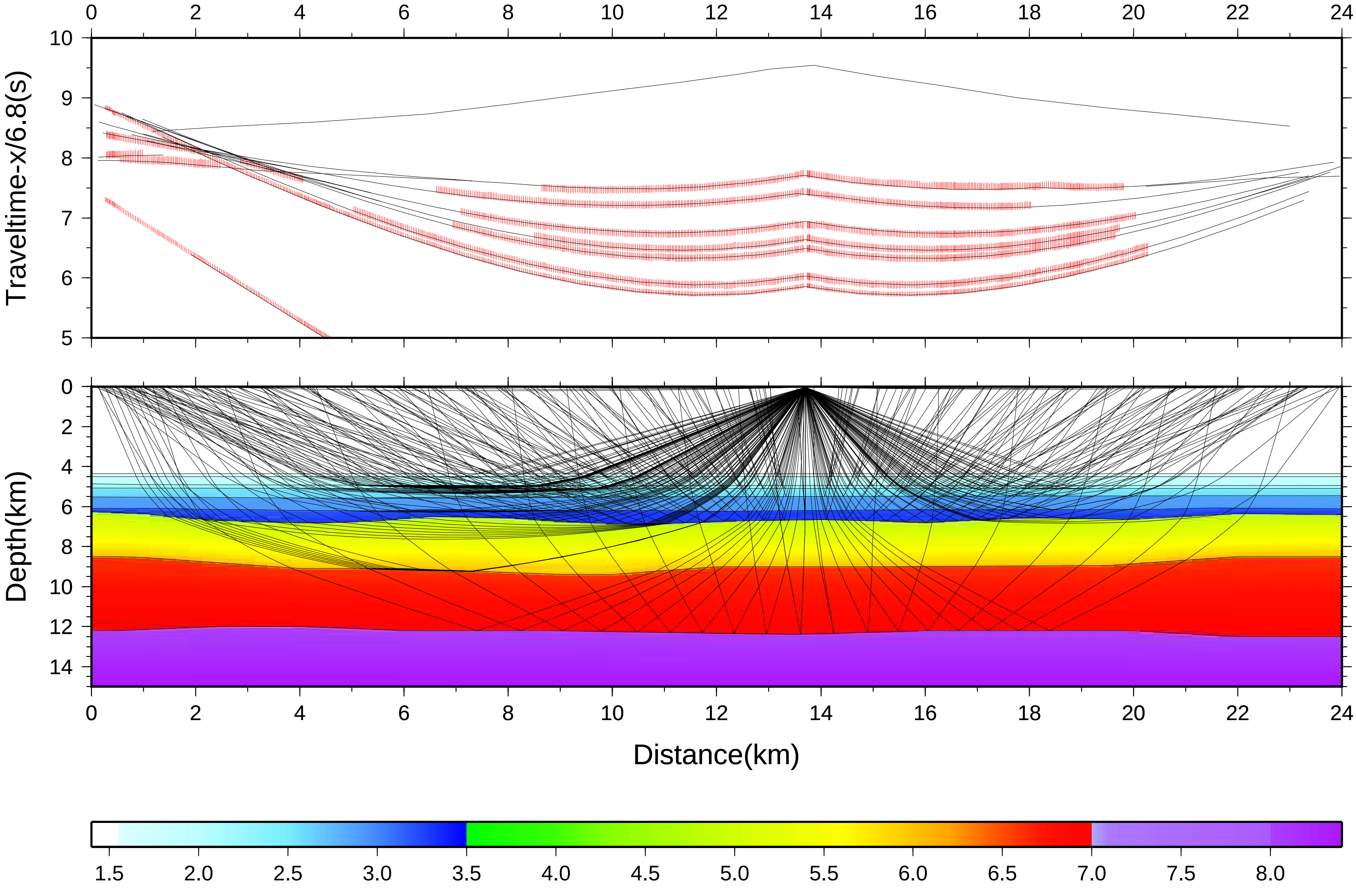

Traveltime-x/6.8(s)
Depth(km)
Distance(km)
0 2 4 6 8 10 12 14 16 18 20 22 24
10 9 8 7 6 5
0 2 4 6 8 10 12 14
1.5 2.0 2.5 3.0 3.5 4.0 4.5 5.0 5.5 6.0 6.5 7.0 7.5 8.0

LOMROG 2012 - Station 42

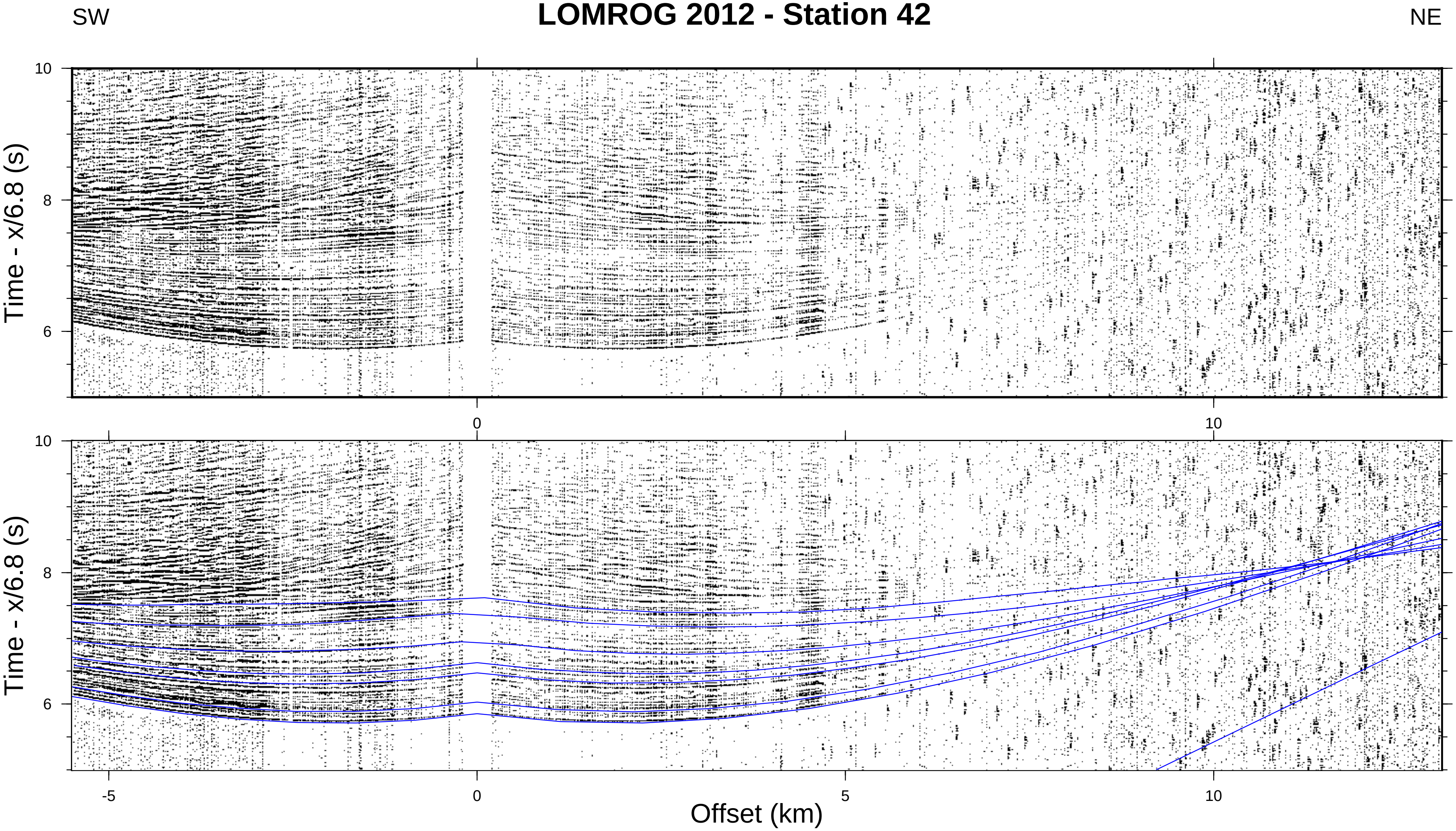

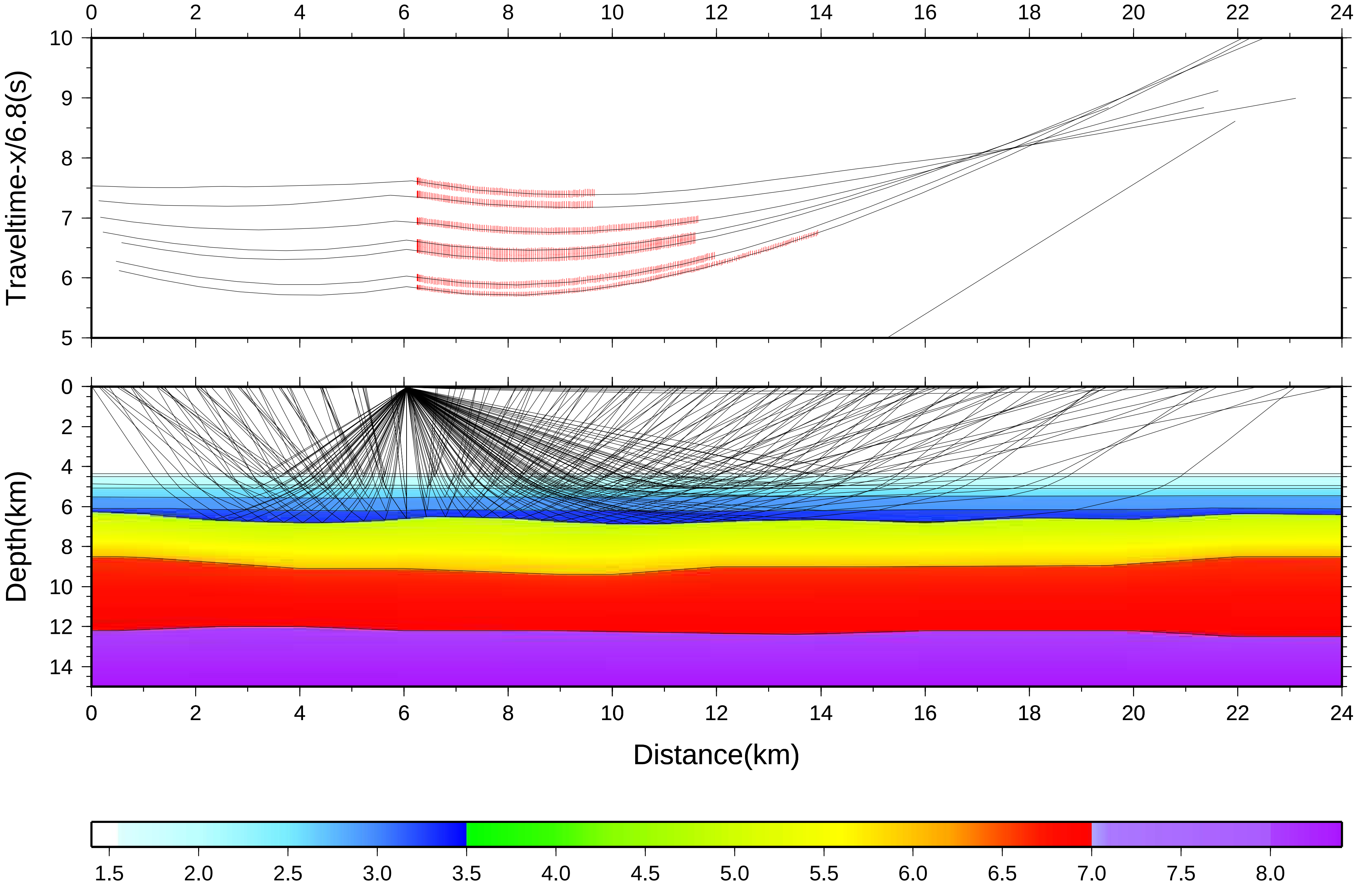

Traveltime-x/6.8(s)
Depth(km)
Distance(km)
0
2
4
6
8
10
12
14
16
18
20
22
24
5
6
7
8
9
10
1.5
2.0
2.5
3.0
3.5
4.0
4.5
5.0
5.5
6.0
6.5
7.0
7.5
8.0

LOMROG 2012 - Station 43

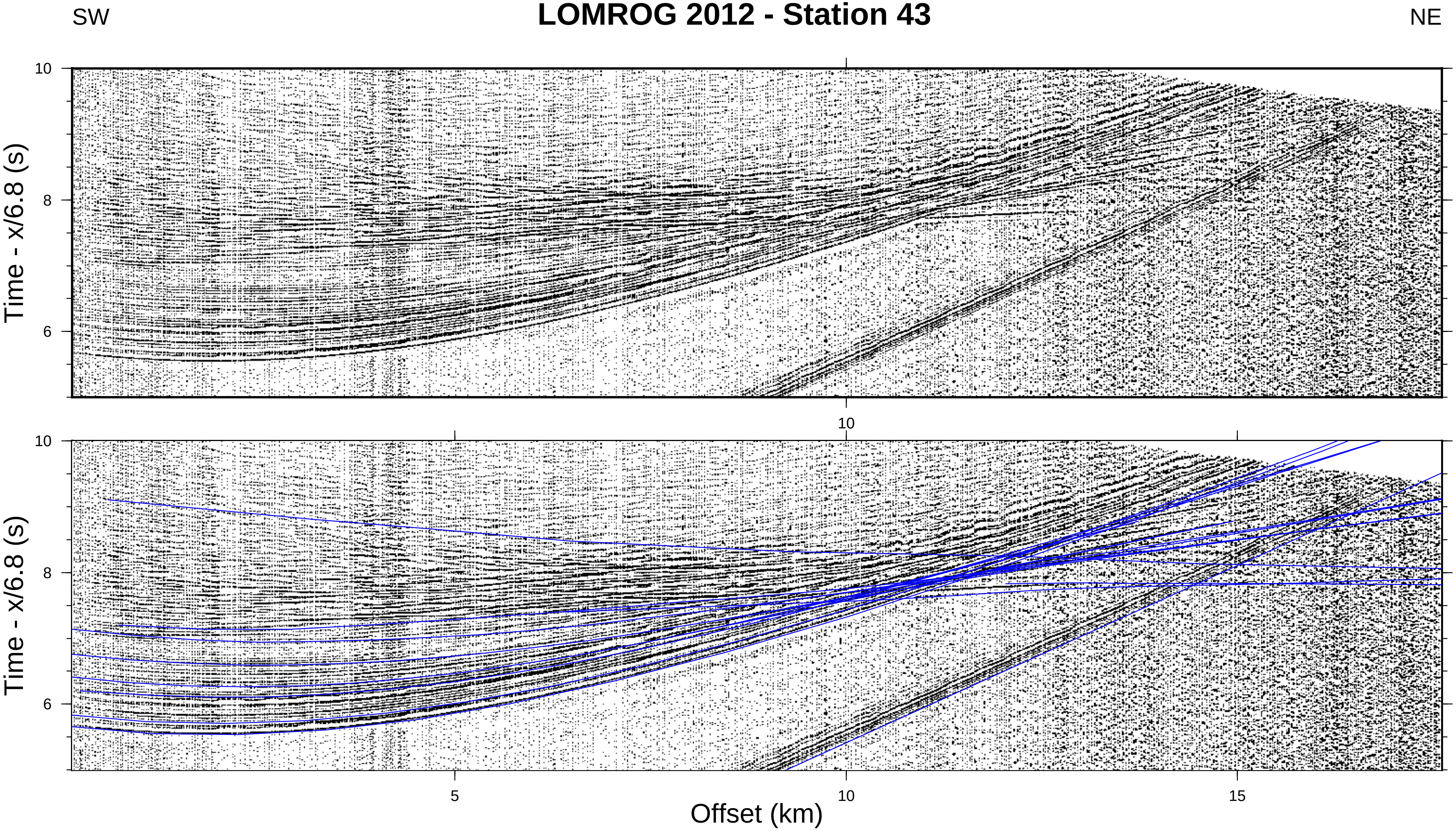

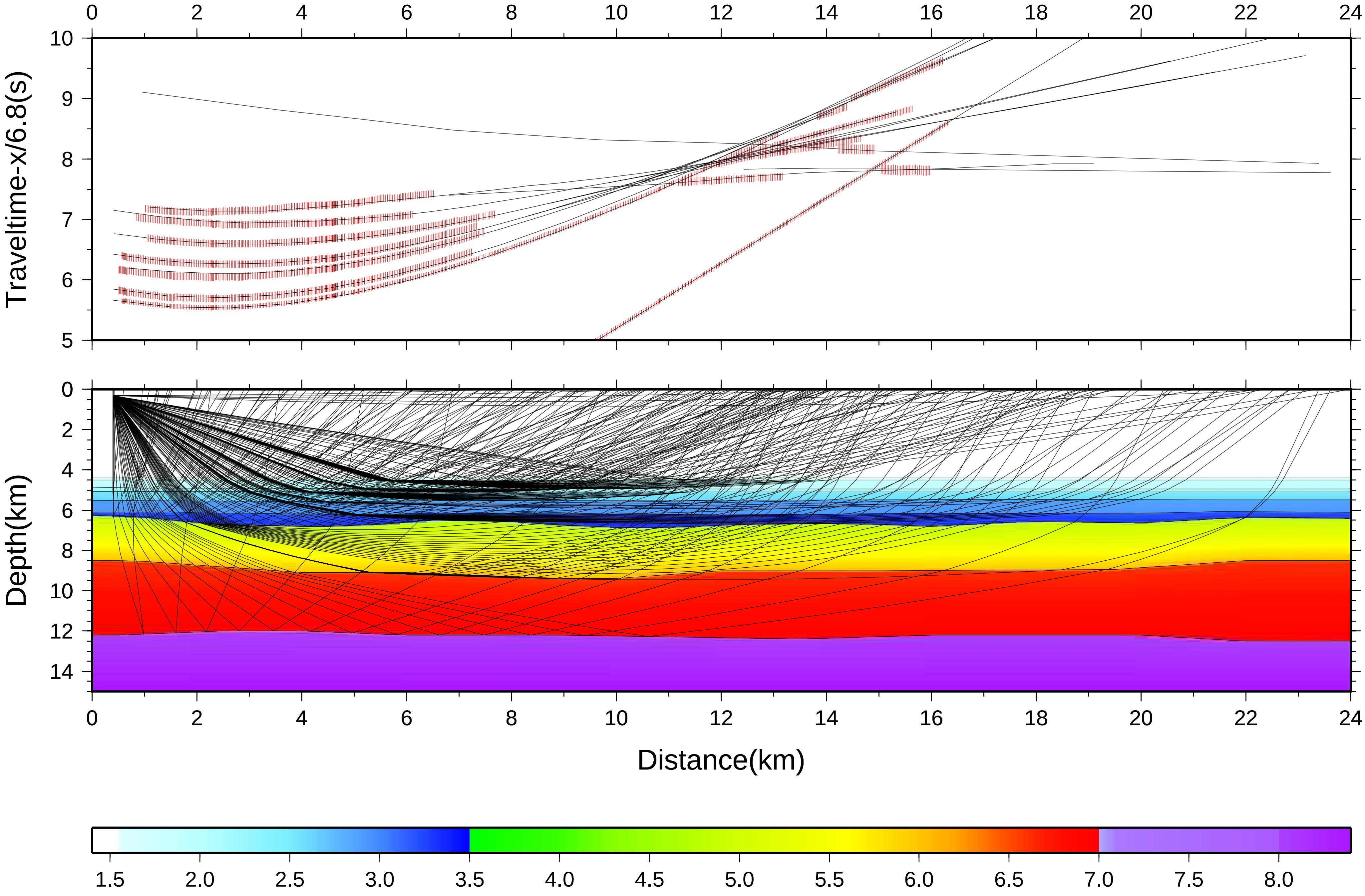
Traveltime-x/6.8(s)
Depth(km)
Distance(km)
0
2
4
6
8
10
12
14
16
18
20
22
24
5
6
7
8
9
10
1.5
2.0
2.5
3.0
3.5
4.0
4.5
5.0
5.5
6.0
6.5
7.0
7.5
8.0

LOMROG 2012 - Station 45

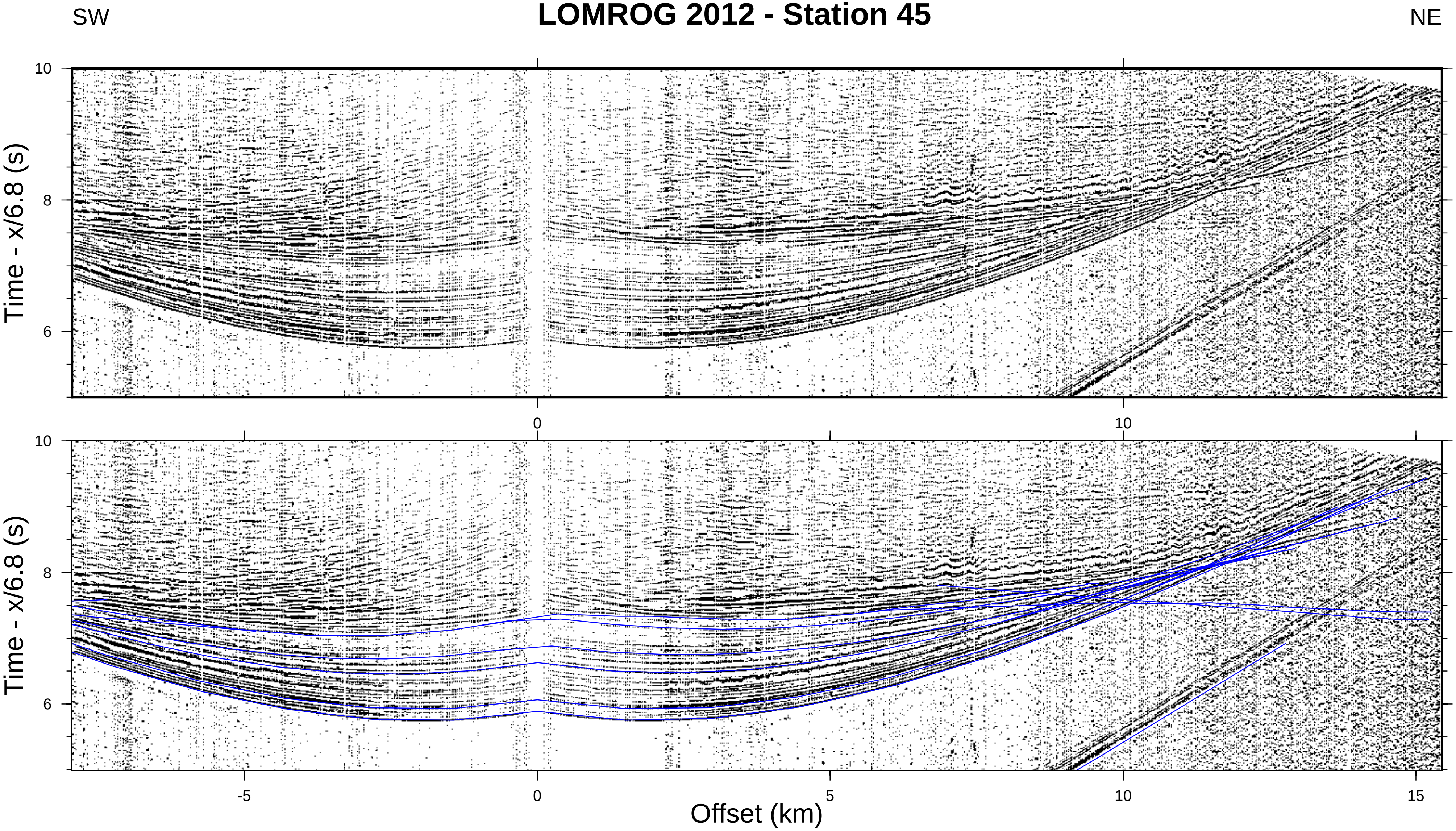

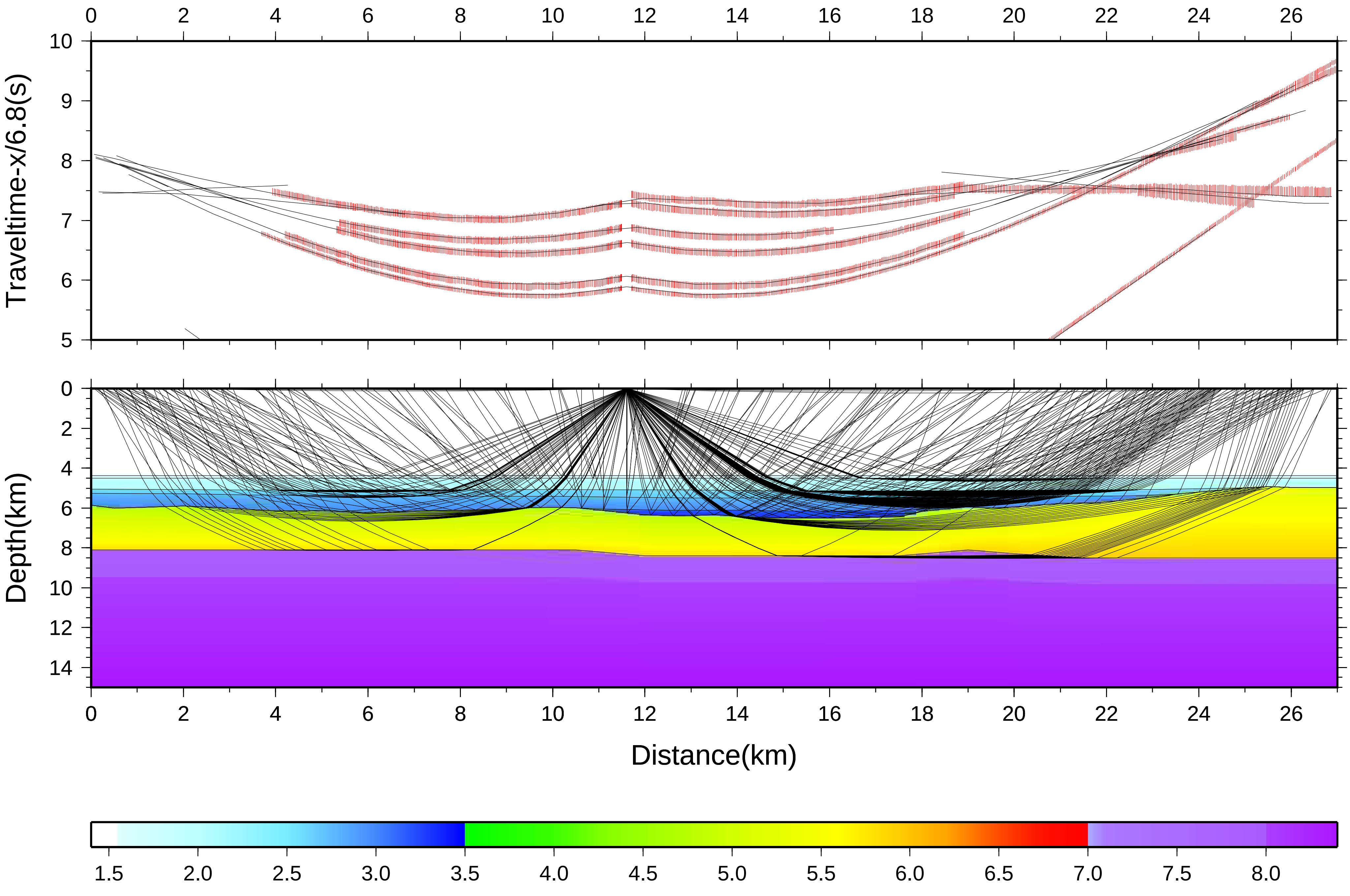
0 2 4 6 8 10 12 14 16 18 20 22 24 26
Traveltime-x/6.8(s)
10 9 8 7 6 5
Depth(km)
0 2 4 6 8 10 12 14
Distance(km)
1.5 2.0 2.5 3.0 3.5 4.0 4.5 5.0 5.5 6.0 6.5 7.0 7.5 8.0

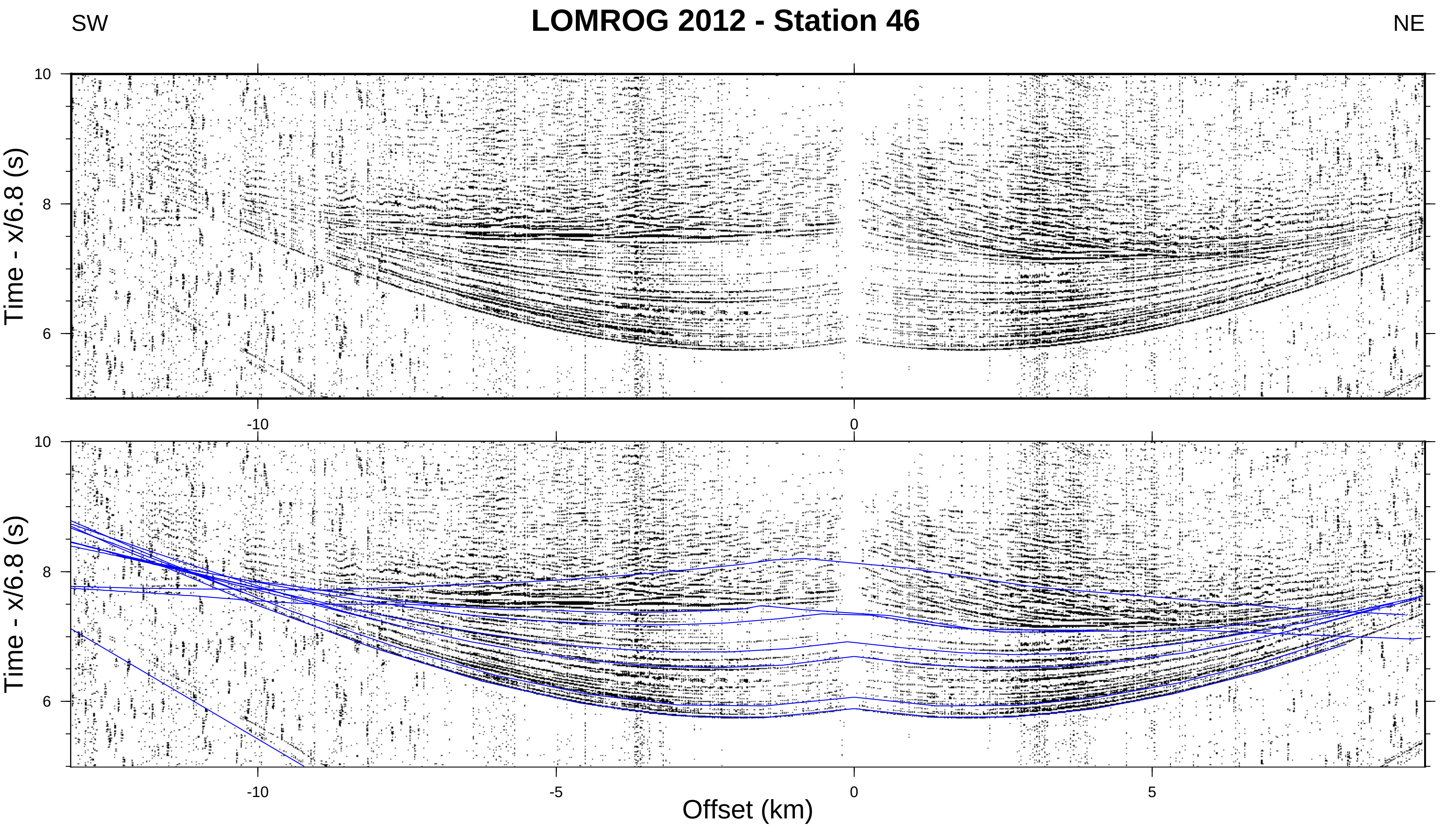
SW
LOMROG 2012 - Station 46
NE
Time - x/6.8 (s)
10
8
6
-10
0
Time - x/6.8 (s)
10
8
6
-10
-5
0
5
Offset (km)

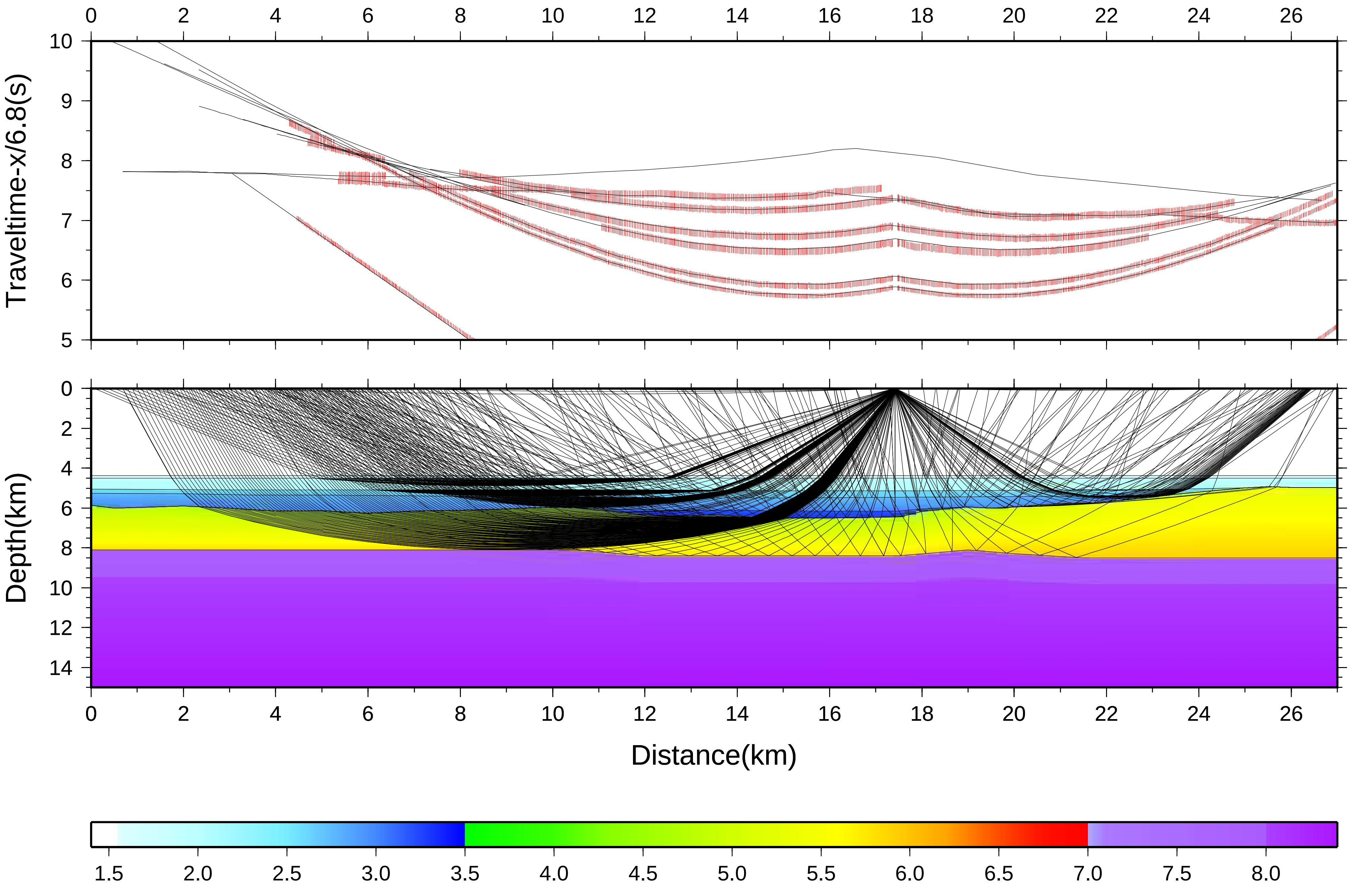
Traveltime-x/6.8(s)
Depth(km)
Distance(km)
0 2 4 6 8 10 12 14 16 18 20 22 24 26
10 9 8 7 6 5
0 2 4 6 8 10 12 14
1.5 2.0 2.5 3.0 3.5 4.0 4.5 5.0 5.5 6.0 6.5 7.0 7.5 8.0

LOMROG 2012 - Station 47

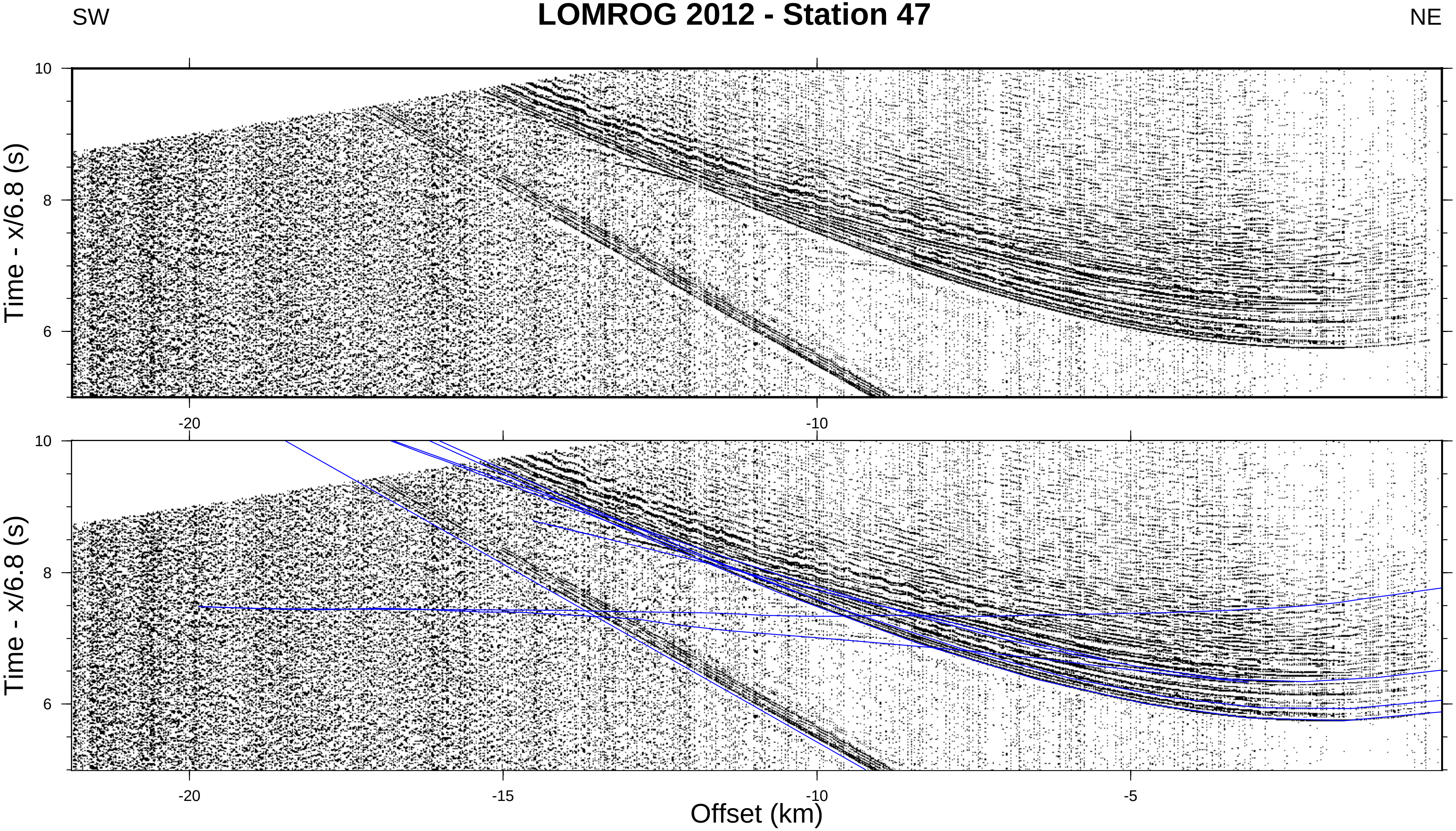

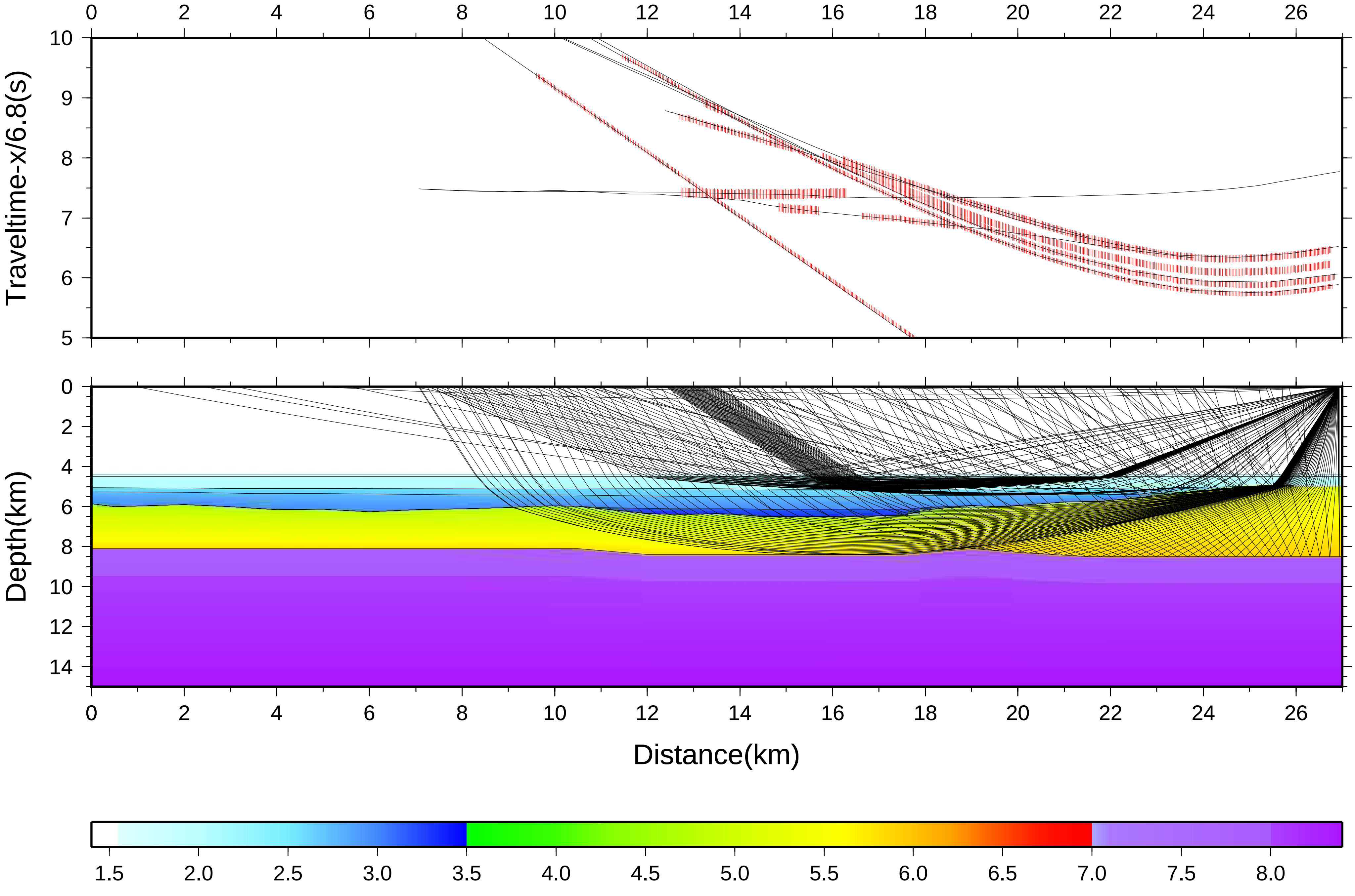

Traveltime-x/6.8(s)
Depth(km)
Distance(km)
1.5
2.0
2.5
3.0
3.5
4.0
4.5
5.0
5.5
6.0
6.5
7.0
7.5
8.0

LOMROG 2012 - Station 48

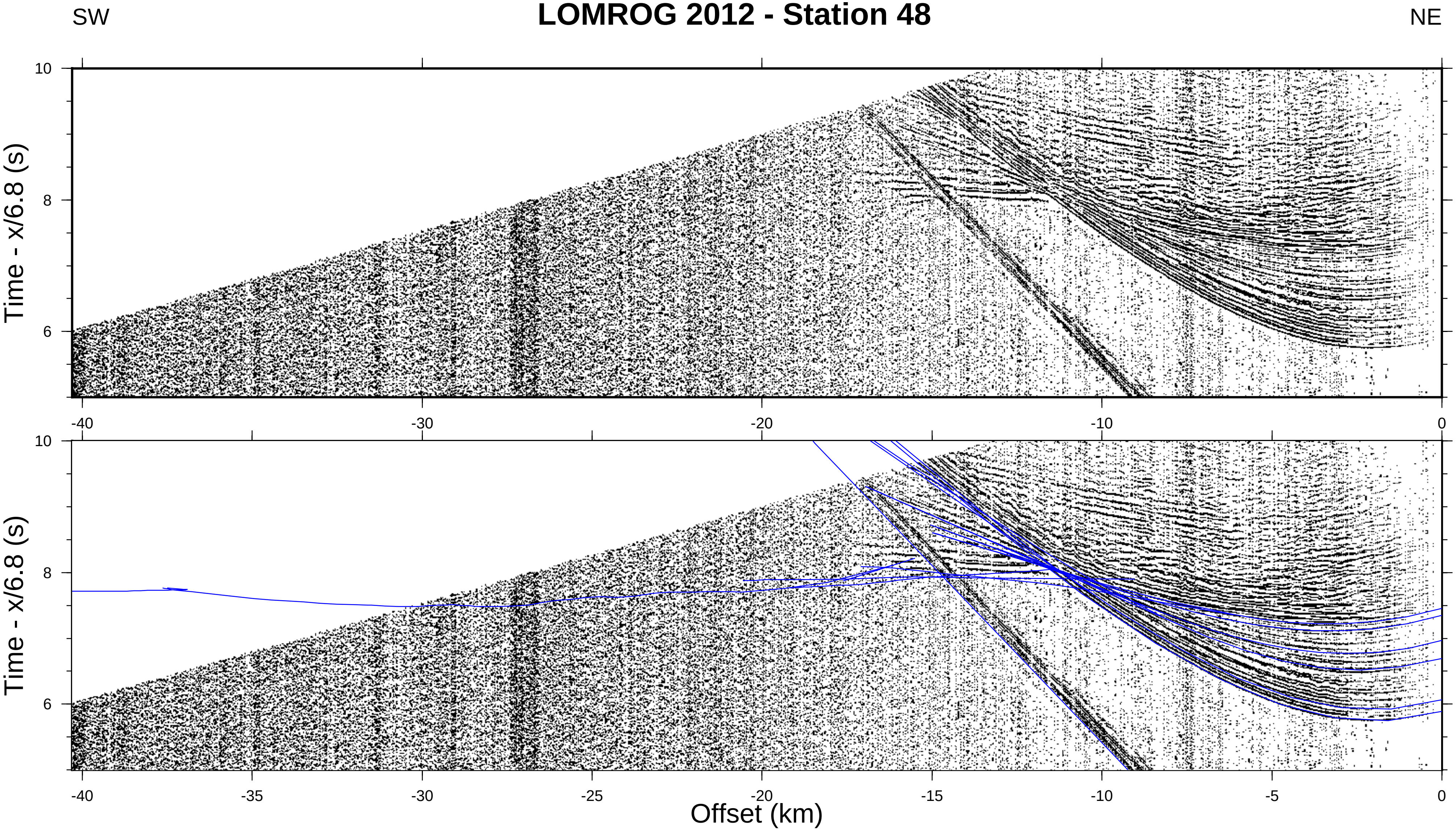

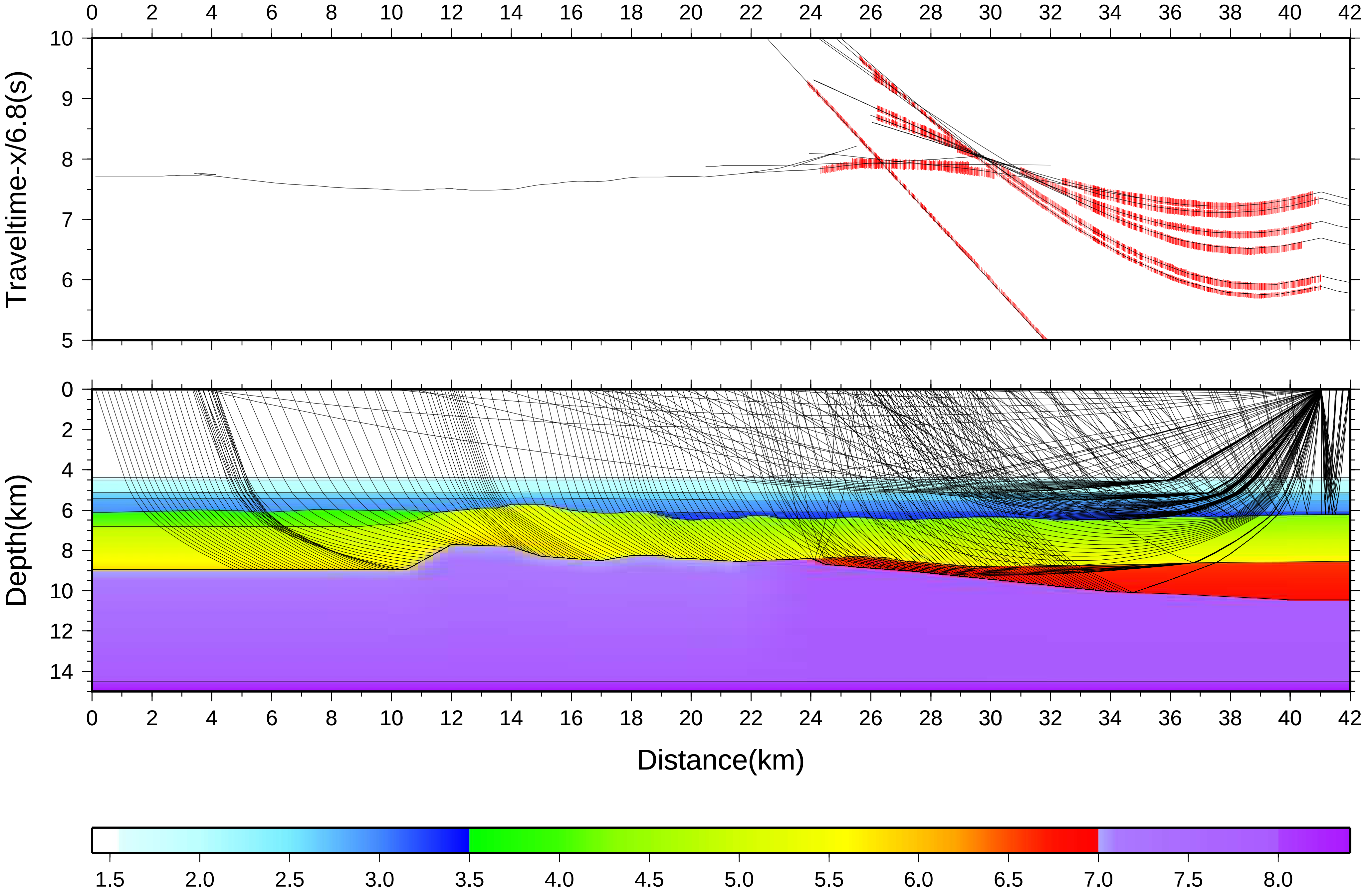
Traveltime-x/6.8(s)
Depth(km)
Distance(km)
0 2 4 6 8 10 12 14 16 18 20 22 24 26 28 30 32 34 36 38 40 42
10 9 8 7 6 5
0 2 4 6 8 10 12 14
1.5 2.0 2.5 3.0 3.5 4.0 4.5 5.0 5.5 6.0 6.5 7.0 7.5 8.0

LOMROG 2012 - Station 49

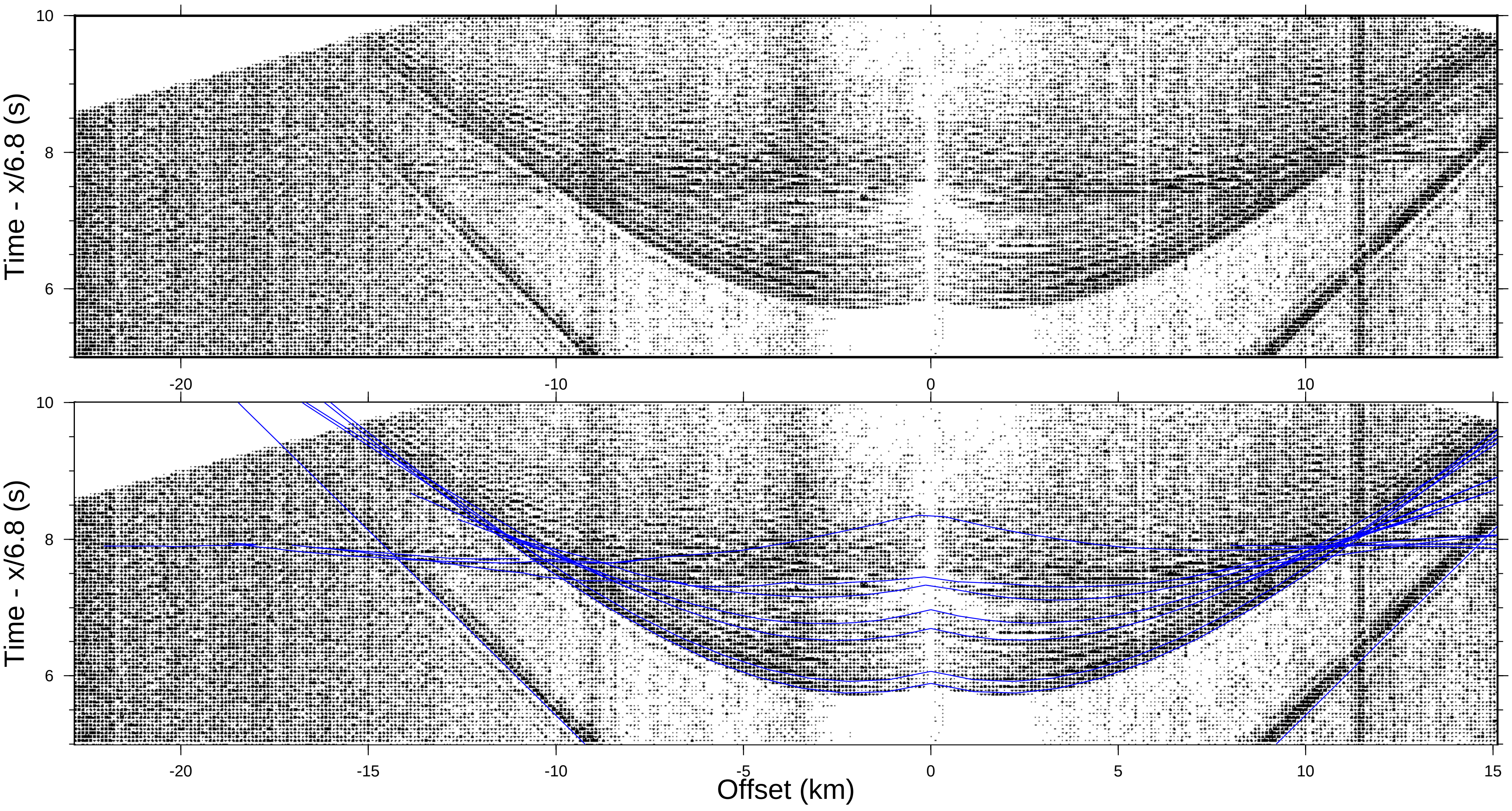

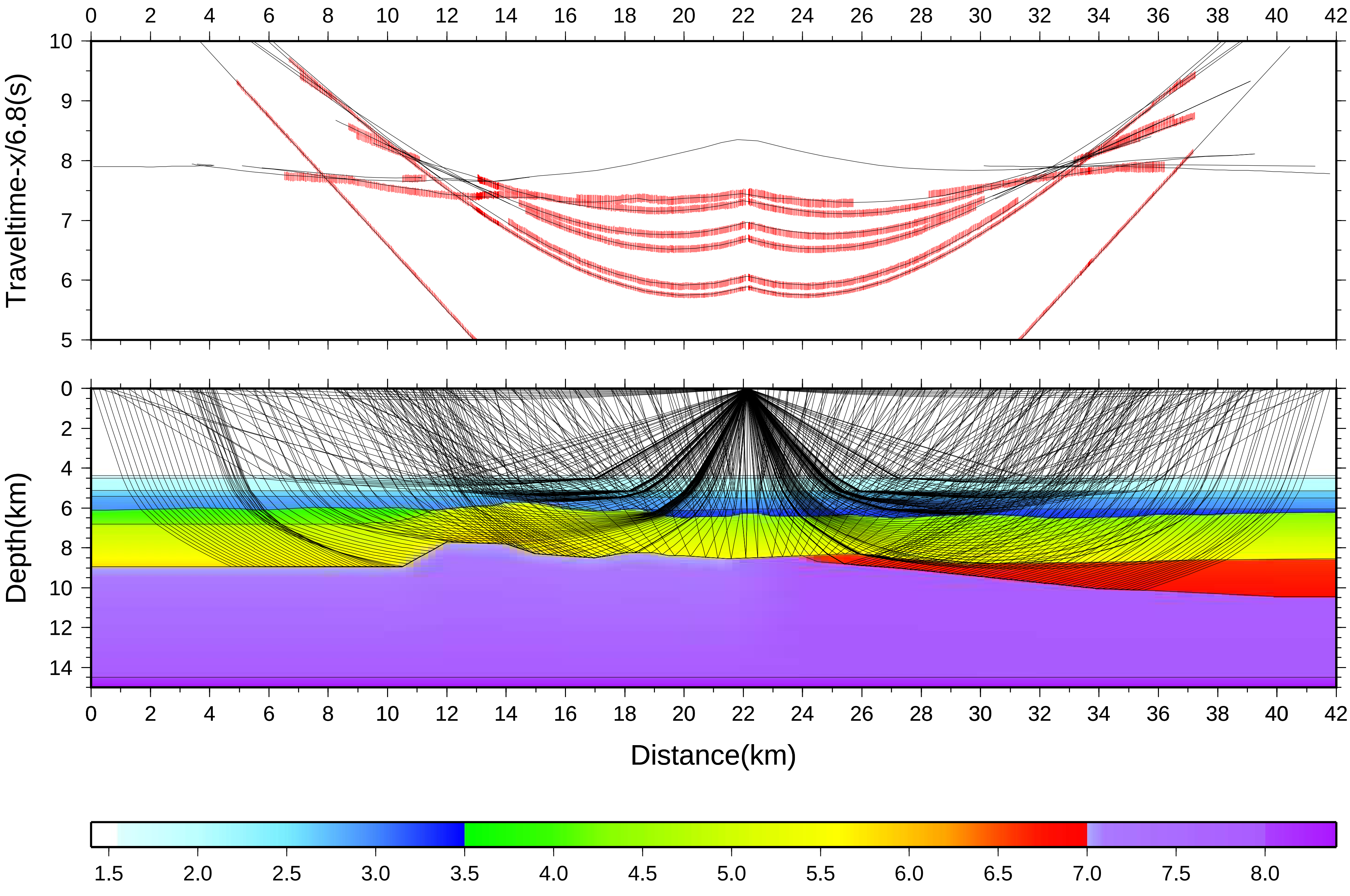
Traveltime-x/6.8(s)
Depth(km)
Distance(km)
0 2 4 6 8 10 12 14 16 18 20 22 24 26 28 30 32 34 36 38 40 42
1.5 2.0 2.5 3.0 3.5 4.0 4.5 5.0 5.5 6.0 6.5 7.0 7.5 8.0

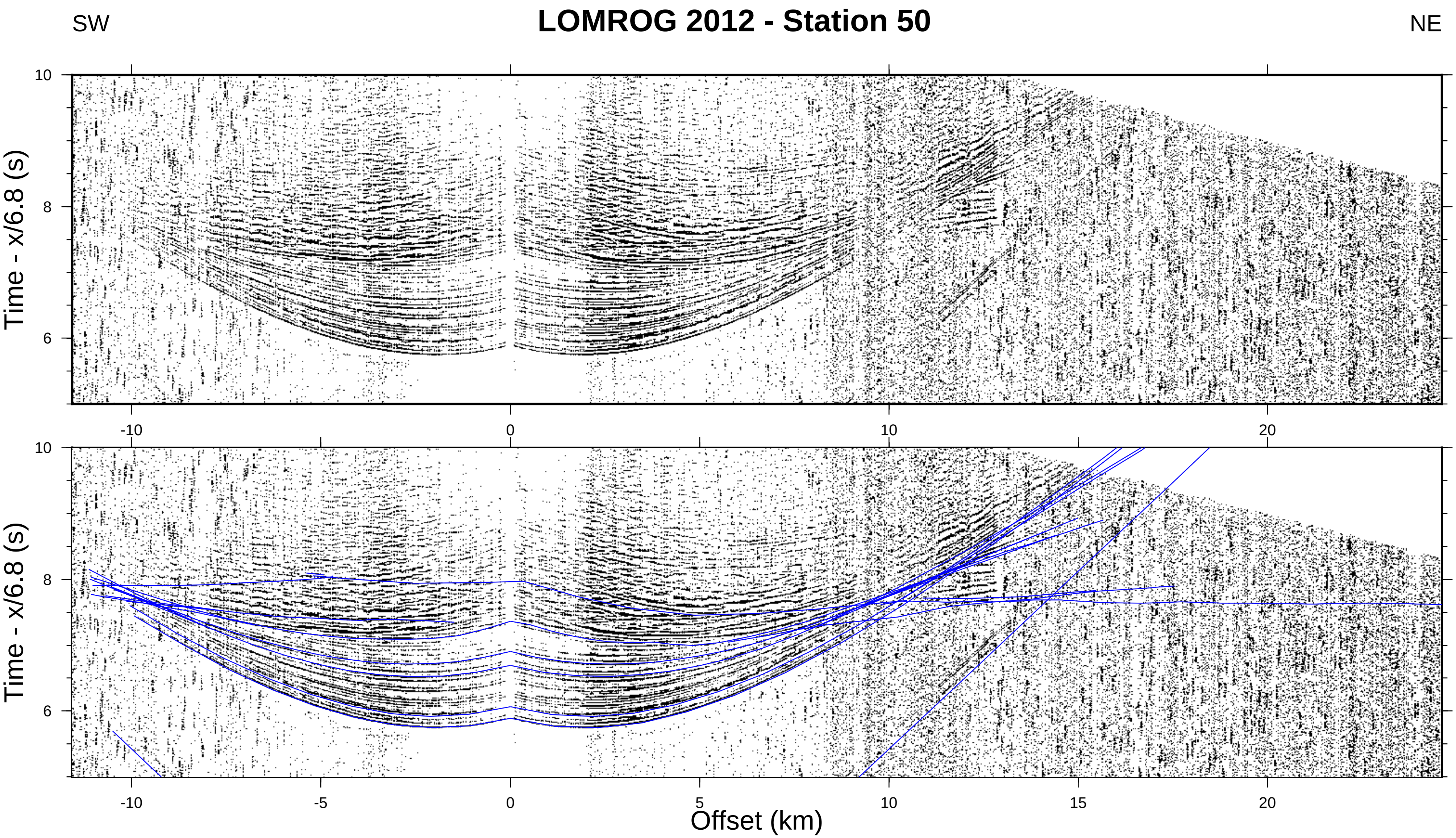
SW
LOMROG 2012 - Station 50
NE
Time - x/6.8 (s)
10
8
6
-10
0
10
20
Time - x/6.8 (s)
10
8
6
-10
-5
0
5
10
15
20
Offset (km)

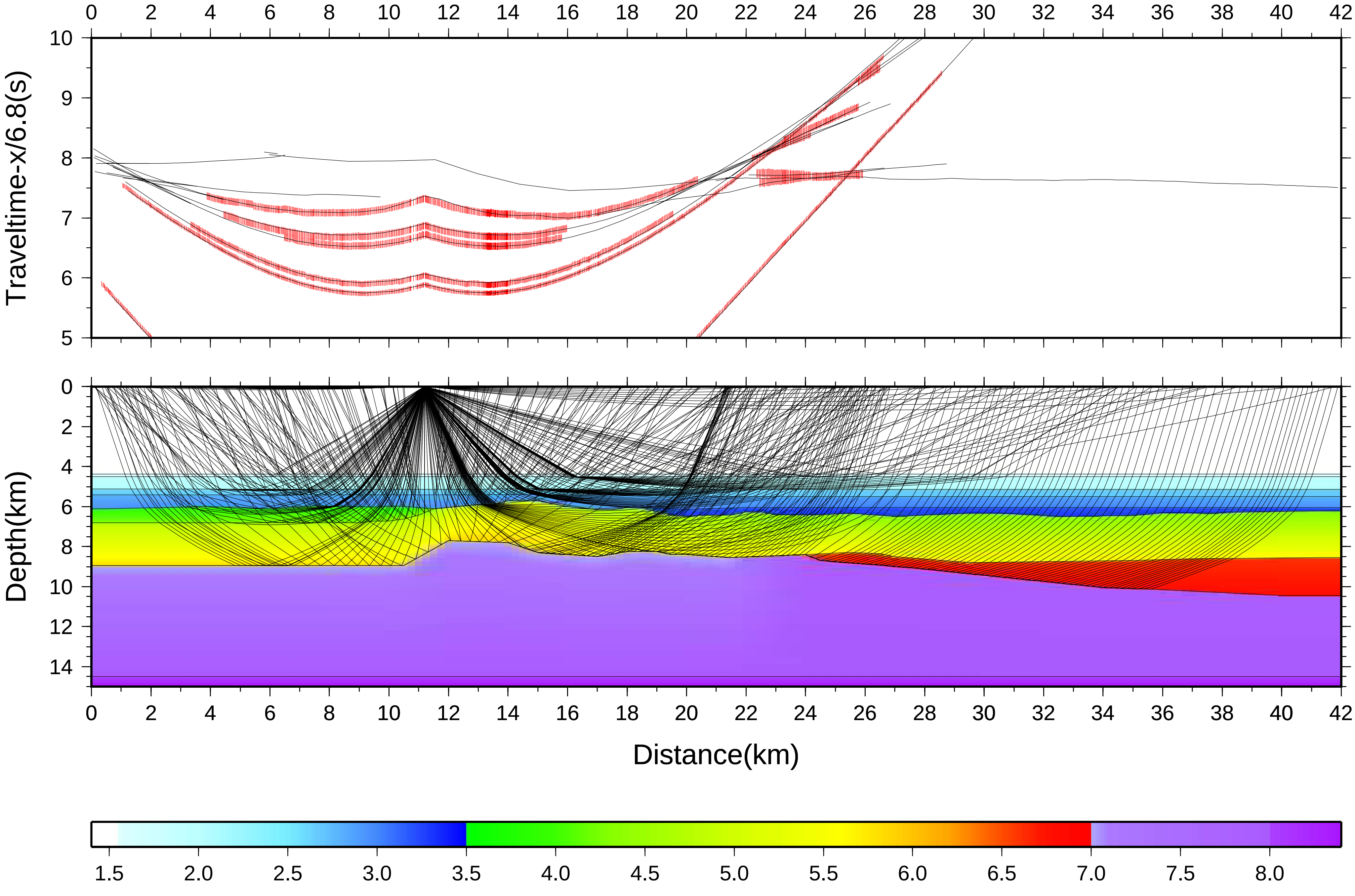

Traveltime-x/6.8(s)
Depth(km)
Distance(km)
0 2 4 6 8 10 12 14 16 18 20 22 24 26 28 30 32 34 36 38 40 42
1.5 2.0 2.5 3.0 3.5 4.0 4.5 5.0 5.5 6.0 6.5 7.0 7.5 8.0

LOMROG 2012 - Station 51

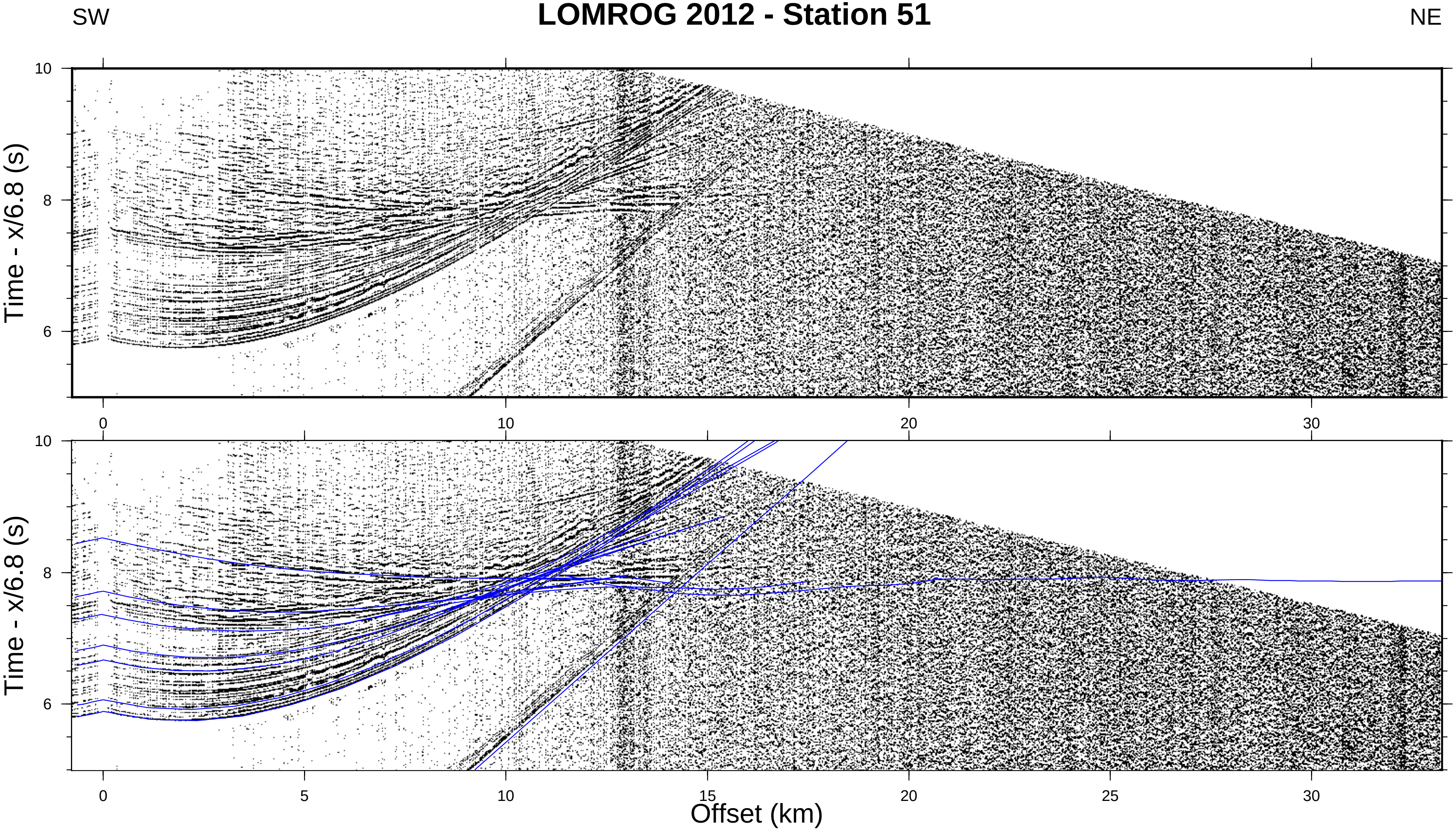

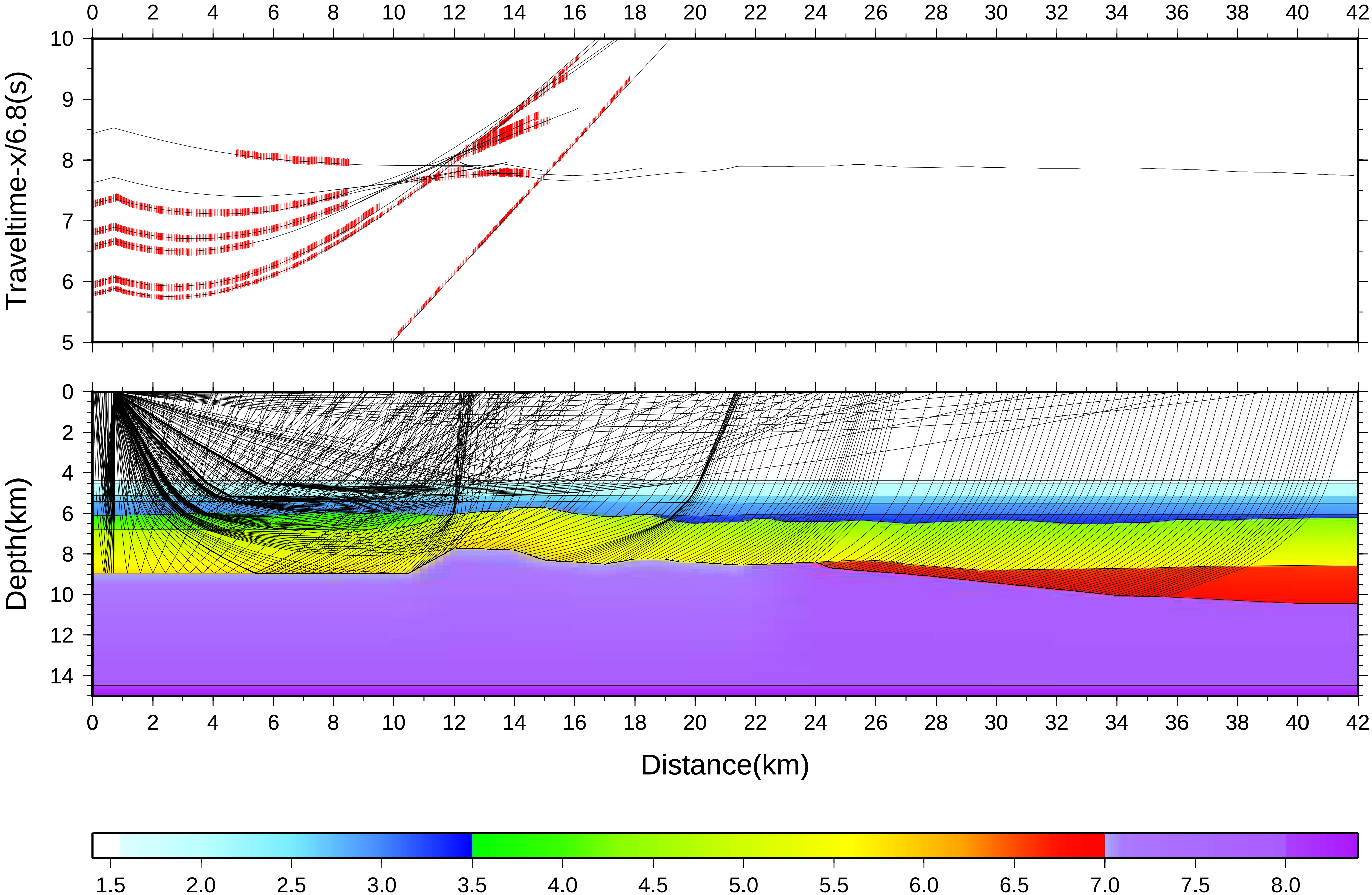

Traveltime-x/6.8(s)
Depth(km)
Distance(km)
1.5 2.0 2.5 3.0 3.5 4.0 4.5 5.0 5.5 6.0 6.5 7.0 7.5 8.0

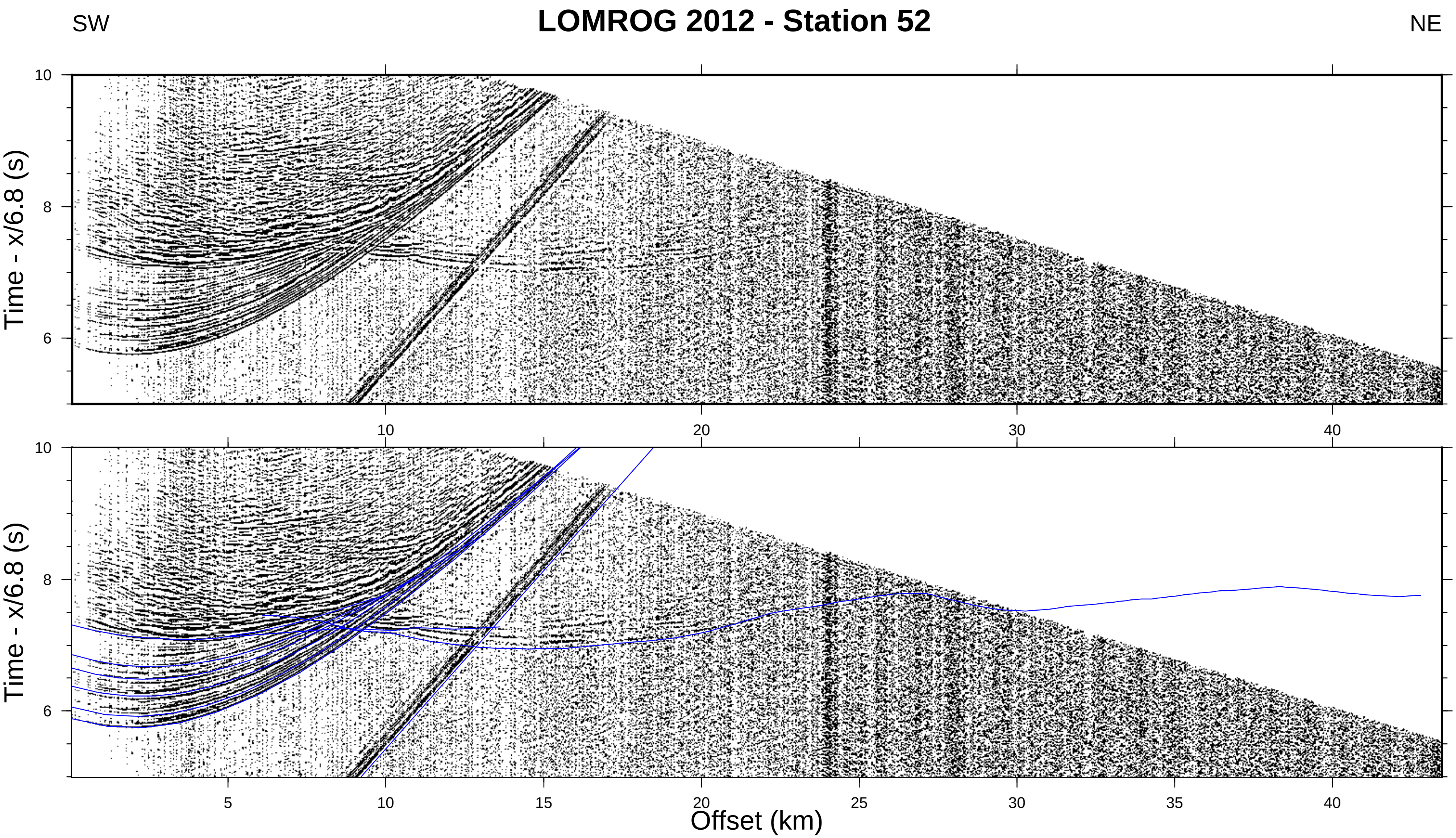
SW
LOMROG 2012 - Station 52
NE
Time - x/6.8 (s)
Offset (km)
10
8
6
5
10
15
20
25
30
35
40

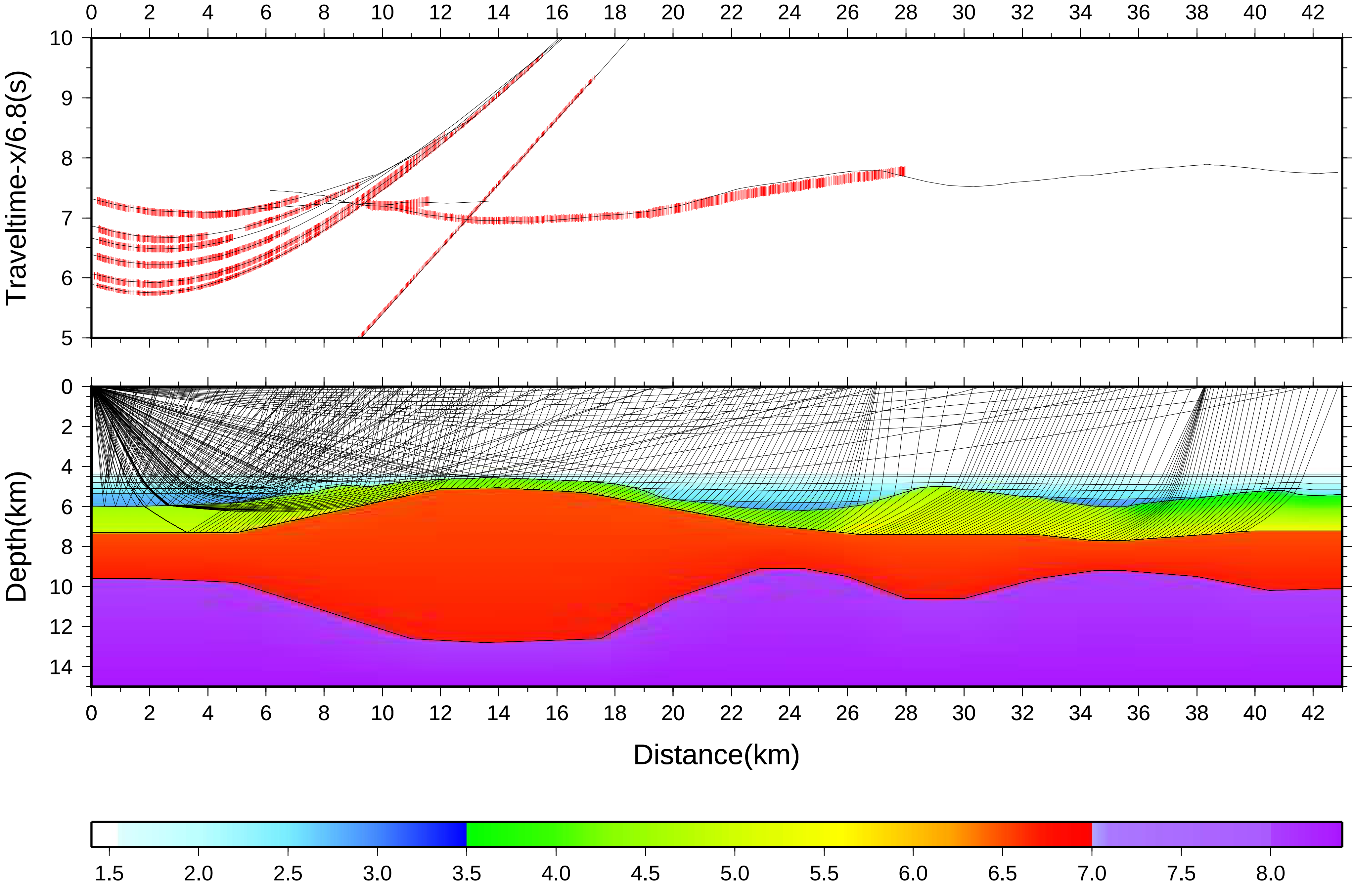
Traveltime-x/6.8(s)
Depth(km)
Distance(km)
1.5 2.0 2.5 3.0 3.5 4.0 4.5 5.0 5.5 6.0 6.5 7.0 7.5 8.0

LOMROG 2012 - Station 53

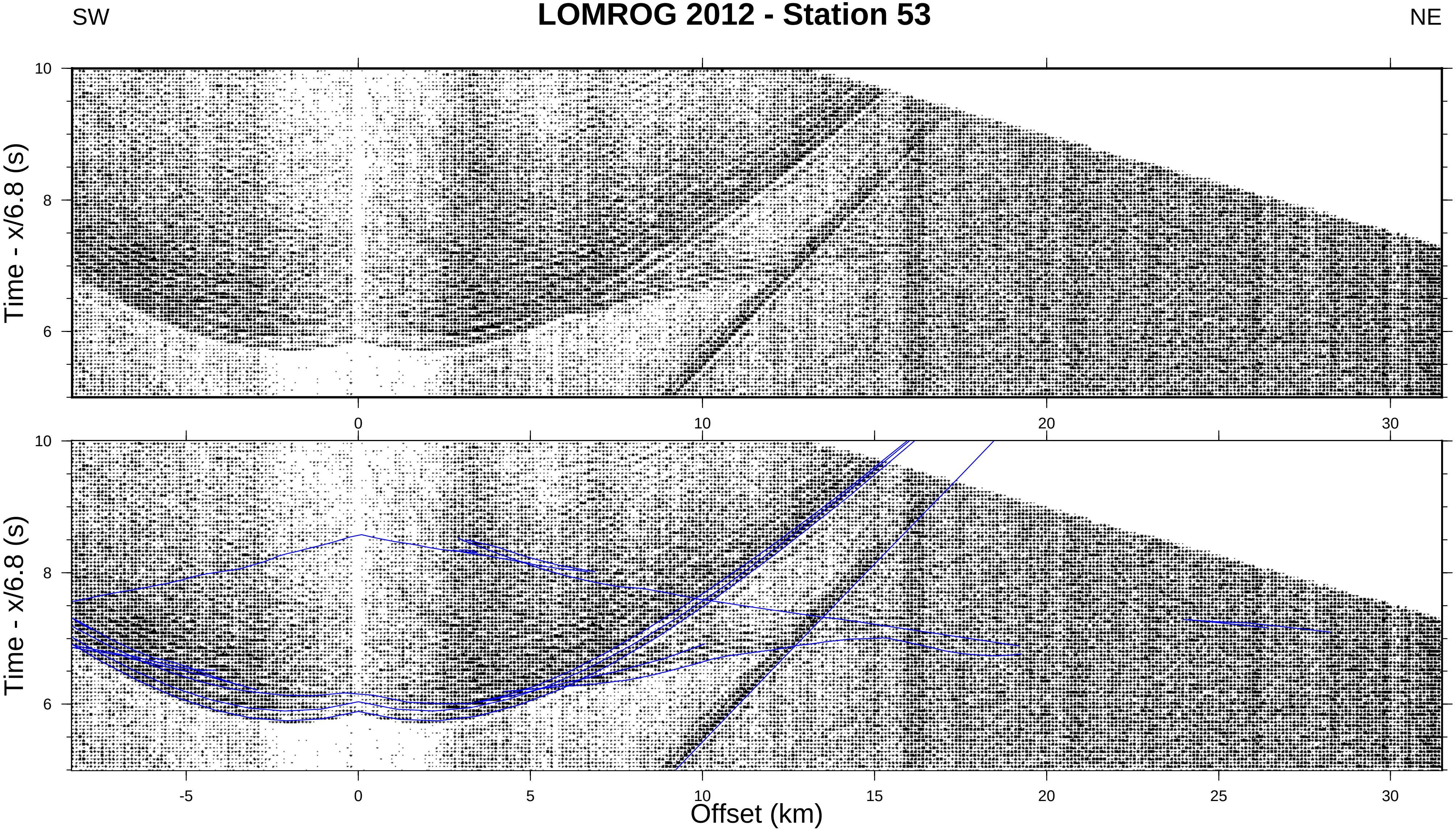

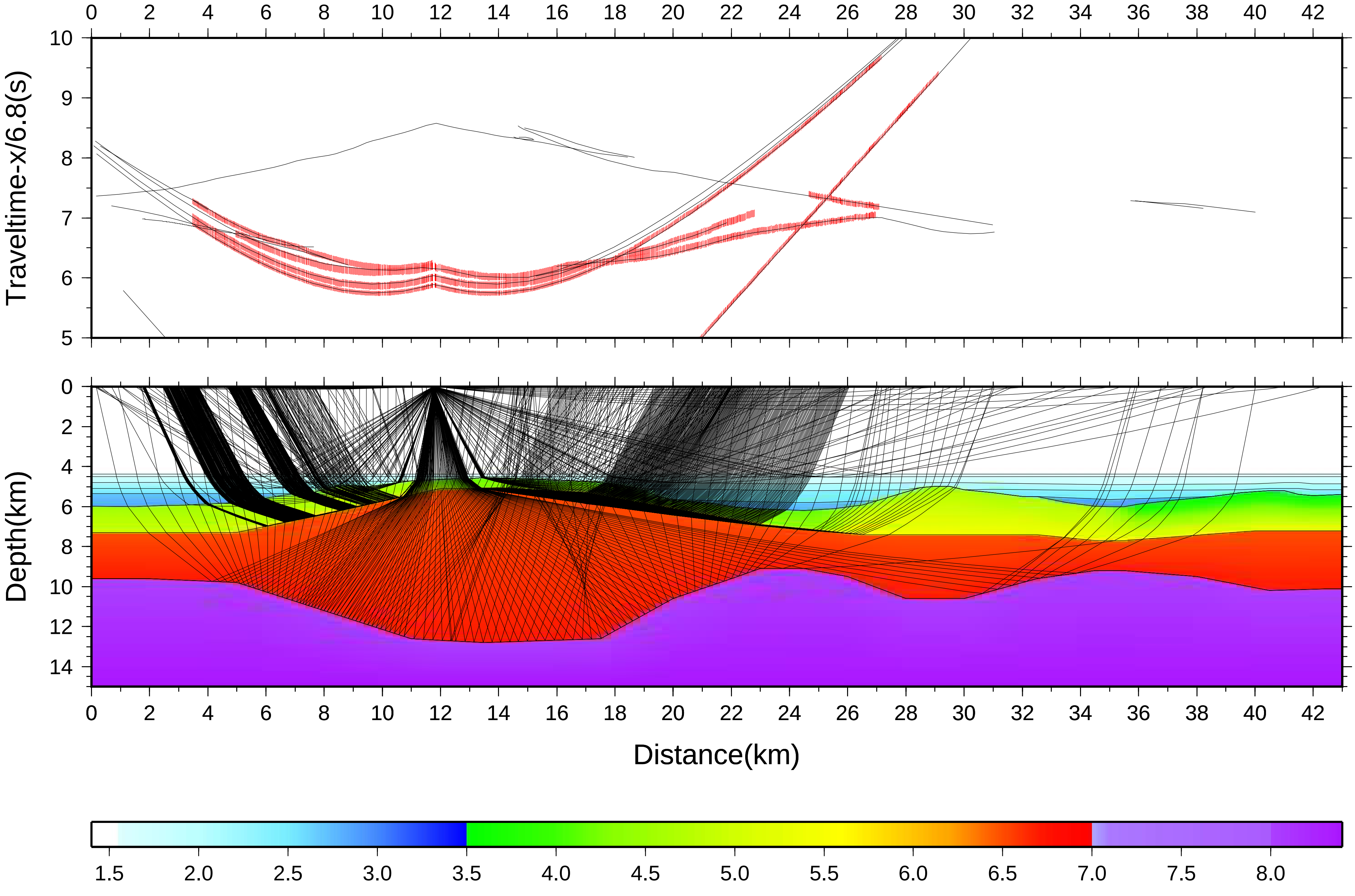
Traveltime-x/6.8(s)
Depth(km)
Distance(km)
0 2 4 6 8 10 12 14 16 18 20 22 24 26 28 30 32 34 36 38 40 42
1.5 2.0 2.5 3.0 3.5 4.0 4.5 5.0 5.5 6.0 6.5 7.0 7.5 8.0

LOMROG 2012 - Station 54

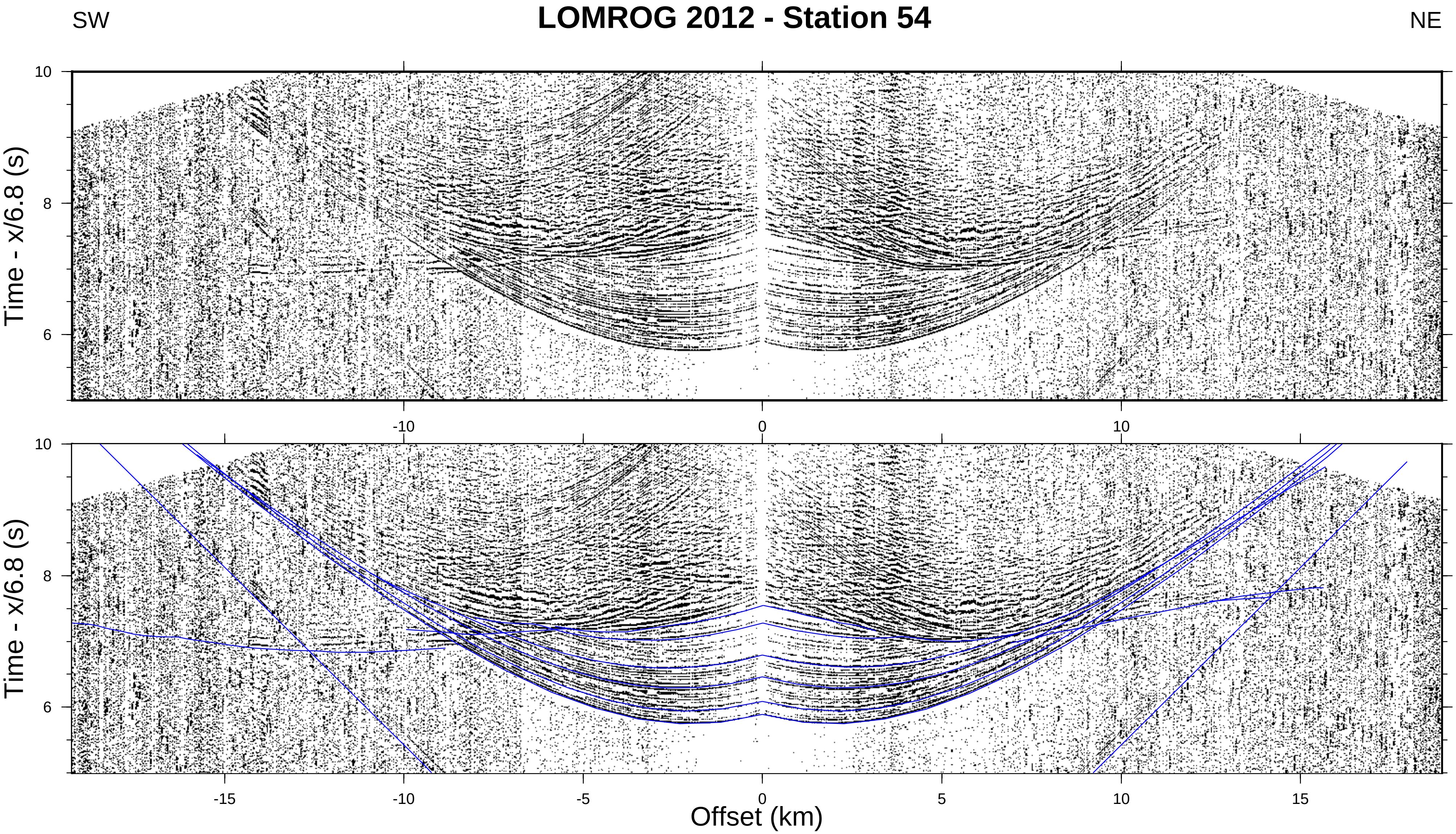

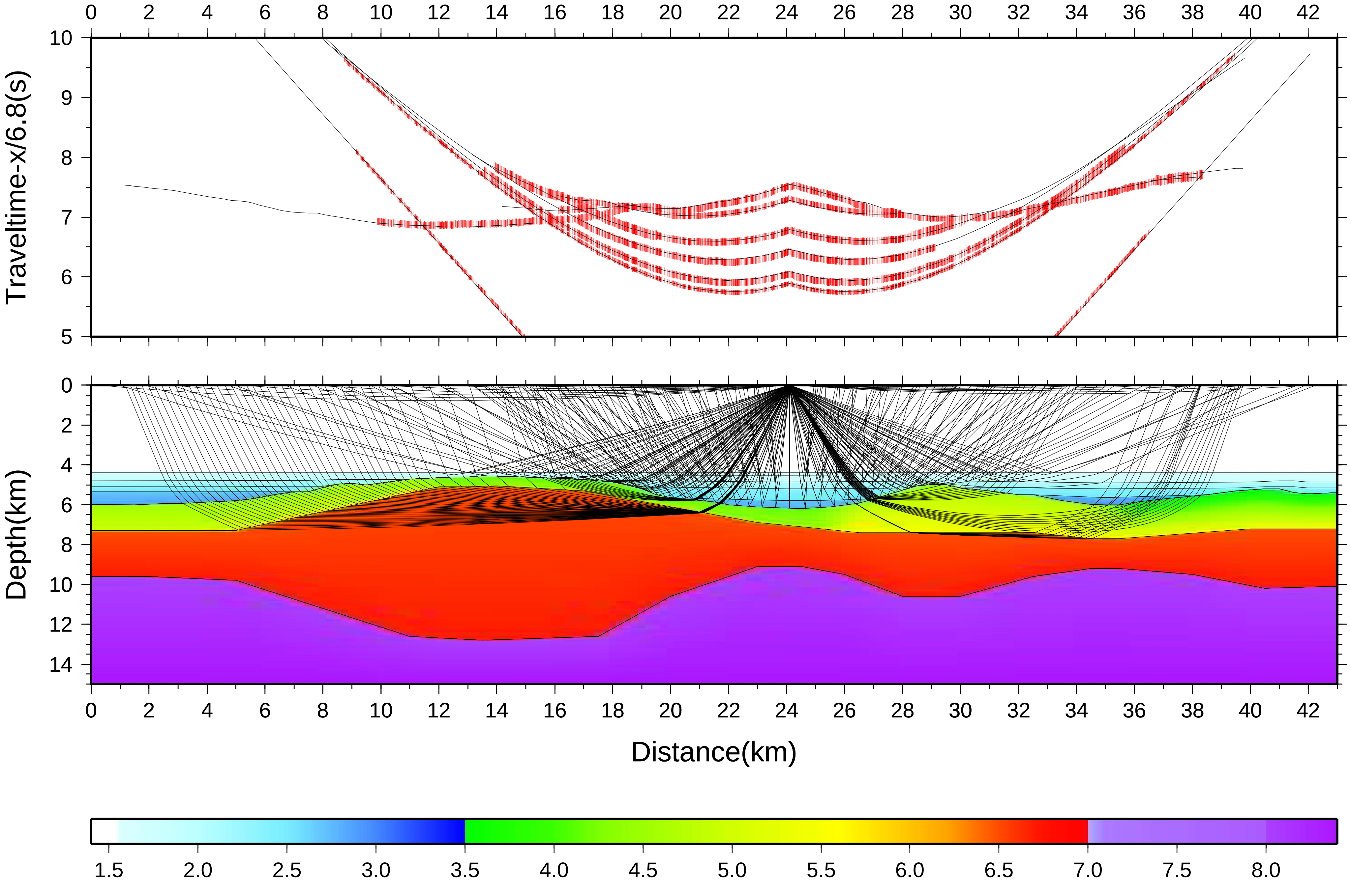

Traveltime-x/6.8(s)
Depth(km)
Distance(km)
0 2 4 6 8 10 12 14 16 18 20 22 24 26 28 30 32 34 36 38 40 42
10 9 8 7 6 5
0 2 4 6 8 10 12 14
1.5 2.0 2.5 3.0 3.5 4.0 4.5 5.0 5.5 6.0 6.5 7.0 7.5 8.0

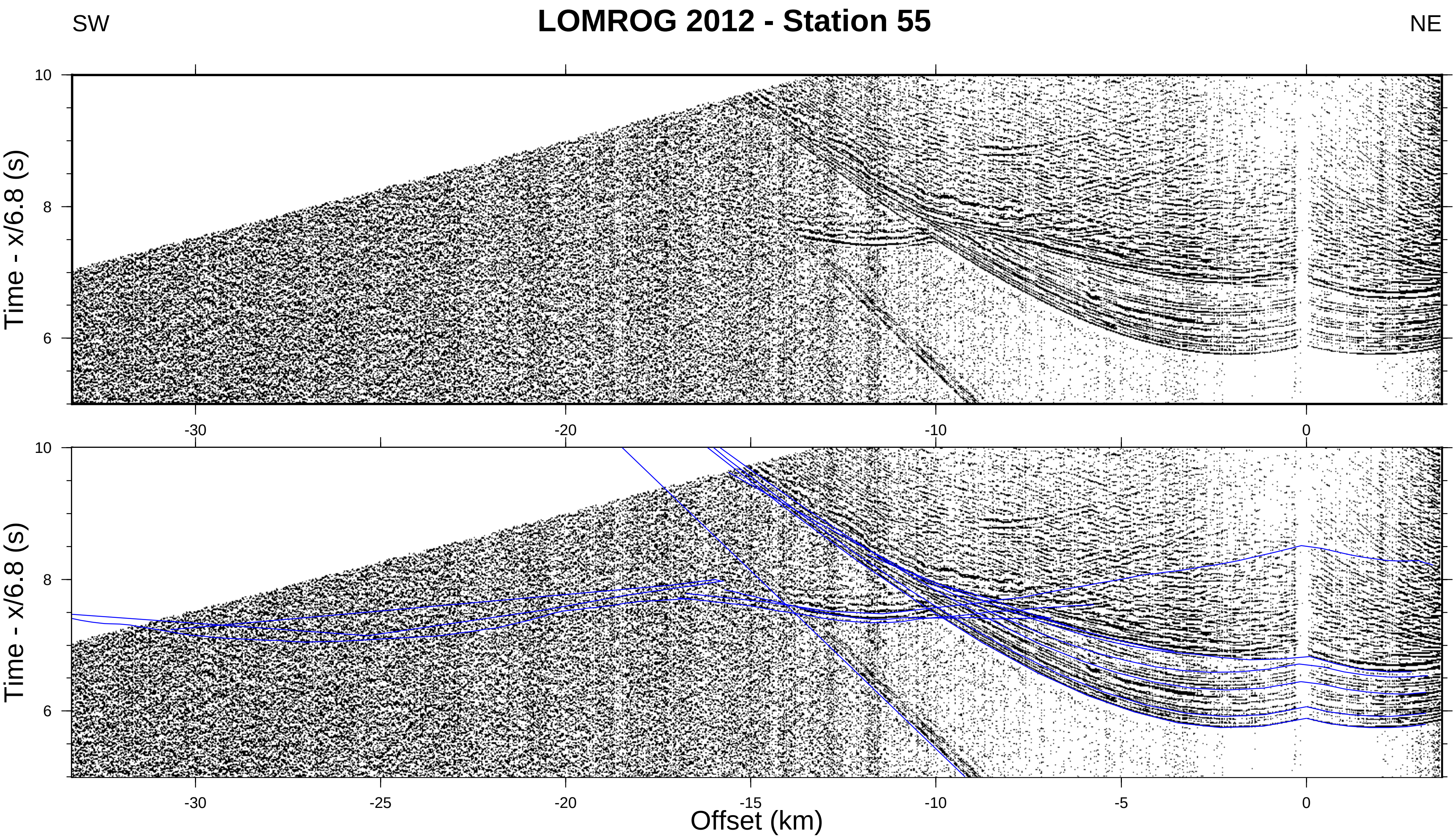
SW
LOMROG 2012 - Station 55
NE
Time - x/6.8 (s)
10
8
6
-30
-20
-10
0
-25
-15
-5
Offset (km)

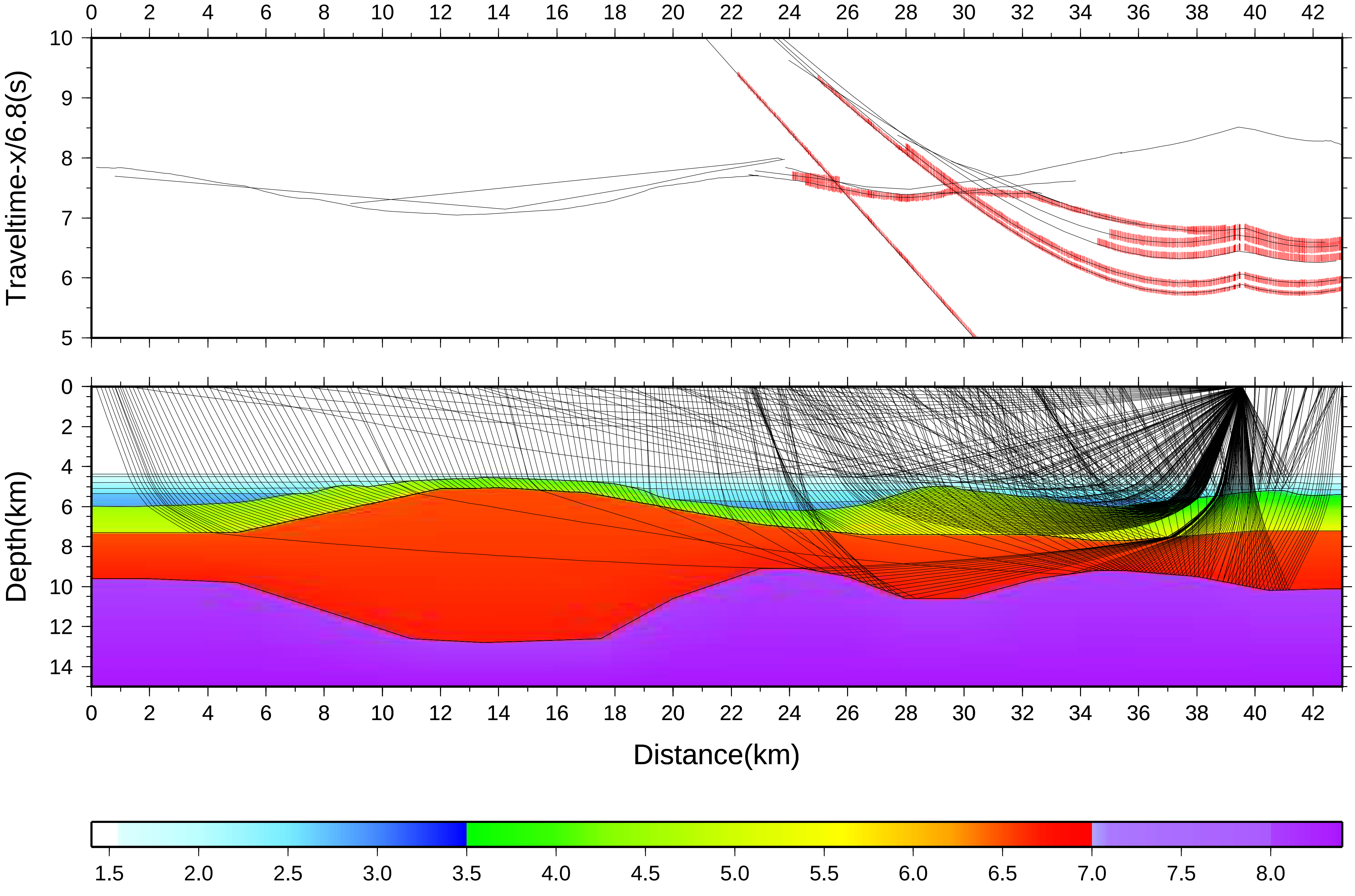
Traveltime-x/6.8(s)
Depth(km)
Distance(km)
0 2 4 6 8 10 12 14 16 18 20 22 24 26 28 30 32 34 36 38 40 42
1.5 2.0 2.5 3.0 3.5 4.0 4.5 5.0 5.5 6.0 6.5 7.0 7.5 8.0

LOMROG 2012 - Station 56

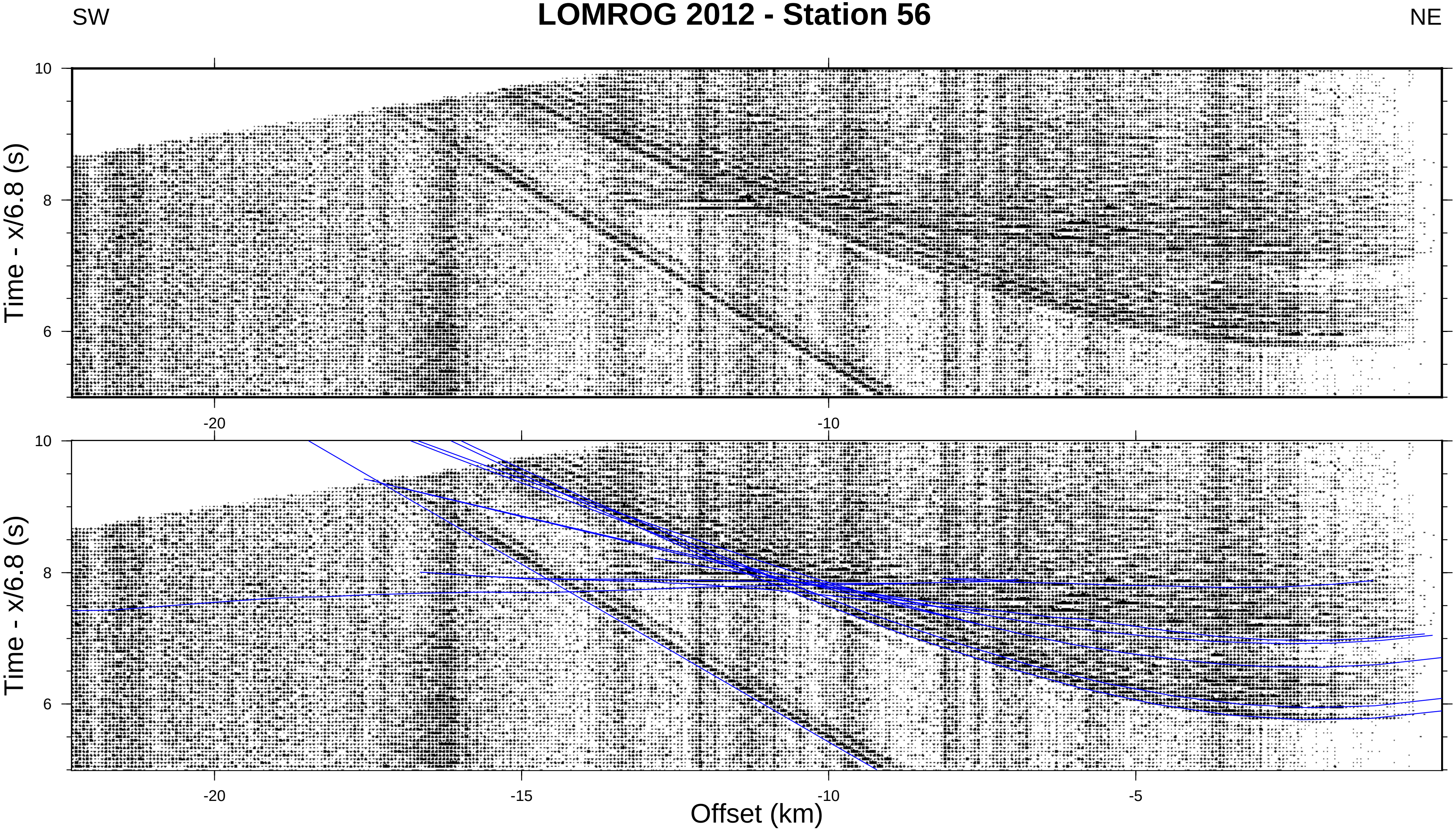

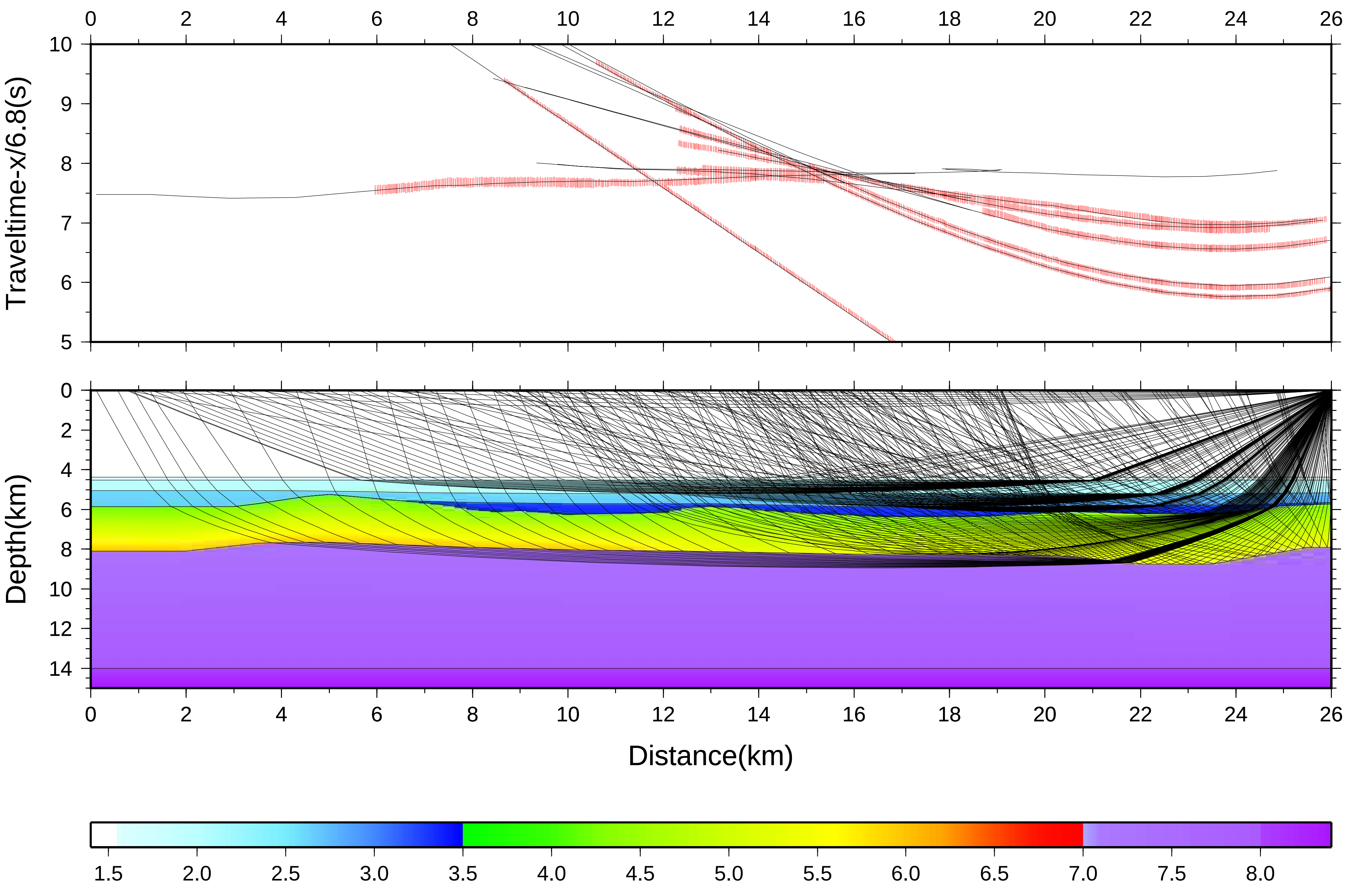

Traveltime-x/6.8(s)
Depth(km)
Distance(km)
0 2 4 6 8 10 12 14 16 18 20 22 24 26
10 9 8 7 6 5
0 2 4 6 8 10 12 14
1.5 2.0 2.5 3.0 3.5 4.0 4.5 5.0 5.5 6.0 6.5 7.0 7.5 8.0

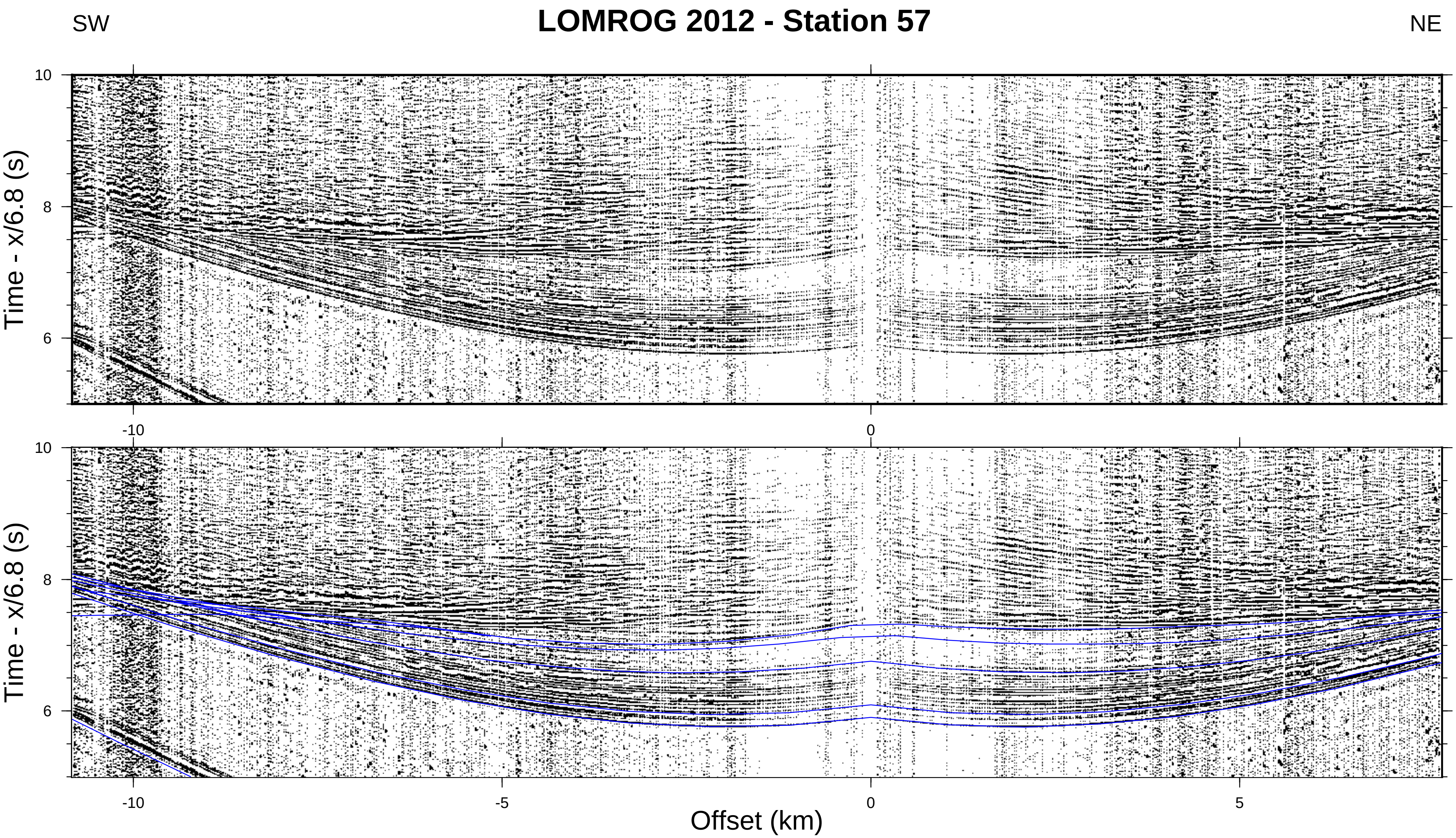
SW
LOMROG 2012 - Station 57
NE
Time - x/6.8 (s)
10
8
6
-10
0
Time - x/6.8 (s)
10
8
6
-10
-5
0
5
Offset (km)

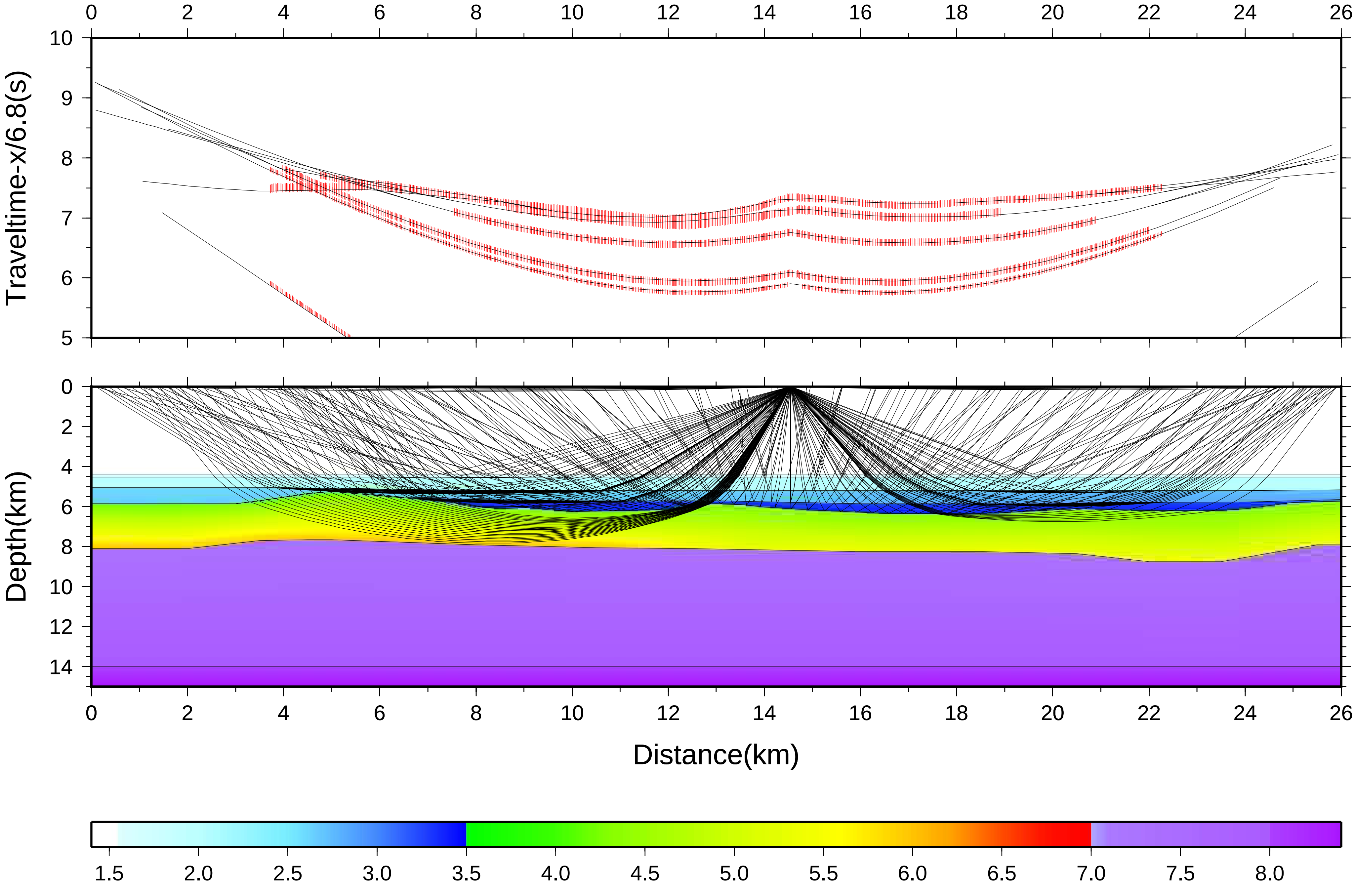

Traveltime-x/6.8(s)
Depth(km)
Distance(km)
1.5 2.0 2.5 3.0 3.5 4.0 4.5 5.0 5.5 6.0 6.5 7.0 7.5 8.0

LOMROG 2012 - Station 59

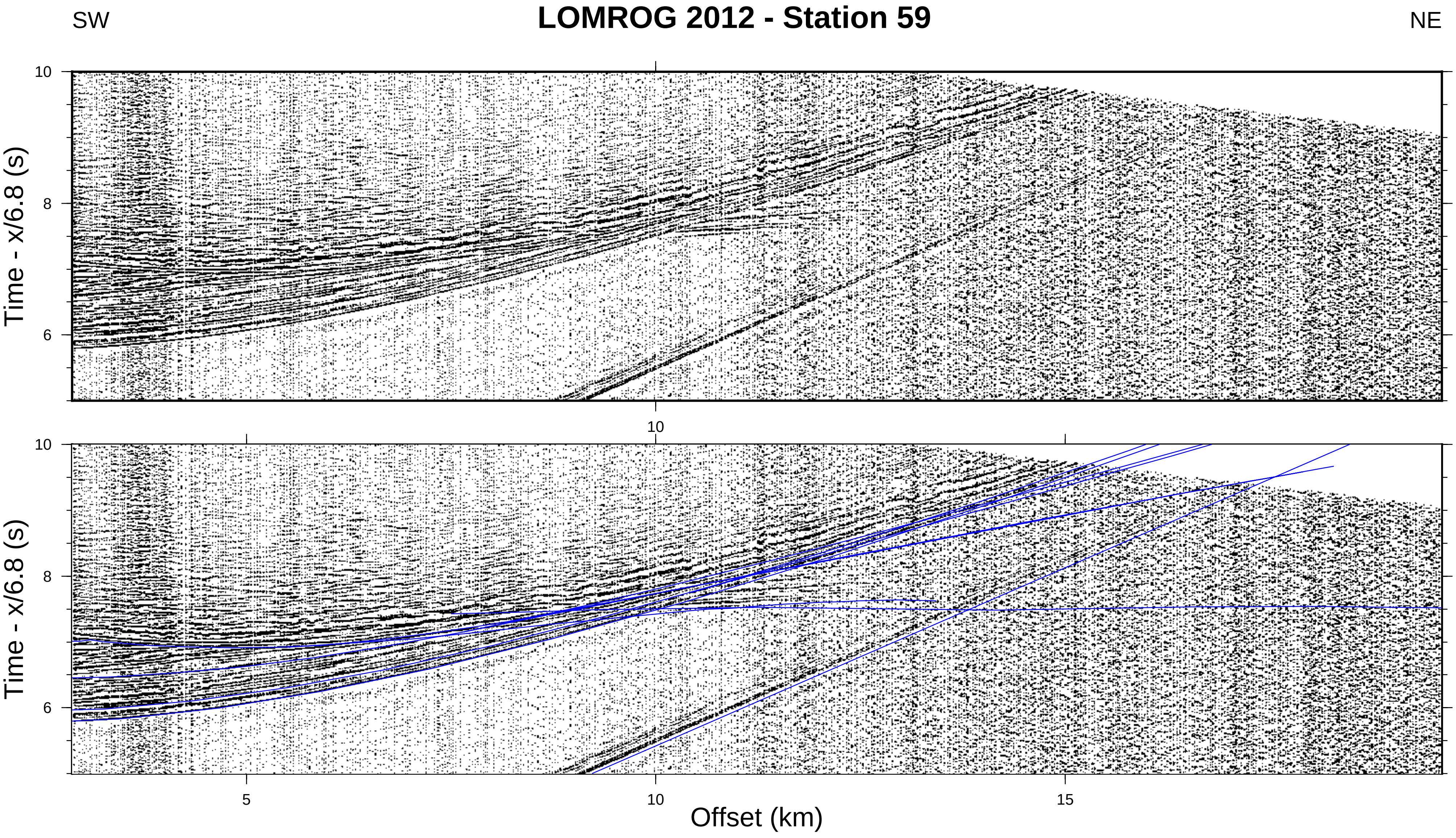

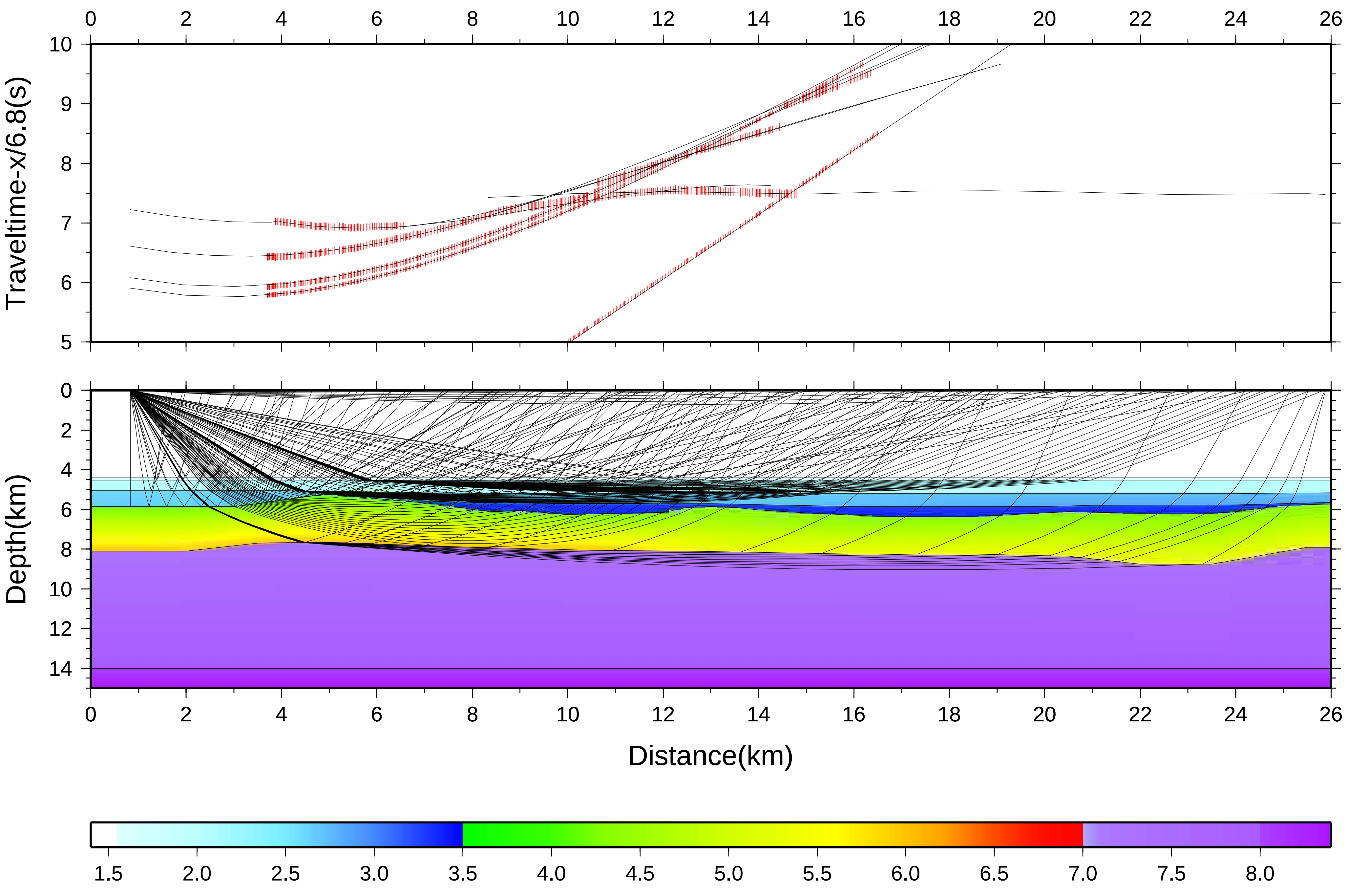

Traveltime-x/6.8(s)
Depth(km)
Distance(km)
0
2
4
6
8
10
12
14
16
18
20
22
24
26
5
6
7
8
9
10
0
2
4
6
8
10
12
14
1.5
2.0
2.5
3.0
3.5
4.0
4.5
5.0
5.5
6.0
6.5
7.0
7.5
8.0

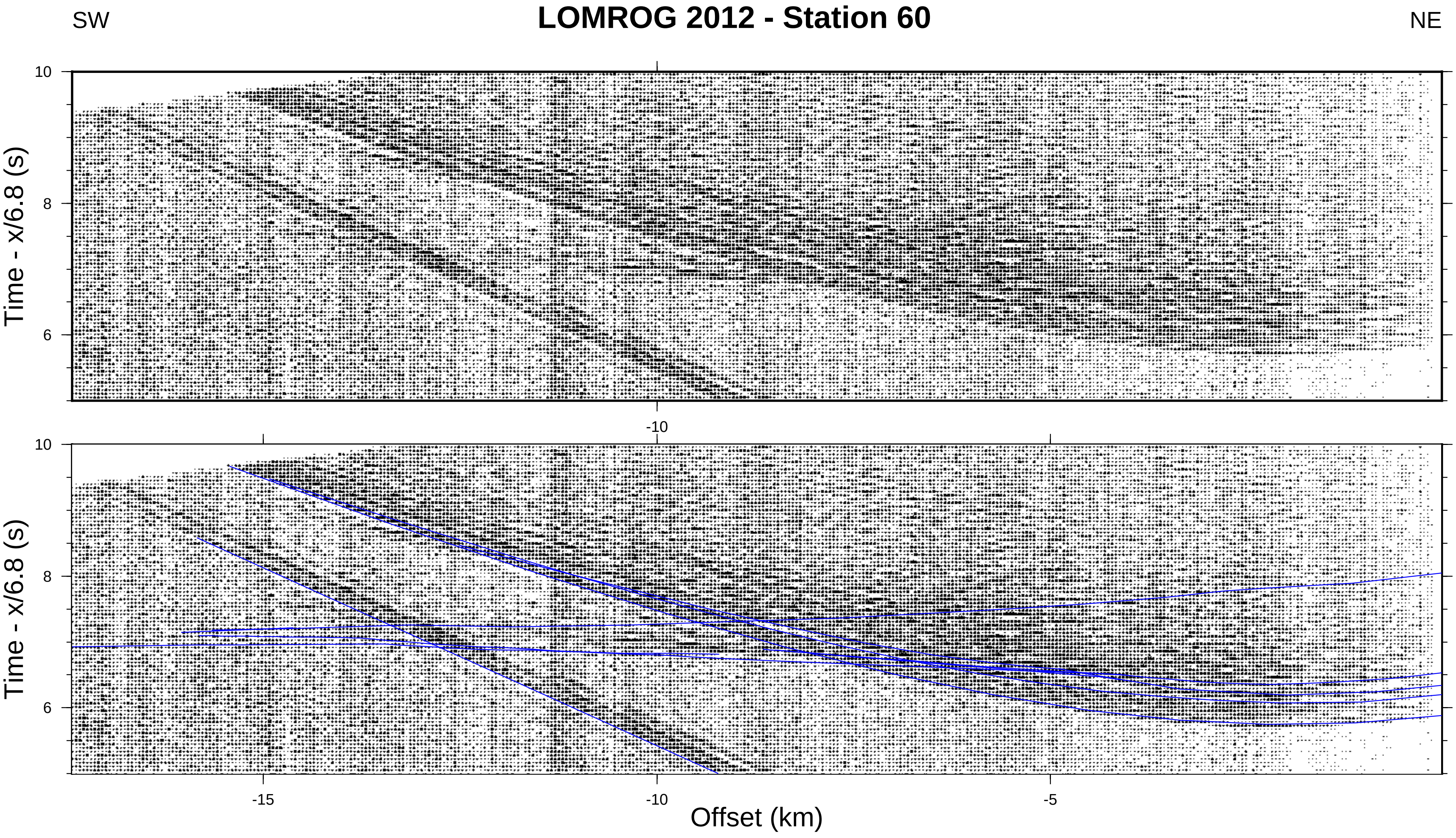

SW
LOMROG 2012 - Station 60
NE
10
8
6
Time - x/6.8 (s)
-10
-15
-5
Offset (km)

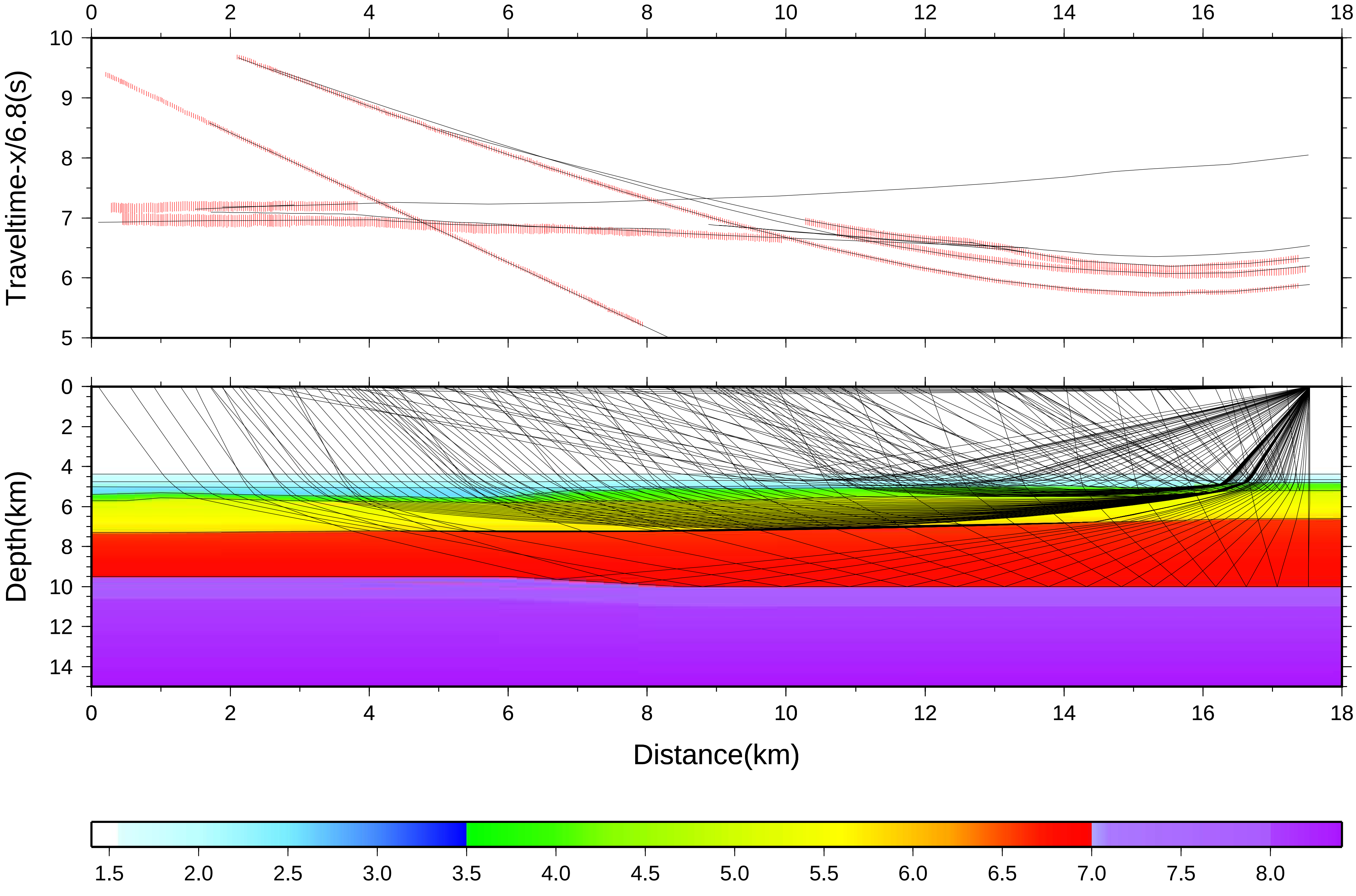
Traveltime-x/6.8(s)
Depth(km)
Distance(km)
0 2 4 6 8 10 12 14 16 18
10 9 8 7 6 5
0 2 4 6 8 10 12 14
1.5 2.0 2.5 3.0 3.5 4.0 4.5 5.0 5.5 6.0 6.5 7.0 7.5 8.0

LOMROG 2012 - Station 61

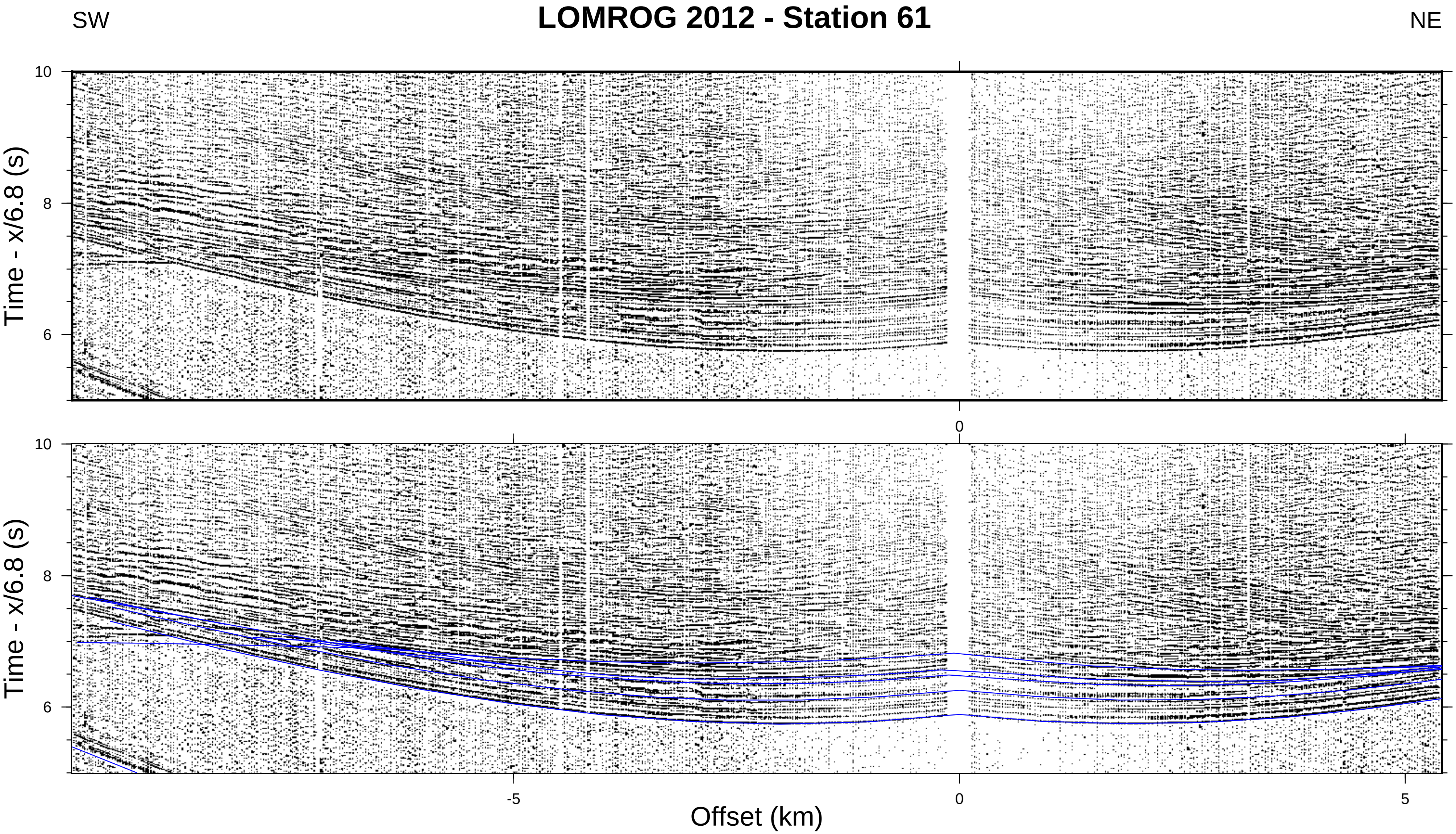

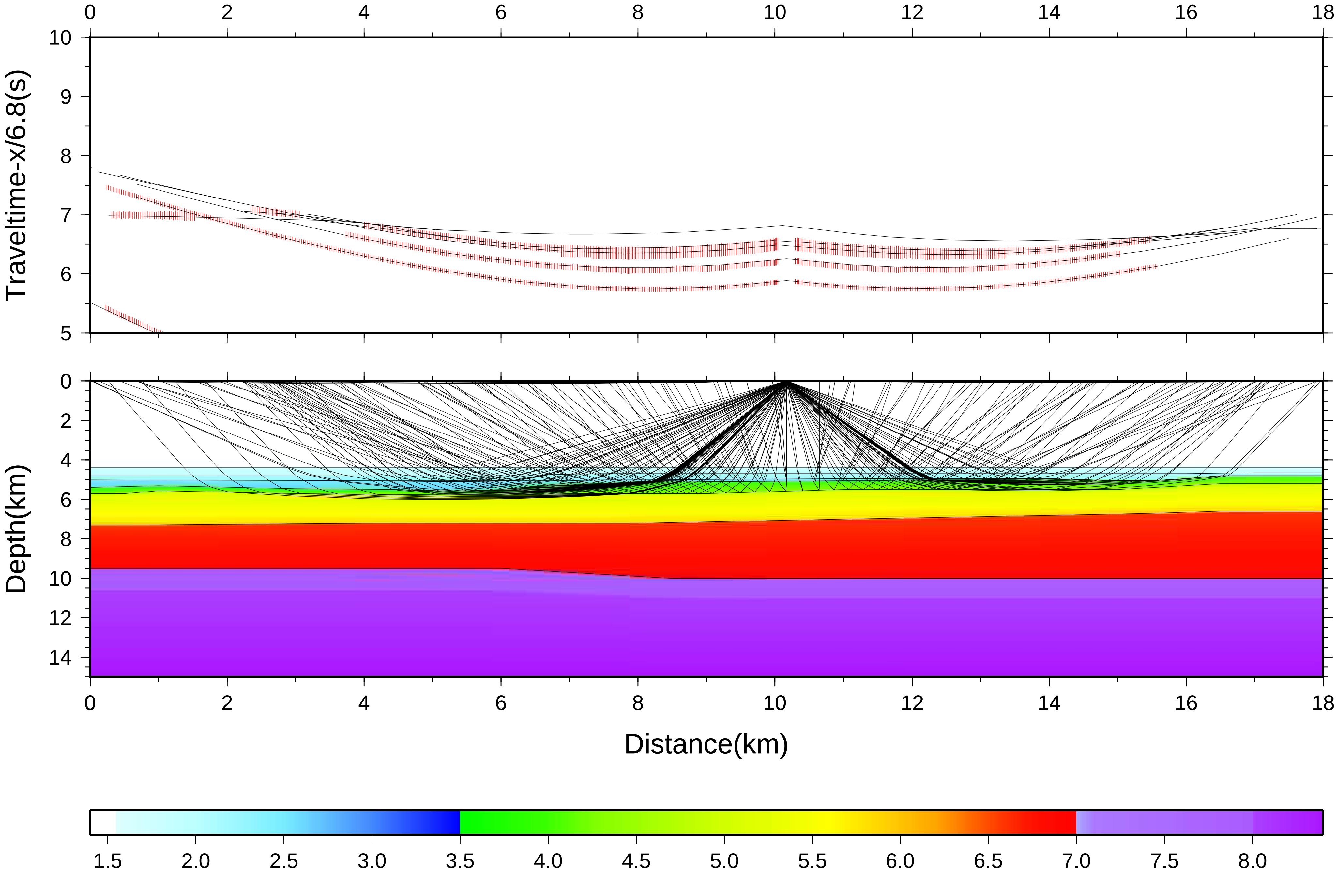
Traveltime-x/6.8(s)
Depth(km)
Distance(km)
0 2 4 6 8 10 12 14 16 18
1.5 2.0 2.5 3.0 3.5 4.0 4.5 5.0 5.5 6.0 6.5 7.0 7.5 8.0

LOMROG 2012 - Station 62

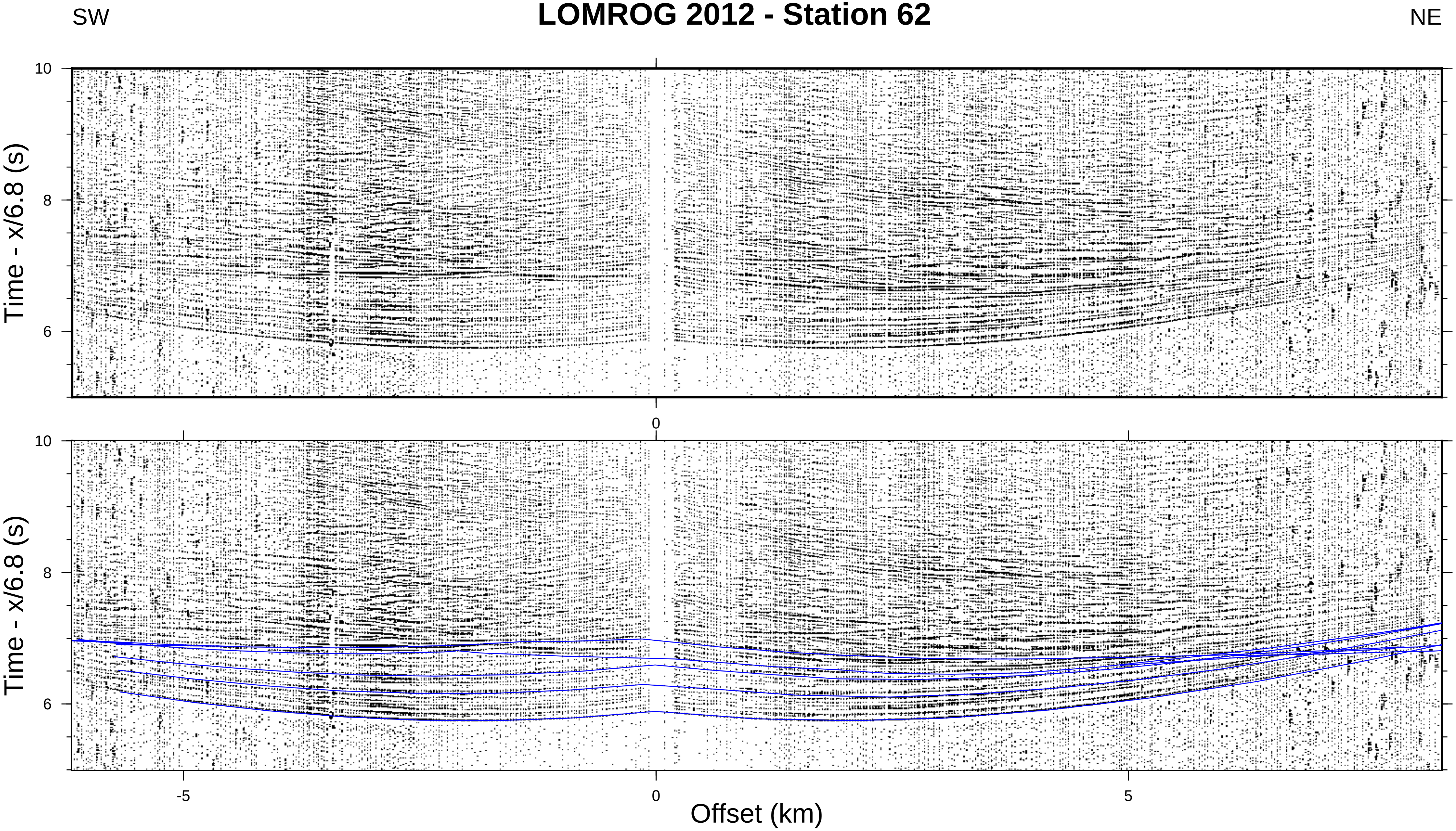

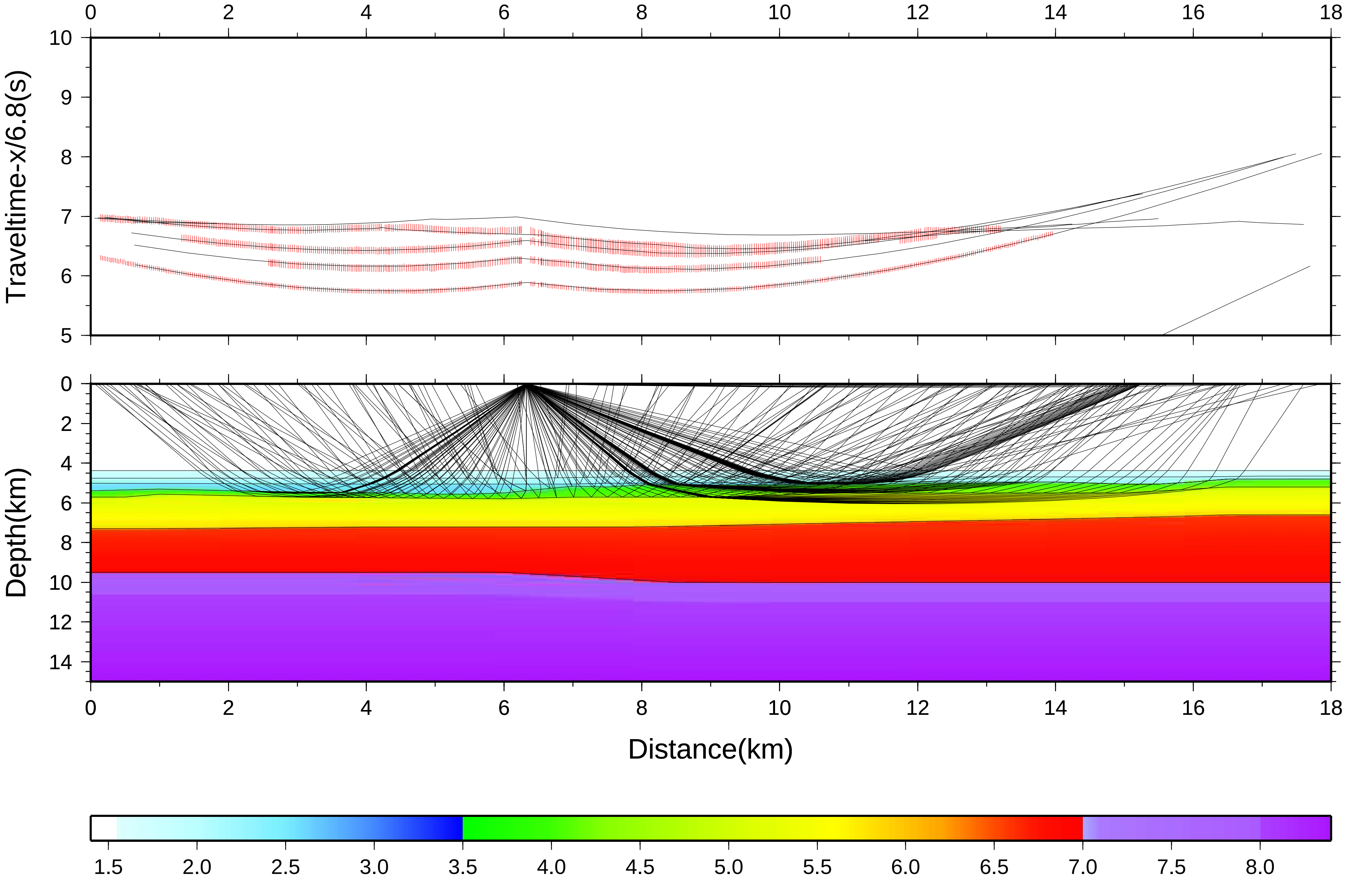

Traveltime-x/6.8(s)
Depth(km)
Distance(km)
0 2 4 6 8 10 12 14 16 18
10 9 8 7 6 5
0 2 4 6 8 10 12 14
1.5 2.0 2.5 3.0 3.5 4.0 4.5 5.0 5.5 6.0 6.5 7.0 7.5 8.0

LOMROG 2012 - Station 63

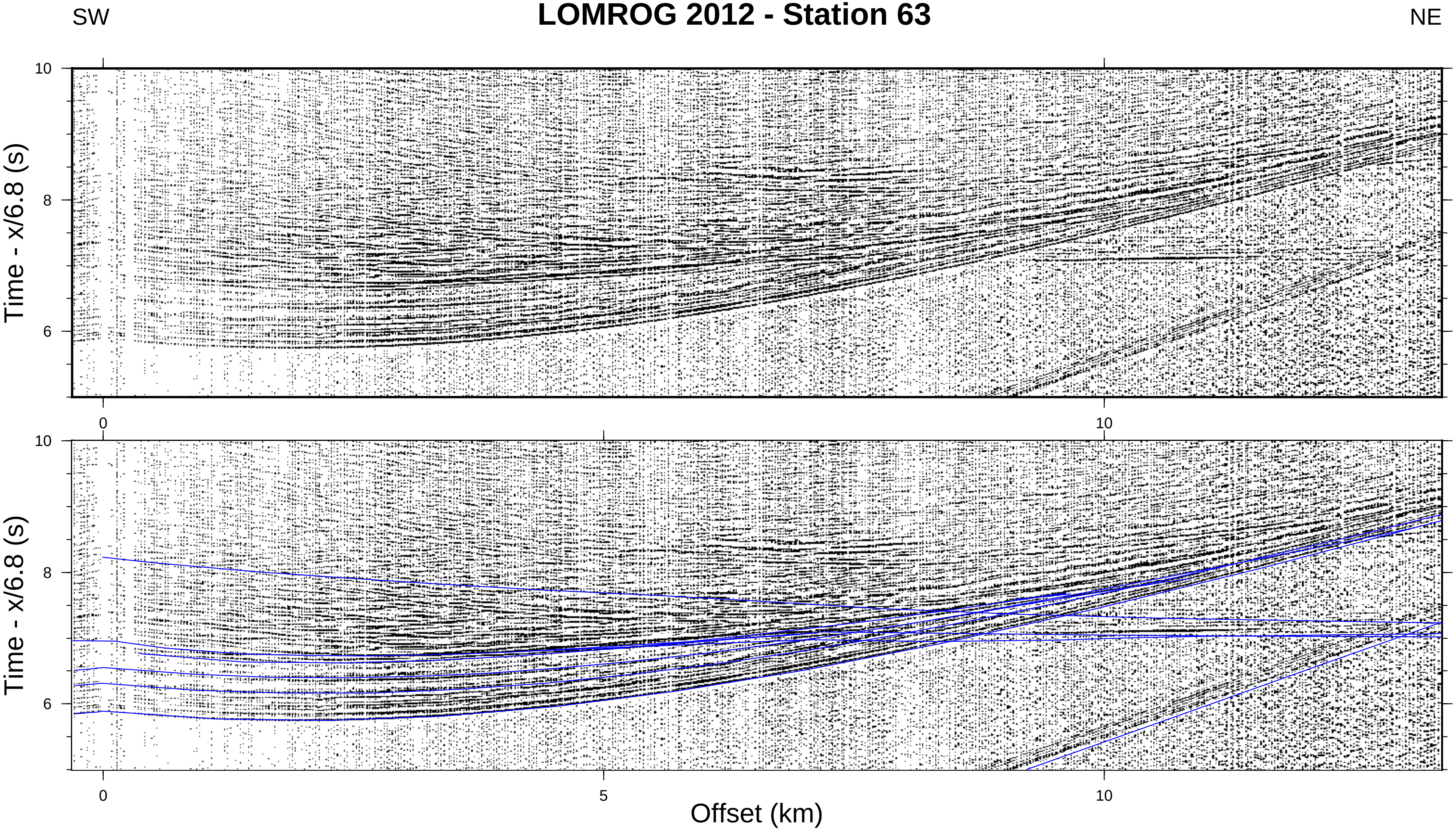

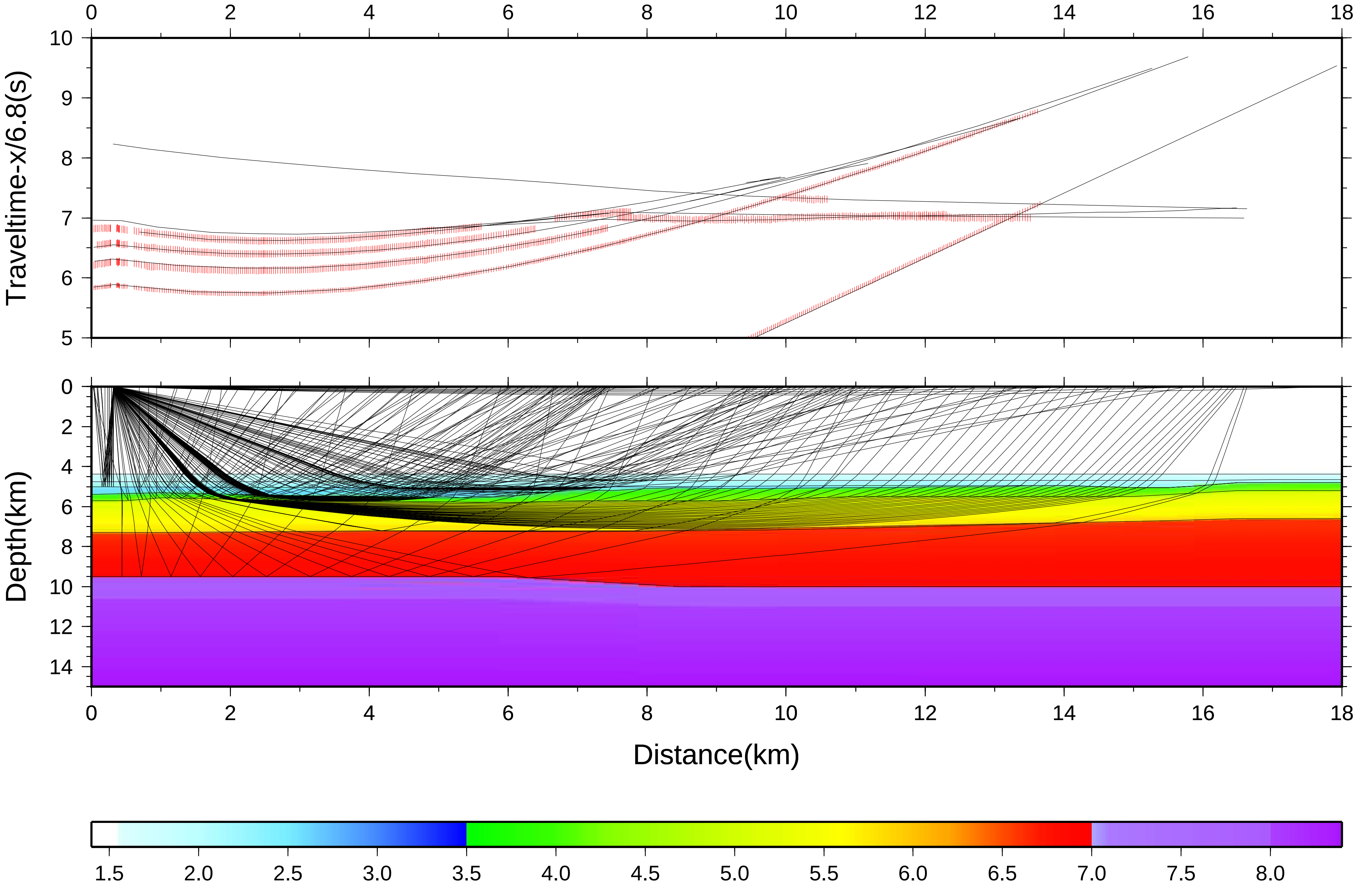

Traveltime-x/6.8(s)
Depth(km)
Distance(km)
0
2
4
6
8
10
12
14
16
18
5
6
7
8
9
10
1.5
2.0
2.5
3.0
3.5
4.0
4.5
5.0
5.5
6.0
6.5
7.0
7.5
8.0